7-29-2015

Understanding Mechanistic Details of Neuroinflammatory Pathways Stimulated by the Alzheimer's Disease Amyloid-Beta Protein

Shana Usery
University of Missouri-St. Louis, set5g8@mail.umsl.edu

UNDERSTANDING MECHANISTIC DETAILS OF NEUROINFLAMMATORY PATHWAYS STIMULATED BY THE ALZHEIMER'S DISEASE AMYLOID-BETA PROTEIN

By

Shana E. Usery

M.S. Chemistry and Biochemistry, University of Missouri-St. Louis, 2011
B.S. Chemistry with an emphasis in Biochemistry, Lindenwood University, 2009

A Dissertation

Submitted to the Graduate School of the

UNIVERSITY OF MISSOURI-ST. LOUIS

In Partial Fulfillment of the

Requirements for the Degree

of

Doctor of Philosophy

in

CHEMISTRY

with an emphasis in Biochemistry

August 2014

University of Missouri-St. Louis

Saint Louis, Missouri

Advisory Committee
Michael R. Nichols, PhD
Cynthia M. Dupureur, PhD
Chung F. Wong, PhD
Wendy M. Olivas, PhD

For my husband and family

ACKNOWLEDGEMENTS

First of all I would like to thank my advisor, Dr. Michael R. Nichols. When joining the program, I knew nothing about graduate school but he accepted me into his lab anyways. Along this journey he has given me so much guidance and support and it is greatly appreciated. Not only has he taught me a lot about science and research, but also about how to professionally handle certain situations. I would also like to thank my committee members, Dr. Chung Wong, Dr. Cynthia Dupureur, and Dr. Wendy Olivas. They have provided me with much support, given many valuable suggestions and always had their door opened if I ever had any questions.

I would not be in the position I am right now if it were not for my past and present colleagues. I would specifically like to thank Geeta Paranjape for taking the time to train me during her remaining time in the laboratory; I truly enjoyed working alongside her. I also sincerely appreciate Sanjib Karki, Ben Colvin, and Lisa Gouwens along with our many masters and undergraduate students for all their excellent team-work and stimulating discussions. I would like to extend my gratitude to David C. Osborn for his microscopy imaging and also the other laboratories that I have collaborated with like the Demchenko and Stine (specifically Dr. Yih Horng Tan) laboratories.

Last but not least, I would truly like to thank my family and friends, especially my husband, mom, and dad. They have been my rocks throughout not only my PhD career, but in life and I appreciate them more then they will ever know.

TABLE OF CONTENTS

PAGE

LIST OF TABLES

LIST OF FIGURES

LIST OF ABBREVIATIONS

Aβ	Amyloid-beta
AD	Alzheimer's disease
AFM	Atomic force microscope
ApoE	Apoliporotein E
APLP	APP-like protein
BACE	β-site APP-cleaving enzyme
BBB	Blood brain barrier
BCA	Bicinchoninic acid
BSA	Bovine serum albumin
c*	Critical concentration
CD	Circular dichroism
CNS	Central nervous system
DAMPs	Danger-associated molecular patterns
DMSO	Dimethyl sulfoxide
ECL	Enhanced chemiluminescence
ELISA	enzyme-linked immunosorbent assay
EM	Electron microscopy
EPR	Electron paramagnetic resonance
aCSF	Artificial cerebrospinal fluid
ADDLs	Aβ-derived diffusible ligands
AICD	APP intracellular domain
APP	Amyloid precursor protein
ASC	apoptosis-associated speck-like protein containing a CARD
BM	Bone marrow
C	Protein concentration
CARD	caspase recruitment domain
CGA	Chromogranin A
CSF	Cerebrospinal fluid
DLS	Dynamic light scattering
DMEM	Dulbecco's modified Eagle's medium
EDS	energy dispersive X-ray spectroscopy
EOAD	early-onset AD
ER	Endoplasmic reticulum
FBS	Fetal bovine serum

FPLC	Fast protein liquid chromatography	FTIR	Tourier-transform infrared
GFP	Green fluorescent protein	GM-CSF	Granulocyte macrophage colony-stimulating factor
GuHCl	Guandium hydrochloride		
HDX-MS	Hydrogen/deuterium exchange mass spectrometry	HFIP	Hexafluoroisopropanol
		HPC	high pathology control
HRP	horseradish peroxidase	IFN	Interferon
IgG	immunoglobulin G	IL	Interleukins
KO	Knock out	LBP	LPS-binding protein
LDH	Lactate dehydrogenase	LOAD	Late-onset AD
LPS	Lipopolysaccharide	LTP	Long term potentiation
M-CSF	Macrophage- colony-stimulating factor	MnSOD	Manganese superoxide dismutase
MyD88	Myeloid differentiation protein 88	$MyD88^{-/-}$	MyD88 Knock out
ND	Nondemented	NFT	Neurofibrillary tangles
NLR	Nod-like receptor	NMDA	N-methy-D-aspartate
NMR	Nuclear magnetic resonance	NO	Nitric oxide
PAMPs	Pathogen associated molecular patterns	PBS	Phosphate buffered saline
		PET	Positron emission tomography
PHF	Paired helical filaments		
PMA	Phorbol 12-myristate 13-acetate	PMS	phenazine methosulfate
PRR	Pattern recognition receptor	PS	Presenilin
PVDF	Polyvinylidene difluoride	QLS	Quasielastic light scattering
R_H	Hydrodynamic radius	ROS	Reactive oxygen species

RQ	Relative quantities
SDS	Sodium dodecyl sulfate
SEC	Size exclusion chromatography
SEM	Scanning electron microscopy
STEM	Scanning transmission electron microscopy
TEM	Transmission electron microscopy
ThT	Thioflavin-T
TMB	tetramethylbenzidine
TNFR	TNF receptor
UT np-Au	Ultra-thin nanporous gold
WT	Wild type
XTT	2,3-bis(2-methoxy-4-nitro-5-sulfophenyl)-2H-tetrazolium-5-carboxanilide
RT-qPCR	Reverse transcription quantitative polymerase chain reaction
SR	Scavenger receptors
SSNMR	Solid state NMR
TACE	TNFα converting enzyme
THF	tetrahydrofuran
TLR	Toll-like receptors
TNFα	Tumor necrosis factor-alpha
UF-Au	Ultra-flat gold np-Au
	Nanoporous gold monolith
XRD	X-ray diffraction

ABSTRACT

Terrill-Usery, Shana., Ph.D., University of Missouri-St. Louis, August 2014. Understanding Mechanistic Details of Neuroinflammatory Pathways Stimulated by the Alzheimer's Disease Amyloid-Beta Protein. Major Professor: Michael. R. Nichols.

Alzheimer's disease (AD) is characterized by neuroinflammation. Senile plaques composed of aggregated amyloid-β protein (Aβ) are found in AD patients' brains. The Aβ is formed by the proteolytic cleavage of the amyloid precursor protein (APP) resulting in Aβ fragments that are 39-42 amino acids in length. The two most common peptides are Aβ(1-40) and Aβ(1-42), which differ by two amino acids, isoleucine and alanine. Within the brain of AD patients, Aβ monomer self-assembles to form several aggregate morphologies, including oligomers, protofibrils, and fibrils. Activated microglial cells and associated secreted proinflammatory cytokines surround these plaques producing a localized inflammatory environment in the brain. Several innate-immune pathways, including Toll-like receptors (TLRs) and the NLRP3 inflammasome, have been implicated in AD inflammation. Aβ plays a primary role in activating these pathways likely contributing to the progressive neurodegeneration in AD. In order to better understand the complexities of this interaction, I investigated the inflammatory response of microglia to Aβ(1-42) and Aβ(1-42)/Aβ(1-40) protofibrils, along with additional biophysical properties. Increased understanding of these pathological events will expand the current model of Aβ neuroinflammatory pathways and help identify new therapeutic targets for AD.

My research has demonstrated that the Aβ(1-42) protofibrils triggered a time- and TLR/MyD88-dependent process that produced inflammatory cytokines tumor necrosis factor alpha (TNFα) and interleukin-1β (IL-1β) mRNA and intracellular pro and mature forms of IL-1β protein. Despite previous reports suggesting that NLRP3 activation requires two signals from two distinct molecules, my research indicated that Aβ(1-42) protofibrils alone could efficiently prime (TLR-dependent pro-IL-1β production) and activate (cleavage of pro-IL-1β to mature-IL-1β) the NLRP3 inflammasome. However, the increased intracellular mature-IL-1β did not translate into greater IL-1β secretion. Instead, we found that Aβ was able to elicit a very rapid, unsustainable, yet re-inducible quantized burst of secreted IL-1β, which occurred prior to Aβ priming of the microglia. These findings suggested a basal level of either pro- or mature-IL-1β in the cultured primary microglia yet revealed multiple sites of IL-1β regulation by Aβ(1-42) protofibrils. These sites, which are potential therapeutic targets, include TLR/MyD88-mediated priming, NLRP3 inflammasome activation, and modulation of the IL-1β secretory process.

Different ratios of Aβ(1-42)/Aβ(1-40) were used in studies aimed at exploring the effect of Aβ(1-40) on Aβ(1-42) aggregation. Reconstitution of dry Aβ(1-42)/Aβ(1-40) peptide mixtures at different ratios resulted in immediate protofibril formation. However, size exclusion chromatography (SEC)-purification of the mixed solutions indicated that as the ratio of Aβ(1-42)/Aβ(1-40) decreased, the amount of SEC-isolated protofibrils decreased and the monomer increased. Subsequent SEC studies showed that if the Aβ(1-42) concentration was held constant while increasing the Aβ(1-40) concentration, there was no change in the amount of SEC-isolated protofibrils formed, while monomer increased. An Aβ C-terminal-selective ELISA was employed to directly measure the Aβ(1-42)/Aβ(1-40) ratio of protofibrils and monomers after SEC-separation. The combination of these two strategies as well as other biological and biophysical studies suggested that Aβ(1-40) may not significantly interact with Aβ(1-42) during protofibril formation.

Separate collaborative studies with the Stine and Demchenko laboratories in the UMSL Department of Chemistry and Biochemistry were also conducted in order to study the biocompatibility of BV-2 microglial cells on different gold substrates and the antagonistic properties of Lipid A analogs in LPS-induced THP-1 macrophages, respectively. The gold surface biocompatibility studies (Stine collaboration) showed that all four surfaces (glass, UF-Au, UT np-Au, and np-Au) tested were metabolically non-toxic, non-disruptive to the cellular membranes and compatible with microglia functional assays, while all but one (np-Au) supported microglia growth and proliferation. The LPS-induced antagonist studies (Demchenko collaboration) analyzed the antagonistic or inhibitory effect of six different Lipid A analogs, while also observing each compounds toxicity and agonistic or stimulatory activity. The results determined one compound that inhibited the LPS-induced TNFα response with the lowest IC_{50}, while remaining non-toxic and producing no agonistic activity.

THE INFLUENCE OF GOLD SURFACE TEXTURE ON MICROGLIA MORPHOLOGY ACTIVATION

Yih Horng Tan, Shana E. Terrill, Geeta S. Paranjape, Keith J. Stine and Michael R. Nichols

This publication was due to the collaborative efforts of the Nichols and Stine laboratories. The gold surface biocompatibility studies showed that most of the gold substrates tested were metabolically non-toxic, non-disruptive to the cellular membranes and compatible with microglia functional assays, while one (np-Au) was unable supported microglia growth and proliferation. All imaging within this publication was performed by Dr. Y.H. Tan, who also produced all surfaces necessary. My role in this publication was to perform all cellular plating and further biocompatibility studies. Further descriptions of this publications and my experimental work is found in Chapter 5.

Biomaterials Science

PAPER

View Article Online
View Journal | View Issue

The influence of gold surface texture on microglia morphology and activation†

Cite this: *Biomater. Sci.*, 2014, **2**, 110

Yih Horng Tan,‡ Shana E. Terrill,‡ Geeta S. Paranjape, Keith J. Stine and Michael R. Nichols*

Received 11th April 2013,
Accepted 11th September 2013

DOI: 10.1039/c3bm60096c

www.rsc.org/biomaterialsscience

Microglial cells play a critical role in the propagation of neuroinflammation in the central nervous system. Microglia sense and respond to environmental signals including chemical, physical and biological cues from the surrounding cell/tissue components. In this project, our goal was to examine the effects of surface texture on BV-2 microglia morphology and function by comparing flat and nanoporous gold (np-Au) surfaces to the more conventional glass. The biocompatibility of np-Au with microglia was evaluated using functional cell assays and high resolution imaging with scanning electron microscopy (SEM). Microglia seeded on glass, ultra-flat gold (UF-Au), ultra-thin (UT) np-Au and np-Au monolith were adherent to all surfaces and their viability was not compromised as assessed by multiple toxicity assays. SEM revealed detailed morphological characteristics of adherent microglia and indicated few dramatic changes as a result of the different surfaces. Microglia proliferation was hampered by np-Au monolith but less by UT np-Au and not at all on UF-Au or glass. Microglial activation, measured by tumor necrosis factor α (TNFα) production, was fully functional (and equivalent) on all gold surfaces compared to glass. The present findings should help further the understanding of basic microglia biology on textured surfaces and more fully evaluate np-Au as a multi-functional biocompatible material. The knowledge obtained and technology developed will have a significant impact in the fabrication of nanoelectronic devices, chemical sensor development, porous nanostructured materials for BioMEMs/NEMs integration, and functional biomaterial coatings for drug delivery.

Introduction

Over the past few decades, significant efforts have focused on the development of new intelligent biomaterials or biomembrane-mimicking substrates/interfaces. These materials have the ability to monitor, investigate, and modulate biological behavior. The development of this capability will improve, and perhaps revolutionize therapeutics such as the repair of damaged tissues due to trauma, disease, or congenital abnormalities. However, such novel biomimetic interfaces must continually be evaluated for biocompatibility properties including *in vivo* stability, stimulation of the host immune response, and interaction with living cells.[1] Gold has been investigated for many years as a potential biomaterial, both for application in biomedical devices and for use as a cell culture substrate. Many of these studies have investigated the effect of gold nanoscale topography or chemical modification of the gold surface on cellular response.[2–5] The advantages of gold stem from its chemical stability, high conductivity[6] and the advances in gold-thiol chemistry for presenting ligands or immobilized proteins for cell adhesion studies.[4,7–9] Numerous examples of cell culture on gold or chemically-modified gold substrates have been reported and these studies demonstrate that cell adhesion is influenced by the size and geometric shape of the gold surface, the chemical and protein composition on the substrate surface or the mechanical properties of the substrate.[10,11] In addition to bulk gold substrates, subnanometer size colloidal Au clusters or nanoparticles have attracted interest for potential applications for drug delivery or use as imaging contrast agents.[12–14] Recently, it was demonstrated that microglial uptake of gold nanoparticles and subsequent microglial activation was influenced by the shape of the nanoparticles.[15]

Nanoporous gold is a member of a new class of mesoporous metals that possess pores and ligaments ranging from tens to hundreds of nanometers in scale. These features are of increasing interest due to their potential applications in

Department of Chemistry and Biochemistry and Center for Nanoscience, University of Missouri-St. Louis, One University Boulevard, St. Louis, Missouri 63121, USA. E-mail: nicholsmic@umsl.edu; Fax: +1 (314) 516-5342; Tel: +1 (314) 516-7345

†Electronic supplementary information (ESI) available. See DOI: 10.1039/c3bm60096c

‡These two authors contributed equally to this work.

biosensors,[6,16] catalysis,[17] and cell culture platforms.[5] The naturally occurring rough surface features of nanoporous gold are ideal for decreasing surface impedance and enhancing electrical potential stability in an implantable biomedical device.[18,19] The resistance of nanoporous gold to corrosion and oxidation combined with its porosity makes it a unique material with significant feasibility as a potential platform for adherent cell culture and drug delivery.[5] Numerous compatibility studies between mammalian cells and metallic surfaces, particularly gold, have been conducted recently reflecting the increased interest in this area. These studies have utilized both neurons and immune cells and have investigated a variety of interactions including internalization of gold nanoparticles, microglial activation by metal surfaces, differential cell adherence to electrodes, and gold surface effects on astrocyte morphology.[5,15,20] Despite these important advances there are still numerous questions surrounding cell–gold surface interactions and it is important to demonstrate the effects of new types of substrates on cell adherence, viability, morphology, and function within the same study.

In the current study, gold substrates with different porosities, including ultra-thin nanoporous gold, were evaluated for their ability to support microglial survival, growth, and functional cytokine production upon stimulation. Scanning electron microscopy (SEM) was used in conjunction with cellular assays to evaluate, at high resolution, whether microglia morphology and function is perturbed by varied surfaces. The knowledge obtained in the present study may have implications for the fabrication of nanoelectronic devices and the design or improvement of microelectrode arrays for chronic deep-brain microstimulation and recording.[21]

Materials and methods

Preparation of nanoporous gold (np-Au) monoliths

Preparation of np-Au plates (monoliths) was performed as previously described,[6,8,22] with a few modifications. Briefly, 10 carat yellow gold sheets (4.0 inch × 2.0 inch × 0.0098 inch, $L \times W \times H$, respectively) were purchased from Hoover and Strong (Richmond, Virginia, USA). The stated atomic composition of this commercial alloy is 41.7% Au, 20.3% Ag, and 38% Cu. Depending on the experiment protocols, the 10 carat sheet was cut into pieces of size of 8.0 mm × 8.0 mm × 0.25 mm, $L \times W \times H$, respectively, and placed in a concentrated nitric acid bath for 48 hours (the acid solution was refreshed at the 24 hour time point). Trace metal grade nitric acid was purchased from Fisher Scientific (Pittsburgh, USA). After the nitric acid dealloying treatment, samples were rinsed thoroughly with Milli-Q water (18.2 MΩ cm resistivity at 25 °C, Millipore Corporation, Boston, USA) to neutral pH, followed by rinsing with HPLC grade ethanol (Sigma Aldrich, St. Louis, Missouri, USA). The microstructure of np-Au was characterized using scanning electron microscopy using a JEOL JSM-6320F field emission SEM (JEOL USA, Inc., California, USA).

Fabrication of ultra-thin nanoporous gold (UT np-Au) and ultra-flat gold (UF-Au)

UT np-Au was prepared from commercially available gold/silver leaf (used as received, Sepp Leaf Products, Inc. New York, NY, USA) which was cut into a 2.0 inch × 2.0 inch dimension and floated on a concentrated nitric acid bath for 4 hours. After the nitric acid de-alloying treatment, the acid solution was carefully exchanged with Milli-Q water to neutral pH. The free floating np-Au leaf was then removed by dipping a circular coverslip (1.0 cm diameter), previously coated with polydimethylsiloxane (PDMS) (Dow Corning, USA), underneath the porous gold leaf. As the glass slide was removed, the free-floating leaf adhered smoothly onto the surface of the coverslip. After curing the PDMS pre-polymer in an oven for 3 hours, the sample was rinsed and kept in deionized water. For UF-Au preparation, freshly cleaved ruby muscovite mica was coated with a gold film, 200 nm thick, and glued onto a glass coverslip.[16] The UF-Au is acceptable for cell seeding after stripping off from the mica sheet.

Scanning electron microscopy analysis

Surface morphology and general structure of np-Au monolith, UF-Au, UT np-Au and glass were studied by SEM using a JEOL JSM-6320F field emission instrument. Microglia plated on substrate surfaces were fixed with 3.5% glutaraldehyde followed by 4% osmium tetroxide. Fixed cell samples were sputter-coated with 50 nm gold using an Anatech LTD instrument and imaged.

Energy dispersive X-ray analysis (EDS)

The presence of gold in the acid dealloy substrates was determined with EDS by examination of the spectrum for peaks near 2.13 and 9.71 keV (gold); 2.98 keV (silver); and 0.93 and 8.04 keV (copper). No special preparation of the samples was required for EDS analysis. Five EDS spectra were captured and analyzed from different regions of each type of gold substrate. For comparison, the EDS spectrum was obtained for 10 carat yellow gold sheet and gold/silver leaf prior to acid treatment (ESI, Fig. S1†). All EDS spectra were captured using a Link Pentafet 6886 Model accessory (Oxford Microanalysis Group, UK).

Cell culture and stimulation

BV-2 murine microglial cells were cultured in Dulbecco's modified Eagle's medium (DMEM, 4.5 g L^{-1} glucose) (Hyclone, Thermo Fisher Scientific, Pennsylvania, USA) containing 50 U mL^{-1} penicillin, 50 μg mL^{-1} streptomycin, 50 μM β-mercaptoethanol, and 5% fetal bovine serum (FBS, Hyclone).[23] For cellular studies, microglia were removed from culture flasks with 0.25% trypsin and seeded at a density of 5×10^5 cells mL^{-1} onto prepared glass or gold substrates situated in individual wells of a sterile 24-well cell culture plate in growth medium. Prior to cell treatment, medium was replaced with fresh serum-free medium followed by stimulation with ultra-pure lipopolysaccharide (LPS) from *E. coli* K12 (InvivoGen, San Diego, CA, USA) at a final concentration of

10 ng mL^{-1} (or otherwise stated). The cells were incubated at 37 °C for 24, 48, or 72 h in 5% CO_2 and the medium was collected and stored at −20 °C for subsequent analysis by enzyme-linked immunosorbent assay (ELISA) or for counting of the cells in the medium. The background cellular response was assessed with the same volume of sterile water used as the vehicle for LPS.

ELISA analysis

Measurement of microglia-secreted TNFα levels in the medium was determined by ELISA as previously detailed.[23] Briefly, 96-well plates were coated overnight with monoclonal anti-mouse TNFα capture antibody, washed with phosphate-buffered saline (PBS) containing 0.05% Tween-20 and blocked with PBS containing 1% BSA, 5% sucrose and 0.05% NaN_3 followed by a wash step. Successive treatments with washing in between were done with samples and standards, biotinylated polyclonal anti-mouse TNFα detection antibody in 20 mM Tris with 150 mM NaCl and 0.1% BSA, streptavidin-horseradish peroxidase (HRP) conjugate, and equal volumes of HRP substrates 3,3′,5,5′-tetramethylbenzidine and hydrogen peroxide. The reaction was stopped by the addition of 1% H_2SO_4 solution. The optical density of each sample was analyzed at 450 nm with a reference reading at 630 nm using a SpectraMax 340 absorbance plate reader (Molecular Devices, Union City, CA, USA). The concentration of TNFα in the experimental samples was calculated from a mouse TNFα standard curve of 15–2000 pg mL^{-1}. When necessary, samples were diluted to fall within the standard curve.

XTT cell viability assay

Viability of BV-2 microglia was determined by using an XTT [2,3-bis(2-methoxy-4-nitro-5-sulfophenyl)-2*H*-tetrazolium-5-carboxanilide] assay as previously described.[23] Cellular metabolic activity was monitored by mitochondria-mediated reduction of XTT (Sigma Aldrich, St. Louis, MO, USA). XTT assay was also used in a cell-free manner to rule out the possibility of any bacterial contamination or contribution of the glass or gold substrates to XTT reduction. In the cellular XTT assay, control cells or cells exposed to LPS for 24 h were further incubated with 0.33 mg mL^{-1} XTT and 8.3 μM phenazine methosulfate (PMS) (Acros, Morris Plains, NJ, USA) in RPMI medium without phenol red for 2 h at 37 °C. The extent of XTT reduction was determined from the absorbance of the reduced form of XTT at 467 nm.

LDH release assay

The viability of the BV-2 microglia was also measured by the release of intracellular lactate dehydrogenase (LDH) into the cell medium. The LDH activity assay which involves LDH-mediated reduction of nicotinamide adenine dinucleotide (NAD^+), was coupled to XTT reduction to increase sensitivity, in a procedure modified from Korzeniewski *et al.*[24] Briefly, following cell incubation for 24 h in the absence or presence of LPS, the medium was removed and centrifuged to remove any detached microglia. 25 μL conditioned medium was added to a 2 : 1 ratio of LDH reaction cocktail and XTT/PMS resulting in final concentrations of 1 mM NAD^+, 25 mM lactate and 95 mM CAPS buffer pH 10.0 (all from Sigma Aldrich, St. Louis, MO, USA), 0.33 mg mL^{-1} XTT and 8.3 μM PMS. The extent of LDH released (LDH activity) was measured by the change in absorbance of reduced XTT at 467 nm over a linear time course of 5 minutes.

Cell adhesion and growth

BV-2 microglia were plated overnight and stimulated as described above. After 24 hours of treatment, the medium was removed and the cells in the medium were counted using a Cellometer Auto T4 Plus SK-150 cell counter (Nexcelom Bioscience LLC, Lawrence, MA, USA). The number of cells recovered in the medium was divided by the total number of cells plated to determine the percentage of detached cells, and indirectly, the percentage of cells attached to the glass and gold substrates. The extent of microglia proliferation was determined by direct counting of the adherent cells over time. At each time point, the medium was removed and the adherent cells were detached with 0.25% trypsin and counted as described above.

Results

Characterization of gold substrate surfaces

Four substrates, including glass, ultra-flat gold (UF-Au), ultrathin nanoporous gold (UT np-Au) and nanoporous gold monolith (np-Au), were characterized by SEM. UF-Au substrate was generated using a well-recognized gold deposition technique which produces a 200 nm thick layer of gold on mica that can be subsequently glued to a glass coverslip.[16] Stripping off the mica sheet leaves templated gold on glass. For comparison, a glass coverslip was used as a control in this study. Since glass is a poor conductor, approximately 10 nm of gold was sputtered on one side of the glass coverslip in order to enable SEM characterization. SEM images revealed relatively flat and smooth surfaces for the glass and the UF-Au substrate (Fig. 1A and B). In contrast, the corrugated morphology of the np-Au substrate was prepared as previously described.[6,8,16] The porous metals, UT np-Au and np-Au, were formed by de-alloying and exhibited a completely irregular morphology for both the metallic gold ligaments and pore channels (Fig. 1C and D). The irregular structure made it difficult to quantitate differences between the gold substrates. However, randomized manual measurements were made using the images in Fig. 1C and D which are representative of numerous samples. These measurements revealed an average ± standard error pore diameter and ligament thickness for UT np-Au of 52.8 ± 2.0 nm (n = 157 measurements) and 51.7 ± 1.5 nm (n = 185 measurements), respectively. Values for the np-Au monolith plate average pore diameter and ligament thickness were 25.1 ± 0.9 nm (n = 228 measurements) and 40.5 ± 1.2 nm (n = 210 measurements), respectively. In addition to the notable pore diameter difference between the two nanoporous gold

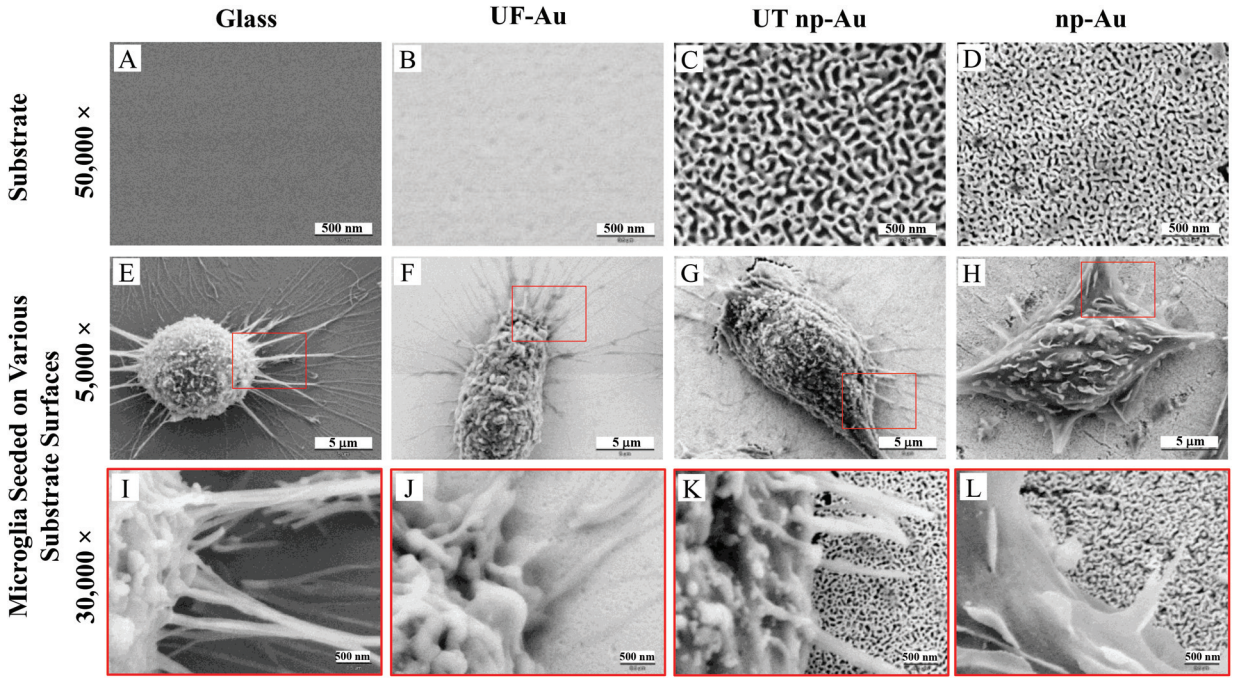

Fig. 1 Scanning electron microscopy images of BV-2 murine microglial cells seeded on different substrate surfaces. (A–D) 2.4 μm × 1.8 μm SEM images of blank glass coverslip, UF-Au, UT np-Au and np-Au monolith plates. (E–H) 24.0 μm × 18.0 μm (or 5000× magnification) SEM images of BV-2 microglia adhered on the respective substrate surfaces in the top panel. (I–L) SEM images at 30 000× magnification showing major and minor processes of microglia interacting with the substrate surfaces. The red boxes in panels E–H indicate areas that are shown at higher magnification in panels I–L. Presented images are representative of n = 12 images for each condition at each time point over four separate experiments.

substrates, another physical difference of these substrates was their thickness (z dimension). From our analysis, the UT np-Au substrate was about 125 nm thick after transfer onto a glass coverslip, while SEM cross-section imaging indicated that the thickness of the np-Au monolith plate was approximately 250 μm.

Qualitative X-ray analysis of substrate specimens

The nanoporous gold substrates were prepared by acid de-alloying to remove the less noble metals. However, residual amounts of these metals may form metal oxides that could directly affect microglia by impeding their proliferation or viability. The cellular toxicity may occur *via* interference with the cell's normal metabolic process or metal-induced production of reactive oxygen species causing oxidative stress in cells.[25,26] To rule out the presence of high amounts of residual metals remaining after the acid de-alloying process, energy dispersive X-ray spectroscopy (EDS) analysis was conducted to determine the composition of metals (such as, gold, copper and silver) on the gold substrates. This approach is simple and promising because (1) each element has a unique set of peaks in its X-ray spectrum and (2) energy dispersive X-ray analysis, also known as EDX or XEDS, has detection limits of approximately 0.1% in bulk materials.[8] Gold is known to be biocompatible but the presence of other metals may yield metal oxides that can damage and kill cells.[25,26] If the residual content of the copper or silver is high, then oxidative stress might reduce microglia density on the np-Au substrate. Fig. 2 shows the EDS spectra of the four different substrates used in our investigation. The major peaks near 2.13 and 9.71 keV are the unique set of peaks for gold and are observed for UF-Au (panel B), UT np-Au (panel C), np-Au monolith (panel D) but not glass (panel A). Trace amounts of other metals were noted based on the minor peaks observed at different X-ray energies. A noticeable peak near 0.50 keV (Fig. 2A) is the typical X-ray energy peak for oxygen (0.53 keV) and is due to the oxide compositions (~64% SiO_2) of the glass coverslip. The other peaks in Fig. 2A near 1.04 and 1.74 keV belong to sodium and silicon, respectively. Based on the four X-ray spectra collected, various minute amounts of residual metals were present on these substrate surfaces. The X-ray energy peaks for copper (0.93 and 8.04 keV) and silver (2.98 keV) are insignificant when compared to those of gold. Therefore, the potential for silver or copper oxide toxicity or oxidative stress that may damage cells or prevent their adherence to the np-Au substrate is minimal. EDS spectra for yellow gold and gold foil before the acid de-alloying procedure are provided in Fig. S1.† The prepared and characterized gold surfaces were then examined for their ability to support microglial growth and function.

SEM provided topographical imaging of each material surface. Additionally, this high resolution technique was also used to visually characterize temporal changes in microglial cell morphology and cell–cell interactions. The immortalized BV-2 murine microglial cell line was used in this investigation and the cells were seeded onto the four surfaces as described in the Materials and methods section. Fig. 1E & I, F & J, G & K,

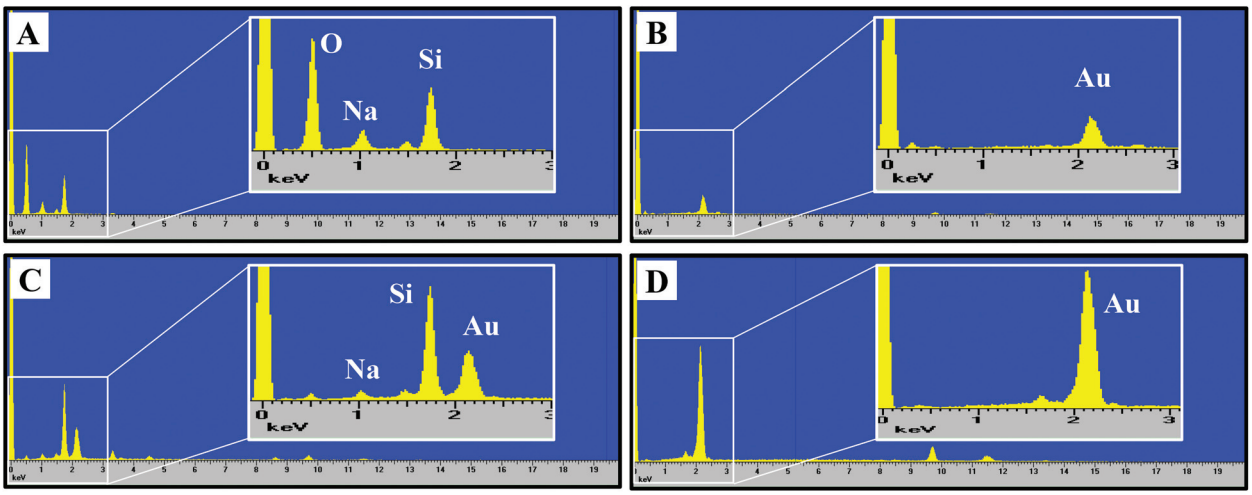

Fig. 2 Energy-dispersive X-ray spectra for (A) glass, (B) UF-Au, (C) UT np-Au, (D) np-Au monolith. The K emission lines for O (0.53 keV), Na (1.04 keV) and Si (1.74 keV) were observed for glass. The typical X-ray energy peaks for gold are 2.13 and 9.71 keV.

and H & L showed microglia cells on glass, UF-Au, UT np-Au and np-Au surfaces, respectively. Since BV-2 microglia are adherent cells, no prior surface modification of these substrates was necessary to artificially assist or improve cell adhesion onto the substrate surfaces. SEM images showed a variety of microglia morphologies including rounded, unipolar, bipolar, and flattened (amoeboid) and all were observed routinely on all four types of substrate surfaces. Microglia on each of the four substrate surfaces tended to exhibit many short and branched processes extending outward from the cell and interacting with neighboring cells and the substrate surfaces. Although major processes were observed on many of the immobilized microglia, we cannot conclude that a distinct, or favored, cell morphology was adopted by microglia for any of the specific types of substrate used. The dimensions of the microglia were between 15–20 μm on the long axis, and 10–15 μm on the short axis and did not appear to be influenced by the type of substrate used as a platform.

Adherence of microglia to the substrate surfaces

The ability of BV-2 microglia to adhere to glass and different gold substrates was determined by quantifying the number of adherent microglia after plating of the cells and overnight incubation at 37 °C in 5% CO_2. Microglia adherence was exceptional for glass, UF-Au, and UT np-Au (>94% adherent cells) but somewhat lower for np-Au (83% adherent cells) (Fig. 3). There was no significant statistical difference between glass, UF-Au, and UT np-Au. However, there was a significant difference in microglia adherence between glass and np-Au ($p < 0.001$).

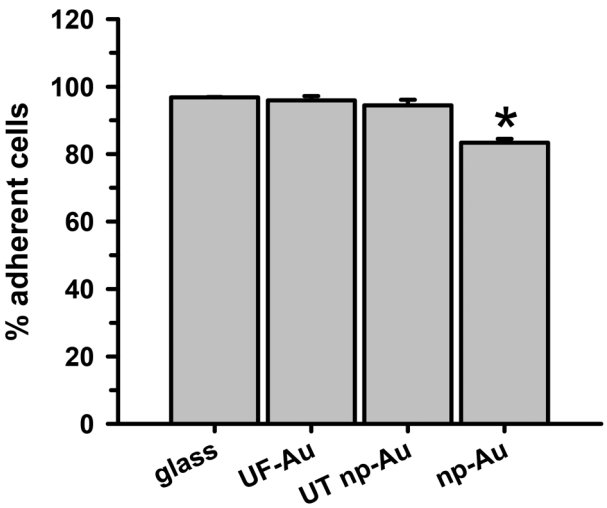

Fig. 3 Ability of microglia to adhere to different substrates. BV-2 microglia (2×10^5 cells) were plated on different substrates ($n = 4$ for each surface) and incubated overnight at 37 °C and 5% CO_2 to allow for cell adherence. The number of adherent cells was determined as described in the Methods. Data and error bars represent the mean and std error for $n = 4$ trials in one experiment. A statistically significant difference, using a student t-test, was found in microglia adherence between glass and np-Au (*$p < 0.001$).

Viability of BV-2 microglia

In order to determine whether there were toxic effects of the gold substrates (with various textures) on microglia after surface adherence, the metabolic integrity of the seeded microglia was determined using an XTT cell viability assay. The standard XTT assay relies on mitochondrial-mediated reduction of XTT by nicotinamide adenine dinucleotide (NADH) *via* trans-plasma membrane electron transport and an electron mediator.[27] This approach generates a water-soluble orange-colored reduced formazan product which rapidly dissolves into the medium eliminating the need for additional steps that may interfere with the assay. Since this conversion only occurs in viable cells, the reduced orange formazan solution can be quantified spectrophotometrically (absorbance at 467 nm). Microglia attached to glass, UF-Au, and UT np-Au were comparable in their viability (similar production of reduced XTT) (Fig. 4) and very little toxicity was observed.

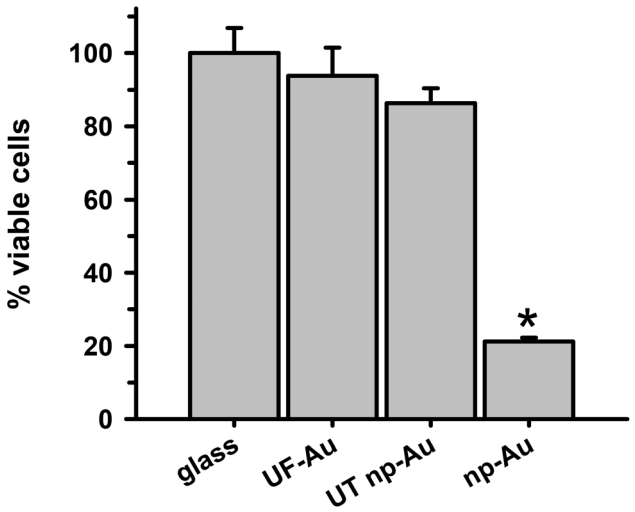

Fig. 4 Analysis of microglia viability by XTT assay. BV-2 microglia (2×10^5 cells) were plated overnight to allow cell adherence followed by incubation for 24 h at 37 °C in 5% CO_2. The medium was removed and cell viability was assessed using a XTT assay as described in the Methods. Reduced XTT absorbance was measured at 467 nm. % cell viability was determined by comparing metabolism of reduced XTT by microglia on UF-Au, UT np-Au, and np-Au to microglia on glass. Data and error bars represent the mean and std error for $n = 12$ measurements for each condition over two separate experiments. A statistically significant difference was found in microglia viability between glass and np-Au ($*p < 0.001$). The other data points were not statistically different from each other.

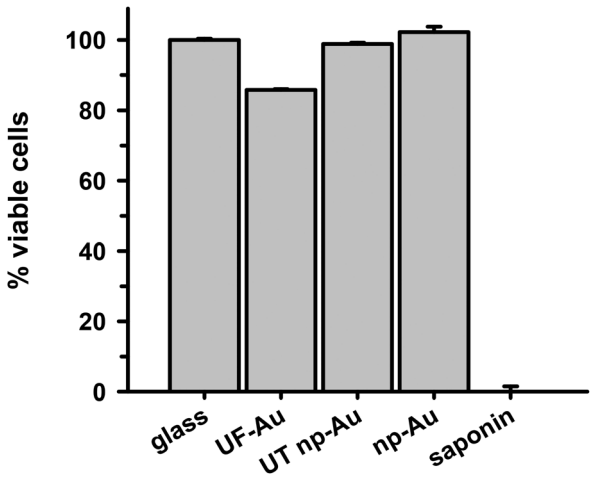

Fig. 5 Cell cytotoxicity determined by LDH release assay. BV-2 microglia (2×10^5 cells) were plated overnight on the four substrate surfaces to allow adherence and then incubated for 24 h as described in the Materials and methods section. Conditioned medium was collected for each sample and analyzed for LDH activity (absorbance per min) as described. The levels of LDH activity in the conditioned medium from untreated or saponin-treated microglia on glass were used as 100% or 0% viability controls respectively. % cell viability for the other samples was determined by comparing LDH activity to the viability controls. Data and error bars represent the mean and std error for $n = 3$ measurements in one experiment for all conditions.

However, cells incubated on np-Au were significantly restricted in their ability to metabolize and reduce XTT. Control (cell-free) wells containing each substrate and XTT showed the background levels of reduced XTT for each sample (Fig. S2†). All of the cell-free substrates showed insignificant absorbance (reduced XTT) when compared to substrate platforms with microglia present. This was expected, as the blank substrates used in this investigation are not known to react or cause reduction of XTT. The low absorbance observed for the microglia on np-Au monolith was rather unexpected since the np-Au monolith contains a similar porous morphology as the UT np-Au substrate (Fig. 1). The cell viability data indicated that the microglia on np-Au monolith were metabolically compromised despite the earlier findings of morphological normality and sufficient adherence of the microglia on np-Au (Fig. 1 and 3). However, it is also possible that the thickness of the np-Au monolith interfered with the production or detection of reduced XTT. Although gold is known for its inertness, either flat or in the presence of variable porosity, this scenario was possible due to the lower levels of background reduced XTT observed for the np-Au control compared to the other substrates (Fig. S2†).

An alternative analysis of cell viability was used to further probe the viability of microglia on the np-Au monolith substrate. A lactate dehydrogenase (LDH) release assay was used to validate the XTT analysis. The presence of LDH activity in the medium is a general indicator of the leakage of intracellular LDH from the cells due to disruption or damage of the membrane integrity. Following incubation of microglia with the various substrates, the cell culture media was collected, centrifuged and the cell free supernatant examined for LDH activity (Fig. 5). Minimal LDH activity was observed in the microglia medium after incubation with all four substrates (Fig. 5). In particular, the np-Au substrate did not elicit LDH release from the adherent microglia indicating that the np-Au monolith was not toxic to microglia. Saponin, a known cellular toxin *via* cholesterol removal and membrane integrity disruption, caused significant LDH release from microglia cultured on glass and served as a positive toxicity control in these experiments (Fig. 5).

Microglia proliferation on substrate surfaces

Cell survival and proliferation are important criteria for substrate biocompatibility. In addition to morphology and toxicity, the four substrates used in our investigation were evaluated for their ability to support cell growth and proliferation. Time dependent studies of microglia seeded onto the four substrate surfaces were carried out at 24, 48 and 72 h (Fig. 6). Quantification of cell density on these surfaces over time indicated that the number of adherent microglia progressively increased on the flat substrate surfaces, such as glass and UF-Au. Microglia density more than doubled from the initial number of seeded cells on the flat surfaces (circles, triangles, Fig. 6). An increase in microglia density was also observed on the UT np-Au substrate (squares, Fig. 6) at the 48 h time point; however, microglia density leveled off after that. The density of

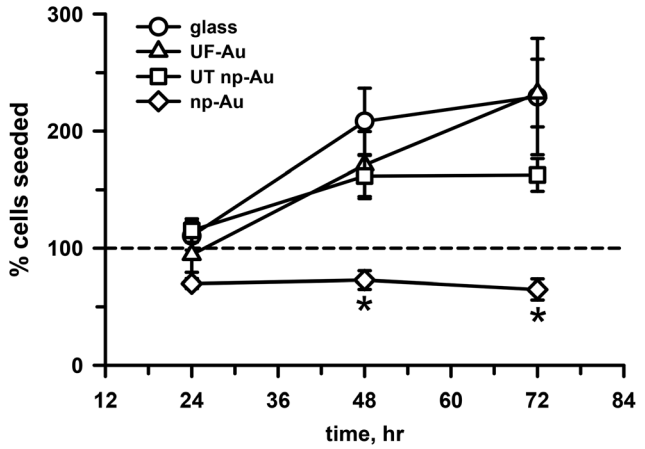

Fig. 6 Microglia density on different substrate surfaces. BV-2 microglia (2×10^5 cells, dashed line) were plated and allowed to grow at 37 °C and 5% CO_2 on glass (circles), UF-Au (triangles), UT np-Au (squares), and np-Au (diamonds) substrates. Cell number was quantified as described in the Materials and methods section at 24, 48, and 72 h. Data points and error bars represent the mean and std error for $n = 7$ measurements for each condition and time point from two separate experiments. Statistical analysis was performed using a student *t*-test and significant differences in microglia density were observed between np-Au and the other samples at both 48 and 72 h ($*p < 0.001$). The other data points were not statistically different from each other.

microglia cultured on np-Au (diamonds, Fig. 6) after 24 hours of seeding was slightly less than the number of cells plated (dashed line, Fig. 6) and did not increase or decrease over time. The difference in microglia growth was particularly striking at 48 h between np-Au and the other substrates. The additional observation that continued growth on UT np-Au was also hampered suggested that the texture had a negative effect on the process of cell division. To ensure consistency in the given experiment, all microglial proliferation studies were carried out simultaneously and similar observation were attained with repeated experiments. The inability of the microglia to grow or proliferate on the texturized np-Au surface helped to explain the contradiction between the earlier XTT and LDH release toxicity results in Fig. 4 and 5. Since the XTT assay was conducted after overnight plating and an additional 24 h incubation, the number of microglia was significantly lower on the np-Au compared to the other substrates. The disparity in microglia cell number explained the notably lower reduced XTT absorbance values for np-Au in Fig. 4.

Microglia morphology upon LPS challenge

LPS, a bacterial-derived endotoxin, is a potent immune system stimulant and the most commonly used trigger for inducing microglial activation.[23,28,29] In this investigation, a time-dependent morphological examination of LPS-stimulated microglia on glass and gold surfaces was carried out. Microglia immobilized onto glass, UF-Au, UT np-Au, and np-Au were challenged with 10 ng mL^{-1} LPS or control vehicle and imaged using high-resolution (2000× magnification) SEM after glutaraldehyde fixation at 0, 2, 6, 10 and 24 hour time points (Fig. 7A). Data for 2 and 10 h time points is not shown. The most frequently observed morphologies again included rounded, unipolar, bipolar, and flattened (amoeboid) shapes. In general, the outer surface morphology of the microglia was generally observed as having rough protrusive structures, such as filopodia, lamellipodia, and surface ruffles. Furthermore, most of the microglia contained many long and short processes (5 μm to 30 μm in length) projecting out of the cell body. Additionally, some cells contained a major process extending from one end of the microglial pole (unipolar), while other microglia had two major processes extending or stretching from two opposite ends of the microglial poles (bipolar) (Fig. 7A). The length of these major processes varied from cell to cell with some of the longest axis extending 20 μm or more. One common, but striking, observation during SEM acquisition was the direct interactions between extended major and minor processes of neighboring microglia. These connecting microglia processes appeared to form conjoining junctions. A global analysis of microglia morphologies was conducted on lower-resolution SEM images to determine the effect of both surface composition and LPS treatment on microglia morphology. A representative image is shown in Fig. S3† along with a description of how the analysis was conducted. The population of rounded, unipolar, bipolar, and flattened microglia states at 24 h was analyzed in the absence or presence of LPS and this distribution is shown in Fig. 7B. By far, the most common microglia morphology was rounded, ranging from 70–85% of the total number of microglia. Varying amounts of the other three populations were observed but a consistent trend was not seen indicating that the four surfaces did not induce cell morphological changes. Furthermore, the morphology of the microglia after 10 ng mL^{-1} LPS challenge did not appear dramatically different compared to unstimulated microglia under the same culture conditions (Fig. 7A, B). However, a slight increase in non-rounded morphologies was noted in the LPS-treated microglia. In a separate experiment, a higher concentration of LPS (100 ng mL^{-1}) was used to treat microglia on the different surfaces and microglia morphology was compared to both untreated and 10 ng mL^{-1} LPS-treated cells. Fig. S4† shows a similar distribution to that in Fig. 7B for the lower LPS concentration with only small differences observed at the higher LPS concentration (Fig. S4†).

Additional studies were done to assess the adherence and viability of LPS-stimulated microglia on glass and gold substrate surfaces. These experiments were conducted in the same manner as those presented in Fig. 3–5 using adherence, XTT, and LDH release assays. No differences were observed in microglia adherence or vulnerability to the glass and gold surfaces between unstimulated and LPS-stimulated microglia (data not shown). The results for LPS-stimulated microglia mirrored those for control microglia in Fig. 3–5 within statistical error.

Cytokine release from microglia on the substrate surfaces

TNFα is a well-documented pleiotropic proinflammatory cytokine and can be produced in the central nervous system by

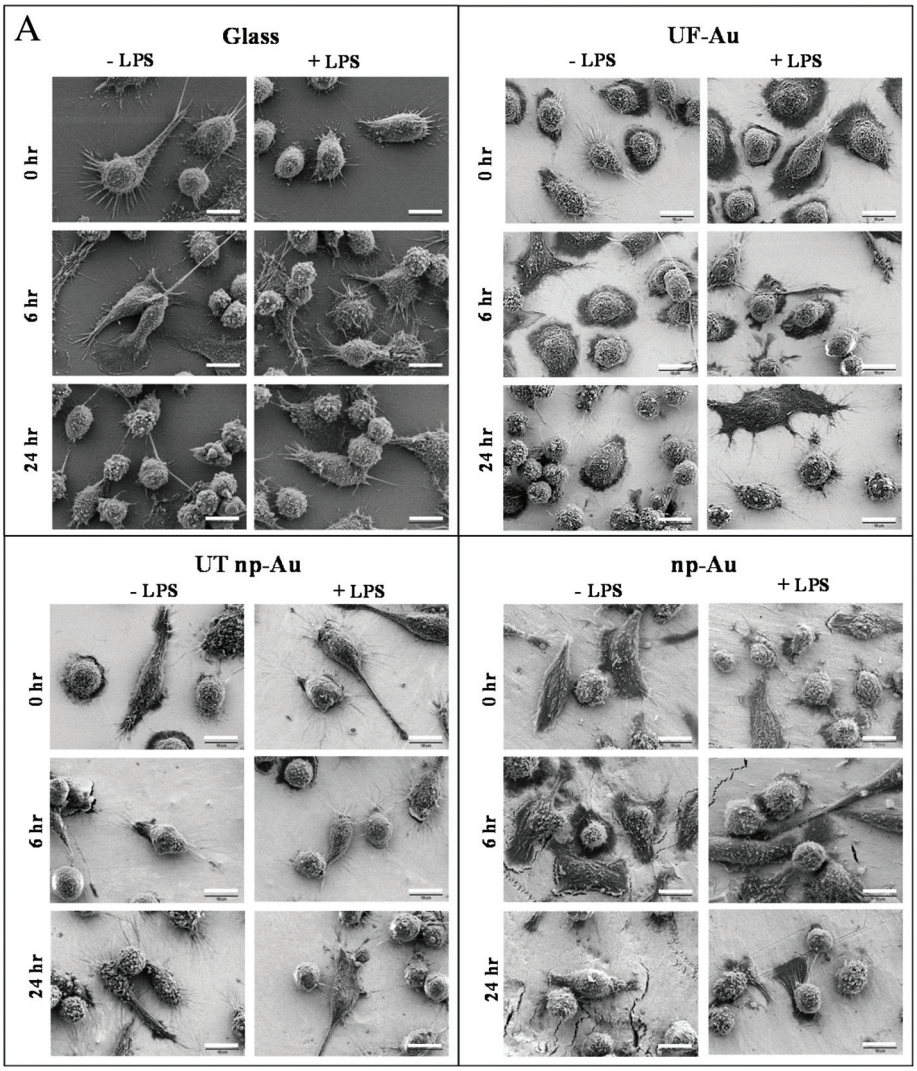

Fig. 7 Microglia morphology on different substrate surfaces with and without challenge by LPS (10 ng mL^{-1}). Panel A. BV-2 microglia were allowed to adhere to glass, UF-Au, UT np-Au and np-Au monolith followed by LPS exposure for 0, 2, 6, 10 and 24 h. At each time point the samples were prepared for SEM imaging as described in the Materials and methods section. Images were captured at an accelerating voltage of 5 kV. Data for 2 and 10 hour time points are not shown for space reasons. All images are 58 μm × 43 μm in size (2000× magnification) and the scale bar is equal to 10 μm. Presented images are representative of n = 12 images for each condition at each time point over four separate experiments. Panel B. Distribution of microglia morphologies on glass, UF-Au, UT np-Au and np-Au monolith in the absence or presence of LPS were analyzed as described in Fig. S3† using lower-resolution SEM images (250× magnification). Four distinct shapes were categorized and depicted in the above plot. Data bars represent the average of six image analyses from two separate experiments. Standard error values are provided in Table S1† in the supplementary material. The percentage of microglia displaying each morphology was determined by dividing the counted number for each by the total number of microglia representing all four shapes in the image. Average total microglia for each condition were glass (–LPS), 424, glass (+LPS), 427, UF-Au (–LPS), 435, UF-Au (+LPS), 268, UT np-Au (–LPS), 316, UT np-Au (+LPS), 282, np-Au (–LPS), 300, and np-Au (+LPS), 306.

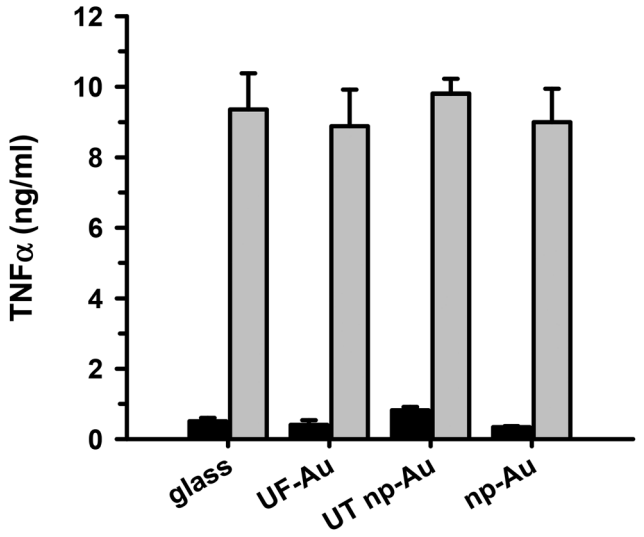

Fig. 8 Microglial inflammatory response upon LPS challenge. BV-2 microglia were allowed to adhere to the substrate surfaces overnight, treated with 10 ng mL^{-1} final concentration of LPS or the same volume of sterile water and incubated for 24 h at 37 °C and 5% CO_2. Subsequently, the supernatant was collected and analyzed for secreted TNFα by ELISA. The black bars are unstimulated control microglia and the gray bars are microglia stimulated with LPS. Values and error bars represent the mean and std error for n = 6 measurements for each condition over two separate experiments.

activated microglia and astrocytes during the inflammatory response.[30] It is well-established that LPS infection induces microglial production of TNFα along with other proinflammatory cytokines interleukin (IL)-1 and IL-6. We, and others, have assessed the level of microglial activation based on the amount of TNFα production[23,31] and we used it here as a primary marker of the microglia inflammatory response to LPS. In order to determine if microglia adherence to texturized gold surfaces had an impact on microglia function, seeded microglia on glass, UF-Au, UT np-Au and np-Au substrates were stimulated with LPS (10 ng mL^{-1}) for 24 hours and the levels of secreted TNFα were measured. This analysis revealed comparable levels of TNFα production by microglia among the four substrate surfaces studied (Fig. 8). The findings indicated that these surfaces did not markedly alter microglial cytokine production and were biocompatible with microglia proinflammatory studies. The negligible TNFα production observed for the unstimulated microglia demonstrated that the substrates alone do not elicit a microglial TNFα response. Therefore, microglial TNFα production is solely caused by LPS stimulation without any interference from the substrates themselves. The ability of microglia to retain their normal specific response to LPS stimulation on glass and both flat and texturized gold surfaces was a good indicator of biocompatibility for functional microglial assays.

Discussion

The present study describes the general morphology of BV-2 murine microglia cultured on different gold substrate surfaces. UF-Au, UT np-Au, and np-Au substrates were prepared to investigate their biocompatibility with microglia. SEM provided high resolution images of microglia morphologies and allowed detailed visualization of classic rounded, elongated, unipolar and bipolar microglial shapes along with numerous short and branched processes projecting outward of the cell body. These processes varied in length from 5 μm to 30 μm, although some major processes were many times the length of a cell body. The *in vitro* studies demonstrated that microglia were able to adhere to flat glass and gold surfaces as well as texturized gold surfaces, albeit with slightly less avidity to np-Au. The gold surfaces, even the highly grooved UF np-Au and np-Au monolith, were not toxic to microglia and did not interfere with LPS-induced TNFα production suggesting good biocompatibility for microglial functional and morphological studies.

The use of flat gold as a substrate platform for cell culture has been widely reported in the literature due to its known biocompatibility,[18,19] ease of modification with alkanethiolate self-assembled monolayers[7] and with tailored self-assembled monolayer-based micropatterned arrays for controlling protein adsorption and cell adhesion.[4,7] Furthermore, a variety of gold-based compounds have been investigated for their interaction with immune cells. A recent report by Hutter *et al.* in 2010 demonstrated the uptake of gold nanoparticles (spheres, rods, or urchin geometries) and microglial activation *in vivo*, *via* bioluminescence imaging. In their study using transgenic mice, they demonstrated that the geometry of the nanoparticle (especially the rod and urchin shaped) can influence microglial activation and that the urchin shaped nanoparticles are preferentially taken up by microglia.[15] In this same report, *in vitro* studies with microglia demonstrated that gold nanoparticles stimulated several proinflammatory molecules including granulocyte macrophage colony-stimulating factor, IL-1α, and nitric oxide, but not TNFα. In the current study, the gold surfaces alone did not stimulate microglial TNFα production although other proinflammatory molecules were not measured. However our studies investigated gold macrosurface effects which would not have involved particle internalization and activation of uptake signaling pathways. In 2012, Seker *et al.* presented the first effort to utilize the high surface-to-volume ratio of np-Au (compared to flat gold) as a potential platform for culturing adherent astrocyte cells and investigated its feasibility for application as a drug delivery platform.[5] They used an anti-mitotic drug cocktail known to reduce cellular growth (in a dose-dependent manner) to evaluate the performance of the material for drug release and efficient suppression of astrocyte proliferation. Their result indicated that the porous surfaces were minimally fouled by either the adherent astrocytes or the cell culture media, rendering it a prospective material favorable for sustained drug delivery.[5]

Microglia, the phagocytes of the brain, are known to respond to a myriad of cues (soluble and insoluble) in their physical environment (temperature, pressure, stiffness property of the substrate). Many of these cues induce microglial migration towards sites of damage or injury in the central

nervous system. A recent study by Persheyev *et al.* indicated that BV-2 microglial morphology can be greatly impacted upon interaction with nanoparticles that possess micro-protrusions. The specific protrusions were in the form of either sharp, homogeneous cones or spikes on a textured substrate prepared using hydrogenated amorphous silicon (a-Si : H).[32] The features on the texturized a-Si : H film in the range of 0.30–2.6 μm greatly impacted the overall cell morphology and the actin cytoskeleton with the most significant effects observed when the micro-protrusions were in the range of 0.90–2.6 μm. The low impact of the flat and texturized gold surfaces on microglia morphology in our study may be because the gold pores and ligaments are significantly smaller than the reported dimensions in Persheyev *et al.* However the presence of pores and the discontinuous gold area may hinder the formation of the needed focal adhesion sites for cell adhesion. Yarmush and colleagues found that shorter processes were observed when astrocytes were cultured on porous gold surfaces compared to non-porous surfaces.[5] They suggested that the presence of "nanopits" in the nanoporous gold substrate may accommodate only a limited number of focal adhesion sites compared to the non-porous gold substrates, thereby reducing cellular spreading.

The use of SEM at high resolution revealed very little distinction in microglia morphology whether they were cultured on UF-Au, UT np-Au or np-Au. These observations may be due to minimal disruption of integrin clustering, resulting in negligible alteration of the microglial shapes by these surfaces. However, it has been reported that nanotopography or RGD ligand spacing can greatly impact the focal adhesion of these cells on the surface.[3,32] The ideal spacing of ~70 nm between the neighboring features or ligands can effectively promote integrin clustering, leading to the formation of focal adhesion complexes and the F-actin network.[3] A larger separation distance of the neighboring features or ligands tend to disrupt the integrin clustering and dramatically influence cell adhesion quality and dynamic cell behaviors. In the case of the np-Au substrate, the corrugated surface contains both irregular ligaments and pores. The lack of a continuous smooth surface and the presence of these gold surface features (pores and ligaments) may not impact the exterior morphology of the microglia, but might directly affect the quality of focal adhesion or the number of focal adhesion sites. However, microglia adhesion to UT np-Au was not hampered and only slightly affected by np-Au (~14%).

The UT np-Au and np-Au substrates were biocompatible with cultured microglia in most of our assays except for cell growth or proliferation. UT np-Au was supportive of microglia proliferation during the first 48 h but did not sustain growth at subsequent times. Microglial growth was completely absent on the texturized np-Au surface which is consistent with a previous observation reported by Leung *et al.* in 2008.[20] In that study, antiserum against CD11b was used to label endogenous microglia and macrophages from the retrieved implanted electrode from rats' brain. A higher number of adherent microglia were observed on the smooth side of the electrode compared to the recording site side, which was composed of grooved structures, and the number of cells decreased with the implantation time. The greatly diminished microglia growth on the np-Au monolith surface may be due to several physical properties of the gold that reduce diffusion of cell culture medium and CO_2. These include a smaller pore size than UT np-Au (25 nm *vs.* 53 nm) and much greater overall thickness compared to UT np-Au (~250 μm *vs.* ~125 nm). Surface roughness may play a role as well. This property has been well-documented for glass and UF-Au by atomic force microscopy (AFM) with root-mean-square roughness values of 0.245 nm and 0.2–0.3 nm respectively.[33,34] Stine and colleagues have extensively characterized np-Au monoliths[8] which have a greater degree and variability of surface roughness (30–40 nm, data not shown). Furthermore, they have demonstrated that np-Au monoliths are open-ended mesoporous materials by (1) AFM characterization of the np-Au exterior and interior continuous porous structure,[8] (2) successful immobilization of proteins within the np-Au structure using a flow-through approach,[35] and (3) quantification of the surface area and pore volume of np-Au using nitrogen adsorption/desorption isotherms and Brunauer, Emmett, and Teller (BET) and Barrett–Joyner–Halenda (BJH) analysis.[36] However, even with flow-through permitted by the np-Au monolith there may be some nutrient restrictions compared to the much thinner UT np-Au material.

Conclusions

The findings from this study demonstrated that np-Au as a microglial cell culture platform was metabolically non-toxic, non-disruptive to cell membranes, and compatible with microglia functional assays, but did not support microglial growth. UT np-Au, however did support microglia growth and matched the other characteristics of np-Au. These materials may have potential as effective substrates for coating or constructing nanoelectronic devices, biosensors, and functional biomaterial coatings for drug delivery.

Abbreviations

EDS	Energy dispersive X-ray spectroscopy
LPS	Lipopolysaccharide
SEM	Scanning electron microscopy
TNFα	Tumor necrosis factor α

Conflict of interest

The authors declare that they have no conflict of interest.

Acknowledgements

This work was supported by Award Number R15AG033913 from the National Institute on Aging (MRN).

References

1 Y. Zhong and R. V. Bellamkonda, *J. R. Soc., Interface*, 2008, **5**, 957–975.
2 A. I. Teixeira, G. A. Abrams, P. J. Bertics, C. J. Murphy and P. F. Nealey, *J. Cell Sci.*, 2003, **116**, 1881–1892.
3 J. Huang and J. Ding, *Soft Matter*, 2010, **6**, 3395–3401.
4 M. Mrksich and G. M. Whitesides, *Annu. Rev. Biophys. Biomol. Struct.*, 1996, **25**, 55–78.
5 E. Seker, Y. Berdichevsky, K. J. Staley and M. L. Yarmush, *Adv. Healthcare Mater.*, 2012, **1**, 172–176.
6 O. V. Shulga, K. Jefferson, A. R. Khan, V. T. D'Souza, J. Liu, A. V. Demchenko and K. J. Stine, *Chem. Mater.*, 2007, **19**, 3902–3911.
7 Y. H. Tan, M. Liu, B. Nolting, J. G. Go, J. Gervay-Hague and G.-y. Liu, *ACS Nano*, 2008, **2**, 2374–2384.
8 Y. H. Tan, J. Schallom, N. V. Ganesh, K. Fujikawa, A. V. Demchenko and K. J. Stine, *Nanoscale*, 2011, **3**, 3395–3407.
9 M. Mrksich, *Acta Biomater.*, 2009, **5**, 832–841.
10 T. H. Park and M. L. Shuler, *Biotechnol. Prog.*, 2003, **19**, 243–253.
11 M. Nikkhah, F. Edalat, S. Manoucheri and A. Khademhosseini, *Biomaterials*, 2012, **33**, 5230–5246.
12 H. Jans and Q. Huo, *Chem. Soc. Rev.*, 2012, **41**, 2849–2866.
13 E. C. Dreaden, A. M. Alkilany, X. Huang, C. J. Murphy and M. A. El-Sayed, *Chem. Soc. Rev.*, 2012, **41**, 2740–2779.
14 R. A. Sperling, P. Rivera Gil, F. Zhang, M. Zanella and W. J. Parak, *Chem. Soc. Rev.*, 2008, **37**, 1896–1908.
15 E. Hutter, S. Boridy, S. Labrecque, M. Lalancette-Hébert, J. Kriz, F. M. Winnik and D. Maysinger, *ACS Nano*, 2010, **4**, 2595–2606.
16 B. Pandey, Y. H. Tan, K. Fujikawa, A. V. Demchenko and K. J. Stine, *J. Carbohydr. Chem.*, 2012, **31**, 466–503.
17 A. Wittstock, V. Zielasek, J. Biener, C. M. Friend and M. Bäumer, *Science*, 2010, **327**, 319–322.
18 G. Voskerician, M. S. Shive, R. S. Shawgo, H. v. Recum, J. M. Anderson, M. J. Cima and R. Langer, *Biomaterials*, 2003, **24**, 1959–1967.
19 J. Wegener, C. R. Keese and I. Giaever, *Exp. Cell Res.*, 2000, **259**, 158–166.
20 B. K. Leung, R. Biran, C. J. Underwood and P. A. Tresco, *Biomaterials*, 2008, **29**, 3289–3297.
21 P. S. Motta and J. W. Judy, *IEEE Trans. Biomed. Eng.*, 2005, **52**, 923–933.
22 O. V. Shulga, D. Zhou, A. V. Demchenko and K. J. Stine, *Analyst*, 2008, **133**, 319–322.
23 G. S. Paranjape, L. K. Gouwens, D. C. Osborn and M. R. Nichols, *ACS Chem. Neurosci.*, 2012, **3**, 302–311.
24 C. Korzeniewski and D. M. Callewaert, *J. Immunol. Methods*, 1983, **64**, 313–320.
25 J. C. Wataha, C. T. Hanks and Z. Sun, *Dent. Mater.*, 1994, **10**, 156–161.
26 N. Ercal, H. Gurer-Orhan and N. Aykin-Burns, *Curr. Top. Med. Chem.*, 2001, **1**, 529–539.
27 M. V. Berridge, P. M. Herst and A. S. Tan, *Biotechnol. Annu. Rev.*, 2005, **11**, 127–152.
28 U.-K. Hanisch and H. Kettenmann, *Nat. Neurosci.*, 2007, **10**, 1387–1394.
29 C. U. A. Kloss, M. Bohatschek, G. W. Kreutzberg and G. Raivich, *Exp. Neurol.*, 2001, **168**, 32–46.
30 M. Angeles Muñoz-Fernández and M. Fresno, *Prog. Neurobiol.*, 1998, **56**, 307–340.
31 M. M. Syed, N. K. Phulwani and T. Kielian, *J. Neurochem.*, 2007, **103**, 1461–1471.
32 S. Persheyev, Y. Fan, A. Irving and M. J. Rose, *J. Biomed. Mater. Res., Part A*, 2011, **99A**, 135–140.
33 M.-Y. Wei, L. J. Leon, Y. Lee, D. Parks, L. Carroll and P. Famouri, *J. Colloid Interface Sci.*, 2011, **356**, 182–189.
34 M. Hegner, P. Wagner and G. Semenza, *Surf. Sci.*, 1993, **291**, 39–46.
35 Y. H. Tan, K. Fujikawa, P. Pornsuriyasak, A. J. Alla, N. Vijaya Ganesh, A. V. Demchenko and K. J. Stine, *New J. Chem.*, 2013, **37**, 2150–2165.
36 Y. H. Tan, J. A. Davis, K. Fujikawa, N. V. Ganesh, A. V. Demchenko and K. J. Stine, *J. Mater. Chem.*, 2012, **22**, 6733–6745.

DEVELOPMENT OF LPS ANTAGONISTIC THERAPEUTICS: SYNTHESIS AND EVEALUATION OF GLUCOPYRANOSIDE-SPACER-AMINO ACID MOTIFS

Sophon Kaeothip, Geeta Paranjape, Shana E. Terrill, Aileen F. G. Bongat, Maria L. D. Udan, Teerada Kamkhachorn, Hope L. Johnson, Michael R. Nichols, and Alexei V. Demchenko

This publication was due to the collaborative efforts of the Nichols and Demchenko laboratories. The LPS-induced antagonist studies analyzed the antagonistic or inhibitory effect of six different Lipid A analogs, while also observing each compounds toxicity and agonistic or stimulatory activity. The results determined one compound that inhibited the LPS-induced TNFα response with the lowest IC_{50}, while remaining non-toxic and producing no agonistic activity. The Demchenko laboratory was responsible for the synthesis of the necessary Lipid A mimics, while the Nichols laboratory was responsible for all the cellular activity assays. Previous Nichols' research assistants (Dr. Geeta Paranjape and Dr. Maria L. D. Udan) started all the cellular assays on the first five compounds, while all my work was completed on the last compound (compound 24) and the positive control. Further descriptions of this publications and my experimental work is found in Chapter 5.

RSC Advances

Cite this: *RSC Advances*, 2011, **1**, 83–92

www.rsc.org/advances

PAPER

Development of LPS antagonistic therapeutics: synthesis and evaluation of glucopyranoside-spacer-amino acid motifs†

Sophon Kaeothip, Geeta Paranjape, Shana E. Terrill, Aileen F. G. Bongat, Maria L. D. Udan, Teerada Kamkhachorn, Hope L. Johnson, Michael R. Nichols* and Alexei V. Demchenko*

Received 5th May 2011, Accepted 6th June 2011
DOI: 10.1039/c1ra00145k

Sepsis is a serious medical condition characterized by bacterial infection and a subsequent massive systemic inflammatory response. The release of proinflammatory products and mediators from responding innate immune cells, such as mononuclear phagocytes, directly contributes to the pathogenesis of sepsis. The primary bacterial trigger of inflammation is lipopolysaccharide (LPS), which interacts with the germline-encoded macrophage receptor cluster of differentiation 14 (CD14) *via* its Lipid A moiety. In an effort to identify compounds that block LPS-induced inflammation we investigated a series of Lipid A analogs that lack a disaccharide core yet still possess potent antagonistic activity against LPS. We found it beneficial to develop molecules that contain the following: a glucopyranoside core, hydrophobic ether substituents, and an amino acid to provide an ionic character to the constructs. Here we report an efficient synthesis of molecules of this type and the ensuing biological studies thereof.

Introduction

Septicemia is a serious world-wide health problem associated with mortality rates of 40–60%.[1] It has been estimated that 1% of hospital patients and 20–30% of ICU patients develop sepsis. The cardiovascular consequences of septic shock resulting from bacterial infections include myocardial dysfunction that develops in nearly all patients,[2] vascular tone and permeability abnormalities, as well as abnormal oxygen delivery and metabolism. As a result, vital organs such as the brain, heart, kidneys, and liver may be affected or may fail, and this reflects in over 100 000 deaths annually in the US.[1] It is well established that septic shock is initiated by the introduction of a bacterial endotoxin (or lipopolysaccharide, LPS) into the blood stream. LPS (Fig. 1), a vital component of the outer leaflet of the gram-negative outer membrane, has been shown to be a principle mediator of the depression of left ventricular function and myocardial contractility.[3] LPS is comprised of three structural regions. One of these, the Lipid A region, consists of a polyacylated glucosamine disaccharide and is largely responsible for the toxic activity.[4] The results of recent studies suggest that the ensuing proinflammatory response to LPS is by far more dangerous than the mere presence of LPS in circulation.[5,6] LPS exerts its effects *via* interaction with a plasma LPS-binding protein (LBP), which has strong affinity for both the Lipid A region of the endotoxin and glycosylphosphatidyl inositol-anchored LPS receptor CD14 on mononuclear phagocytes. The LPS-LBP complex then interacts with CD14 followed by further complex formation with Toll-like receptor 4 (TLR4) and its co-receptor MD-2.[7] TLR4 is an integral membrane protein that transmits the LPS signal to the inside of the cell and initiates the signaling pathways that lead to production of proinflammatory molecules, such as the cytokine, tumor necrosis factor α (TNFα).

Recent advances in the understanding of LPS structure-function relationships have provided some clues on the structural determinants responsible for the endotoxic activity of Lipid A.[8] These determinants include the number and chain length of fatty acids (lipids), the disaccharide core, and the 1,4′-diphosphate groups of the *E. coli* type (**1**, Fig. 1). The fair stability (chemical or *in vitro*) of this class of compounds has been a major drawback in their synthesis and application. Although the exact role of the phosphate moieties is still unknown, the observation that a 1-hydroxyl-4′-*O*-phosphate derivative was inactive gave rise to a belief that the omission of at least one phosphate results in a complete loss of activity.[8,9]

In an effort to explore molecules that antagonize LPS signaling without activating the inflammatory cascade, our laboratory has designed simplified Lipid A analogs that lack the complexity of the highly lipidated diphosphorylated disaccharide core yet still maintain potent antagonistic activity against LPS. Herein we present the synthesis and unprecedented LPS-antagonistic activity of the methyl glucopyranoside-amino acid conjugates. This project was inspired by published reports of compounds that are structurally dissimilar to Lipid A yet still exhibit potent antagonistic activity. Amongst a myriad of

Department of Chemistry and Biochemistry, University of Missouri – St. Louis, One University Boulevard, St. Louis, MO 63121, USA. E-mail: nicholsmic@umsl.edu; demchenkoa@umsl.edu

† Electronic supplementary information (ESI) available. See DOI: 10.1039/c1ra00145k

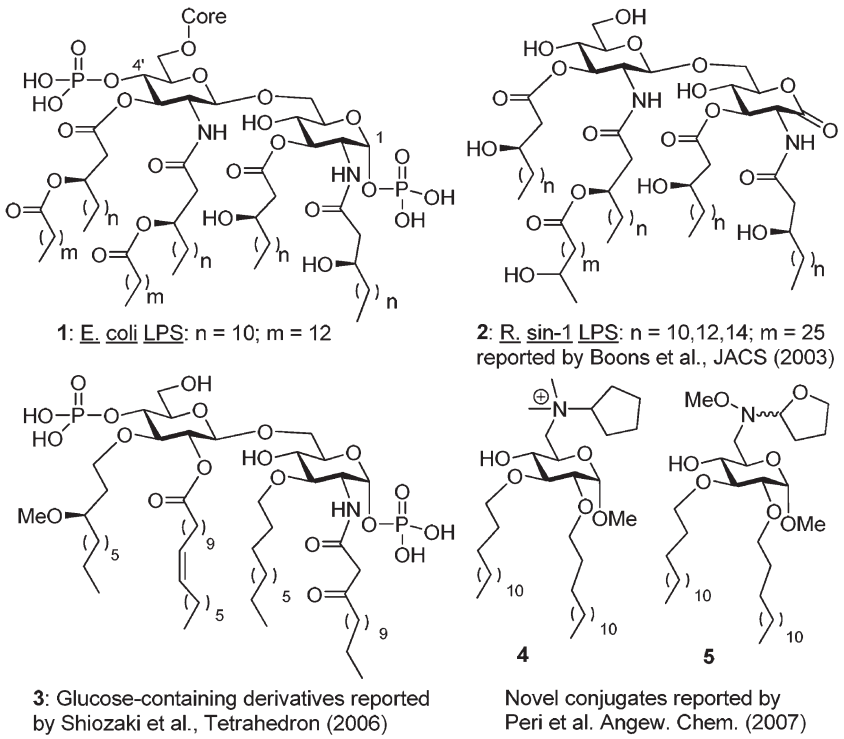

Fig. 1 Structures of the Lipid A region of *E. coli* LPS (**1** and structural mimetics thereof (**2–5**).

research articles that have been disseminated in the past years, the following three noteworthy discoveries served as a justification and guide for our own studies.

First, as reported by Boons *et al.*, a strong binding and antagonistic effect was achieved even with 'phosphateless' *Rhizobium syn*-1 disaccharide **2**, which bears a lactone moiety at the reducing end (Fig. 1).[10,11] This finding indicated that one could avoid hurdles associated with labile phosphate group installation, handling, and storage. Second, Shiozaki *et al.* showed that a strong anti-LPS antagonistic response can be achieved, even with disaccharide **3**, in which the non-reducing glucosamine is replaced with glucose.[12] In addition, instead of chiral β-hydroxy/acyl esters, relatively simple alkyl chains were used at the C-3 and 3′ positions, whereas a β-ketoamide moiety was used at C-2.

Third, Peri *et al.* demonstrated that even simple methyl glycoside-heterocycle conjugates **4** and **5** which bear alkyl chains instead of traditional lipids provide antagonistic activity.[13] To this end, we found it attractive to develop molecules that contain the following: a methyl glucoside monosaccharide core to simplify the synthesis, hydrophobic chains to facilitate membrane intercalation, and an amino acid to provide an ionic character. Here we report an efficient synthesis of conjugates of this type and biological studies of their endotoxic activity *in vitro*.

Results and discussion

The synthesis began with the conversion of methyl α-D-glucopyranoside **6** into methyl 2,3-di-*O*-benzyl-α-D-glucopyranoside **7**[14] *via* sequential 4,6-benzylidene acetal formation, 2,3-dibenzylation, and acetal cleavage accomplished in 67% yield over three steps (Scheme 1). 4,6-Diol **7** was then regioselectively succinoylated at the primary position with succinic anhydride in the presence of 4-dimethylaminopyridine (DMAP) in pyridine to afford the derivative **8** in 71% yield. The carboxyl moiety of the linker was then coupled with 3-hydroxyl of the protected L-serine derivative **9**.[15,16] This was accomplished using *N*,*N*′-diisopropylcarbodiimide (DIC) as the coupling reagent in the presence of DMAP in pyridine to afford conjugate **10** in 80% yield.

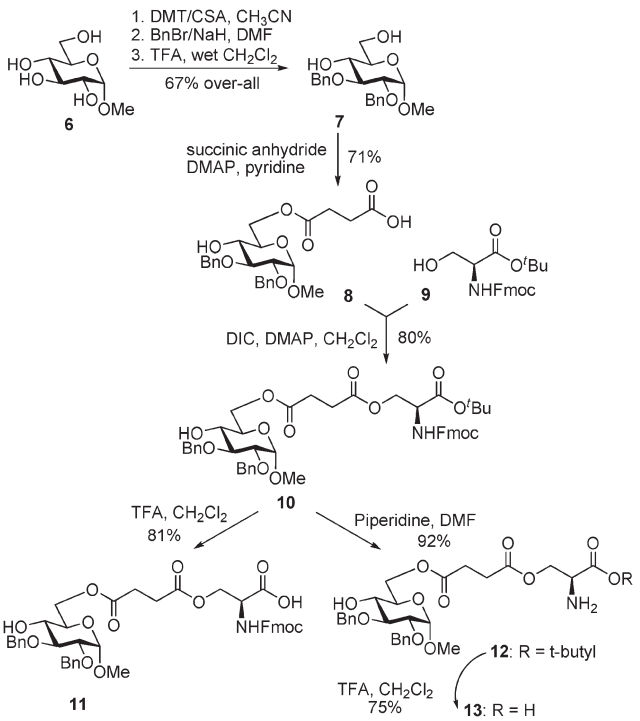

Scheme 1 Synthesis of monosaccharide–aminoacid conjugates **10–13**.

Having obtained the key construct **10**, we decided to pursue further functional group transformations. The main driving force for these synthetic manipulations was to obtain a series of simple analogs that would allow us to investigate the effect of cationic and anionic character on LPS-antagonistic activity *in vitro*. With this objective in mind, carboxylated compound **11** was obtained from **10** by cleavage of *tert*-butyl ester in the presence of TFA/DCM in 81% yield. Alternatively, the Fmoc protecting group could also be removed from compound **10** with piperidine in DMF to afford free amine **12**. Subsequently, we also obtained compound **13** with both carboxyl and amine groups unprotected. This was accomplished by the treatment of compound **12** with TFA/CH_2Cl_2 to give derivative **13** in 75% yield.

The inhibitory activity of compounds **10–13** on LPS-induced TNFα production was investigated *in vitro* using THP-1 macrophages prepared as described in the Experimental section. THP-1 cells are an excellent system for studying inflammatory processes and serve as a model for peripheral monocytes/macrophages and their responses to bacterial infection. Compounds **10**, **12**, and **13** exhibited no inhibitory activity against LPS-induced TNFα production in the concentration range of 0.1 nM to 10 μM (Fig. 2A–C). These compounds were also tested in the absence of LPS and demonstrated no agonist activity (data not shown). Compound **11**, which has a free carboxylic group, was able to significantly inhibit LPS-induced TNFα production at concentrations greater than 10 μM (Fig. 3). Unfortunately, cell viability measurements using an XTT reduction assay indicated that compound **11** was toxic to the cells in the 30–100 μM range. Although there was a notable gap between inhibition and toxicity at 30 and 50 μM, the similarities between the inhibition and toxicity curves suggested that much of the antagonistic activity by **11** was related to toxicity.

With the purpose of gaining further insight into the effect of various substituents on the endotoxic activity of monosaccharide-amino acid conjugates, we obtained an analog of compound **11** in which benzyl groups have been replaced with acyl (myristoyl, C14) fatty acid chains. The synthesis of lipidated analog **19** was accomplished as depicted in Scheme 2. Methyl glycoside **6** was protected as 4,6-*O*-(*p*-methoxybenzylidene) acetal **14** by treatment with anisaldehyde dimethylacetal in the presence of camphorsulfonic acid in 89% yield. **14** was acylated with myristoyl chloride in the presence of the pyridine furnished compound **15** in 85% yield. The benzylidene ring in **15** was reductively opened by treatment with BH_3-THF catalyzed with $Cu(OTf)_2$ to obtain the unexpected product **16**, which was lacking the C-2 acyl chain, in

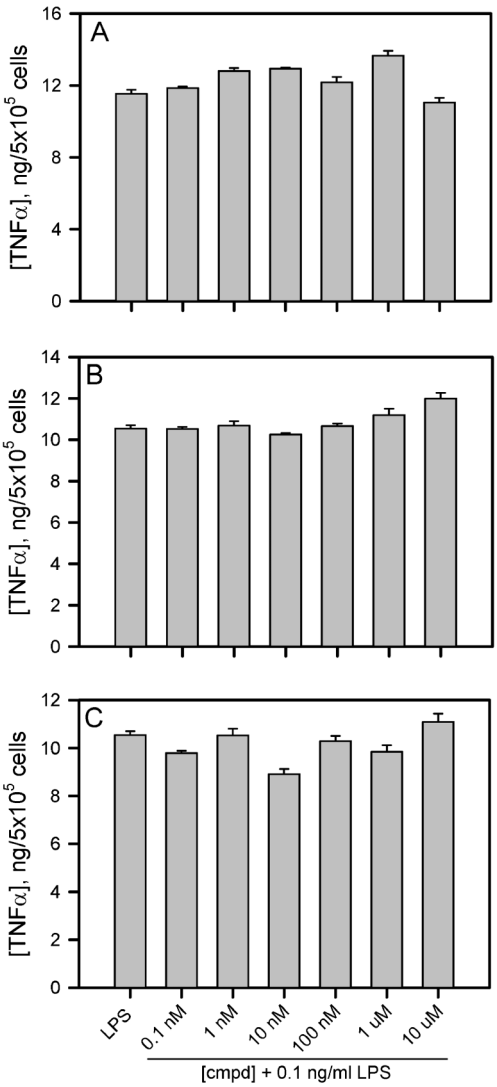

Fig. 2 Compounds **10**, **12**, and **13** do not display LPS antagonistic activity. THP-1 human monocytes were treated as described in the Experimental section with 10 ng mL^{-1} PMA for 24 h at 37 °C and 5% CO_2. The medium was then removed and adherent macrophages were further treated as described with increasing concentrations of compounds **10** (panel A), **12** (panel B) and **13** (panel C) for 30 min followed by incubation with 10 ng mL^{-1} LPS for 6 h. Secreted TNFα was measured by ELISA and the levels (ng mL^{-1}) were reported on the *y*-axis after normalization by the number of counted macrophages (cells mL^{-1}). Error bars represent the standard error (std err) for 3 different TNFα measurements from each cell treatment.

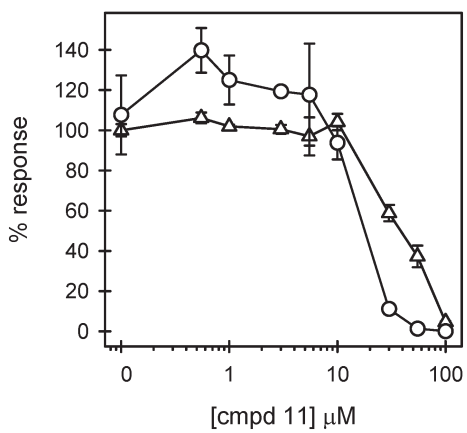

Fig. 3 Compound **11** displays LPS antagonistic activity and cell toxicity. THP-1 macrophages were treated as described in the legend of Fig. 2, with increasing concentrations of compound **11**. Secreted TNFα levels (circles) are the average ± std err for $n = 2$ trials and are reported as the % response of LPS in the absence of an antagonist compound. Immediately following the cell treatment described above and in the Fig. 2 legend, the macrophage viability (triangles) ($n = 2$ trials) was determined by XTT reduction as described in the Experimental. Cell viability is presented as a percentage of the cell viability measured in the absence of antagonists.

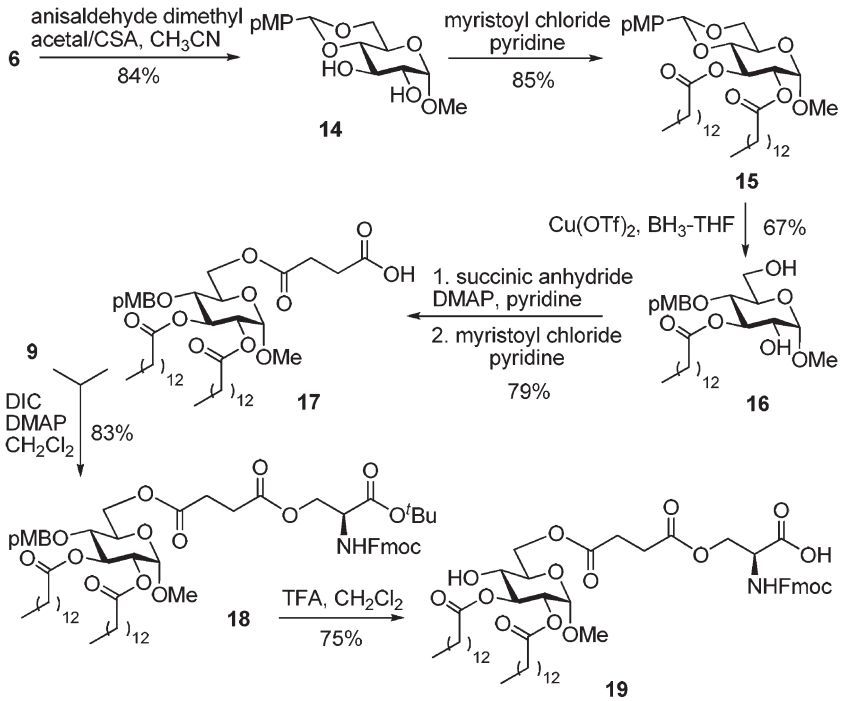

Scheme 2 Synthesis of monosaccharide–fatty acid–amino acid conjugate **19**, a lipidated analog of compound **11**.

67% yield. The loss of the acyl chain was rather unexpected, but this glitch was overcome by regioselective acylation with succinic anhydride in pyridine at the primary C-6 position followed by C-2 acylation with myristoyl chloride. This two-step one-pot procedure allowed us to obtain compound **17** in 79% yield.

L-serine derivative **9**[15] was linked to the carboxyl group of **17** *via* DIC-mediated coupling in the presence of DMAP. The monosaccharide–fatty acid–amino acid conjugate **18** was obtained in 83% yield. Acid treatment of the fully protected compound **18** led to concomitant cleavage of the *p*-methoxybenzyl (pMB) group at C-4 and *tert*-butyl ester. As a result, compound **19** was isolated in 75% yield.

For comparative biological studies, we also accomplished the synthesis of the alkylated analog **24** as depicted in Scheme 3. The intermediate **14** was di-alkylated at C-2 and C-3 with myristyl bromide in the presence of NaH to afford compound **20** in 72% yield. The benzylidene ring in **20** was reductively opened by treatment with BH_3-THF catalyzed with $Cu(OTf)_2$ to obtain product **22** in 87%. Acylation of **22** with succinic anhydride led to compound **22** in 89% yield. L-serine derivative **9**[15] was then linked to the carboxyl group of **22** *via* DIC-mediated coupling in the presence of DMAP. The resulting monosaccharide-amino acid conjugate **23** was obtained in 79% yield. Acid treatment of the fully protected compound **23** led to concomitant cleavage of the pMB group at C-4 and *tert*-butyl ester. As a result, target compound **24** was isolated in 81% yield.

Having obtained compounds **19** and **24**, lipidated and alkylated analogs of compound **11**, respectively, we were well positioned to perform comparative studies. In addition, as the comparison point, we obtained the standard positive control compound **4** as described by Peri *et al.*[13] The lipidated compound **19** displayed a marked improvement in LPS-antagonistic ability. Inhibition of LPS-induced TNFα was found beginning at 550 nM **19** (Fig. 4). A reproducible biphasic response was consistently seen in the activity of **19**. This may indicate multiple binding sites on the macrophages, both higher and lower affinity for the antagonist compound. 80% of the LPS

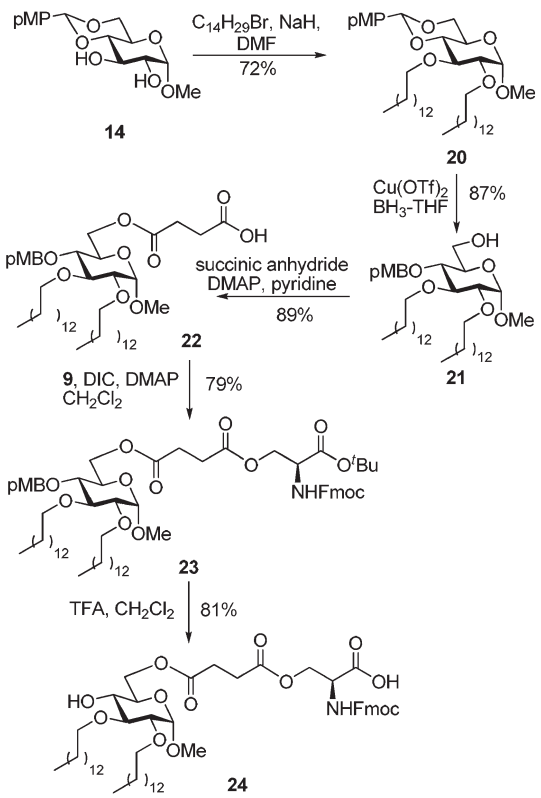

Scheme 3 Synthesis of the monosaccharide–alkyl–amino acid conjugate **24**, an alkylated analog of compound **11**.

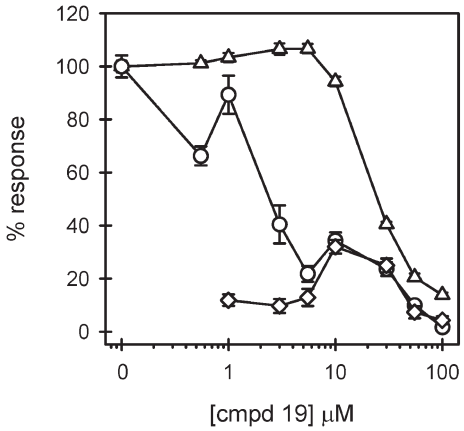

Fig. 4 Compound **19** displays more potent LPS antagonistic activity. THP-1 macrophages were treated in 3 separate experiments as described in the Fig. 2 legend, with increasing concentrations of compound **19**. Secreted TNFα levels were determined in the presence (circles) (n = 9 trials) and absence (diamonds) (n = 6 trials) of LPS. Cell viability (triangles) (n = 9 trials) was also assessed and presented as described in the Fig. 3 legend.

response was blocked with 5 μM of compound **19** with no observable toxicity. Cell viability began to be compromised at 10 μM and some agonist activity was found in the 10–30 μM range (Fig. 4).

The alkylated compound **24** was found to be a very effective inhibitor of LPS-induced TNFα production in human macrophages (Fig. 5). 70% inhibition was observed at 1 μM of **24** and overall inhibition reached 90% at 40 μM. Compound **24** exhibited no toxicity or agonist activity in the tested 0.2 to 40 μM range. Curve fitting of the inhibition data in Fig. 5 produced an IC_{50} value of 470 nM. These results were superior to those obtained with compound **4**[13] which had an inhibition range from 3–10 μM and began to show agonist activity at concentrations > 10 μM (Fig. 6). Compound **4** was only toxic at high concentrations.

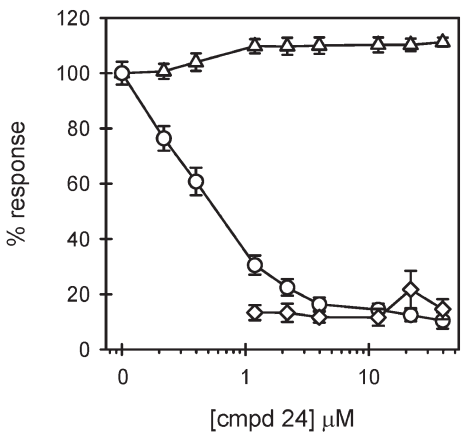

Fig. 5 Compound **24** displays significant LPS antagonistic activity without toxicity. THP-1 macrophages were treated in 4 separate experiments, as described in the Fig. 2 legend, with increasing concentrations of compound **24**. Secreted TNFα levels were determined in the presence (circles) (n = 12 trials) and absence (diamonds) (n = 8 trials) of LPS. Cell viability (triangles) (n = 12 trials) was also assessed and presented as described in the Fig. 3 legend.

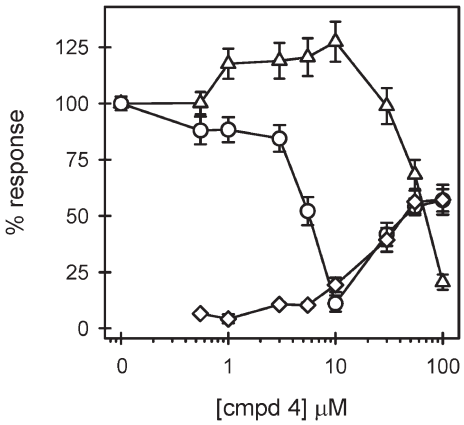

Fig. 6 LPS antagonistic activity displayed by compound **4**. THP-1 macrophages were treated in 3 separate experiments, as described in the Fig. 2 legend, with increasing concentrations of compound **4**. Secreted TNFα levels were determined in the presence (circles) (n = 8 trials) and absence (diamonds) (n = 5 trials) of LPS. Cell viability (triangles) (n = 11 trials) was also assessed and presented as described in the Fig. 3 legend.

The potent inhibition displayed by compound **24** of LPS-induced TNFα production without associated toxicity establishes this compound and those in its class as potential therapeutic and research compounds. These results extend the work of Boons and co-workers with phosphateless Lipid A derivatives[11] by transitioning from disaccharide-based to monosaccharide-based compounds. The IC_{50} inhibition constant of 470 nM for compound **24** is the lowest reported for a monosaccharide compound and its potency in human macrophages significantly improves on the monosaccharide compounds tested in mouse bone-marrow-derived macrophages by Peri *et al.*[13] Our monosaccharide-based compound in the current form is not as potent as some of the best disaccharide compounds such as E5531 (IC_{50} 1.2 nM), E5564 (IC_{50} 1.1 nM) and E5564 analogues (IC_{50} 0.97 nM).[8,12,17] This difference in potency is balanced by the ease of synthesis and modification of monosaccharide-based compounds. In fact, the observation that the replacement of the acyl chains in **19** with alkyl chains (**24**) produced a significantly more potent antagonist with less toxicity suggests that additional modifications may further enhance the activity. From these studies, it also became clear that subtle structural changes have an impact on whether a particular compound displays antagonist or agonist activity. The balance between these two activities has been explored before[18] and suggests that small modifications to the compounds described in this investigation may enhance agonist activity, thus providing a basis for adjuvant development.[19–21]

In summary, studies described herein provide new information regarding the structure–activity relationship of a novel class of compounds that mimic classic Lipid A analogs, and the scientific basis for future studies to prevent the deleterious effects of endotoxemia. We believe that the results of these studies summarized in Table 1 will have far reaching impact on the treatment of patients diagnosed with endotoxemia. As a consequence, we can foresee additional efforts to investigate the molecular mechanisms underlying the antagonistic actions of the synthetic Lipid A analogs.

Table 1 Summary of biological activity in human macrophage cells.

Compound	TNFα inhibition (IC_{50})	Toxicity	Agonist activity
10, **12**, **13**	None observed	None observed	None observed
11	46 μM	>10 μM	None observed
19	3 μM	>10 μM	10–30 μM
24	0.5 μM	None observed	None observed
4	6 μM	>30 μM	30–100 μM

Experimental

General

Column chromatography was performed on silica gel 60 (70–230 mesh) and reactions were monitored by TLC on Kieselgel 60 F_{254}. The compounds were detected by examination under UV light and by charring with 10% sulfuric acid in methanol. Solvents were removed under reduced pressure at < 40 °C. CH_2Cl_2 and CH_3CN were distilled from CaH_2 directly prior to application. Pyridine was dried by refluxing with CaH_2 and then distilled and stored over molecular sieves (3 Å). $Cu(OTf)_2$ was co-evaporated with toluene (3 × 10 mL) and dried *in vacuo* for 2–3 h directly prior to application. *N*,*N*'-Diisopropylcarbodiimide, 4-dimethylaminopyridine, piperidine, and anhydrous DMF were used without further conditioning. Optical rotations were measured by a 'Jasco P-1020' polarimeter. Unless noted otherwise, ^{1}H-NMR spectra were recorded in $CDCl_3$ at 300 MHz (Bruker Avance) or at 500 MHz (Bruker ARX-500), ^{13}C-NMR spectra and two-dimensional experiments were recorded in $CDCl_3$ at 75 MHz (Bruker Avance) or at 125 MHz (Bruker ARX-500). HR FAB-MS determinations were made with the use of JEOL MStation (JMS-700) Mass Spectrometer, matrix *m*-nitrobenzyl alcohol, with NaI as necessary.

Methyl 2,3-di-*O*-benzyl-6-*O*-(3-carboxypropanoyl)-α-D-glycopyranoside (8)

4-Dimethylaminopyridine (DMAP, 32 mg, 0.26 mmol) and succinic anhydride (0.16 g, 1.56 mmol) were added to a stirred solution of methyl 2,3-di-*O*-benzyl-α-D-glucopyranoside **7**[14] (0.5 g, 1.3 mmol) in dry pyridine (5 mL) and the resulting mixture was stirred for 16 h at room temperature (rt) under argon. After that, the reaction mixture was concentrated under reduced pressure, the residue was dissolved in CH_2Cl_2 (30 mL) and washed with water (3 × 15 mL). The organic phase was separated, dried over $MgSO_4$, filtered and concentrated *in vacuo*. The residue was purified by column chromatography on silica gel (ethyl acetate-hexane gradient elution) to give the title compound **8** (0.45 g, 0.95 mmol) as a colorless syrup in 71% yield. Analytical data for **8**: R_f 0.43 (ethyl acetate); $[\alpha]_D^{22}$ +7.19° (*c* = 1.0, $CHCl_3$); ^{1}H NMR (300 MHz, $CDCl_3$): δ, 2.60 (m, 4H, 2 × CH_2), 3.38 (s, 3H, OCH_3), 3.44 (dd, 1H, $J_{2,3}$ = 9.5 Hz, H-2), 3,51 (dd, 1H, $J_{4,5}$ = 9.5 Hz, H-4), 3.73 (m, 1H, $J_{5,6b}$ = 4.8 Hz, H-5), 3.80 (dd, 1H, $J_{2,3}$ = 9.2 Hz, H-3), 4.26 (dd, 1H, $J_{6a,6b}$ = 10.0 Hz, H-6a), 4.42 (dd, 1H, H-6b), 4.61 (d, 1H, $J_{1,2}$ = 3.5 Hz, H-1), 4.65 (d, 1H, ^2J= 12.1 Hz, ½ CH_2Ph), 4.74–4.79 (m, 2H, CH_2Ph), 4.99 (d, 1H, ^2J = 11.3 Hz, ½ CH_2Ph), 7.26–7.36 (m, 10H, aromatic) ppm; ^{13}C NMR (75 MHz, $CDCl_3$): δ, 55.4, 63.7, 69.4, 69.9, 73.3, 75.3, 79.7, 81.0, 98.3, 128.0 (×2), 128.1 (×2), 128.2 (×4), 128.6 (×2), 128.7 (×2), 138.1, 138.6, 172.6, 177.2 ppm; HR FAB MS $[M+Na]^+$ calcd for $C_{25}H_{30}O_9Na$ 497.1788, found 497.1770.

Methyl 2,3-di-*O*-benzyl-6-*O*-(4-((S)-2-(9-fluorenylmethoxycarbonyl)amino-3-(*tert*-butoxy)-3-oxopropyl)oxy-4-oxobutanoyl)-α-D-glycopyranoside (10)

DMAP (12.7 mg, 0.01 mmol) and *N*,*N*'-diisopropylcarbodiimide (DIC, 0.16 mL, 1.04 mmol) were added to a stirred solution of *O*-*tert*-butyl *N*-fluorenylmethoxycarbonyl-L-serine ester **9**[15,16] (0.19 g, 0.52 mmol) in CH_2Cl_2 (4 mL). After 1 h, carboxylic acid derivative **8** (0.29 g, 0.62 mmol) was added and the reaction was stirred for 5–9 h at rt until no further conversion of the starting material could be detected by TLC. The reaction mixture was diluted with CH_2Cl_2 (20 mL), washed with water (2 × 15 mL) and brine (15 mL). The organic phase was separated, dried over $MgSO_4$, filtered and concentrated *in vacuo*. The residue was purified by column chromatography on silica gel (ethyl acetate–hexane gradient elution) to afford the title compound **10** (0.34g, 0.41 mmol) as a white powder in 80% yield. Analytical data for **10**: R_f 0.34 (ethyl acetate/hexane, 1/1, *v*/*v*); $[\alpha]_D^{27}$ +12.1° (*c* = 1.0, $CHCl_3$); ^{1}H NMR (300 MHz, $CDCl_3$): δ, 1.48 (s, 9H, *t*-Bu), 2.53 (d, 1H, *J* = 2.8 Hz, OH), 2.66 (m, 4H, 2 × CH_2), 3.37 (s, 3H, OCH_3), 3.42 (d, 1H, $J_{2,3}$ = 9.0, H-2), 3.73 (m, 1H, H-5), 3.78 (dd, 2H, $J_{3,4}$ = 9.1 Hz, H-3, C*H*Fmoc), 4.25 (m, 2H, H-6b, SerC^{β}-*H*), 4.38 (m, 2H, H-6a, SerC^{β}-*H*), 4.44 (m, 2H, OCH_2Fmoc), 4.52 (m, 1H, SerC^{α}-*H*), 4.61 (d, 1H, $J_{1,2}$ = 3.2 Hz, H-1), 4.64 (d, 1H, ^2J = 12.1 Hz, ½ CH_2Ph), 4.75 (dd, 2H, *J* = 12.0 Hz, CH_2Ph), 4.98 (d, 1H, ^2J = 11.3 Hz, ½ CH_2Ph), 4.75 (d, 1H, $J_{NH,CH}$ = 8.0 Hz, Ser-NH), 7.27–7.77 (m, 18H, aromatic) ppm; ^{13}C NMR (125 MHz, $CDCl_3$): δ, 28.1 (×3), 29.1 (×2), 47.3, 54.1, 55.5, 63.9, 64.8, 67.4, 69.4, 70.1, 73.4, 75.7, 79.7, 81.3, 83.3, 98.4, 120.2 (×2), 125.4 (×2), 127.3, 127.9 (×2), 128.1, 128.2 (×2), 128.3 (×3), 128.7, 128.8 (×3), 138.2, 138.9 , 141.5 (×2), 144.0 (×2), 144.1, 156.0, 168.5, 171.8, 172.6 ppm; HR FAB MS $[M+Na]^+$ calcd for $C_{47}H_{53}NO_{13}Na$ 862.3415, found 862.3432.

Methyl 2,3-di-*O*-benzyl-6-*O*-(4-((S)-2-(9-fluorenylmethoxycarbonyl)amino-2-carboxyethyl)oxy-4-oxobutanoyl)-α-D-glycopyranoside (11)

Conjugate **10** (0.25g, 0.29 mmol) was dissolved in TFA/wet CH_2Cl_2 (1/5, *v*/*v*, 2 mL) and the resulting mixture was stirred for 2 h at rt. After that, the volatiles were evaporated under reduced pressure, the residue was diluted with CH_2Cl_2 (5 mL) and neutralized with triethylamine (until pH ~ 7). The volatiles were removed under reduced pressure and the residue was purified by column chromatography on silica gel (ethyl acetate/hexane, 1/1, *v*/*v*) to afford the title compound **11** (0.18 g, 0.24 mmol) as a white foam in 81% yield. Analytical data for **11**: R_f 0.5 (methanol/ethyl acetate, 1/4, *v*/*v*); $[\alpha]_D^{26}$ +22.5° (*c* = 1.0, $CHCl_3$); ^{1}H NMR (500 MHz, $CDCl_3$/$(CD_3)_2SO$, 2/1, v/v): δ = 2.49–2.54 (m, 4H), 3.26 (s, 3H, OCH_3), 3.39 (m, 2H), 3.57 (m, 2H), 4.01 (br. s, 1H), 4.12 (m, 2H), 4.22 (m, 2H), 4.32 (dd, 2H, *J* = 6.6 Hz), 4.43 (d, 1H, *J* = 5.1 Hz), 4.60 (s, 2H), 4.76 (m, 2H), 7.24–7.93 (m, 18H, aromatic) ppm; ^{13}C NMR (75 MHz, $CDCl_3$/$(CD_3)_2SO$, 2/1, *v*/*v*): δ, 28.8, 28.9, 31.1, 47.0, 54.7, 54.8, 63.4, 63.9, 65.3, 65.9, 69.8, 70.2, 71.8, 74.5, 79.4, 81.5, 97.3, 120.5 (×2), 125.5 (×2), 127.4 (×2), 127.5, 127.8 (×4) , 127.9 (×4), 128.0 (×3), 128.3 (×3), 128.5 (×3), 138.9, 139.6, 141.1 (×2), 144.2, 156.0, 172.1, 172.2 (×2) ppm; HR FAB MS $[M+Na]^+$ calcd for $C_{43}H_{45}NO_{13}Na$ 806.2789, found 806.2780.

Methyl 2,3-di-*O*-benzyl-6-*O*-(4-((S)-2-amino-3-(*tert*-butoxy)-3-oxopropyl)oxy-4-oxobutanoyl)-α-D-glycopyranoside (12)

Piperidine (0.5 mL) was added dropwise to a solution of monosaccharide **10** (0.1 g, 0.12 mmol) in DMF (2.0 mL) and the resulting mixture was stirred for 20 min at rt. After that, the reaction mixture was concentrated *in vacuo* and co-evaporated with toluene (×3). The residue was purified by flash column chromatography (ethyl acetate/hexane, 1/1, *v*/*v*) to give the title compound **12** (67 mg, 0.1 mmol) as a yellow syrup in 92% yield. Analytical data for **12**: R_f 0.62 (methanol/ethyl acetate, 1/9, *v*/*v*); $[\alpha]_D^{26}$ +17.3° (*c* = 1.0, $CHCl_3$); ^{1}H NMR (500 MHz, $CDCl_3$): δ = 1.49 (s, 9H, *t*-Bu), 2.52–2.66 (m, 3H), 2.73–2.78 (m, 1H), 3.02 (broad s, 1H, OH), 3.38 (s, 3H, OCH_3), 3.46 (d, 1H, $J_{2,3}$ = 9.4 Hz, H-2), 3.50 (ddd, 1H, $J_{4,5}$ = 9.5 Hz, H-4), 3.75 (m, 2H, H-5, Ser-C$^{\beta}$*H*), 3.80 (m, 2H, H-3, Ser-C$^{\beta}$*H*), 4.18 (dd, 1H, $J_{6a,6b}$ = 10.19 Hz, H-6a), 4.46 (m, 1H, Ser-C$^{\alpha}$*H*), 4.52 (dd, 1H, $J_{5,6b}$ = 4.19 Hz, H-6b), 4.61 (d, 1H, $J_{1,2}$ = 3.53 Hz, H-1), 4.65 (d, 1H, ^2J = 12.5 Hz, ½ C*H*$_2$Ph), 4.77 (dd, 2H, *J* = 11.5 Hz, CH_2Ph), 4.99 (d, 1H, ^2J = 9.0 Hz, ½ C*H*$_2$Ph), 6.49 (d, 1H, $J_{NH,CH}$ = 6.95 Hz, Ser-N*H*), 7.27–7.31 (m, 10H, aromatic) ppm; ^{13}C NMR (125 MHz, $CDCl_3$): δ, 28.2 (×3), 29.8, 31.0, 31.1, 55.5 (×2), 55.7, 63.3, 63.6, 69.5, 69.8, 73.5, 75.9, 79.8, 81.5, 83.0, 98.5, 128.1, 128.2, 128.3(×2), 128.4 (×2), 128.7 (×2), 138.2, 138.7, 169.6, 172.0, 173.1 ppm; HR FAB MS $[M+Na]^+$ calcd for $C_{32}H_{43}NO_{11}Na$ 640.2734, found 640.2741.

Methyl 2,3-di-*O*-benzyl-6-*O*-(4-((S)-2-amino-2-carboxyethyl)oxy-4-oxobutanoyl)-α-D-glycopyranoside (13)

Conjugate **12** (0.1 g, 0.12 mmol) was dissolved in TFA/wet CH_2Cl_2 (1/5, *v*/*v*, 2 mL) and stirred for 2 h. Upon completion as assessed by TLC analysis, solvents were evaporated *in vacuo*. The residue was dissolved in CH_2Cl_2 (5 mL) and neutralized with triethylamine (until pH ~ 7). Solvents were removed under reduced pressure. The residue was subjected to column chromatography on silica gel (methanol–ethyl acetate gradient elution) to obtain the product **13** (50 mg, 0.09 mmol) as white foam in 75% yield. Analytical data for **13**: R_f 0.5 (methanol/ethyl acetate, 1/4, *v*/*v*); ^{1}H NMR (500 MHz, D_2O): δ, 1.68 (m, 2H), 1.82 (m, 3H), 2.73 (m, 4H), 3.19 (dd, 3H, *J* = 5.7 Hz), 3.4 (s, 3H, OCH_3), 3.58 (ddd, 2H, *J* = 9.5, 10.0 Hz), 3.80 (dd, 1H, *J* = 9.2 Hz), 3.87 (d, 3H, *J* = 4.7 Hz), 4.33–4.37 (m, 2H, *J* = 4.7 Hz), 4.54 (d, 1H, *J* = 10.9 Hz), 7.44 (s, 10H, aromatic) ppm; ^{13}C NMR (75 MHz, D_2O): δ 29.5, 30.5, 55.4 (×2), 61.4, 63.7, 69.7, 69.8 (×2), 73.4, 75.5, 79.1 (×2), 81.1, 97.8, 128.7, 128.8 (×3), 129.0, 129.1 (×3), 137.7, 137.9, 174.5 (×2), 174.6 ppm; HR FAB MS $[M+Na]^+$ calcd for $C_{28}H_{35}NO_{11}Na$ 584.2108, found 584.2104.

Methyl 4,6-*O*-(*p*-methoxybenzylidene)-2,3-di-*O*-tetradecanoyl-α-D-glucopyranoside (15)

Myristoyl chloride (2.34 mL, 8.67 mmol) and DMAP (70 mg, 0.57 mmol) were added to a stirred solution of methyl 4,6-*O*-(*p*-methoxybenzylidene)-α-D-glucopyranoside **14**[22] (1.0 g, 2.89 mmol) in pyridine (15 mL) at 0 °C. The mixture was stirred under an atmosphere of argon for 16 h. Upon completion, the reaction mixture was concentrated *in vacuo*. The residue was dissolved in CH_2Cl_2 (30 mL), and washed with 1N HCl (2 × 15 mL), water (2 × 15 mL) and brine (15 mL). The organic phase was separated, dried over $MgSO_4$, filtered and concentrated *in vacuo*. The residue was purified by column chromatography on silica gel (ethyl acetate–hexane gradient elution) to afford derivative **15** (1.81 g, 2.48 mmol) as a white foam in 86% yield. Analytical data for **15**: R_f 0.47 (ethyl acetate/hexane, 3/7, v/v); $[\alpha]_D^{23}$ +23.6° (*c* = 1.0, $CHCl_3$); ^{1}H NMR (300 MHz, $CDCl_3$): δ, 0.88 (t, 6H, 2 × CH_3), 1,26 (br. s, 40H, 20 × CH_2), 1.59 (m, 4H, 2 × CH_2), 2.29 (m, 4H, 2 × CH_2), 3.40 (s, 3H, OCH_3), 3.62 (dd, 1H, $J_{4,5}$ = 9.7 Hz, H-4), 3.75 (dd, 1H, $J_{6a,6b}$ = 10.2 Hz, H-6a), 3.78 (s, 3H, OCH_3), 3.92 (m, 1H, H-5), 4.28 (dd, 1H, $J_{5,6b}$ = 4.7 Hz, H-6b), 4.82 – 2.94 (m, 2H, H-1, 2), 5.46 (s, 1H, > C*H*Ph), 5.60 (dd, 1H, $J_{3,4}$ = 9.7 Hz, H-3), 6.86 (d, 2H, *J* = 8.8 Hz, aromatic), 7.25 (d, 2H, *J* = 8.7 Hz, aromatic) ppm; ^{13}C NMR (75 MHz, $CDCl_3$): δ, 14.3 (×2), 22.9 (×2), 25.1 (×2), 25.28, 29.2 (×2), 29.4, 29.5 (×3), 29.6, 29.7, 29.8 (×2), 29.9, 32.1 (×2), 34.3, 34.5, 55.4, 55.5, 62.5, 68.8, 68.9, 71.6, 76.8, 77.2, 77.6, 79.5, 97.8, 101.6, 113.7 (×2), 127.6 (×2), 129.62, 160.2, 172.6, 173.4ppm; HR FAB MS $[M+Na]^+$ calcd for $C_{43}H_{72}O_9Na$ 755.5074, found 755.5090.

Methyl 4-*O*-*p*-methoxybenzyl-3-*O*-tetradecanoyl-α-D-glucopyranoside (16)

A 1 M solution of BH_3-THF in tetrahydrofuran (5 mL, 5 mmol) was mixed with compound **15** (0.75 g, 1.02 mmol) and the resulting mixture was stirred for 10 min at rt under argon. Freshly conditioned copper(II) trifluoromethanesulfonate (18 mg, 0.05 mmol) was added, and the reaction mixture was stirred for 2 h at rt. After that, the reaction mixture was cooled to 0 °C and then quenched by the sequential addition of triethylamine (0.14 mL, 1 mmol) and methanol (1.8 mL). The resulting mixture was concentrated under reduced pressure followed by co-evaporation with methanol. The residue was purified by flash column chromatography on silica gel (ethyl acetate–hexane gradient elution) to give the title compound **16** (0.35g, 0.67 mmol) as white solid in 67% yield. Analytical data for **16**: R_f 0.40 (ethyl acetate/hexane, 7/3, *v*/*v*); $[\alpha]_D^{22}$+78.5° (*c* = 1.0, $CHCl_3$); ^{1}H NMR (300 MHz, $CDCl_3$): δ = 0.88 (t, 3H, *J* = 7.02 Hz, CH_3), 1.24 (br. s, 20H, 10 × CH_2), 1.63 (m, 2H, CH_2), 1.97 (br. s, 1H, OH), 2.23–3.82 (m, 3H, CH_2, OH), 3.41 (s, 3H, OCH_3), 3.52–3.82 (m, 5H, H-2, 4, 5, 6a, 6b), 3.79 (s, 3H, OCH_3), 4.57 (dd, 2H, *J* = 12.4 Hz, C*H*$_2$Ph), 4.75 (d, 1H, $J_{1,2}$ = 3.7 Hz, H-1), 5.30 (dd, 1H, *J* = 9.1 Hz, H-3), 6.85 (d, 2H, *J* = 8.6 Hz, aromatic), 7.20 (d, 2H, *J* = 8.6 Hz, aromatic) ppm; ^{13}C NMR (75 MHz, $CDCl_3$): δ = 14.3, 22.9, 25.1, 29.3, 29.5 (×2), 29.6, 29.8 (×4), 29.9, 32.1, 34.7, 55.4, 55.5, 61.7, 71.0, 71.9, 74.3, 74.9, 99.6, 114.0 (×2), 129.6 (×2), 130.1, 159.5, 174.3 ppm; HR FAB MS $[M+Na]^+$ calcd for $C_{29}H_{48}O_8Na$ 547.3247, found 547.3254.

Methyl 6-*O*-(3-carboxypropanoyl)-4-*O*-*p*-methoxybenzyl-2,3-di-*O*-tetradecanoyl-α-D-glucopyranoside (17)

DMAP (8.1 mg, 0.06 mmol) and succinic anhydride (67 mg, 0.67 mmol) were added to a stirred solution of derivative **16** (0.35g, 0.67 mmol) in dry pyridine (5 mL) and the resulting mixture was stirred for 16 h at rt under argon. After that, myristoyl chloride (0.21 ml, 0.80 mmol) was added dropwise, and the reaction mixture was stirred for 2 h at rt. After that, the resulting mixture was concentrated under reduced pressure. The residue was dissolved in CH_2Cl_2 (30 mL) and washed successively with 1N HCl (2 × 15 mL), water (2 × 15 mL) and brine (15 mL). The organic phase was separated, dried over $MgSO_4$,

filtered and concentrated *in vacuo*. The residue was purified by column chromatography on silica gel (ethyl acetate–hexane gradient elution) to give compound **17** (0.43 g, 0.52 mmol) as white syrup in 79% yield. Analytical data for **17**: R_f 0.55 (ethyl acetate-hexane 1/1, *v*/*v*); $[\alpha]_D^{24}$ +42.4 ^{o} (*c* = 1.0, $CHCl_3$); ^{1}H NMR (300 MHz, $CDCl_3$): δ, 0.87 (t, 6H, 2 × CH_3), 1.25 (br. s, 40H, 20 × CH_2), 1.59 (m, 4H, 2 × CH_2), 2.26 (m, 2H, CH_2), 2.33 (m, 2H, CH_2), 2.61 (m, 4H, 2 × CH_2), 3.36 (s, 3H, OCH_3), 3.59 (dd, 1H, $J_{4,5}$ = 9.5 Hz, H-4), 3.90 (m, 1H, H-5), 4.28 (dd, 2H, $J_{5,6b}$ = 4.4 Hz, $J_{6a,6b}$ = 11.5 Hz, H-6a, 6b), 4.44 (d, 1H, ^2J = 10.7 Hz, ½ CH_2Ph), 4.54 (d, 1H, ^2J = 10.7, ½ CH_2Ph), 4.87 (m, 2H, H-1, 2), 5.55 (dd, 1H, $J_{3,4}$ = 9.5 Hz, H-3), 6.84 (d, 2H, *J* = 8.7 Hz, aromatic), 7.16 (d, 2H, *J* = 8.6 Hz, aromatic) ppm; ^{13}C NMR (75 MHz, $CDCl_3$): δ, 14.3 (×3), 22.8 (×3), 25.1 (×2), 28.8, 29.2, 29.3, 29.4 (×2), 29.5, 29.6, 29.7 (×4), 29.8 (×4), 32.1 (×4), 34.2, 34.5, 55.4 (×2), 62.7, 68.6, 71.8, 71.9, 74.3, 75.7, 96.9, 114.0 (×2), 129.5, 129.8 (×2), 159.6, 171.7, 172.8, 173.7 ppm; HR FAB MS $[M+Na]^+$ calcd for $C_{47}H_{78}O_{12}Na$ 857.5391, found 857.5410.

Methyl 6-*O*-(4-((S)-2-(9-fluorenylmethoxycarbonyl)amino-3-(*tert*-butoxy)-3-oxopropyl)oxy-4-oxobutanoyl)-2,3-di-*O*-tetradecanoyl-α-D-glucopyranoside (18)

DMAP (9.5 mg, 0.07 mmol) and DIC (0.12 mL, 0.78 mmol) were added to a stirred solution of *O*-*tert*-butyl-*N*-fluorenylmethoxycarbonyl-L-serine **9**[15,16] (0.15 g, 0.39 mmol) in CH_2Cl_2 (3 mL). After 1 h, the carboxylic acid derivative **17** (0.39 g, 0.46 mmol) was added and the reaction was stirred for 5–9 h at rt until no further conversion of the starting material could be detected by TLC. The reaction mixture was diluted with CH_2Cl_2 (20 mL), washed with water (2 × 10 mL) and brine (10 mL). The organic phase was separated, dried over $MgSO_4$, filtered and concentrated *in vacuo*. The residue was purified by column chromatography on silica gel (ethyl acetate-hexane gradient elution) to afford the title compound **18** (0.38 g, 0.32 mmol) as a white solid in 83% yield. Analytical data for **18**: R_f 0.5 (ethyl acetate/hexane, 3/7, *v*/*v*); $[\alpha]_D^{24}$ +25.7^o (*c* = 1.0, $CHCl_3$); ^{1}H NMR (300 MHz, $CDCl_3$): δ, 0.88 (t, 6H, 2 × CH_3), 1.25 (br. s, 40H, 20 × CH_2), 1.49 (s, 9H, *t*-Bu), 1.59 (m, 4H, 2 × CH_2), 1.59 (m, 4H, 2 × CH_2), 2.30 (m, 4H, 2 × CH_2), 3.37 (s, 3H, OCH_3), 3.48 (dd, 1H, $J_{4,5}$ = 9.5 Hz, H-4), 3.76 (s, 3H, OCH_3), 3.90 (m, 1H, H-5), 4.16–4.26 (m, 3H, H-6a, 6b, Ser-C$^\beta H$), 4.35–4.55 (m, 6H, CH_2Ph, Ser-C$^\alpha H$, C*H*Fmoc, OCH_2Fmoc), 4.90 (m, 2H, H-1, 2), 5.58 (dd, 1H, $J_{3,4}$ = 9.7 Hz, H-3), 5.82 (d, 1H, $J_{NH,CH}$ = 8.3 Hz, Ser-N*H*), 6.18–7.77 (m, 12H, aromatic) ppm; ^{13}C NMR (75 MHz, $CDCl_3$): δ, 14.2 (×3), 22.8 (×3), 25.0, 28.0 (×4), 29.3 (×2), 29.4 (×2), 29.5 (×3), 29.6 (×3), 29.8 (×5), 32.0 (×3), 34.2, 34.4, 47.2, 54.0, 55.3 (×2), 62.6, 67.4, 68.5, 71.7, 71.9, 74.3, 76.7, 83.0, 96.8, 113.9 (×3), 120.1 (×2), 125.4, 127.2 (×2), 127.8 (×2), 129.3 (×2), 129.6 (×2), 141.4 (×2), 144.0 (×2), 156.0, 159.5, 168.4, 171.5, 171.8, 172.7, 173.5 ppm; HR FAB MS $[M+Na]^+$ calcd for $C_{69}H_{101}NO_{16}Na$ 1222.7018, found 1222.7023.

Methyl 6-*O*-(4-((S)-2-(9-fluorenylmethoxycarbonyl)amino-2-carboxyethyl)oxy-4-oxobutanoyl)-2,3-di-*O*-tetradecanoyl-α-D-glucopyranoside (19)

Compound **18** (0.2 g, 0.16 mmol) was dissolved in TFA/wet CH_2Cl_2 (1/5, *v*/*v*, 4 mL) and stirred for 2 h at rt. After that, the volatiles were evaporated *in vacuo*, and the residue was diluted with CH_2Cl_2 (5 mL) and neutralized with triethylamine (until pH ~ 7). The volatiles were removed under reduced pressure and the residue was purified by column chromatography on silica gel (ethyl acetate/hexane, 1/1, *v*/*v*) to afford the title compound **19** (0.13 g, 0.12 mmol) as a white foam in 75% yield. Analytical data for **19**: R_f 0.5 (methanol-ethyl acetate 1/9, *v*/*v*); ^{1}H NMR (300 Hz, $CDCl_3$): δ, 0.88 (t, 6H, 2 × CH_3), 1.25 (br. s, 40H, 20 × CH_2), 1.58 (m, 4H, 2 × CH_2), 2.33 (m, 4H, 2 × CH_2), 2.64 (br. s, 4H, 2 × CH_2), 3.27 (br. s, 1H, OH), 3.38 (s, 3H, OCH_3), 3.47 (dd, 1H, $J_{4,5}$ = 9.4 Hz, H-4), 3.83 (m, 1H, H-5), 4.21–4.51 (m, 7H, H-6a, 6b, Ser-C$^\beta H_2$, C*H*Fmoc, OCH_2Fmoc), 4.67 (m, 1H, Ser-C$^\alpha H$) 4.86 (m, 1H, H-2), 4.90 (br. s, 1H, H-1), 5.31 (dd, 1H, $J_{3,4}$ = 9.1 Hz, H-3), 5.96 (br. s, 1H, $J_{NH,CH}$ = 8.3 Hz, Ser-NH), 7.27–7.76 (m, 8H, aromatic) ppm; ^{13}C NMR (75 MHz, $CDCl_3$); δ, 14.3 (×3), 22.9 (×3), 25.0 (×2), 25.1, 28.9, 29.2, 29.30, 29.4 (×2), 29.5 (×2), 29.6, 29.8 (×2), 29.9, 32.1 (×2), 34.2 (×2), 34.5, 47.2, 55.5, 62.9, 64.3, 67.6, 69.4, 69.6, 69.9, 71.2, 72.7, 77.4, 96.8, 114.1, 120.2 (×2), 124.9 (×2), 125.3 (×2), 127.3 (×2), 127.9 (×2), 141.4 (×2), 143.8, 143.9, 171.7, 171.8, 174.3, 174.6, 175.1 ppm; HR FAB MS $[M+Na]^+$ calcd for $C_{57}H_{85}NO_{15}Na$ 1046.5817, found 1045.5822.

Methyl 6-*O*-(3-carboxypropanoyl)-4-*O*-*p*-methoxybenzyl-2,3-di-*O*-tetradecanyl-α-D-glucopyranoside (22)

DMAP (7.0 mg, 0.05 mmol) and succinic anhydride (71 mg, 0.70 mmol) were added to a stirred solution of methyl 4-*O*-*p*-methoxybenzyl-2,3-di-*O*-tetradecanyl-α-D-glucopyranoside **21**[13] (0.40 g, 0.56 mmol) in dry pyridine (5 mL) and the resulting reaction mixture was stirred for 16 h at rt under argon. After that, the reaction mixture was concentrated under reduced pressure. The residue was dissolved in CH_2Cl_2 (30 mL) and washed successively with 1N HCl (2 × 15 mL), water (2 × 15 mL) and brine (15 mL). The organic phase was separated, dried over $MgSO_4$, filtered and concentrated *in vacuo*. The residue was purified by column chromatography on silica gel (ethyl acetate–hexane gradient elution) to give the title compound **22** (0.41 g, 0.50 mmol) as a colorless syrup in 89% yield. Analytical data for **22**: R_f 0.55 (ethyl acetate/hexane, 7/3, *v*/*v*); $[\alpha]_D^{24}$ +42.9^o (*c* = 1.0, $CHCl_3$); ^{1}H NMR (300 MHz, $CDCl_3$): δ, 0.88 (t, 6H, 2 × CH_3), 1.26 (br. s, 40H, 22 × CH_2), 1.63 (m, 4H, 2 × CH_2), 2.64 (m, 2H, 2 × CH_2), 3.30 (dd, 1H, $J_{2,3}$ = 9.7 Hz, H-2), 3.38 (s, 3H, OCH_3), 3.39 (m, H-4), 3.59–3.76 (m, 5H, H-3, 5, OCH_2, OCH_2^a), 3.80 (s, 3H, OCH_3), 3.86 (m, 1H, OCH_2^b), 4.28 (m, 2H, $J_{5,6b}$ = 4.7 Hz, $J_{5,6a}$ = 2.3 Hz, $J_{6a,6b}$ = 12.0 Hz, H-6a, 6b), 4.49 (d, 1H, ^2J = 10.5 Hz, ½ CH_2Ph), 4.76 (d, 1H, $J_{1,2}$ = 3.5 Hz, H-1), 4.81 (d, 1H, ^2J = 10.5 Hz, ½ CH_2Ph), 6.89 (d, 2H, *J* = 8.9 Hz, aromatic), 7.22 (d, 2H, *J* = 9.7 Hz, aromatic) ppm; ^{13}C NMR (125 MHz, $CDCl_3$): δ = 14.3 (×3), 22.9 (×3), 26.2, 26.5, 28.8, 28.9, 29.5 (×5), 29.7 (×4), 29.8, 29.9, 30.3, 30.8, 32.1 (×4), 55.3, 55.5, 63.6, 68.8, 72.0, 74.1, 74.8, 80.9, 81.9, 98.1, 114.1 (×3), 130.1 (×3), 130.4, 159.6, 172.0, 176.5 ppm; HR FAB MS $[M+Na]^+$ calcd for $C_{47}H_{82}O_{10}Na$ 829.5805, found 829.5806.

Methyl 6-*O*-(4-((S)-2-(9-fluorenylmethoxycarbonyl)amino-3-(*tert*-butoxy)-3-oxopropyl)oxy-4-oxobutanoyl)-2,3-di-*O*-tetradecanyl-α-D-glucopyranoside (23)

DMAP (6.2 mg, 0.05 mmol) and DIC (0.16 mL, 1.01 mmol) were added to a stirred solution of *O*-*tert*-butyl-*N*-fluorenylmethoxycarbonyl-L-serine **9**[15,16] (0.39 g, 0.60 mmol) in CH_2Cl_2 (3 ml).

After 1 h, the carboxylic acid derivative **22** (0.41 g, 0.50 mmol) was added and the reaction was stirred for 5–9 h until no further conversion of the starting material could be detected by TLC. The reaction mixture was diluted with CH_2Cl_2 (20 mL), washed with water (2 × 10 mL) and brine (10 mL). The organic phase was separated, dried over $MgSO_4$, filtered and concentrated *in vacuo*. The residue was purified by column chromatography on silica gel (ethyl acetate–hexane gradient elution) to afford the title compound **23** (0.47 g, 0.40 mmol) as a colorless amorphous solid in 79% yield. Analytical data for **23**: R_f 0.43 (ethyl acetate/hexane, 3/7, *v*/*v*); $[\alpha]_D^{24}$ +36.1° (*c* = 1.0, $CHCl_3$); ^{1}H NMR (300 MHz, $CDCl_3$): δ, 0.88 (t, 6H, 2 × CH_3), 1.17 (m, 40H, 20 × CH_2), 1.38 (s, 9H, *t*-Bu), 1.54 (m, 4H, 2 × CH_2), 2.53 (m, 4H, 2 × CH_2), 3.18 (dd, 1H, $J_{2,3}$ = 9.7 Hz, H-2), 3.26 (s, 3H, OCH_3), 3.28 (m, 1H, H-4), 3.42–3.66 (m, 5H, H-3, 5, OCH_2, OCH_2^a), 3.67 (s, 3H, OCH_3), 3.79 (m, 1H, OCH_2^b), 4.11–4.46 (m, 9H, H-6a, 6b, ½ CH_2Ph, Ser-C$^\alpha H$, Ser-C$^\beta H_2$, , C*H*Fmoc, OCH_2Fmoc), 4.66 (d, 1H, $J_{1,2}$ = 3.3 Hz, H-1), 4.71 (d, 1H, ^2J = 10.5 Hz, ½ CH_2Ph), 5.71 (d, 1H, $J_{NH,CH}$ = 8.1 Hz, Ser-N*H*), 6.75–7.64 (m, 12H, aromatic) ppm; ^{13}C NMR (75 MHz, $CDCl_3$): δ, 14.2 (×3), 22.8 (×3), 26.1, 26.4, 28.0 (×3), 28.7, 28.9 (×3), 29.5, 29.6 (×3), 29.7 (×5), 29.8, 30.2, 30.7, 32.0 (×3), 47.0, 54.0, 55.2, 55.3 (×2), 64.7, 67.3, 68.6, 71.8, 73.8, 74.6, 80.8, 81.8, 83.0, 97.9, 99.7, 113.9 (×2), 120.1 (×2), 125.2, 125.3, 127.2 (×2), 127.8 (×2), 129.9 (×2), 130.3, 141.4 (×2), 143.9 (×2), 155.9, 159.4, 168.4, 171.7, 172.0, 181.3 ppm; HR FAB MS $[M+Na]^+$ calcd for $C_{69}H_{105}NO_{14}Na$ 1194.7433, found 1194.7433.

Methyl 6-*O*-(4-((S)-2-(9-fluorenylmethoxycarbonyl)amino-2-carboxyethyl)oxy-4-oxobutanoyl)-2,3-di-*O*-tetradecanyl-α-D-glucopyranoside (24)

Conjugate **23** (0.2 g, 0.17 mmol) was dissolved in TFA/wet CH_2Cl_2 (1/5, *v*/*v*, 4 mL) and the resulting mixture was stirred for 2 h at rt. After that, the volatiles were evaporated under the reduced pressure, the residue was diluted with CH_2Cl_2 (5 mL) and neutralized with triethylamine (until pH ~ 7). The volatiles were removed under the reduced pressure and the residue was purified by column chromatography on silica gel (ethyl acetate/hexane 1/1, *v*/*v*) to obtain the title compound **24** (0.13 g, 0.14 mmol) as a white amorphous solid in 81% yield. Analytical data for **24**: R_f 0.58 (methanol/ethyl acetate, 1.5/8.5, *v*/*v*); $[\alpha]_D^{26}$ +34.9° (*c* = 1.0, $CHCl_3$); ^{1}H NMR (500 MHz, $CDCl_3$/$(CD_3)_2SO$, 2/1, *v*/*v*): δ, 0.78 (t, 6H, 2 × CH_3), 1.45 (br. s, 40 H, 20 × CH_2), 1.47 (m, 4H, 2 × CH_2), 2.5 (m, 4H, 2 × CH_2), 3.10 (dd, 1H, $J_{2,3}$ = 9.4 Hz, H-2), 3.22–3.33 (m, 7H), 3.41–3.51 (m, 3H), 3.55 (m, 1H, H-5), 3.64 (t, 2H, *J* = 6.7 Hz), 4.14–4.32 (m, 7H), 4.42 (d, 1H, *J* = 9.5 Hz), 4.63 (d, 1H, $J_{1,2}$ = 3.2 Hz,, H-1), 6.52 (br. s, 1H, Ser-N*H*), 7.22–7.82 (m, 8H, aromatic) ppm; ^{13}C NMR (125 MHz, $CDCl_3$/$(CD_3)_2SO$, 2/1, *v*/*v*): δ, 13.6 (×3), 21.9 (×3), 25.4 (×2), 25.5 (×2), 28.6 (×3), 28.8, 28.9 (×4), 29.0 (×5), 29.5, 31.2 (×3), 46.6, 54.3 (×2), 63.4, 64.9, 65.6, 69.2, 69.4, 70.6, 72.7, 79.6, 80.7, 97.3, 119.4 (×2), 124.6, 124.8, 126.6 (×2), 127.1 (×2), 140.1 (×2), 143.4 (×2), 155.4, 171.3, 171.6, 178.3, 178.7 ppm; HR FAB MS $[M+Na]^+$ calcd for $C_{57}H_{89}NO_{13}Na$ 1018.6232, found 1018.6182.

Preparation of compounds for cellular treatment

Synthetic compounds in solid form were dissolved in tetrahydrofuran (THF), aliquotted in small volumes, vacuum-centrifuged for 1 h and stored at −80 °C as dry compounds. For cellular treatment, an aliquot was dissolved in an appropriate volume of dimethylsulfoxide (DMSO) to give a concentrated working stock solution. This stock solution was further diluted in DMSO to give the desired concentration range. The final concentration of DMSO in the cell treatments was always maintained at 0.6%. Concentrations of Fmoc-containing compounds were verified by absorbance using an extinction coefficient of 7800 $M^{-1}cm^{-1}$ at 301 nm.

Cell culture and LPS antagonism assays

THP-1 cells were obtained from ATCC (Manassas, VA) and maintained in a RPMI-1640 culture medium (HyClone, Logan, UT) containing 2 mM L-glutamine, 25 mM HEPES, 1.5 g L^{-1} sodium bicarbonate, 10% fetal bovine serum (FBS) (HyClone), 50 units mL^{-1} penicillin, 50 μg mL^{-1} streptomycin (HyClone), and 50 μM β-mercaptoethanol at 37 °C in 5% CO_2. For cellular assays, THP-1 monocytes were centrifuged and resuspended in a fresh growth medium to a cell density of 5 × 10^5 cells mL^{-1}. Cells were then seeded in a 48-well plate and differentiated into adherent macrophages by treatment with 10 ng mL^{-1} phorbol 12-myristate 13-acetate (PMA) (Sigma) for 24 h at 37 °C in 5% CO_2. The non-adherent cells were removed and the adherent cells were washed and replenished with reduced FBS growth medium. For the two wells set aside for calculating percent differentiation, the cells were washed with PBS (Hyclone) prior to removal by 0.25% trypsin-EDTA. Cells in a separate well were removed with 0.25% trypsin and counted under the microscope using a hemocytometer to determine the number of adherent macrophages. For the remaining wells, the cells were pre-incubated with LPS antagonist compounds at different concentrations for 30 min followed by the addition of 10 ng mL^{-1} ultrapure LPS from *E. coli* K12 (InvivoGen, San Diego, CA) for 6 h at 37 °C in 5% CO_2. 0.6% DMSO was used as a control. The cell medium was collected and stored at −20 °C until analyzed by ELISA for secreted TNFα production.

Cell viability measurements

Cell viability was monitored using an XTT [2,3-bis(2-methoxy-4-nitro-5-sulfophenyl)-2*H*-tetrazolium-5-carboxanilide] assay. Macrophage metabolic activity was assessed by probing mitochondrial reduction of XTT (Sigma) which is a measure of viability (or toxicity) in response to the synthetic antagonists. Following 6 h treatment with antagonist compounds and LPS, the macrophages were washed with PBS (Hyclone) and incubated with XTT (0.33 mg mL^{-1}) and phenazine methosulfate (PMS) (8.3 μM) (Acros, Morris Plains, NJ) to a final concentration of 0.33 mg mL^{-1} and 8.3 μM respectively for 2 h at 37 °C in 5% CO_2. The cellular toxicity was then assessed in a platereader using absorbance of reduced XTT at 467 nm.

Acknowledgements

This work was supported by awards from the AHA (0855743G to AVD) and NIH (1R15AG033913-01 to MRN). AFGB, MLDU, and SK are grateful to the UM—St. Louis Graduate School for awarding them with the Dissertation Fellowship in 2008, 2009, and 2010, respectively. Dr Winter and Mr. Kramer (UM—St. Louis) are thanked for HRMS determinations.

References

1 *Gram-negative septicemia and septic shock*, ed., L. Young and M. Glauser, WB Saunders, Philadelphia, 1991.
2 S. Tabbutt, *Crit. Care Med.*, 2001, **29**, S231–S236.
3 A. F. Suffredini, R. E. Fromm, M. M. Parker, M. Brenner, J. A. Kovacs, R. A. Wesley and J. E. Parrillo, *N. Engl. J. Med.*, 1989, **321**, 280–287.
4 U. Zahringer, B. Lindner and E. T. Rietschel, *Adv. Carbohydr. Chem. Biochem.*, 1994, **50**, 211–276.
5 C. R. H. Raetz, R. J. Ulevitch, S. D. Wright, C. H. Sibley, A. Ding and C. F. Nathan, *FASEB J.*, 1991, **5**, 2652–2660.
6 T. A. Garrett and C. R. H. Raetz, *Carbohydrates in Chemistry and Biology*, ed. B. Ernst, G. W. Hart and P. Sinay, Wiley-VCH, Weinheim, New York, 2000, pp. 435–447.
7 M. S. Jin and J. O. Lee, *Immunity*, 2008, **29**, 182–191.
8 D. P. Rossignol, L. D. Hawkins, W. J. Christ, S. Kobayashi, T. Kawata, M. Lynn, I. Yamatsu and Y. Kishi, *Endotoxin in Health and Disease*, ed. H. Brade, S. M. Opal, S. N. Vogel and D. C. Morrison, Marcel Dekker, Inc., New York - Basel, 1999, pp. 699–717.
9 W. J. Christ, P. D. McGuinness, O. Asano, Y. Wang, M. A. Mullarkey, M. Perez, L. D. Hawkins, T. A. Blythe, G. R. Dubuc and A. L. Robidoux, *J. Am. Chem. Soc.*, 1994, **116**, 3637–3638.
10 N. P. J. Price, B. Jeyaretnam, R. W. Carlson, J. L. Kadrmas, C. R. H. Raetz and K. A. Brozek, *Proc. Natl. Acad. Sci., USA*, 1995, **92**, 7352–7356.
11 A. V. Demchenko, M. A. Wolfert, B. Santhanam, J. N. Moore and G. J. Boons, *J. Am. Chem. Soc.*, 2003, **125**, 6103–6112.
12 M. Shiozaki, H. Doi, D. Tanaka, T. Shimozato and S. Kurakata, *Tetrahedron*, 2006, **62**, 205–225.
13 F. Peri, F. Granucci, B. Costa, I. Zanoni, C. Marinzi and F. Nicotra, *Angew. Chem., Int. Ed.*, 2007, **46**, 3308–3312.
14 H. G. Bazin, M. W. Wolff and R. J. Linhardt, *J. Org. Chem.*, 1999, **64**, 144–152.
15 M. Schultz and H. Kunz, *Tetrahedron: Asymmetry*, 1993, **4**, 1205–1220.
16 L. Le Corre, C. Gravier-Pelletier and Y. Le Merrer, *Eur. J. Org. Chem.*, 2007, 5386–5394.
17 W. J. Christ, O. Asano, A. L. C. Robidoux, M. Perez, Y. Wang, G. R. Dubuc, W. E. Gavin, L. D. Hawkins, P. D. McGuinness, M. A. Mullarkey, M. D. Lewis, Y. Kishi, T. Kawata, J. R. Bristol, J. R. Rose, D. P. Rossignol, S. Kobayashi, L. Hishinuma, A. Kimura, N. Asakawa, K. Katayama and I. Yamatsu, *Science*, 1995, **268**, 80–83.
18 M. Akamatsu, Y. Fujimoto, M. Kataoka, Y. Suda, S. Kusumoto and K. Fukase, *Bioorg. Med. Chem.*, 2006, **14**, 6759–6777.
19 K. Deng, M. M. Adams and D. Y. Gin, *J. Am. Chem. Soc.*, 2008, **130**, 5860–5861.
20 K. K. Maiti, M. DeCastro, A. B. M. A. A. El-Sayed, M. I. Foote, M. A. Wolfert and G. J. Boons, *Eur. J. Org. Chem.*, 2010, 80–91.
21 S. Tang, Q. Wang and Z. Guo, *Chem.–Eur. J.*, 2010, **16**, 1319–1325.
22 N. Moitessier, P. Englebienne and Y. Chapleur, *Tetrahedron*, 2005, **61**, 6839–3853.

CHAPTER 1

INTRODUCTION

1.1 Protein Misfolding and Amyloids

One of the most fundamental and universal examples of self-assembly is the folding of a protein into its three-dimensional structure. The folding of a protein is connected to many biological processes, such as trafficking of molecules to their specific cellular locations and regulation of cellular growth and differentiation. However, only correctly folded proteins are able to withstand biological environments and, therefore, selectively interact with their natural partners. Folding of proteins can be variable. *In vivo*, some proteins are co-translational; meaning the folding of the protein was initiated before the completion of the protein synthesis, while the protein was still attached to the ribosome. However, other proteins endure the majority of their folding in the cytoplasm, after its synthesis and release from the ribosome. Also, some proteins remain unfolded until they are in specific compartments, such as the mitochondria or endoplasmic reticulum (ER) (Dobson, 2003).

The accumulation of proteins with highly abnormal conformations within a cell is a continuous threat to the cell's function and viability. If the conformation of a protein is lost through mutation or post synthetic damage, the cell will attempt to evolve to prevent the aggregation of unfolded proteins and correctly refold them. But if this is not possible, the cell is programed to hydrolyze the abnormal polypeptide back to its amino acids. One

preventative protein is the chaperone protein; which is a major cell constituent that is essential to ensure the proper folding and intracellular localization of newly synthesized polypeptides. However, there are still a large portion of the newly synthesized polypeptides that fail to achieve their correct configurations and are rapidly digested. The degradation process of a cellular protein is very selective. This mechanism is marked by a small polypeptide cofactor, ubiquitin, which leads to the rapid breakdown by the proteolytic complex, the proteasome (Sherman and Goldberg, 2001, Wang and Terpstra, 2013).

Many distinct diseases have been linked to the progressive misfolding of specific proteins into aggregates. Amyloidosis occurs when normally soluble proteins form insoluble deposits of fibrils, which are high in β-sheet structure (Figure 1.8) and accumulate in the extracellular space of various tissues. One disease associated with amyloidosis is Alzheimer's disease (AD), which is the accumulation of the protein amyloid-β (Aβ) (Selkoe, 2003). The term amyloid was first coined due to the deposits having a resemblance to starch due to it positive iodine staining (Virchow, 1851); however, later, when the amyloids were found to be protein, the term amyloid remained (Kyle, 2001). In the past, amyloids had solely been associated with human disease; however, a functional discovery has also been revealed in organisms such as bacteria (Fowler et al., 2007). Bacteria have been shown to express several cell-surface proteinaceous filaments which can promote colonization of an epithelial surface, entry into host cells, exchange of DNA between bacteria, and development of bacterial communities organized as biofilms, colonies, or multicellular fruiting bodies (Chapman et al., 2002). The presence of the bacterial biofilms demonstrates that amyloids can be

formed in a highly regulated manner and may not always represent a 'misfolded' toxic protein structure (Fowler et al., 2007).

Conformational diseases occur when a specific protein undergoes a conformational rearrangement that causes it to have a tendency to aggregate and become deposited in specific tissues or cellular compartments (Kopito and Ron, 2000). These aggregates show resemblance to extracellular aggregates, due to their insolubility, β-rich secondary structure, and birefringence with Congo-red (Carrell and Lomas, 1997). A few examples of conformational diseases include Alzheimer's and Parkinson's disease, amyloidosis, α_1-antitrypsin deficiency and the prion encephalopathies. Some of these diseases can be inherited or induced; however, most of these diseases have unknown etiology (Kopito and Ron, 2000). Despite the lack of sequence homologies among these conformational disease proteins and the deficiency in structural folding similarities during normal non-pathological conditions, all of these proteins form a common amyloid fibril structure under appropriate conditions. The amyloid fibrils have a cross-β structure resulting in a β-sheet propagating fibril (Figure 1.4A). However, Chiti and colleagues showed that this specific fibril formation was not a feature of only a few proteins, but could be produced by proteins that are not associated with any amyloid diseases (Chiti et al., 1999). This knowledge shows the importance of understanding the structure and aggregation of protein folding in order to possibly prevent associated diseases.

1.2 Alzheimer's Disease: Understanding the Etiology of the Disease

Among the many different neurodegenerative disorders, AD has become one of the most common types of dementia (Selkoe, 2001). Dementia is a term used to describe

many of the neurodegenerative disorders that develop when nerve cells in the brain either die or no longer retain their normal function. In AD patients, the neuronal loss usually results in the decline of one's memory, motor skills, and ability to think clearly. It has been estimated that in 2013 5.2 million Americans were living with AD and in the coming decades the baby boom generation is projected to add about 10 million to the total of Americans with AD. AD is ultimately fatal, with it being the sixth leading cause of death in the United States and the fifth leading cause of death of Americans over the age of 65 (Thies and Bleiler, 2013).

Those studying AD have had their share of controversy due to the cytological and biochemical complexity of the disease. Through the years it has been difficult to agree on the sequence of events leading to the dementia and which events are the most important for intervention. However, there has been substantial progress on untangling the disease due to extremely high incidence. A considerable amount of research has shown that there are certain molecular events which occur in the brain years or even decades prior to the first symptoms (Selkoe, 2011). This stage has been termed the preclinical phase and can last for a decade or more (Bateman et al., 2012). During this stage of AD, the patient appears to be cognitively intact with normal scores on neuropsychiatric test, but show evidence of the disease through cerebrospinal fluid (CSF) analysis or through brain imaging (Zahs and Ashe, 2013). As of now, patients with AD only marginally and briefly respond to available drugs as treatment and unless new, disease-modifying drugs become accessible, soon, the number of AD cases will continue to rise (Bloom, 2014, Thies and Bleiler, 2012).

1.3 AD Pathology

The signs of AD were observed long before the Bavarian psychiatrist, Alois Alzheimer, diagnosed AD in 1906. This diagnosis came after the observation of a 51-year-old female postmortem autopsy (Selkoe and Podlisny, 2002). Through the observation of postmortem brain slices, Alzheimer was able to discover that AD is characterized by two distinctive lesions, the neurofibrillary tangles (NFTs) and senile plaques (Selkoe, 2004) (Figure 1.1). The NFTs are composed of hyperphosphorylated tau protein (Grundke-Iqbal et al., 1986), while the major constituent of the senile plaques is Aβ protein. The plaques are routinely found in the parenchyma and cerebral vessels (Selkoe, 1994) and are typically found associated with dystrophic neuritis and activated immune cells, such as astrocytes and microglia (Wisniewski et al., 1989). More recent observations of senile plaques (Aβ) and NFTs (tau) have shown that the Aβ is more clearly associated with the cause of AD, while the tau protein is most closely related to the clinical manifestations of AD (Dickson, 2004).

1.3.1 Neurofibrillary Tangles

The fibrous system of eukaryotic cells is mainly comprised of microtubules, where tubulin is the basic subunit. The microtubules are generally involved in cellular or intracellular motion or maintenance of cellular shape, but they are also a large component of the nerve axons. In the nerve axons, the microtubules are associated with transport and neurotransmission. In 1975, Weingarten and colleagues isolated a heat stable protein called tau in which its normal function was to induce microtubule formation (Weingarten et al., 1975). However, about ten years later, observations were made by several research

groups showing that tau was one of the main components of the paired helical filaments (PHFs) and the NFTs (Johnson and Jenkins, 1999), which were found in the entorhinal cortex, hippocampus, amygdala, association cortices of the frontal, temporal and parietal lobes, and certain subcortical nuclei that project to these regions (Selkoe, 2011).

Tau was found to be highly asymmetric with little defined secondary structure, which may result from high number of proline and glycine residues in its primary structure (Johnson and Jenkins, 1999). Jameson and colleagues presented data in 1980 that suggested the increase in phosphorylation of the tau protein decreased its ability to promote microtubule assembly (Jameson et al., 1980). This information led to the observation that hyperphosphorylated tau was the predominant tau structure of the PHFs and NFTs in the AD brain (Johnson and Jenkins, 1999). The hyperphosphorylated tau was found to form oligomers, which are thought to be converted to highly insoluble fibrils in the frontal cortex of the brain (Figure 1.2). An increase in the tau oligomer levels may be a very early sign of the formation of NFTs and AD (Giacobini and Gold, 2013, Maeda et al., 2006). The fibrillar formation is not clearly associated with the phosphorylation of the tau protein, but the phosphorylation is known to reduce the affinity of tau for the microtubules, thus decreasing its ability to promote microtubule assembly, as mentioned above. The reduced affinity for the microtubules leads to the destabilization of the microtubules and increased degeneration of associated neurons (Bramblett et al., 1993). The tau aggregates within the NFTs are also commonly associated with ubiquitin. This association may be the cells attempt at removing the tau filaments by degradation in the proteasome, but the process appears to be unsuccessful (Selkoe, 2011).

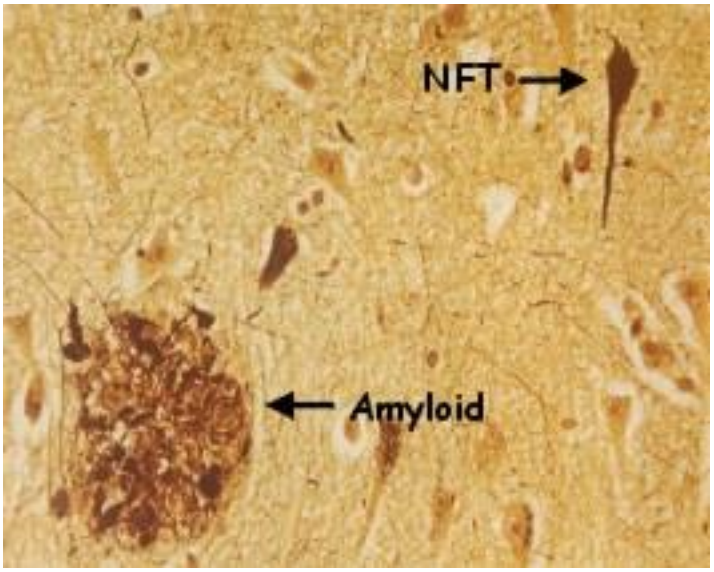

Figure 1.1. Pathology of AD, showing the senile plaques and the NFTs. AD has been characterized by these two pathological hallmarks, which are composed of Aβ and tau protein, respectively. http://petridishtalk.com/2011/05/

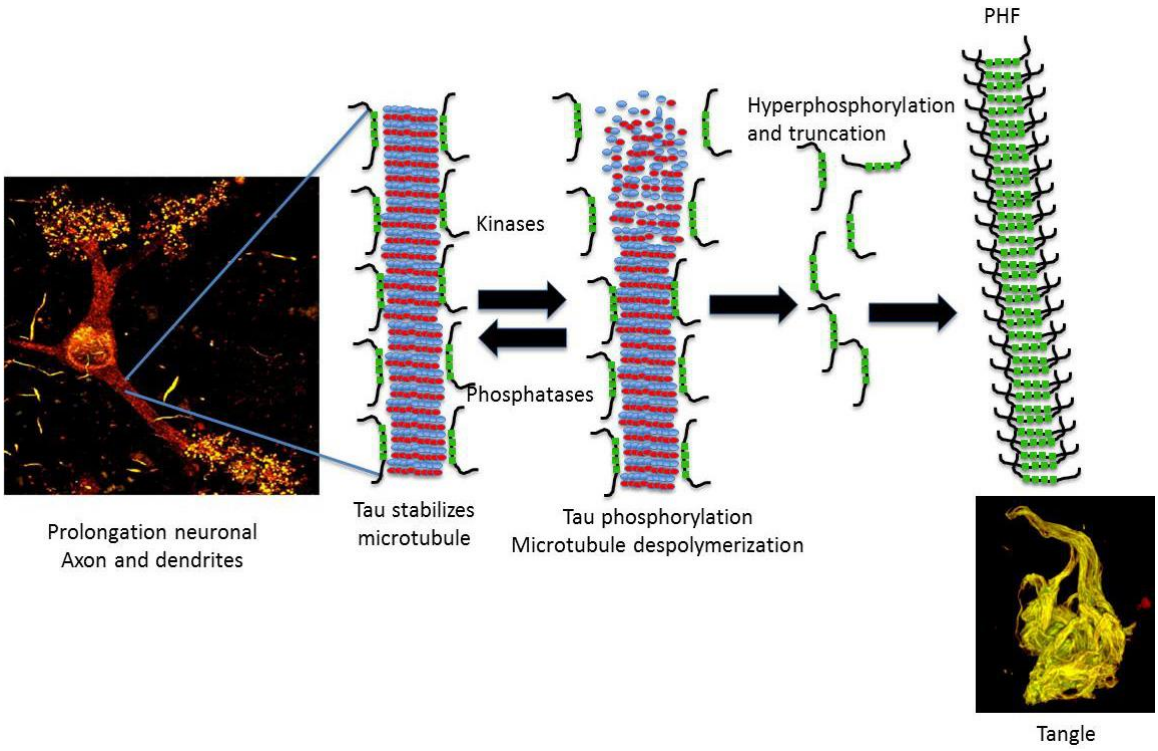

Figure 1.2. Formation of NFTs (Luna-Muñoz et al., 2013). The tau protein forms part of the microtubule, which helps transport nutrients and other important substances from one part of the nerve cell to another. However, in AD the tau protein becomes phosphorylated and causes the microtubules to destabilize. The hyperphosphorylated tau can then aggregate in the PHFs and cause NFTs within the neurons (Luna-Muñoz et al., 2013).

1.3.2 Senile Plaques

Senile or neuritic plaques consist of extracellular deposits of Aβ protein (Figure 1.1). In 1984, high performance liquid chromatography (HPLC) along with automated amino acid sequencing showed the presence of two nearly identical proteins which make up the vast majority of the senile plaques of AD patient's brains (Glenner and Wong, 1984). A few years later it was identified that those proteins were two different isoforms of the Aβ protein, Aβ(1-42) and Aβ(1-40), differing by the addition of two amino acids, isoleucine and alanine (Kang et al., 1987). The core of the senile plaques are composed of insoluble Aβ fibrils, while immunological research has shown the presence of other more diffused Aβ forms within and surrounding the plaque-like deposits (Tagliavini et al., 1988, Yamaguchi et al., 1988).

Early characterization of the Aβ plaques led to the assumption that the plaques mostly consisted of the Aβ(1-40) peptide (Mori et al., 1992); however, more current data supports the predominance of Aβ(1-42) (Roher et al., 1993). It is likely, however, that these two peptides probably both exist in the Aβ plaques. Different ratios of Aβ(1-42):Aβ(1-40) were found when investigating the Aβ plaques from different regions of the AD brain. Roher and colleagues observed that the plaques found within the leptomeningeal vessels had an average ratio of 58:42 Aβ(1-42):Aβ(1-40), while plaques found within the parenchymal vessels had an average ratio of 75:25 Aβ(1-42):Aβ(1-40) (Roher et al., 1993). These and many other studies have provided knowledge showing that the ratio of Aβ(1-42):Aβ(1-40) plays a more significant role in the load of Aβ plaques compared to the overall total amount of Aβ (Yin et al., 2007).

1.3.3 The Influence of Tau on Aβ

The building blocks of the insoluble plaques and tangles, soluble Aβ and tau, have been more recently shown as the main toxic components of AD and have also been shown to have a connection in their pathways that lead to the AD pathology (Bloom, 2014). Through the use of transgenic mice with a P301L mutation that causes the accumulation of tau tangles, along with the injection of Aβ into the brain of the mice, it was found that there is an increase in the accumulation of the tangles near the injection site (Gotz et al., 2001). These *in vivo* mouse studies showed that Aβ causes an increase in the tau pathology and functions upstream of the tau protein (Bloom, 2014). More *in vivo* transgenic mouse models have shown that the tau pathology is not a secondary effect of the Aβ pathology, but that Aβ initiates the cascade of events that leads to the tau-dependent synaptic dysfunction and neuronal death (Bloom, 2014, Roberson et al., 2007). In contrast, some data has shown evidence that the tau protein influences Aβ and challenges the notion that Aβ exclusively works upstream of tau (Leroy et al., 2012). Considering both possible pathways, leads to the possibility that Aβ could starts a pathological feedback loop with the tau protein (Figure 1.3) (Bloom, 2014).

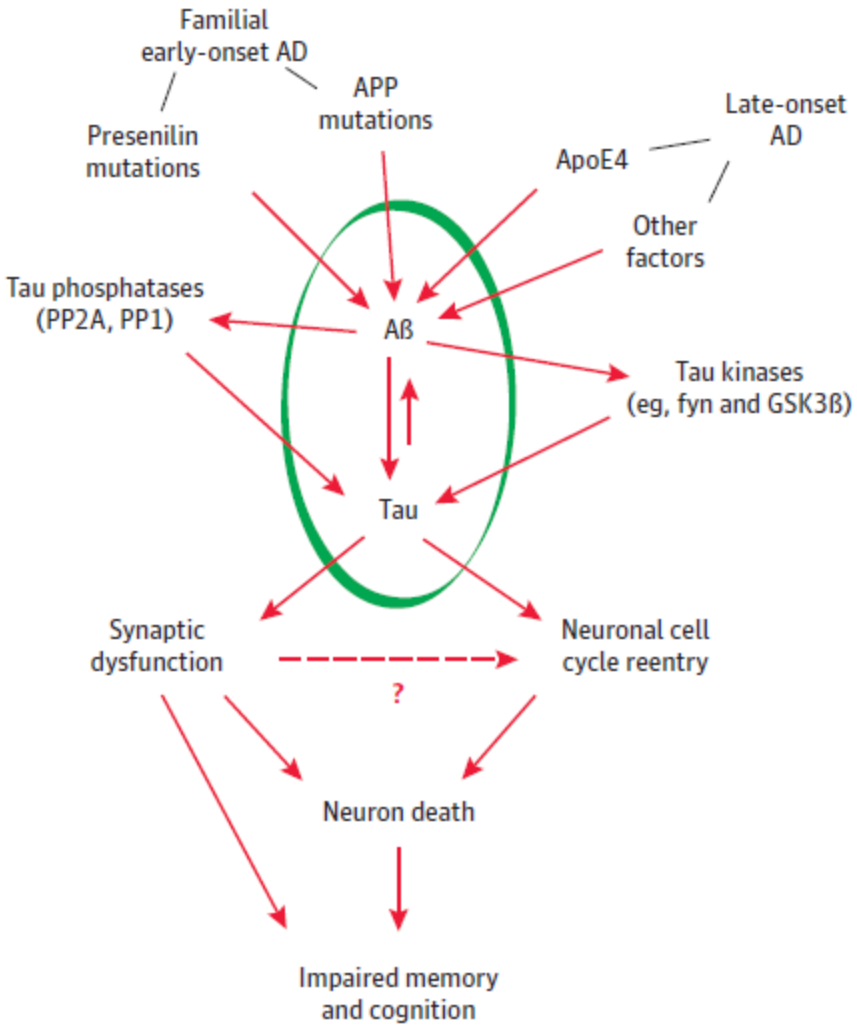

Figure 1.3. Possible feedback loop through Aβ and tau drives AD (Bloom, 2014). Aβ senile plaques accumulate in the brains of AD patients because off different genetic insults, while other genetic interactions and environmental risks also contribute. The toxic Aβ species are able to activate the formation of pathological tau through modulating protein kinases and phosphatases that regulate tau phosphorylation (Bloom, 2014).

1.4 Amyloid-β Metabolism

The Aβ peptide which makes up the senile plaques in AD patient's brain is formed through the proteolytic cleavage of a larger single transmembrane polypeptide, amyloid precursor protein (APP). This glycoprotein is 770 amino acids in length and its gene is localized on chromosome 21. The location of the APP gene led to the realization of the development of cerebral amyloid deposits within the brains of patients with Down's syndrome, due to trisomy 21 (three copies of chromosome 21). However, the plaques of Down's syndrome patients were observed to be unassociated with any neuritic dystrophy, gliosis, or NFTs (Selkoe, 1994).

APP is part of a conserved type 1 membrane protein, including APP-like protein (APLP) 1 and APLP2 (Coulson et al., 2000, Senechal et al., 2006). The function of APP remains unclear; however, it has been proposed that it plays a role in trafficking, neurotrophic signaling, cell adhesion and cell signaling (Dawkins and Small, 2014, Hoareau et al., 2008, Reinhard et al., 2005, Zheng and Koo, 2006). Through the use of Northern blot analysis and *in situ* hybridization, it was found that APP is widely expressed in the majority of all neural and non-neural mammalian tissues with the highest expression levels being located in the brain and kidney. Within the brain, it was observed that the neurons showed very high levels of expression (Selkoe, 1994). *In vivo* studies have shown that knocking out APP did not have any adverse phenotypes, but knocking out both APP and its homolog resulted in a lethal phenotype (von Koch et al., 1997). However, it was shown later that APP knock out (KO) mice actually had behavioral defects in locomotor activity and passive avoidance learning, defective long term

potentiation (LTP) and increased gliosis (Dawson et al., 1999, Phinney et al., 1999, Senechal et al., 2008).

After obtaining the full-length cDNA sequence of APP, it was known that the precursor polypeptide contains a single hydrophobic stretch near its carboxyl terminus and has properties of a membrane-spanning domain (Kang et al., 1987). The protein also contains a large cysteine-rich globular ectodomain (E1), a helix-rich acidic domain (E2) and part of the Aβ domain that begins 28 amino acids amino terminal to the single transmembrane domain and extends several residues into the transmembrane domain (Figure 1.5) (Dawkins and Small, 2014, Selkoe, 1994).

APP can also undergo a variety of proteolytic cleavages to eventually release secreted Aβ derivatives into the vesicle lumens and extracellular space. The first proteolytic cleavage is through α- or β-secretase (Figure 1.4). The specific secretase determines the pathway in which the APP will continue. If APP is first cleaved by α-secretase, it will then continue through the non-amyloidogenic pathway. The α-secretase cleaves the APP, within the Aβ domain, creating a soluble amino-terminal ectodomain (sAPPα) and a carboxyl-terminal domain within the cell membrane (Selkoe, 2001). When the α-secretase cleaves in the middle of the Aβ domain, it prevents the formation of intact Aβ (Sisodia et al., 1990). The carboxyl-terminal domain is then cleaved within the membrane by a second secretase, known as γ-secretase. γ-secretase is a multiprotein complex, which contains 4 different proteins including presenilin 1 (PS-1), an aspartyl protease which carries out the catalysis, nicastrin, APH-1 and presenilin 2 (PS-2). When the complex is formed, it becomes an active enzyme complex which catalyzes the cleavage within the transmembrane APP domain (De Strooper et al., 1998, Edbauer et al.,

2003). In the nonamyloidogenic pathway, the cleavage by γ-secretase leaves a short fragment, known as the P3 fragment and an APP intracellular domain (AICD). The second pathway in that APP can pursue is the amyloidogenic pathway. In this pathway, the APP is first cleaved by β-secretase, which only acts upon APP that has not already been cleaved by α-secretase (Selkoe, 2001). β-secretase is known as β-site APP-cleaving enzyme (BACE-1). BACE-1 is an aspartyl protease and its activity is present in most tissues (Haass, 2004). BACE-1 cleaves near the amino-terminus of the Aβ domain, at or near the cell surface (Haass, 2004, Seubert et al., 1993). This initial cleavage creates a slightly shorter amino-terminal ectodomain (sAPPβ) and a slightly longer carboxyl-terminal domain within the cell membrane. The carboxyl-terminal domain created by the cleavage of β-secretase can then be cleavage by γ-secretase. Cleavage by the γ-secretase in the amyloidogenic pathway creates the same AICD as in the nonamyloidogenic pathway but also creates the Aβ fragment that is 39-42 amino acids in length (Figure 1.4) (Nixon, 2007, Selkoe, 2001).

The Aβ fragments that are most abundantly produced by the cleavage of APP are Aβ(1-40) followed by Aβ(1-42). These peptides are found in low concentrations (nanomolar) in normal individuals' CSF. The Aβ peptides are also found in other biological fluids and cell culture medium during normal circumstances of APP processing. Even though these two isoforms have very similar primary structures, their biophysical properties are very different. Aβ(1-42) is widely known as the isoform that is highly fibrillogenic and more prone to aggregate compared to Aβ(1-40) (Pauwels et al., 2012). This leads to the belief that AD may be due to impairment in the balance between

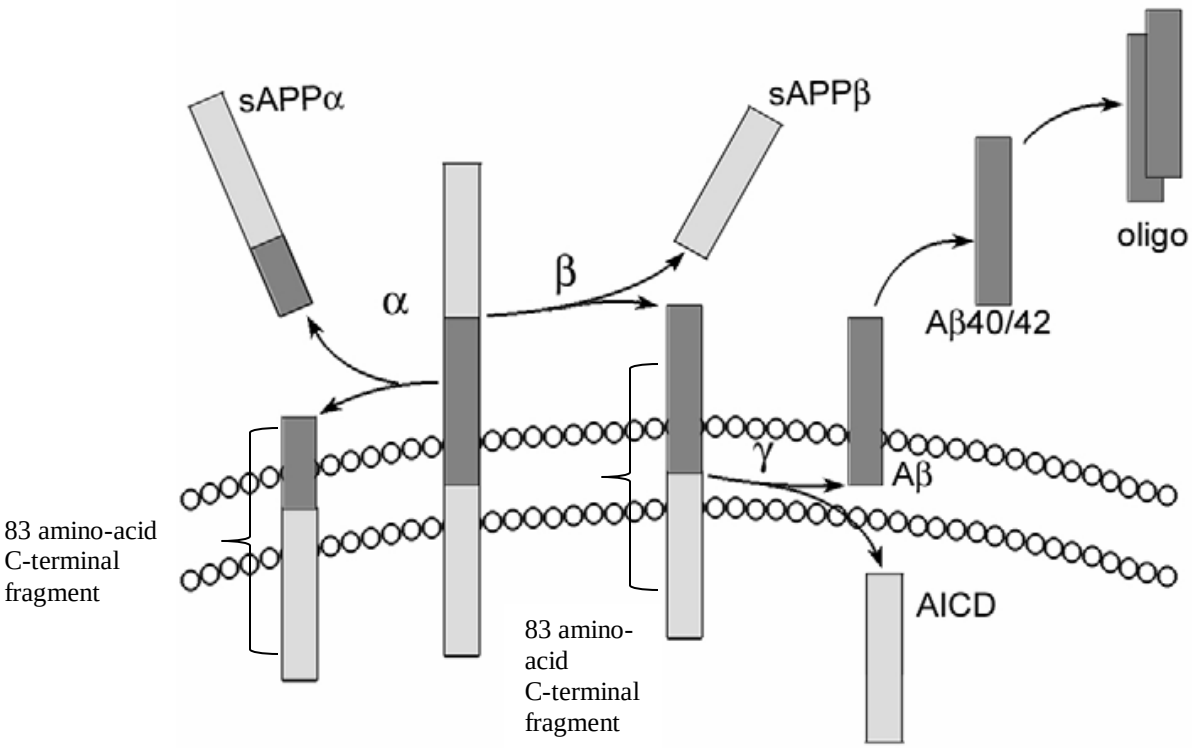

Figure 1.4. APP proteolytic processing and generation of Aβ fragments (modified from (Nixon, 2007)). The proteolytic cleavage of APP requires the activity of α-, β-(BACE-1), and γ-secretase. α-secretase cleaves the APP transmembrane protein creating a soluble APP fragment (sAPPα) and leaves an 83-amino acid C-terminal fragment within the membrane. BACE-1 cleavage also results in a soluble APP fragment (sAPPβ) and a membrane spanning C-terminal fragment, however the sAPPβ is slightly shorter than the sAPPα and this membrane spanning C-terminal fragment is 99 amino acids in length. The resulting C-terminal fragments can then be further processed by γ-secretase. γ-secretase processing after β-secretase cleavage creates an amyloidogenic peptide that is 39-42 amino acids long. This cleavage also generates an APP intracellular domain (AICD) (Nixon, 2007).

the production of Aβ and its ability to be cleared (Haass et al., 1994, Seubert et al., 1993, Shoji et al., 1992, Walsh et al., 2000), which raises the possibility that proteins involved in the amyloidogenic processing of APP could be a good choice for drug targets against AD.

1.5 Genes Associated with the Development of AD

The majority of AD cases are seen in patients over the age of 65 and known as late-onset AD (LOAD); however, familiar cases of AD have also been identified. The familiar or hereditary cases are seen at earlier stages of the patient's life and are primarily documented as early-onset AD (EOAD). There are four different known genes that cause all heritable AD cases: APP, PS1, PS2 and ApoE. Mutations of the initial three genes have been linked to rare, autosomal dominant forms of AD and are associated with less than 1% of all known AD cases (Daw et al., 2000, Selkoe and Podlisny, 2002, Thies and Bleiler, 2013). APP, PS1 and PS2, discussed earlier in Section 1.4, play a role in APP processing and the production of Aβ through the amyloidogenic pathway. Mutations in these genes have shown to generate the 42 amino acid Aβ peptide to a greater extent (Selkoe and Podlisny, 2002).

Mutations within the APP gene are heterozygote mutations, where the mutation is of only one allele. The mutations within the APP gene that cause AD occur at or near α-, β-, and γ-secretase cleavage sites (Selkoe and Podlisny, 2002) (Figure 1.5). These mutations result in an increase in overall Aβ peptide (Citron et al., 1992), an increase of Aβ(1-42) over Aβ(1-40) (Scheuner et al., 1996) and/or an increase in the aggregation propensity (Fraser et al., 1992, Selkoe and Podlisny, 2002). There are also known

mutations located near the middle of the Aβ sequence of APP clustered around the central hydrophobic region of the Aβ peptide (Selkoe and Podlisny, 2002). Five point mutations have been associated with hereditary diseases that are similar to or identical to AD. These mutations include: A21G Flemish mutation, E22K Italian mutation, E22G Arctic mutation, E22Q Dutch mutation and the D23N Iowa mutation (Figure 1.5). The intra-Aβ mutations impact the production, degradation and aggregation of the Aβ peptide; therefore, all the factors that regulate Aβ monomer levels (Betts et al., 2008, Hendriks et al., 1992, Levy et al., 1990).

Recently, a mutation within the APP gene has been discovered that actually protects against the development of AD and cognitive decline. This gene mutation (A673T) leads to a 40% reduction in the processing of the amyloidogenic pathway and formation of the causative Aβ peptide (Tiiman et al., 2013). The mutation is located next to the β-secretase cleavage site in the APP gene; therefore, it reduces the cleavage of APP by β-secretase and protects against the disease (Jonsson et al., 2012).

Around the same time that the APP gene mutations were being discovered, research was suggesting a link between the presence of EOAD and chromosome 14. Soon thereafter, another homologous gene on chromosome 1 was found to be the site of missense mutations in EOAD patients. The two genes were renamed PS1 and PS2 (Selkoe and Podlisny, 2002). PS1 and PS2 encode for homologous transmembrane proteins localized in the ER (Haass, 1997, Schon and Area-Gomez, 2010) and make up part of the enzyme complex of γ-secretase, as mentioned above. ELISA studies showed that AD patients from pedigrees with PS1/PS2-linked mutations have a significantly higher extracellular ratio of Aβ(1-42) to Aβ(1-40) compared to family members who are

A

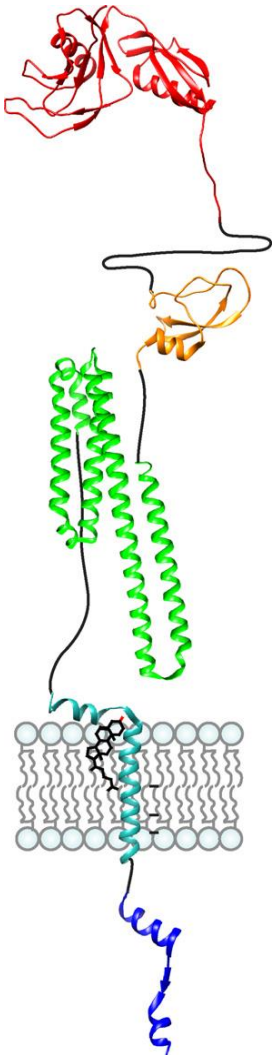

B

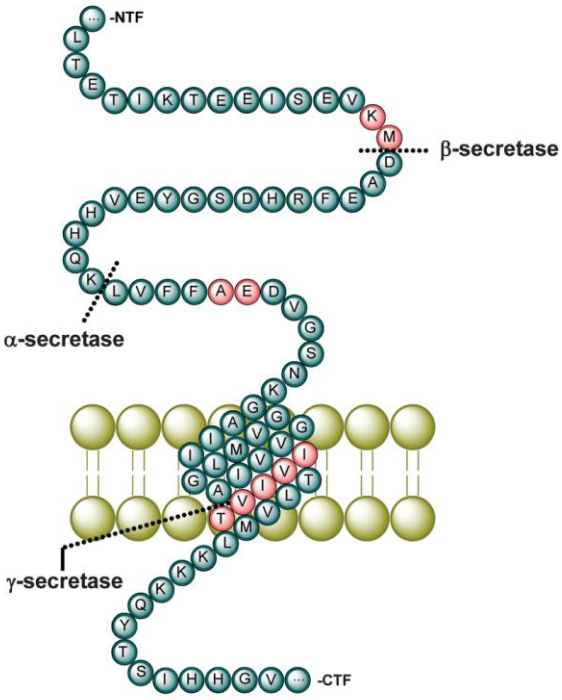

COMMON APP MUTATIONS		
Mutation	**Type**	**Effect**
K670N/M671L	Swedish	Increase in β-secretase processing
A692G	Flemish	Increased Aβ aggregation
E693Q	Dutch	Increased Aβ aggregation
T714I	Austrian	Increase in Aβ42 levels
V715M	French	Increase in Aβ42 levels
I716V	Florida	Increase in Aβ42 levels
V717L/V717F	Indiana/London	Increase in Aβ42 levels
L723P	Australian	Increase in Aβ42 levels

Figure 1.5. APP structure and mutations. (Panel A) Represents the hypothetical 3-dimensional structure of APP based on the protein data bank files of each individual domain (Dawkins and Small, 2014). (Panel B) This figure points out the α-, β-, and γ-secretase cleavage sites and the transmembrane domain of APP. The known sites (amino acids) for missense mutations are indicated in the table, along with the given name of that particular mutation and effect to the levels of Aβ (Ghosh and Osswald, 2014).

unaffected by AD (Scheuner et al., 1996). Similar results were found when observing transfected cells and transgenic mouse models that co-expressed human PS and APP genes. Cells transfected with PS1 or PS2 mutants showed an increase in the Aβ(1-42) secretion, while PS1 transgenic mice showed overproduction of Aβ(1-42) within the brain. In this study, different PS mutations were observed and all showed differential effects on the production of Aβ. However, they all showed a dominant gain in function by increasing the production of Aβ(1-42) and therefore increasing the amount of cerebral β-amyloidosis (Citron et al., 1997). A double missense mutation (K595N/M596L) has also been observed in a Swedish AD family. In transfected cell lines and primary skin fibroblast, this double missense mutation initiated an increase of the overall amount of Aβ released into the conditioned media and an increase of BACE-1 activity (Citron et al., 1995). Missense mutations in PS1 cause the earliest and most-aggressive forms of AD. These patients are known to have the onset of symptoms in the fifth decade of life and most likely to face death in the sixth decade. PS2 mutations, on the other hand, usually start showing symptoms slightly later in life (Selkoe and Podlisny, 2002).

The fourth gene associated with sporadic and familiar AD is apolipoprotein E (ApoE). ApoE is important in the regulation of plasma lipoprotein metabolism and is found in the liver and central nervous system (CNS) (Holtzman et al., 2000). This protein is located on chromosome 19 and has three common known alleles in humans: ε2, ε3 and ε4 (Corder et al., 1993, Holtzman et al., 2000, LaDu et al., 1994). In AD, the ε4 allele has shown to be a genetic risk factor, while ε2 allele has shown to be protective (Cleary et al., 2005, Corder et al., 1993, Holtzman et al., 2000). Data has revealed that ApoE-ε4 is an important factor in the etiology of over half of all AD patients. It is

estimated that between 40% and 65% of people with AD have one or two copies of the ApoE-ε4 gene (Thies and Bleiler, 2013). ApoE has been discovered to accumulate extracellularly in the senile plaques and intracellularly in the NFTs (LaDu et al., 1994), which may suggest that ApoE may be involved in the formation of these lesions (Strittmatter et al., 1993). There have been many different mechanisms which have explained the ApoE isoform dependency on the predisposition to AD, including variation in total Aβ concentrations, the formation and clearance of plaques, formation of tau tangles, and the impairment of neuronal signaling pathways (Beffert and Poirier, 1996, Buttini et al., 2002, Herz and Beffert, 2000, Holtzman et al., 2000, LaDu et al., 1994). The clearance of Aβ has shown dependency on the ApoE isoforms with the amount of clearance being in the order of 4<3<2 (Ulrich et al., 2013). Many mechanisms have been proposed how each ApoE isoform contributes to the pathogenesis of AD, but the exact mechanism still remains unknown. However, many *in vitro* and *in vivo* genetic studies have shown importance in implicating AD and provide a basis for potential therapeutic approaches.

1.6 Mechanisms of Aβ Aggregation

Aβ is formed by the proteolytic cleavage of APP by β- and γ-secretase (Nixon, 2007, Selkoe, 2001). The Aβ peptide was able to be isolated, purified, and characterized from the post mortem brain of AD patients in 1985. Using techniques like liquid chromatography and Western blot, it was discovered that the Aβ peptide monomers are 4-5 kDa in size (Masters et al., 1985). Under normal physiological conditions the monomeric Aβ peptide is highly soluble, but by a mechanism that is not fully understood

the Aβ starts to aggregate and form amyloid deposits within the brain (Jarrett et al., 1993).

The main focus of research on the Aβ peptide has been on its ability to aggregate and form fibrils as well as its role in neurodegeneration. Many research groups have shown that synthetic Aβ peptides are able to form fibrils *in vitro* that are indistinguishable from the fibrils that have been isolated from AD brains (Halverson et al., 1990, Hilbich et al., 1991, Kirschner et al., 1987). These realizations led to further investigations on understanding the structural and functional properties of fibril assembly, such as aggregation mechanism, kinetics, and intermediates. During the past decade, studies have used X-ray fibril diffraction (XRD) (Madine et al., 2008), solid state nuclear magnetic resonance (SSNMR) (Lynn and Meredith, 2000, Middleton, 2011), spectroscopic methods (Fernandez-Busquets et al., 2008) and molecular dynamics to explore the conformation and aggregation of Aβ peptides. The C-terminus of Aβ contains 14 consecutive hydrophobic residues, along with the prevalence of residues valine and isoleucine, which are β-branched residues, and glycine every fourth residue. The β-branched residues are satirically constrained and allow for extension of conformation, therefore likely populating the β-sheet structure of the Aβ fibrils (Jarrett and Lansbury, 1992). Due to the conformational flexibility of the glycine residue, the Aβ peptide may be able to obtain confirmations that are not normally populated by crystalline proteins (Chou et al., 1982, Jarrett and Lansbury, 1992).

Aβ aggregation studies have provided knowledge on the process in which the monomer noncovalently self-assembles into higher-ordered Aβ morphologies. However, these studies have been limited by the capability or sensitivity of certain techniques.

Early methods included turbidity or retention of the insoluble filtrate to observe fibril formation, but these were limited to only observing the final insoluble stages of aggregation (Bush et al., 1994, Jarrett et al., 1993). Thioflavin T (ThT) fluorescence and atomic force microscopy (AFM) or electron microscopy (EM) can also be used to observe Aβ aggregate but they have limitations too. ThT is dependent on the concentration, size and extent of fibrillar structure; as the fluorescent compound does not bind to oligomeric Aβ as well as fibrillar Aβ (Lee et al., 2011). Microscopic techniques have been shown to be less effective at imaging lower-ordered Aβ species. AD research has recently been focused on understanding the soluble oligomeric and protofibrillar Aβ species and the use of conformation-specific antibodies to detect specific aggregated species not only in solution, but also in human tissue and CSF. Conformation-specific antibodies has been one strategy that has shown significant sensitivity (Coalier et al., 2013, Gong et al., 2003, Kayed et al., 2003, Lee et al., 2006).

Similar to crystallization, amyloid formation follows a nucleation-dependent kinetic mechanism which results in ordered protein polymerization. This mechanism is kinetically controlled by the nucleation and elongation rates of the Aβ peptide (Jarrett and Lansbury, 1992). The first step in the nucleation-dependent polymerization is the formation of a nucleus, seed, or paranuclei, which are the initial and minimal structure for Aβ assembly (Figure 1.6). The nucleus formation is a slower phase and represents the lag phase before the addition of monomers to the previously formed nucleus resulting in a linear growth phase and formation of protofibrils and eventually fibrils. The equilibrium between the monomer and the paranucleus is very rapid, which was proven by its presence immediately after the peptide was resuspended. The paranuclei can also

oligomerize by themselves to form larger beaded oligomers. The extent of the lag phase is dependent upon the concentration of the Aβ monomer. The conversion to protofibrils is slower due to the fact that the monomers, paranuclei and large oligomers are predominately unstructured and have to undergo substantial conformation rearrangement to predominately β-sheet/β-turn structures. The final stage is the maturation of the protofibrils to fibrils, where the fibrils will reach a plateau and the monomer is at equilibrium with the fibrils (Figure 1.6) (Bitan et al., 2003, Burdick et al., 1992, Jarrett and Lansbury, 1992). Circular dichroism (CD) analysis has provided evidence in which the soluble morphologies transition structurally from predominately random coil, as monomer, to increasing amounts of β-sheet structure and continue to eventually produce insoluble fibrils (Harper et al., 1999, Walsh et al., 1999).

Burdick and colleagues showed that the length of the hydrophobic carboxyl terminus is an important parameter for assembly of the Aβ peptide into amyloid structures, but so are pH, peptide concentration and time of incubation. pH has been shown to affect both the rate and the extent of Aβ assembly. The sequence of Aβ has an equal number of acidic residues (aspartic acid and glutamic acid) and basic residues (lysine, arginine, and histidine) and a predicted isoelectric point of approximately 5.18 – 5.31 (Burdick et al., 1992, Hortschansky et al., 2005). The pH range of insolubility can be explained by the precipitation of the peptide when the net charge is close to zero (Burdick et al., 1992).

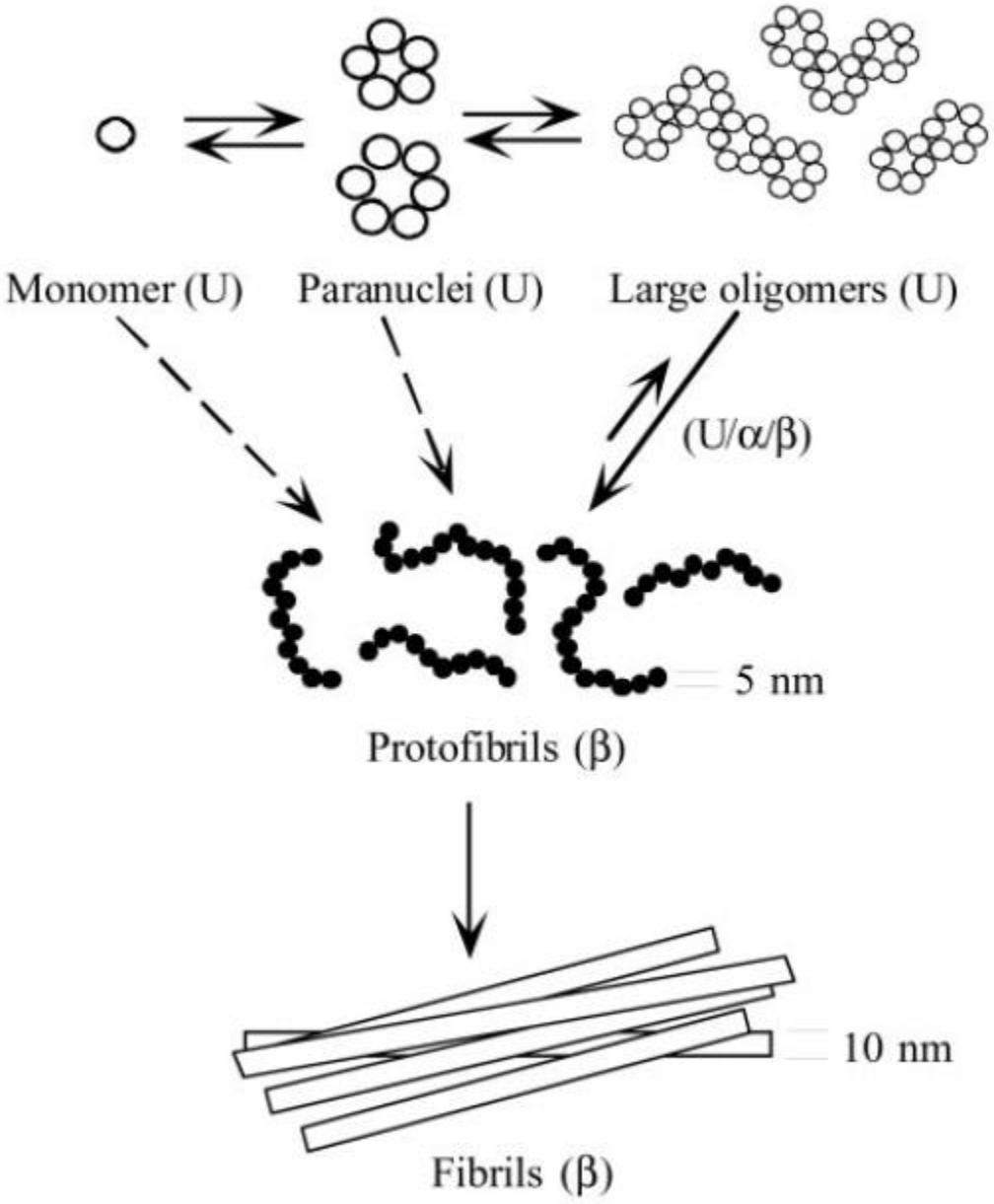

Figure 1.6. Aβ assembly model (Bitan et al., 2003). The monomer rapidly forms into a paranuclei, which oligomerizes into a larger beaded structure. The equilibrium between monomer and the paranuclei is very rapid whereas the formation to protofibrils is slower but also reversible. There are many different pathways in which the protofibrils may form and this "linear" pathway many not be the only one. However the final step in the overall pathway is the maturation of the protofibril into fibrils.

1.7 Aβ Aggregation Kinetics

As mentioned above, the Aβ protein undergoes nucleation-dependent polymerization. This process is characterized by a slow nucleation phase, a growth phase, and a steady state phase. The nucleation, or lag phase, occurs when the protein undergoes multiple unfavorable association steps to form an ordered oligomeric nucleus (Harper and Lansbury, 1997, Nilsson, 2004). This rate-determining, or slowest, step may be the one of the keys to understanding AD because it may be responsible for protecting the normal individuals from amyloid formation. The growth phase occurs when the nucleus quickly grows to form larger polymers. The steady state phase occurs when the fibrils and monomers reach equilibrium. During this process, polymers are unable to form until the monomer concentration is above its critical concentration (Harper and Lansbury, 1997). Identifying the key steps and knowing the numerical values of nucleation and elongation rates in the formation of fibrils may aid in revealing promising therapeutic targets for inhibition.

Studies have shown that fibrillogenesis pathways may differ depending on whether or not the protein concentration (C) is above or below its critical concentration (c*) (Lomakin et al., 1997), which is determined by measuring the concentration in which the rate of fibril formation and dissolution are equal (Harper and Lansbury, 1997). When $C > c^*$, the initial rate of elongation is independent from the concentration, also when the concentration is much greater then c*, the fibril size is also independent of total protein concentration. However, when $C < c^*$, the elongation rate is proportional to the concentration and the fibril size surpasses the size of the fibrils when $C > c^*$ (Lomakin et al., 1997).

The critical concentration should be equal to the remaining Aβ concentration after reaching equilibrium and formation of amyloid fibrils. When comparing the critical concentration of Aβ(1-40) and Aβ(1-42), it was found that Aβ(1-42) has a critical concentration which is five-times lower than that of Aβ(1-40) (Harper and Lansbury, 1997). However, these concentrations are higher than the concentrations observed *in vivo*. *In vivo* concentrations are in the nanomolar range. Therefore, it is thought that *in vivo* there is local supersaturation which allows the nucleation and polymerization to occur in cellular compartments (Harper and Lansbury, 1997, Jarrett and Lansbury, 1992, Lomakin et al., 1997).

1.8 Amyloid Cascade Hypothesis

1.8.1 Original Hypothesis

The amyloid cascade hypothesis was first declared by Hardy and Higgins in 1992. The purpose of the hypothesis was to provide a possible sequence of events that would lead to the development of AD. Their hypothesis stated that the deposition of the Aβ protein is the cause of Alzheimer's pathology. They claimed that the Aβ protein deposition directly results in the presence of NFTs, cellular loss, vascular damage, and dementia (Giacobini and Gold, 2013, Hardy and Higgins, 1992, Selkoe, 2000, Tamaoka, 2013). In this hypothesis, there are two sequential events which must happen to produce AD pathology. First, the Aβ has to be generated and then the peptide must enable or cause neuronal death and formation of NFTs (Hardy and Higgins, 1992). This causative hypothesis has also been implicated in other neurodegenerative diseases, such as

Parkinson's disease (Tiiman et al., 2013). Numerous studies have provided confirmation as to why this hypothesis may be true. The most prevalent evidence is genetics (Tiiman et al., 2013). Another indication is the presence of AD in Down syndrome patients caused by trisomy of chromosome 21, which contains the APP gene. This shows that deposition of Aβ is probably an early event in the disease (Mann et al., 1989). *In vitro* studies suggested that the Aβ peptide is neurotoxic by itself, while others have shown that Aβ provoked neurotoxicity by causing the neurons to be more sensitive to excitotoxic damage (Kowall et al., 1991, Pike et al., 1991, Roher et al., 1988, Yankner et al., 1989). One possible mechanism for Aβ to promote neuronal loss is through the known disruption of calcium homeostasis and increased intraneuronal calcium concentration. Therefore, it is possible that the Aβ peptide may induce NFTs through its ability to increase the concentration of intracellular calcium (Lee et al., 1991).

Mutations within the APP gene only account for a small portion of AD cases; therefore indicating that most AD cases are sporadic, which suggests other causes of the disease. According to the amyloid cascade hypothesis, these other causes will most likely act by prompting the deposition of the Aβ peptide; one example may be the relationship between accidental head trauma and the presence of AD where the amyloid deposits due to the response to neuronal injury (Mortimer et al., 1991). These studies show that the Aβ peptide is the most likely candidate for the initiation of the cascade of events leading to AD; however, the entire process takes a long time for the development of the full disease. Future studies in transgenic mice and further discoveries of additional mutation in APP and other genes associated with AD will aid in refining the amyloid

cascade hypothesis and eventually help in finding new therapeutic targets for intervention (Hardy and Higgins, 1992).

1.8.2 Evidence Contrary to the Amyloid Cascade Hypothesis

There is a general consensus that the Aβ peptide is pivotal in the pathology of AD, but there are still some questions left unanswered, such as what causes the Aβ deposition into plaques, which Aβ morphology is most toxic and what are the connections between the events that occur in the brain (Tiiman et al., 2013). While trying to answer some of these questions, some recent findings revealed evidence that conflicts with the original amyloid cascade hypothesis and lead to the identification of other possible hypothesis. Some hypotheses trying to explain the cause of AD are the neuronal cytoskeletal degeneration hypothesis, oligomeric hypothesis, cholinergic hypothesis, inflammation hypothesis, oxidative damage hypothesis, mitochondrial dysfunction hypothesis, and metal hypothesis (Tiiman et al., 2013).

The most evident conflict is the postmortem analysis of non-demented (ND) elderly control patients, AD patients, and high pathology control (HPC) patients showed that there was no correlation between the amount of amyloid plaques and the cognitive decline of the patient. The HPC patients were chosen by meeting certain pathological criteria, but no synaptic loss or symptoms of dementia (Lue et al., 1999, Naslund et al., 2000). The data showed that plaque type was insignificantly different when comparing the HPC and AD patients (Lue et al., 1999). Recent clinical reports have also shown a significant number of human subjects who were cognitively normal, but still have the presence of amyloid plaques within their brains (Morris et al., 2009, Rentz et al., 2010).

Impairment and inhibition of LTP was also observed prior to or even independently of complete plaque formation (Moechars et al., 1999, Mucke et al., 2000).

AD patients and mouse models of the disease have shown that the greatest amount of synaptic loss is found near senile plaques (Koffie et al., 2009), providing evidence supporting the original amyloid cascade hypothesis. However, many studies are reporting that the early Aβ intermediates, such as oligomers and protofibrils, are the most toxic species (McLean et al., 1999, Paranjape et al., 2012, Wang et al., 1999), supporting the oligomeric hypothesis (Tiiman et al., 2013). These soluble species are hypothesized to associate with postsynaptic density around the surface of the plaques, therefore causing a loss of synapses and spines surrounding the plaques (Koffie et al., 2009). The toxicity and synaptic loss caused by the intermediate species contradict the original amyloid cascade hypothesis due to the presence of neuronal damage well before the formation of the Aβ senile plaques.

1.8.3 Modified Amyloid Hypothesis

As mentioned above, extensive work has recently been aimed at understanding the pathways leading to AD and a lot of that effort has been recently focused on the intermediate species. Co-localization imaging techniques have shown the presence of Aβ oligomers and neuronal loss surrounding the senile plaques (Koffie et al., 2009). It has also been found that neuronal death can be mediated by the tau protein (Roberson et al., 2007). Due to all of the reports, either for or against, the original amyloid cascade hypothesis indicates that AD is a very complex process and even though Aβ deposition

may be one of the main triggers of AD, there could be a combination of factors that all contribute to the final pathology (Figure 1.7).

In 2011, Hyman suggested that the amyloid hypothesis needed to be reformulated. Hyman proposed a two-stage process beginning with the initiation of a cascade by the Aβ but followed by pathophysiological consequences that are independent of the initial Aβ. If Hyman's hypothesis is relevant, it would explain the number of individuals who have accumulated amyloid plaques, but do not show signs of dementia. A cross-sectional autopsy study showed that the amount of amyloid deposition in the brain was similar across a variety of clinical severity levels and the number of plaques that accumulate seem to reach a plateau while neuronal loss, synaptic loss, and number of tangles increase along with the disease. The first stage of this hypothesis is the local disruption of the neutrophils, loss of dendritic spines, remodeling of neurites, and an inflammatory response initiated by the Aβ peptide. The second stage is the continuing development of the disease, including the presence of tangles, neuronal loss, synaptic loss, glial responses in limbic and association cortices and eventually organ failure. AD may be adding to the numerous other medical conditions in which the cause of the accumulating illness, such as symptoms and life expectancy, can be separated from the initial insult. One example is how the amyloid deposition causes an increase in calcium dyshomeostasis, oxidative stress, and mitochondrial dysfunction, which together can activate other signaling pathways in the immune and nervous systems. This both explains the failure of drugs designed to target Aβ taken after cognitive impairment has already developed and gives insight to new therapeutic targets which need to be based on the specific stage of progression (Hyman, 2011).

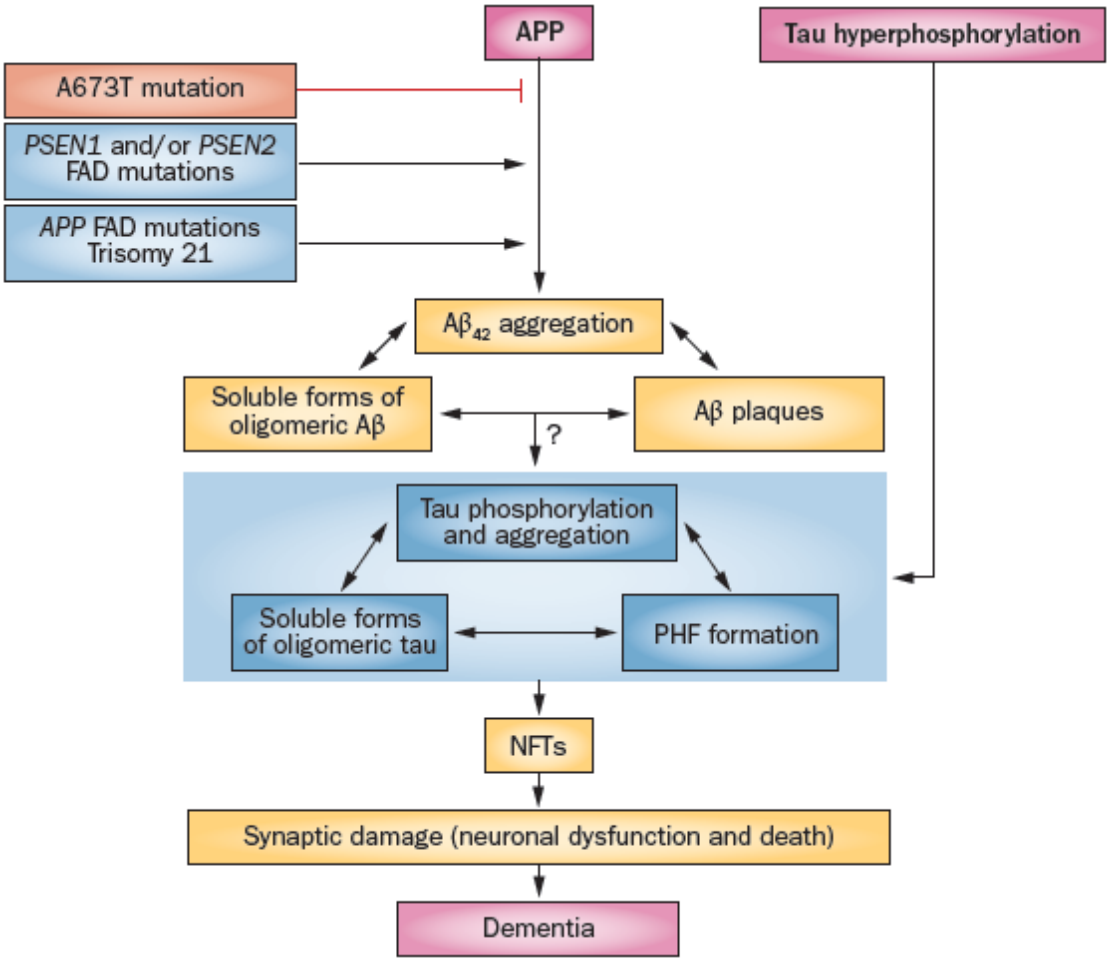

Figure 1.7. Modified amyloid cascade hypothesis (Giacobini and Gold, 2013). The pathway provided in this figure indicates the roles of both Aβ and tau oligomeric aggregates as soluble neurotoxic species that possibly lead to the formation of amyloid plaques and NFTs, respectively. This also includes one of the remaining questions of whether or not Aβ plays a role in triggering tau toxicity resulting in the formation of PHFs and neuronal loss. Lastly this figure recognizes the fact that tau pathology may be able to proceed independently of Aβ, by the direct hyperphosphorylation (Giacobini and Gold, 2013)

1.9 Aβ Morphologies

1.9.1 Aβ Fibrils

The Aβ peptide is able to form many different species through non-covalent interactions, which gives rise to β-sheet secondary structure (Walsh et al., 1999). XRD analysis of filamentous protein of amyloid deposited tissue showed the presence of a cross-β pattern. The interpretation by Eanes and Glenner in 1968 was that the amyloid polypeptide formed a pleated sheet and folded upon itself, so that adjacent peptide segments were laterally arranged in an antiparallel manner. It was also observed that the axes of the peptide ran transversely to the axis of the filament (Eanes and Glenner, 1968). Since then, several other techniques, such as electron diffraction, cryogenic EM, proteolysis, chemical cross-linking, and mutagenesis have supported the presence of the cross-β structure of the amyloid fibrils (Serpell et al., 2000, Sunde and Blake, 1997).

The amyloid fibrils are rigid, unbranched, resistant to denaturation and birefringent when stained with Congo Red (Lansbury et al., 1995). The insoluble and non-crystalline nature of the fibrils makes them unsuitable for high resolution techniques, such as solution-phase nuclear magnetic resonance (NMR) and x-ray crystallography (Benzinger et al., 1998). Therefore, selective incorporation of ^{13}C into the polypeptide backbone allowed for the use of Fourier-transform infrared spectroscopy (FTIR) and SSNMR to further observe the fibrillar structural details. Early structural analysis of a nine-residue peptide, Aβ(34-42), by SSNMR predicted antiparallel β-sheet structure with alternating hydrogen bond registries (Lansbury et al., 1995). SSNMR analysis of a longer Aβ peptide, Aβ(10-35), showed the presence of parallel β-sheet structure

(Benzinger et al., 1998) in accordance with multiple quantum (MQ) NMR and SSNMR of Aβ(1-40) and Aβ(1-42) (Antzutkin et al., 2002, Antzutkin et al., 2000, Balbach et al., 2002). Other techniques such as EM, scanning transmission electron microscopy (STEM), XRD, electron paramagnetic resonance (EPR) and Hydrogen/deuterium exchange mass spectrometry (HDX-MS) further supported the observation of parallel β-sheet structure of the longer to full length Aβ peptides, while shorter fragments of the Aβ peptide including Aβ(16-22), (34-42), and (11-25) continued to adopt the antiparallel β-sheet structure (Balbach et al., 2000, Petkova and Tycko, 2004).

One of the most widely known structural models of Aβ was composed from SSNMR data of Aβ(1-40) fibrils, which incorporated the intermolecular distances and the cross-β motif that is common to all amyloid fibrils. There are several significant features of this model. The model omits residues 1-8 because the N-terminus of the peptide has been found to be unstructured. The structure has a 180° bend formed by residue 25-29 which separates two β-strands. The residues that make up the core of the fibril structure are neutral and primarily hydrophobic with the exception of D23 (aspartic acid) and K28 (lysine), which form a salt bridge across the bend of the fibril. There are also a few charged and polar side chains which are distributed on the outer surface of the fibril (Figure 1.8) (Petkova et al., 2002).

Further evaluation of the Aβ fibrils has shown that they commonly exhibit multiple distinct morphologies. This polymorphism could result from individual modes of lateral association of protofilaments without significant changes is the molecular structure or from variations in the molecular structure at the protofilament stage. Most of the data defends the possibility that the variation is from the molecular structure of the

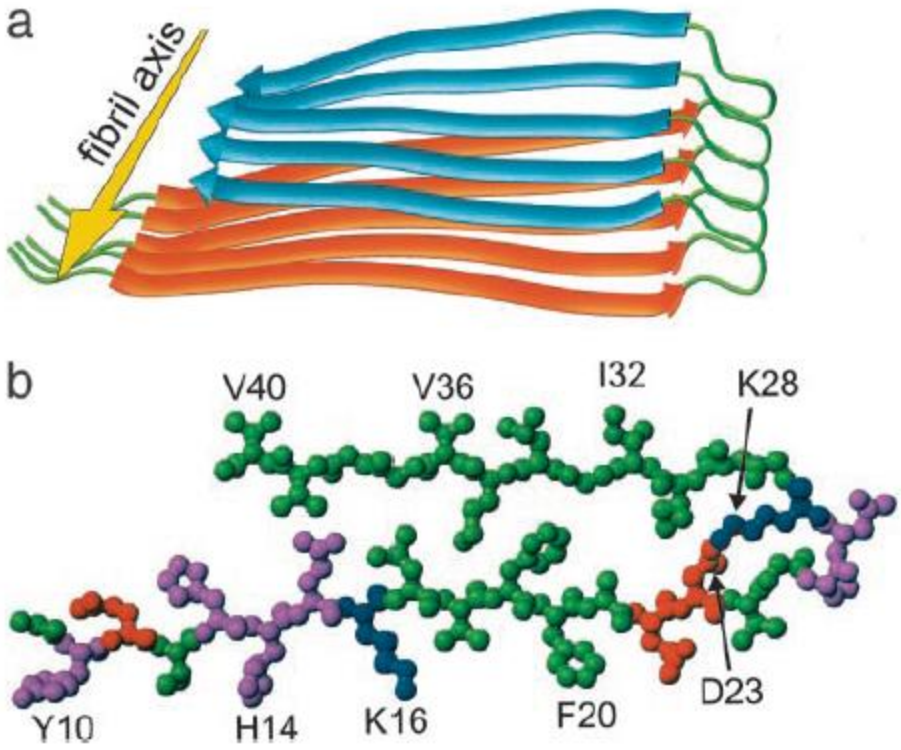

Figure 1.8 Structural model for Aβ(1-40) fibrils (Petkova et al., 2002). Panel A. a schematic of a single molecular layer, or cross-β unit. The yellow arrow shows the direction of the long axis of the fibril, which matches the direction of the intermolecular backbone hydrogen bonds. The cross-β unit is a double-layered structure with in-register parallel β-sheets, represented here by the orange and blue ribbons, residues 12-24 and 30-40, respectively. Panel B. Aβ(1-40) residues 10-40. The colors are coded on the basis of their side chains as hydrophobic (green), polar (magenta), positive (blue) and negative (red).

protofilaments due to their morphology and molecular structures being sensitive to environmental elements during fibril growth, such as pH, temperature, buffer composition, and concentration. (Petkova et al., 2005, Shivaprasad and Wetzel, 2006, Stine et al., 2003, Tycko, 2011).

1.9.2 Aβ Protofibrils

An attempt to structurally and kinetically characterize the beginning stages of Aβ fibrillation discovered additional Aβ intermediates. These intermediates were termed protofibrils. With the use of AFM, the Aβ(1-40) protofibrils were measured at a diameter of 3.1 nm, while the Aβ(1-42) protofibrils were measured at 4.2 nm in diameter (Harper et al., 1997). By TEM, the protofibrils were found to be predominately small, soluble curvilinear structures that were 4-10 nm in diameter (Walsh et al., 1997) and less than 200 nm in length (Harper et al., 1997, Walsh et al., 1997). When observing the kinetics of the protofibril formation and disappearance, it was confirmed that they were intermediates in the pathway to amyloid fibrils (Walsh et al., 1997).

Further observations of the protofibrils concluded that protofibrils irreversibly mature into fibrils. In these studies, the protofibrils were examined by ThT fluorescence and CD. The ThT dye is dependent on β-sheet structure and showed that the protofibrils had significant β-sheet structure (Paranjape et al., 2013, Walsh et al., 1999), while the CD data showed that both the protofibrils and fibrils had extensive and equivalent amounts of β-sheet structure with less random coil and the least amount of α-helix. During the process to fibrils, there is a transitory α-helical component, where the Aβ transitioned from predominately random coil to an increase in α-helix and finally to a predominately

β-sheet structure. The hydrophobic core is an important portion of the Aβ peptide during the formation of protofibrils. This was evident by the substitution of residues within the hydrophobic core with glycine or proline, two residues known to destabilize β-sheet structure. These substitutions caused the peptide to no longer form protofibrils (Hartley et al., 1999, Kheterpal et al., 2003). The core hydrophobic residues were also shown to be protected after the peptides formed the protofibril structure. HDX-MS revealed that 40% of the amide protons within the hydrophobic core were protected and the amount of protection increased as the peptide transitioned from monomer, to protofibril and eventually to fibril (Kheterpal et al., 2003).

The transition from protofibrils to fibrils was thought to involve some structural organization. One observed structure was the "beaded" substructure due to the periodicity of the protofibrils (Walsh et al., 1999). The periodicity was first observed by Harper and colleagues in 1997 by AFM. Harper observed periodicity of both Aβ(1-40) and Aβ(1-42) to be about 22 nm (Harper et al., 1997). A couple years later, Walsh used rotatory shadowing and TEM of the protofibrils and observed a beaded pattern of 3-6 nm (Walsh et al., 1999).

The hydrodynamic radius (R_H) of the Aβ(1-40) protofibrils were initially 27.8 ± 1.8 nm and over time grew to 80.6 ± 14.4 nm (Walsh et al., 1999), while the Aβ(1-42) protofibril were determined to have a R_H of 21.9 ± 4.0 nm (Paranjape et al., 2013). Size exclusion chromatography (SEC) has been used for many years to separate the protofibrils from the lower molecular weight or monomeric Aβ. The separation on a Superdex 75 column elutes the protofibrils in the void volume, while the monomers elute later in the included volume. The protofibrils have consistently been formed at a

physiological pH and in a solution with considerable ionic strength (Paranjape et al., 2013, Walsh et al., 1999). Ionic strength is important in the length of the protofibrils along with the rate at which the protofibrils elongate (Harper et al., 1999). In agreement with the many studies showing that Aβ(1-42) aggregates more rapidly than Aβ(1-40), it was observed by SEC that the Aβ(1-42) protofibrils were able to form very rapidly, while the Aβ(1-40) require an incubation time of 24 hours. The SEC protofibril peak showed an increase in time, while the monomer peak decreased simultaneously; however, both peaks eventually decreased indicating the formation of fibrils and confirming that the protofibrils are intermediates of fibrillogenesis (Paranjape et al., 2012).

Protofibril elongation has been found to be first-order in [Aβ]. This measured first order relationship is from the elongation of monomeric Aβ adding to the growing protofibril ends (Harper et al., 1999) without an increase in the protofibril diameter (Nichols et al., 2002). The elongation process of the protofibrils may be more complex with the possibility that protofibrils may elongate by the coalescence of existing protofibrils (Harper et al., 1999). It has also been seen that the protofibrils association can occur through lateral association which results in a disordered fibril structure (Nichols et al., 2002).

1.9.3 Aβ Oligomers

The soluble Aβ oligomers are another intermediate formed by the Aβ peptide and have been isolated from the brain, plasma, CSF, transfected cells, and cells derived from human brain (Stine et al., 2003). AFM of Aβ(1-42) oligomers showed the appearance of small punctate globular structures with a diameter of 2-5 nm (Dahlgren et al., 2002,

Kayed et al., 2003, Stine et al., 2003). The molecular mass of the oligomers were also observed to range from 10-100 kDa (Roher et al., 2000). Oligomers are a representation of a protein micelle (Kayed et al., 2003) of as few as two molecules or as many as tens of molecules (Pham et al., 2013). These structures include Aβ dimers, trimers, tetramers, hexamers, and dodecamers, and even some larger oligomers with spherical or annular morphologies; however, determining the structure of full-length Aβ oligomers at atomic resolution has been agonizing (Pham et al., 2013). The Aβ oligomers form this structure due to its amphipathic surface. The formation of the oligomer is dependent on a critical concentration and correlates with the hydrophobicity of the environment (Kayed et al., 2003). The assembly of the oligomers seems to form under conditions that block fibril formation (Lambert et al., 1998).

The mechanism the oligomers go through to cause neurodegeneration in AD is still not fully understood, but a few of the plausible mechanisms consist of binding to cell-surface receptors, the generation of pores or channels in the cell membrane, or perturbing the membrane structure (Pham et al., 2013). Data has shown that the oligomers are able to kill hippocampal neurons at concentrations as low as the nanomolar range (Lambert et al., 1998). There is also previous data supporting the existence of synaptic toxicity caused by oligomers. Oligomers have been found, by multiphoton *in vivo* imaging with oligomer-specific antibodies, surrounding the dense plaques in the brain, forming a halo. This is relevant due to the presence of neuronal loss in the immediate region of the oligomeric halo (Koffie et al., 2009). These observations support the oligomer hypothesis and explain the presence of neuronal loss before the detection of plaque formation.

1.10 AD and Inflammation

Despite which cascade hypothesis is correct, the two pathological hallmarks are not sufficient for the full development of the neurodegenerative pathology that is observed in AD transgenic animals (Rogers et al., 1996). Recently, inflammation within the brain has been accepted as a hallmark of AD. The inflammation refers specifically to the innate inflammatory response by the nervous system in an attempt to clear the different Aβ pathological species (Rogers, 2008). The innate immune system is the body's first line of defense against pathogens. The innate immune system is in the CNS and is made up of macrophages, neutrophils, dendritic cells, natural killer cells, and microglia (Kielian, 2006). An inflammatory response involves many different processes including removal of debris and healing (Ferrero-Miliani et al., 2007). The majority of the time, an innate immune response is self-limiting, but in some cases and in some diseases the inflammatory response can linger and cause a state of chronic inflammation. Rather than being beneficial to the host, a chronic state of inflammation can actually become detrimental to the host. In AD, if the innate immune system is unable to remove its activated trigger, then it can lead to a chronic state of inflammation. This chronic state of inflammation has been suggested to be one of the primary mechanisms leading to the neurodegeneration in AD and has even been suggested to intensify the amount of Aβ deposition (Golde, 2002). One piece of evidence suggesting that the innate immune system is involved in AD is the presence of activated immune cells, such as microglia and astrocytes, and proinflammatory markers within and surrounding the Aβ deposits in the brain (Figure 1.9) (Barton, 2006, Heneka and O'Banion, 2007, Rogers et al., 1996); however, how or when inflammation arises during the course of AD is not fully

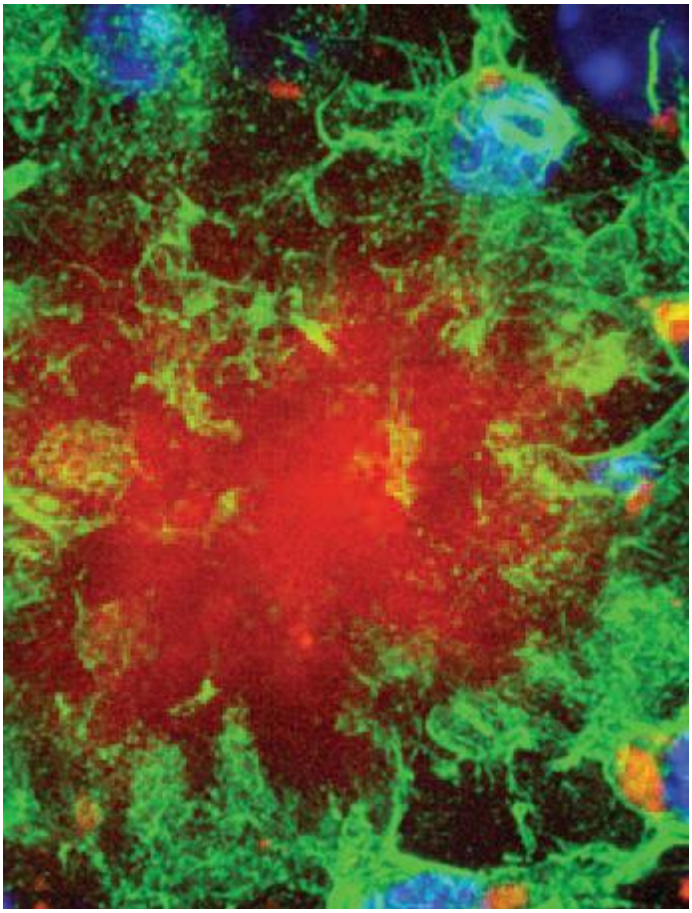

Figure 1.9. Activated microglia surrounding the senile plaque (Barton, 2006). Bone marrow derived microglia (green fluorescent protein-green) are attracted to the senile plaque (red) and are able to clear some of the Aβ by phagocytosis. The nuclei of the microglia are stained blue.

understood (Akiyama et al., 2000).

1.11 Cells Involved in Causing Inflammation in AD

1.11.1 Neurons

Neurons were not originally thought of as immune cells; however, more recent data has shown that neurons exhibit more abundant signal for complement mRNAs than any other cell type in the AD brain. Neurons can express virtually all the proteins like interleukins (IL-1 and IL-6), tumor necrosis factor-alpha (TNFα) and macrophage colony-stimulating factor (M-CSF). Studies have indicated that there is an increase of neuronal proteins in AD brains compared to control brains. Due to the increase of these proteins, it was thought that the neurons might contribute to exacerbation of the AD pathology along with microglia and astrocytes. The activation of neurons by TNFα induces the expression of protective molecules, including manganese superoxide dismutase (MnSOD). Neurons also have a high expression of APP and are suggested to be the primary source of brain Aβ (Akiyama et al., 2000).

1.11.2 Glia

Glia were once overlooked as supportive elements of the nervous system; however, these non-neuronal cells have recently been more appreciated due to their ability to integrate neuronal inputs and modulate synaptic activity. The glia of the CNS consists of microglia, astrocytes, and oligodendrocytes. Altogether, these cells are responsible for neuronal homeostasis, synaptic plasticity and repair (Haydon, 2001).

1.11.2.1 Astrocytes

Astrocytes are highly numerous and have many divergent roles within the CNS (Haydon, 2001). Astrocytes are the major glial cell type of the CNS and can participate in an inflammatory response; however, their immune responses are more limited due to the fact that they are not classical immune cells (Hanke and Kielian, 2011). Astrocytes are closely associated with the neurons of the CNS and can wrap around the synaptic terminals and have extensive contacts with endothelial cells from the capillaries. They are located within the brain and participate in the signaling between astrocyte-astrocyte, neuron-neuron, and neuron-capillary (Haydon, 2001).

Astrocytes have been found to play a vital role in the maintenance of synaptic plasticity, which is linked to cognitive processing in the brain. They are located near many central synapses and are able to respond to many neurotransmitters, including glutamate by an increase in the intracellular calcium levels. In return, the astrocytes release glutamate and other neuroactive molecules that affect the neuronal activity and modulate the strength of the synapse (Schummers et al., 2008). Glia are thought to play an import role in the antioxidant defense within the brain because of their highly resistant nature to oxidative stress compared to neurons. In subcultures of both neurons and glia, the glial cells protect the neurons from hydrogen peroxide (H_2O_2) toxicity via maintenance of the neuronal glutathione levels or by scavenging the free radicals (Iwata-Ichikawa et al., 1999, Langeveld et al., 1995). It was also shown that conditioned media from glial cells were able to promote the survival and differentiation of neuronal cells and protect them from L-DOPA toxicity (Engele et al., 1991, Iwata-Ichikawa et al., 1999, Mena et al., 1996).

Activated astrocytes up-regulate a number of different inflammatory molecules, including cytokines, interleukins, growth factors, proteases and protease inhibitors (Eddleston and Mucke, 1993). Several of these inflammatory molecules have been recognized in the AD pathology and overexpression within astrocytes of these molecules has been shown to increase Aβ deposition and behavioral decline (Wyss-Coray et al., 1997). More recent studies have recognized that astrocytes may not produce cytokines during activation, but are definitely the prevalent source of chemokines after an insult or infection of the CNS (Hanke and Kielian, 2011). One study showed that Aβ was able to stimulate the release of the chemokines that were then able to act as potent *in vitro* microglial and macrophage chemoattractants (Johnstone et al., 1999).

1.11.2.2 Microglia

Microglia are the main immune cells within the CNS and make up as much as 12% of the cells within the CNS (González-Scarano and Baltuch, 1999). Microglia originate from bone marrow (BM) and enter the CNS as monocytes (Barton, 2006). The monocytes migrate through the blood-brain barrier (BBB) into the parenchyma during the early embryonic stages of life and later stages of life and eventually differentiate into microglia. Studies have shown that peripheral monocytes are able to cross the BBB in response to an inflammatory stimulus and differentiate into microglia-like cells indistinguishable from microglia (Malm et al., 2005, Simard and Rivest, 2004).

Microglia can structurally form many different morphologies in accordance to their environment, such as round, amoeboid and ramified. Before this observation was known, the nature and identity of the microglia were under much debate. Now it is

remarkably clear that microglia are highly flexible and able to adapt both structurally and functionally (Graeber, 2010, Graeber and Streit, 2010). SEM images of microglia on different gold surfaces allowed detailed visualization of many different microglial morphologies along with many short and branched processes projecting outward from the microglial cell body. When measuring the length of some of the branches, it was shown that they can range anywhere from 5 μm to 30 μm in length (Tan et al., 2014). Time-lapse imaging using *in vivo* two photon imaging showed that microglia of even a normal, healthy brain are constantly surveying the environment around them representing a constant dynamic state instead of a resting state (Nimmerjahn et al., 2005). In the presence of an injury or insult within the brain, the microglia respond by rapid and direct expansion/growth of the processes towards the site of injury and initiate a signaling cascade (Davalos et al., 2005).

Microglia are known to respond to traumatic injury or the presence of pathogen associated molecular patterns (PAMPs), such as a bacterial coat or viral proteins (Colton et al., 2006). The microglia then migrate to the specific site of injury where they begin to proliferate and become activated. The activated microglia have increased levels of antigens and also become phagocytic. Similar to macrophages of other tissues, the microglia begin to release inflammatory cytokines, which in return amplify the immune response by recruiting more microglia to the injured site (González-Scarano and Baltuch, 1999).

Microglia have a programed response to stimuli that includes the induction of specific gene profiles and production of cytoactive factors, such as TNFα, nitric oxide (NO), and IL-1. These cytoactive factors all protect against tissue invaders. Peripheral

macrophages first phase of activation is "classical activation". This phase involves Th-1 cytokines, such as interferon-γ (IFN-γ). At the site of injury and after the initiation of classical activation, the microglia gene profile changes to start the production of anti-inflammatory factors, such as IL-4, IL-13, IL-10, transforming growth factor –β (TGF-β) and scavenger receptors (SR) for the activation of phagocytosis, which aids in tissue repair and wound healing. The gene induction of IL-4 and IL-13 is known as alternative activation. The second phase of activation produces genes like arginase 1 (AG1), mannose receptors (MRC1) and genes associated with tissue remodeling, such as Found in Inflammatory Zone 1 (FIZZ1) and chitinase 3-like-3 (YM1) (Colton and Wilcock, 2010, Nimmerjahn et al., 2005).

Activated microglia can be assessed by different markers, such as major histocompatibility complex II (MHCII) and cell surface receptors CD11b, CD-45, and peripheral benzodiazepine receptors (Colton and Wilcock, 2010). As the activation of microglia is very important within the CNS and chronic microglia activation sustained over a long period of time may result in microglia over-activation followed by microglial degeneration. This phenomenon has shown an increase prevalence in AD and in Down's syndrome patients (Graeber and Streit, 2010). It was reported that there is an increase in the amount of activated microglia within the cortex of the AD brain, but the increase was not closely correlated with the increase in deposited Aβ plaque, but rather correlated with the amount of cognitive decline (Edison et al., 2008, Okello et al., 2009).

Microglia play a few different roles in AD including amyloid removal and mediation of fibrillar Aβ toxicity (Graeber and Streit, 2010). It is also known that microglia are activated in the presence of Aβ and are able to upregulate the expression of

different pro- and anti-inflammatory genes and ROS (Cameron and Landreth, 2010, Meda et al., 1995, Paranjape et al., 2012, Yates et al., 2000). The microglia are able to internalize soluble Aβ from the extracellular milieu though a fluid phase macropinocytic mechanism. This mechanism is distinctly different from that of phagocytosis and receptor-mediated endocytosis. Within the microglia, Aβ is able to activate a purinergic autocrine/paracrine stimulatory loop in which the P2X receptor is a required component. Other signaling pathways, such as the toll-like receptors (TLRs), have also been implicated in the mediation and activation of the microglia via Aβ (Graeber and Streit, 2010).

Microglia have previously been proven to be associated with cerebral amyloid deposits (Itagaki et al., 1989, Stalder et al., 1999, Wegiel and Wisniewski, 1990). With the use of a double transgenic AD mouse model crossed with the overexpression of green fluorescent protein (GFP) in microglia, it was shown that the microglia of control mice continually survey their environment, while the microglia of the plaque bearing APP/PS1 mice showed ongoing uptake of Aβ (Bolmont et al., 2008). Human *in vivo* positron emission tomography (PET) and carbon-11-labelled (R)-PK11195, a specific ligand for the peripheral benzodiazepine binding site (activated microglia), also showed increased [11C](R)-PK11195 binding in AD demented patients suggesting that the activation of microglia is an early event in AD pathogenesis (Cagnin et al., 2001).

Many studies have examined the microglia association with Aβ plaques. These studies have shown that the Aβ plaques were able to activate the microglia, stimulate microglial proliferation and cause the microglial processes to extend toward the plaque, resulting in rapid movement and clustering around the Aβ plaque (Barton, 2006, Itagaki

et al., 1989). Literature has suggested that neurons and glia cells actually participate in the formation, growth, and morphologies of the Aβ plaques. Data has shown that microglia are able to assist the aggregation of the diffuse soluble Aβ species into a more insoluble aggregate due to failure of the Aβ clearance mechanism (Nagele et al., 2004, Qiao et al., 2001). The amyloid plaques mostly consist of Aβ protein, but microglial cells, dystrophic neurites, and bundles of astrocyte processes have also been detected (Frautschy et al., 1998, Nagele et al., 2004). The microglia-Aβ plaque association was confirmed in an AD mouse model by the co-localization of both IL-1β and TNFα immunopositive microglia with ThT-positive Aβ plaques (Benzing et al., 1999). This association, however, has not been confirmed with the more diffuse Aβ species. In this study, very few of the diffuse Aβ plaques contained activated microglia; however, most of the activated microglia were associated with the classic plaques in the cerebral cortex and cerebellum of AD patients. This study, along with others, has shown that microglial associations are not present in the early stages of Aβ plaque formation but become increasingly apparent during the transition to the classic, insoluble Aβ plaque (Sasaki et al., 1997).

1.12 Aβ Receptors Found on Microglial Cells

The inflammatory process plays a fundamental role in the pathogenesis of AD and studies have indicated that an increase in the production of Aβ species can activate the innate immunity system through pattern recognition receptors (PRRs) and induce AD pathology. The innate immune system is the body's guardian again pathogens and danger insults and the way the body discriminates between self and non-self. The

recognition of pathogens and danger insults have been based on specific structures that are conserved across a broad subclass of pathogens (Kielian, 2006) known as PAMPs. The body can also recognize pathogen-free self-derived danger signals and tissue injuries through danger-associated molecular patterns (DAMPs). In both cases of environmental and inherent threats (PAMPs and DAMPs), organisms use the same PRRs to defend themselves (Salminen et al., 2009). Microglia display many different receptors which interact with specific ligands, usually PAMPs and DAMPs, which initiate a downstream signaling cascade leading to the production of pro- and anti-inflammatory cytokines or Aβ clearance (Graeber, 2010). AD pathogenesis has been shown to be triggered by the innate recognition of microglial receptors of different Aβ species. This recognition causes the activation of overlapping signaling pathways that affect not only the functional phenotype of the microglia, but also the surrounding cells (Salminen et al., 2009).

1.12.1 Toll-Like Receptors (TLRs)

TLRs are part of the PRR family and are expressed on cells of the innate immune system. They allow for the recognition of PAMPs located on bacteria, fungi, and viruses (Kielian, 2006) or for the recognition of DAMPs (Salminen et al., 2009). To date, there have been 11 TLRs identified within humans and mice along with at least one agonist for each receptor with the exception of TLR10 (Kielian, 2006). TLR1, TLR2, TLR4 and TLR6 have been found located on the cell surface, forming the first line of defense against pathogens, while TLR3, TLR7, TLR8 and TLR9 have been found in the endosomes and are particularly adept at recognizing viruses. TLR activation is regulated by several co-receptors, such as MD-2, CD14, and CD36. The stimulation of TLRs

activate several protein kinase cascades that modulate gene expression through various transcription factors, such as AP-1, NF-κB, IRF-3 and IRF-7 (Salminen et al., 2009).

Multiple TLRs and accessory proteins play a role in the proinflammatory response evoked by Aβ in monocyte/macrophages and microglia including CD14, TLR4, and TLR2 (Fassbender et al., 2004, Jana et al., 2008, Liu et al., 2012, Reed-Geaghan et al., 2009, Udan et al., 2008) and TLR4 and TLR6 in concert with CD36 (Stewart et al., 2010). Fassbender et al., 2004, showed that the lipopolysaccharide (LPS)-receptor CD14, which is considered to transmit a signal through TLR2 and TLR4, binds Aβ fibrils and mediate microglia and monocyte activation and neuronal toxicity. This was demonstrated by the use of neutralization with antibodies against CD14 along with genetic deficiency for this receptor, which showed a significant reduction in the Aβ fibril induced microglial activation and toxicity (Fassbender et al., 2004). TLR2 was again shown to be a key receptor in the mediation of an inflammatory response induced by Aβ fibrils, in 2008. This study used methods, such as antisense knockdown of TLR2 and functional blocking of the receptor by antibodies in both primary murine and BV-2 microglia, along with $TLR2^{-/-}$ knockout microglia, where both alleles of the TLR2 gene are knocked out within the mice (Jana et al., 2008). Our lab also provided evidence indicating a major role for TLR2 and TLR4 in the activation of human monocytic THP-1 cells induced by Aβ(1-42) fibrils. TLR2 neutralization resulted in ~50% reduction in the cellular response induced by Aβ(1-42) fibrils, completely blocked the cellular response induced by Pam_3CSK_4 (a known TLR2 ligand), and had no effect on the cellular response induced by LPS (a known TLR4 ligand). However, when TLR4-specific antibodies were used to neutralize the TLR4 receptor, there was ~35% reduction in the cellular response

induced by Aβ(1-42) fibrils, complete reduction in the cellular response induced by LPS and no effect on the cellular response induced by Pam_3CSK_4. Lastly this study showed that a combination of TLR2 and TLR4-specific antibodies for neutralization of both receptors in addition to neutralization of CD14, which was previously shown to mediate Aβ fibril inflammation, was much more effective at blocking the Aβ(1-42) fibril induced cellular response then any of the antibodies by themselves. Taken together, this study showed that Aβ(1-42) fibrils trigger an innate immune response, where both TLR2 and TLR4 receptors play a role (Udan et al., 2008). One year later it was also shown that CD14, TLR2, and TLR4 are important in the Aβ induced innate immune response. The study specifically indicated that CD14, TLR2, and TLR4 functionally interact with other members of the microglial fibrillar Aβ receptor complex, such as α6β1 integrin, CD36, and CD47, to initiate intracellular signaling cascades resulting in an activated microglial phenotype (Reed-Geaghan et al., 2009). TLR2 was shown to be a major receptor in mediating a neuroinflammatory response triggered by Aβ by the use of real-time surface plasmon resonance spectroscopy and conventional biochemical pull-down assays. This study showed a direct interaction between TLR2 and the aggregated Aβ(1-42) of human Aβ. The use of site-directed mutagenesis of tlr2 gene identified amino acids EKKA (741-744) as a critical cytoplasmic domain for the transduction of inflammatory signals (Liu et al., 2012).

TLR4 and TLR6 have also been proven to mediate Aβ-induced inflammation. Stewart et al., 2010, showed that Aβ triggers an inflammatory response through a heterodimer of TLR4 and TLR6 and that the heterodimer is regulated by signals from the SR CD36 (Stewart et al., 2010). Taken altogether, the evidence demonstrates that TLR2,

TLR4 and TLR6 are primary receptors for Aβ induced neuroinflammation and suggests that the inhibition of these receptors could be beneficial in AD pathogenesis.

1.12.2 NOD-Like Receptors (NLRs) and NLRP3 Inflammasome

Recently, the activation of the TLRs has also been recognized as one of two signal processes for the activation of a multi-subunit complex known as the inflammasome (Figure 1.10). The requirement for two signals to produce mature IL-1β represents a regulatory checkpoint to avoid fabricated immune responses that are capable of harming the host (Sutterwala et al., 2014). The inflammasome is formed by the oligomerization of cytoplasmic nucleotide-binding oligomerization domain (Nod)-like receptors (NLRs) and its activation, "signal two", is responsible for the processing of pro-IL-1β to mature IL-1β, via caspase-1 (Hanamsagar et al., 2012). There are many different NLRs families which contain a variance in their N-terminal protein-protein interaction region. For example, the best characterized inflammasome, NLRP3 also known as NALP3, contains common features like a central nucleotide-binding domain (NACHT) and C-terminal leucine-rich repeat (LRR) (Sutterwala et al., 2014), along with an N-terminal pyrin domain which interacts with the adaptor molecule apoptosis-associated speck-like protein containing a CARD (ASC), where CARD is a caspase recruitment domain, through a pyrin-pyrin interactions (Hanamsagar et al., 2012). Additional assembly of the inflammasome involves a CARD-CARD interaction which brings procaspase-1 to the complex (Schroder and Tschopp, 2010). Other inflammasomes, such as NLRC4, contain an N-terminal CARD that interacts directly with caspase-1 (dos Santos et al., 2012). The inflammasome complex then activates pro-

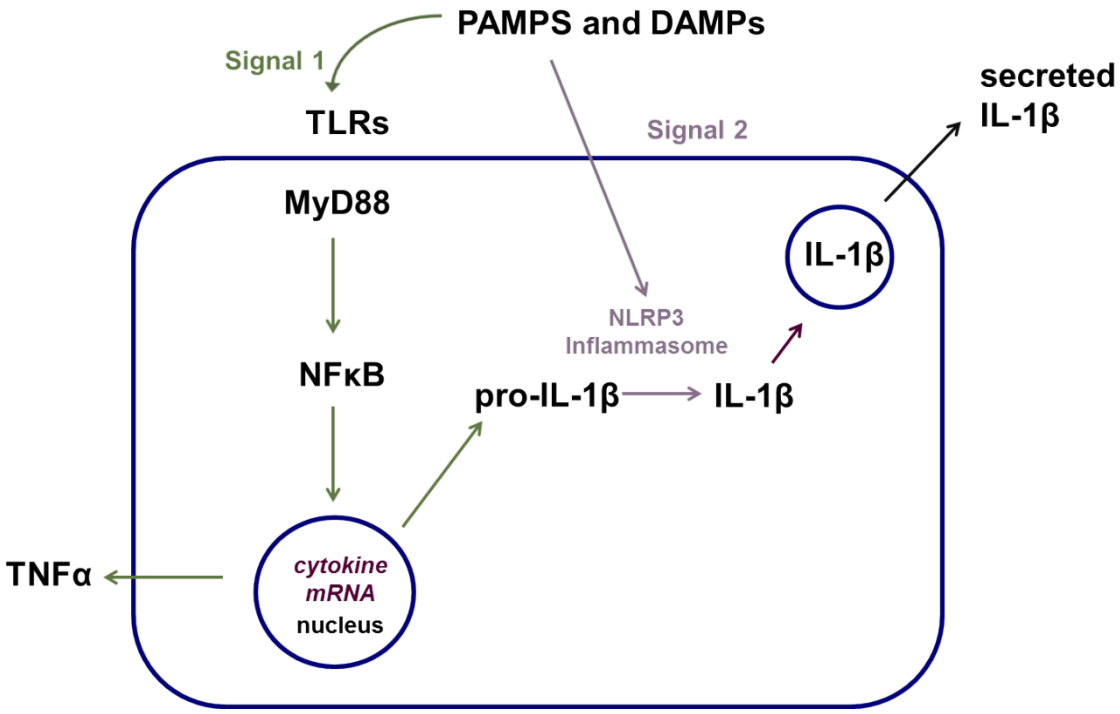

Figure 1.10. Two signal activation of the NLRP3 inflammasome.

caspase-1 by proteolytic cleavage to produce the active form of caspase-1. Active caspase-1 then triggers the proteolytic cleavage of pro-IL-1β to mature IL-1β (Schroder and Tschopp, 2010). NLRP3 and ASC are important in the production of IL-1β. This has been shown by knocking out both the NLRP3 and ASC, which significantly reduced the production of IL-1β after exposure to *S. aureus* (Hanamsagar et al., 2011). NLRP3 is also essential in the amount of AD pathology, which was publicized by Heneka and colleagues. With the use of a well-established AD mouse model also deficient in the NLRP3 inflammasome, they were able to observe a reduction in the AD pathology (Heneka et al., 2013).

The two signals start with the transcriptional induction of pro-IL-1β and NLRP3 mRNA followed by the proteolytic processing though the activation of the inflammasome. Signal one can be elicited by known TLR ligands, such as LPS, or by a number of other ligands that are known to activate NF-κB (Sutterwala et al., 2014), whereas signal two has been found to be activated by several DAMPs, including pore-forming toxins, ATP, K^+ efflux, and silica and uric acid crystals (Hanamsagar et al., 2012). Cellular studies have shown that the different aggregation species of Aβ have distinct toxic and biological activities and potencies, including their ability to be a proinflammatory stimulus (Dahlgren et al., 2002, Paranjape et al., 2012, Walsh et al., 2002). This is most likely the case with the two signal activation of the TLRs and the inflammasome leading to the production and secretion of IL-1β. There have only been a few reports regarding inflammasome activation by soluble Aβ species. Therefore, most of the research investigating the inflammasome and its activation by Aβ has been with fibrillar Aβ. In 2008, Halle and colleagues used a fibrillar Aβ preparation to study the

effect fibrillar Aβ has on the activation of the NLRP3 inflammasome. Using this preparation, a novel inflammasome signaling pathway was observed showing that fibrillar Aβ can activate the NLRP3 inflammasome in microglia. However, the exact process of how the inflammasome is becoming activated was still unknown. Halle et al., 2008 proposed that the mechanism of inflammasome activation may be linked to the physical structure of the stimulus, due to the fact that the use of the reverse Aβ peptide (Aβ42-1) or unaggregated peptide was unable to stimulate the inflammasome (Halle et al., 2008). Their investigation also found that phagocytosis of the fibrillar Aβ was necessary for the activation of the inflammasome. The phagocytosis of the fibrillar Aβ led to the release of the lysosomal component, cathepsin B, into the cytoplasm. IL-1β release was found to be dependent on the release of the cathepsin B (Halle et al., 2008, Murphy et al., 2013). Treatment of primary rat glial cultures with recombinant human Aβ also showed an increase in cathepsin B activation in the cytosol, formation of the inflammasome components ASC and NLRP3, activation of caspase-1 and the release of IL-1β (Murphy et al., 2013). Wu and colleagues came to a similar conclusion while comparing fibrillar Aβ to chromogranin A (CGA). CGA is a neurosecretory acidic glycoprotein known to strongly activate cultured microglia to induce the production and secretion of IL-1β. Along with many of the other studies, fibrillar Aβ was unable to stimulate both signal one and signal two of the inflammasome processing of pro-IL-1β to mature IL-1β. All of the studies mentioned here used LPS as a priming step to initiate the activation of the TLR4 and production of the pro-IL-1β. Fibrillar Aβ was then used as a secondary treatment to activate the second step, the inflammasome, and continue the processing to mature IL-1β (Wu et al., 2013).

Although fibrillar Aβ was originally thought to be the primary entity responsible for AD, more recent studies have suggested that soluble oligomeric Aβ, which is found in the cortex of AD patients and could contribute to the pathogenesis of AD (Lambert et al., 1998). Therefore, more current studies have considered the possibility of soluble Aβ species activating the NLRP3 inflammasome. Sheedy et al., 2013 investigated the role that the CD36 receptor plays in the activation of the NLRP3 inflammasome by cholesterol crystals and Aβ. This investigation found that the uptake of soluble Aβ results in the activation of the NLRP3 inflammasome, similar to that of fibrillar Aβ (Sheedy et al., 2013). Other studies have specifically researched oligomeric Aβ (oAβ) and its activation of the inflammasome. Parajuli et al., 2013 found that oAβ increases the processing of pro-IL-1β into mature IL-1β in microglia by activating caspase-1 and the NLRP3 inflammasome via ROS and partially NADPH oxidase-induced ROS. When comparing oAβ to fibrillar Aβ, it was found that inhibition of phagocytosis and cathepsin B inhibited the fibrillar Aβ-induced IL-1β release and caspase-1 activity, while the oAβ-induced IL-1β secretion and caspase-1 activity was unaffected (Parajuli et al., 2013).

To date, little to no experimental work has been completed on the capability of Aβ protofibril-induced NLRP3 activation. In the past several years, there has been an increase in understanding the link between NLRP3 inflammasome signaling and AD pathology. The research has shown that there are distinct differences in the Aβ-induced NLRP3 inflammasome activation and that it may be dependent on the morphology of the Aβ species. Each individual species along the nucleation-dependent polymerization process to insoluble fibrils could play individual distinct roles in the mechanism of activating the NLRP3 inflammasome and processing pro-IL-1β into its mature form of

IL-1β. Therefore, an improved explanation of the molecular mechanism of how each Aβ species induces inflammasome activation and contributes to the pathology of AD could aid in the development of future therapeutic opportunities.

1.13 Cytokines

There are many inflammatory molecules involved in AD, including proinflammatory cytokines. Proinflammatory cytokines, such as TNFα and IL-1β, are upregulated in microglia which are located near the senile plaques within the brains of AD patients (Dickson et al., 1993, Sardi et al., 2011).

1.13.1 TNFα

TNF is a soluble cytokine termed tumor necrosis factor and is produced by the activation of the immune system. It is produced as a type II transmembrane protein and arranged as a homotrimer. The homotrimer is released by the proteolytic cleavage of the membrane-integrated form by the metalloprotease TNFα converting enzyme (TACE). TNFα regulates several cellular pathways, including inflammation, differentiation, and cell death, through activation of TNF receptor 1 (TNFR1) or TNFR2 (Wajant et al., 2003). In the CNS, microglia are thought to be the primary source of TNFα. Studies have indicated that there is an increased level of TNFα within the brain and plasma of AD patients. It has also been found as a critical mediator in the reduction of LTP induced by Aβ (Medeiros et al., 2007).

TNFα induces the activation of the transcription factor, NF-κB, which results in the regulation of many proinflammatory cytokines, including IL1, IL8, IL6 and

granulocyte macrophage colony-stimulating factor (GM-CSF) and survival factors, such as MnSOD. As the name suggest, TNFα is known to cause cell death by necrosis, which does not involve caspase or ATP as apoptosis does and is linked to inflammation *in vivo*. However, both processes are indirectly triggered by TNFα through the generation of ROS (Wajant et al., 2003).

TNFα protects neurons from Aβ-induced damage by upregulating receptors involved in microglia chemotaxis towards Aβ clearance (Cui et al., 2002). Bruce and colleagues generated mice deficient of TNF receptors to determine the role of TNF in the cells of injured brains. The results showed that the microglial activation was suppressed in TNFR-KO mice, indicating a neuroprotective role for TNF by stimulating antioxidant pathways (Bruce et al., 1996). It was also shown that blocking the action of TNFα by pharmacological inhibitors or genetic deficiency reduces Aβ-induced cognitive dysfunction (Medeiros et al., 2007).

1.14.2 IL-1β

IL-1 has two produced isoforms: IL-1α and IL-1β. Both isoforms are able to activate their only respective receptor, IL1R1, to produce other inflammatory molecules, such as prostaglandins, collagenase, and phospholipids (Arai et al., 1990).

Immunostaining of AD patients' brains and the brains of AD mouse models showed the presence of IL-1β surrounding both diffuse and senile plaques (Benzing et al., 1999, Sardi et al., 2011). IL-1β is an important proinflammatory mediator in the innate immune response in AD and has also been shown to be elevated in both the brain and plasma of Alzheimer patient's postmortem (Ojala et al., 2009). A mouse model

developed to harbor human IL-1β produced a localized inflammatory response when activated, however these same mice crossed with APP/PS1 mice showed reduced amyloid pathology (Rivera-Escalera et al., 2014). An important aspect of TLR signaling is production of IL-1β mRNA and the pro-form of IL-1β protein (pro-IL-1β). IL-1β is processed by the inflammasome. The activation and oligomerization of NLRs of the inflammasome activates caspase-1 which then proteolytically cleaves the pro-IL-1β (31 kDa) to mature IL-1β (17 kDa) (Figure 1.8) (Hanamsagar et al., 2012).

The results, discussed in Section 1.13.2, have shown that the mechanism for oAβ-induced processing of mature IL-1β by the NLRP3 inflammasome is different than that induced by fibrillar Aβ (Parajuli et al., 2013), and it is possible that other species of Aβ, such as protofibrils, maybe able to induce IL-1β by completely different mechanisms, also.

CHAPTER 2

METHODS

2.1 Cell Culture

2.1.1 WT and MyD88$^{-/-}$ Primary Microglia Isolation and Culture

WT and MyD88 knock-out (MyD88$^{-/-}$) primary murine mixed microglia were obtained from neonatal C57BL/6 mouse pups (Harlan laboratories Inc. and Tammy Kielian's lab at University of Nebraska Medical Center, respectively). Post natal mice (3-4 days) were euthanized with inhaled isoflurane (Fisher). The brains were isolated and meninges were removed under sterile conditions by rolling the brains over slightly moistened gauze in a petri dish. The isolated brains were then collected in a 50 mL sterile conical tube that contained 20 mL of phosphate buffered saline (PBS, Hyclone) supplemented with antibiotics and placed on ice. After isolating all of the brains, the brain tissue was transferred to a 100 mm cell-culture dish and minced using the sharp edge of two separate forceps in a scissor action. The minced tissue was then resuspended in 5 mL 0.05% trypsin (Hyclone) followed by an incubation at 37 °C for 20 minutes on a shaker to allow further dissociation of the tissue. Successively, the cells were resuspended in 10 mL of complete Dulbecco's modified Eagle's medium without pyruvate (DMEM, 4.5 g/l glucose, Hyclone) containing 10% heat-inactivated fetal bovine serum (FBS, Hyclone), 4 mM L-glutamine, 100 U/ml penicillin, 0.1 mg/ml streptomycin

and 0.25 μg/mL amphotericin-B (P/S/A triple antibiotic mixture, Fisher Scientific), 10 μM oxaloacetic acid, 4.5 μM pyruvate, 0.002 U/mL insulin (OPI medium supplement, Sigma-Aldrich), and 0.5 ng/ml recombinant mouse GM-CSF (Invitrogen). The cell suspension was triturated using a 10 mL pipette and filtered through a 70-μm cell strainer to remove tissue debris (Fisher Scientific). The flow through cell suspension was centrifuged at 200 x *g* for 5 minutes at 25 °C, resuspended in complete medium, and seeded into a 150 cm^2 flasks (Corning). Each 150 cm^2 flask contained 30 mL of total cells. The number of flasks per single litter of mouse pups was determined by the size of the litter. Each flask contained 3-5 isolated brains. The cells were cultured at 37 °C in 5% CO_2 until confluent (1-2 weeks). The microglia morphology typically looked like round cells resting on the top of a granular astrocytic layer. The microglia were selectively harvested from the adherent astrocyte layer by overnight shaking of the flask at 37 °C in 5% CO_2 (at a speed between 5-6 on the shaker in the cell culture laboratory) and collection of the medium. The flasks were replenished with fresh complete growth medium and incubated further to allow proliferation of remaining microglia. Typically, this procedure was repeated 3-4 times for one flask (Esen and Kielian, 2007) without removal of the astrocyte layer before the flasks were discarded.

2.1.2 BV-2 Microglia Culture

The BV-2 mouse microglia cell line was a gift from Dr. Landreth (Case Western Reserve University). The BV-2 microglia were maintained in DMEM (4.5 g/l glucose, Hyclone) containing 50 U/mL penicillin, 50 μg/mL streptomycin, 50 μM β-mercaptoethanol and 5% FBS (Hyclone). These cells were typically passaged twice a

week, which consisted of washing the confluent cells 1 x with PBS and the addition of 1 mL of 0.25% trypsin. The cells were then incubated at 37 °C and 5% CO_2 for 10 minutes. After the incubation time, 9 mL of growth medium was added to inactivate the trypsin. Of the resuspended 10 mL of cells, 1 mL was centrifuged for 7 minutes at 500 x *g* and resuspended in 10 mL of fresh growth medium. The freshly resuspended cells were then added to a 75 cm^2 flask and incubated at 37 °C and 5% CO_2 until the next passage. BV-2 cells were used until passage #50, after which the cells were discarded. A few passages before passage 50, a new frozen aliquot (frozen in the year 2008 by M.L.D. Udan at passage #33-36) was thawed and cultured in fresh growth medium as described above. However, while thawing the new cells, one washing step was added before culturing, which involved centrifugation for 7 minutes at 500 x *g* to remove any residual dimethyl sulfoxide (DMSO, Sigma-Aldrich, St. Louis) present in the cryopreservation medium.

2.1.3 THP-1 Human Monocyte Culture

The human peripheral blood THP-1 monocytes were obtained from ATCC (Manassas, VA, USA) and maintained in RPMI-1640 culture medium (Hyclone) which contained 2 mmol/L L-glutamine, 25 mmol/L HEPES, and 1.5 g/L sodium bicarbonate and was also supplemented with 10% FBS (Hyclone), 50 U/mL penicillin and 50 μg/mL streptomycin (Hyclone), and 50 μmol/L β-mercaptoethanol (Fisher). The monocytes were grown by incubating at 37 °C and 5% CO_2. The growth of the THP-1 monocytes were maintained by two dilutions a week, with a 1:1 dilution at the beginning of the week and a 3:10 dilution at the end of the week. The 1:1 dilution was completed by removing

half of the cells from the flask and replacing with the same volume of fresh growth medium for propagation. For the 3:10 dilution, 3 mL of the THP-1 cells were removed from the culture flask and centrifuged at 500 x *g* for 10 minutes. After centrifugation, the supernatant was removed and the pelleted cells were resuspended in 10 mL of fresh growth medium. The cells were then transferred to a new cell culture flask and again incubated at 37 °C and 5% CO_2 for further propagation.

While observing these cells over time, it was apparent that the proinflammatory response starts to decrease as the monocytes reach about 2 months of continuous sub-culturing. To avoid this problem, staggering the culture of the THP-1 monocytes was conducted.

2.1.4 THP-1 Human Differentiated Macrophages

THP-1 human monocytes were cultured and maintained as stated above, however the monocytes were differentiated into macrophages by the addition of phorbol 12-myristate 13-acetate (PMA, Sigma). PMA, also known as 12-O-tetrade-canoylphorbol-13-acetate (TPA), was found to change THP-1 cells into cells with the functional characteristics of mature macrophages (Tsuchiya et al., 1982). THP-1 monocytes were treated with a final concentration of 10 ng/ml PMA in 300 uL of ~7.0 x 10^5 cells/mL (48 well plate) and incubated for 24 hours at 37 °C and 5% CO_2. The next day two wells were detached from the bottom of the plate with 0.25% trypsin for the calculation of percent adherence.

2.1.5 Mononuclear Cells

The human peripheral blood mononuclear cells (hMNC-PB) from a single donor were obtained from PromoCell (Heidelberg, Germany) and maintained in mononuclear cell medium provided by PromoCell, which contained all the growth factors and supplements necessary for optimal short-term maintenance. After being thawed the cells were plated at a density of 1 x 10^6 cells per mL and allowed to survive at 37 °C and 5% CO_2 for at least 18-24 hours to avoid clumping. The cells were then harvested after 24 hours by collecting the cellular medium and centrifuging for 10 minutes at 240 x *g* and resuspending in fresh, pre-warmed mononuclear medium. The cellular medium was then changed only when the medium looked diminished. It was observed that these cells do not grow and divide very quickly so they either need to be cryopreserved or used immediately for experiments.

2.2 Preparation of Aβ

Aβ peptide has a high tendency to aggregate and to become highly polymorphous. This aggregation is thought to involve nucleation-dependent polymerization (Jarrett et al., 1993, Walsh et al., 1997), where the monomeric Aβ noncovalently associates and forms nuclei, or "seeds". These seeds can then go on to form soluble protofibrils and oligomers and insoluble fibrils (Harper et al., 1999). Therefore, in order to obtain a homogenous solution of Aβ, any pre-formed seeds needed to be removed, which was accomplished by the treatment of 100% hexafluoroisopropanol (HFIP). High concentrations of fluorinated alcohols, like HFIP, have been commonly used for solubilizing peptides and proteins (Buck, 1998).

Synthetic Aβ(1-40) and Aβ(1-42) peptides (Keck Center, Yale University) were dissolved in 100% HFIP (Sigma) at a concentration of 1 mM for one hour at room temperature with the vial lid closed to prevent evaporation. The completely dissolved Aβ was then aliquotted into sterile microcentrifuge tubes and evaporated overnight under the fume hood, uncovered, at room temperature. The next day the aliquots were vacuum-centrifuged for 1 hour to remove any remaining HFIP and then stored at -20 °C.

When forming the Aβ(1-42):Aβ(1-40) ratios, the individual peptide aliquots were re-aliquotted to form ratios of 5:0, 4:1, 1:1, 1:4, and 0:5. The ratio aliquot volumes were calculated based on a final total Aβ concentration of 200 μM for SEC purification. Briefly, 1 aliquot from each of the individual Aβ(1-42) and Aβ(1-40) 1 mg peptide aliquots from above were resuspended in 243 μL and 254 μL HFIP, respectively, for a concentration of 1 mM. The ratios of 4:1, 1:1, and 1:4 were formed by the same original individual aliquots by aliquotting the Aβ/HFIP into three separate tubes. The 4:1 aliquot was formed by mixing 160 μL of Aβ(1-42) (0.72 mg) and 40 μL of Aβ(1-40) (0.17 mg), while the 1:1 aliquot was formed by mixing 100 μL of Aβ(1-42) (0.45 mg) and 100 μL of Aβ(1-40) (0.43 mg), and lastly the 1:4 aliquot was a mixture of 40 μL of Aβ(1-42) (0.18 mg) and 160 μL of Aβ(1-40) (0.69 mg) (Table 2.1). The 5:0 and 0:5 ratios, however, required their own individual Aβ peptide aliquots. For the 5:0 the Aβ(1-42) was resuspend at 1 mM in 243 μL HFIP and 200 μL (0.90 mg) was aliquotted into a separate tube. The same procedure was used for the 0:5 ratio except Aβ(1-40) was resuspended at 1 mM in 254 μL and 200 μL (0.86 mg) was aliquotted into a separate tube (Table 2.1). Another Aβ(1-42):Aβ(1-40) ratio of 4:1 was also produced, but for this aliquot the volume was determined for a final total Aβ concentration of 250 μM. This 4:1 ratio was

formed by the addition of 200 μL (0.9 mg) from the 1 mM Aβ(1-42)/HFIP and 50 μL (0.22 mg) from the 1 mM Aβ(1-40)/HFIP solutions (Table 2.1). The Aβ(1-42):Aβ(1-40) ratio aliquots were then left in a fume hood uncovered, at room temperature, and overnight to allow for evaporation of the HFIP. The next day the aliquots were vacuum-centrifuged to remove any remaining HFIP and stored in a desiccant at -20°C.

2.2.1 SEC-Purified Aβ Monomer and Protofibril Preparation

SEC has shown to be useful in separating Aβ protofibrils from low molecular weight Aβ (Walsh et al., 1997). Walsh et al., 1997 prepared Aβ protofibrils by resuspending the Aβ peptide in sodium hydroxide (NaOH, Fisher Scientific) and then diluted into PBS and separated all aggregated morphologies by SEC. The use of an initial basic substrate, NaOH, prevents rapid Aβ aggregation around its isoelectric point of (~5.5) (Jan et al., 2010). For isolation of the Aβ monomer and protofibrils, AKTA-fast protein liquid chromatography (FPLC) was used along with a SEC. SEC is a method of protein separation, which separates the proteins based on their shape and size with the larger molecules eluting from the column first in the void peak followed by the smaller protein molecules in the included peak.

For Aβ experiments, our protocol was slightly modified from the original method of Walsh et al.1997, 1 aliquot of 1 mg lyophilized Aβ(1-42), Aβ(1-40) or mixed ratios were dissolved in 100 μL of 50 mM NaOH to give a 2.5 mM Aβ solution. After making sure all the Aβ went into solution, the Aβ was further diluted to 250 μM using artificial cerebrospinal fluid (aCSF, 15 mM $NaHCO_3$, 1 mM Na_2HPO_4, 130 mM NaCl, and 3 mM KCl at pH 7.8), modified from a protocol in Tzounopoulos et al., 2004

Table 2.1. Preparation of Aβ(1-42):Aβ(1-40) ratios.

Ratio	Aβ	Dry Aβ peptide	Volume in HFIP	[Aβ] in HFIP	Aliquot volume	Dry Aβ peptide	SEC [Aβ]	Total [Aβ]
5:0	**Aβ(1-42)**	**1 mg**	**243 µL**	**1 mM**	**200 µL**	**0.90 mg**	**200 µM**	**200 µM**
	Aβ(1-40)	-	-	-	-	-	-	
4:1	**Aβ(1-42)**	**1 mg**	**243 µL**	**1 mM**	**160 µL**	**0.72 mg**	**160 µM**	**200 µM**
	Aβ(1-40)	**1 mg**	**254 µL**	**1 mM**	**40 µL**	**0.17 mg**	**40 µM**	
1:1	**Aβ(1-42)**	**1 mg**	**243 µL**	**1 mM**	**100 µL**	**0.45 mg**	**100 µM**	**200 µM**
	Aβ(1-40)	**1 mg**	**254 µL**	**1 mM**	**100 µL**	**0.43 mg**	**100 µM**	
1:4	**Aβ(1-42)**	**1 mg**	**243 µL**	**1 mM**	**40 µL**	**0.18 mg**	**40 µM**	**200 µM**
	Aβ(1-40)	**1 mg**	**254 µL**	**1 mM**	**160 µL**	**0.69 mg**	**160 µM**	
0:5	**Aβ(1-42)**	-	-	-	-	-	-	**200 µM**
	Aβ(1-40)	**1 mg**	**254 µL**	**1 mM**	**200 µL**	**0.86 mg**	**200 µM**	
4:1	**Aβ(1-42)**	**1 mg**	**243 µL**	**1 mM**	**200 µL**	**0.90 mg**	**200 µM**	**250 µM**
	Aβ(1-40)	**1 mg**	**254 µL**	**1 mM**	**50 µL**	**0.22 mg**	**50 µM**	

This table provides all the volumes, molecular weights, and dry weight of the individual peptides which constitute the Aβ(1-42):Aβ(1-40) ratios.

(Tzounopoulos et al., 2004), that was pre-filtered through a 0.2 μM filter (Thermo Scientific). The Aβ(1-42) and the ratios were either immediately centrifuged at 18,000 x *g* for 10 minutes with a Beckman-Coulter Microfuge®18 or incubated for 4 hours at room temperature before centrifugation to generate more protofibrils, centrifuged and then immediately subjected to SEC. Aβ(1-40), on the other hand, was incubated for 24 hours at room temperature before centrifugation and SEC-purification. The centrifuged supernatant was then eluted from a Superdex 75 HR 10/30 column (GE Healthcare) in aCSF. Before the elution of Aβ, the Superdex 75 column was coated with 2 mg bovine serum albumin (BSA, Sigma) to reduce the amount of non-specific binding of Aβ to the column resin. The Aβ was eluted from the column at 0.5 ml/min, and the amount of eluted Aβ was continuously monitored using in-line UV absorbance at 280 nm. Fractions were continuously collected in 0.5 ml volumes and immediately placed on ice. The fractions that eluted in the void peak were labeled as protofibrils, whereas the fractions that eluted in the included peak were labeled as monomer. The collected fractions either remained as individual fractions or were grouped together. The Aβ was then used to either treat the cells to compare the cellular response between different Aβ species or to perform aggregation studies using the freshly SEC-purified protofibril and monomer. The protofibril and monomer concentrations were determined by using the SEC in-line absorbance measurements at 280 nm along with the Aβ extinction coefficient of 1450 cm^{-1} M^{-1}, which is for the Aβ peptide containing on tyrosine residue (Gill and von Hippel, 1989, Nichols et al., 2002).

2.2.2 SEC-Purified Aβ Monomer Preparation

Aβ(1-42) and Aβ(1-40) monomer was also obtained using an alternate protocol. To obtain solely monomer, 1 mg Aβ peptide was resuspended in 6 M guanidinium hydrochloride (GuHCl, Fisher Scientific) and 10 mM ammonium hydroxide (NH_4OH, Fisher Scientific) at a total volume of 1 mL. The Aβ solution was then subjected to all the same conditions as mentioned above with the protofibril protocol. Briefly, the solution was centrifuged, injected on the column, and eluted in 0.5 mL fractions in aCSF and stored on ice. This preparation elutes only one Aβ peak, monomer, which elutes in the included peak. The collected fractions either remained as individual fractions or were grouped together. The Aβ was then used to either treat the cells to compare the cellular response between different fractions or to perform aggregation studies using the freshly SEC-purified monomer. The monomer concentrations were determined by using the SEC in-line absorbance measurements at 280 nm along with the Aβ extinction coefficient of 1450 cm^{-1} M^{-1}, which is for the Aβ peptide containing on tyrosine residue (Gill and von Hippel, 1989, Nichols et al., 2002).

2.2.3 SEC-Purified Aβ(1-42) Oligomer Preparation

Aβ oligomers were prepared from an aliquot of lyophilized Aβ(1-42), as previously described by Stine et al., 2003 (Stine et al., 2003). Briefly, one 1 mg lyophilized Aβ(1-42) aliquot was resuspended in sterile DMSO at a concentration of 5 mM. After making sure all the Aβ was in solution, the sample was diluted to 100 μM in pre-filtered aCSF and incubated at 4 °C for 24 hours. The sample was then treated exactly the same as the protofibril preparation, as it was centrifuged, loaded on the SEC column to separate the

monomers, and oligomers in 0.5 mL fractions and placed on ice. The fractions that eluted in the void peak were labeled as oligomers; the fractions that eluted in the included peak were labeled as monomer. The fractions of oligomers or monomers were then used to treat the cells and compare the cellular response between the different species of Aβ. The monomer and oligomer concentrations were determined by using the SEC in-line absorbance measurements at 280 nm along with the Aβ extinction coefficient of 1450 cm^{-1} M^{-1}, which is for the Aβ peptide containing on tyrosine residue (Gill and von Hippel, 1989, Nichols et al., 2002).

2.2.4 Aβ(1-42) Fibril Preparation

Aβ fibrils were prepared as previously described by Stine et al., 2003 (Stine et al., 2003). Briefly, a 1 mg lyophilized Aβ(1-42) aliquot by resuspending it in sterile DMSO at a concentration of 5 mM. After making sure all the Aβ was in solution, the sample was diluted to 100 μM in 10 mM HCl and incubated at 37 °C for 24 hours.

2.3 Microglia Stimulation Experiments with Aβ

Literature has shown that Aβ induces a proinflammatory response via TLRs, especially TLR 2, 4, and 6 (Bamberger et al., 2003, Stewart et al., 2010, Udan et al., 2008, Walter et al., 2007). Due to the involvement of the TLRs in the Aβ-induced proinflammatory response, well known TLR ligands were able to be utilized as positive controls for cellular stimulation (Figure 2.4-2.6). For experiments in WT and $MyD88^{-/-}$ primary microglia with Aβ, the cells were released from the astrocytic layer within the cell culture flask by overnight shaking, as mentioned above. The medium containing the

primary microglia was then centrifuged at 200 x *g* for 10 minutes at room temperature. The cellular pellet was resuspended in fresh complete microglial growth medium containing 10% FBS and GM-CSF, plated in a 96 well sterile culture plate at 5 x 10^5 cells per mL (100μL) and incubated for 24 hours at 37 °C and 5% CO_2 to allow adhesion of the microglia to the plate. After a 24-hour incubation, the cell culture medium was replenished with complete microglia assay medium without FBS and GM-CSF. Freshly SEC-purified monomer and protofibrils were added to the primary microglia at a final concentration of 15 μM. In each experiment, the concentration of monomers and protofibrils varied. Therefore, the volume of Aβ that was added to the microglia to achieve a final concentration of 15 μM was slightly different in each experiment. This also meant that the amount of assay medium that was added to the microglia in each experiment varied slightly too, in order to keep the final Aβ concentration consistent and the final volume at 100 μL. For example, a typical experiment would have an Aβ protofibril concentration of about 51 μM and a monomer concentration of 62 μM. Therefore, in this experiment the protofibril treatment would include 29.5 μL of the protofibril fraction and 70.5 μL assay medium, while the monomer treatment would include 24 μL of the monomer fraction and 76 μL of assay medium. Also, for each of these treatments a negative control would be tested. The negative controls consisted of the addition of equal volumes of buffer as compared to the Aβ protofibril or monomer and the equivalent volume of assay medium. After the addition of Aβ the cells were incubated for a specific amount of time at 37 °C in 5% CO_2. For extracellular cytokine analysis, the cellular medium was collected and stored at -20 °C until analyzed by enzyme-linked immunosorbent assay (ELISA). For intracellular cytokine analysis, the

cells were washed with cold, sterile PBS and lysed with cold RIPA buffer containing 150 mM NaCl, 20 mM Tris, 1 mM EDTA, 1% Triton X-100, 1% deoxycholic acid, and 0.1% sodium dodecyl sulfate (SDS). The medium was then supplemented with 40x protease inhibitor cocktail (Sigma) before use and stored at -20 °C until analyzed by ELISA or Western blot. Aβ experiments also included comparing different concentrations of Aβ and different time points of incubations.

All BV-2 microglia cellular experiments were carried out in the same manner as the primary microglia experiments with respect to the number and volume of cells that were plated and the volume of Aβ and assay medium added to the microglia. BV-2 microglia were removed from the flask for an experiment by treatment with 1 mL of 0.25% trypsin. The trypsin was incubated at 37 °C and 5% CO_2 for 7 minutes, and then 9 mL of BV-2 growth medium was added to stop the trypsin reaction. The microglia were centrifuged at 500 x *g* for 7 minutes at room temperature and resuspended in fresh growth medium and plated in a sterile 96-well culture plate. The microglia were then incubated overnight at 37 °C and 5% CO_2. The next day the culture medium was exchanged for fresh BV-2 assay medium without FBS, and the Aβ was added, as mentioned above. Again the treatment was incubated for certain time points, and then the medium was collected and stored at -20 °C until used for analysis.

Caspase-1 inhibition studies were also performed on the microglia. Prior to cellular treatment with the stimulus, the microglia were treated with z-YVAD-fmk caspase-1 inhibitor (EMD Millipore) for 30 minutes at final concentrations of 0 μM, 5 μM, 10 μM, and 20 μM in 0.05% DMSO. The inhibitor was prepared by dissolving in 100% DMSO and then diluting further in sterile water to obtain 25% DMSO and 0 μM,

250 μM, 500 μM, and 1 mM inhibitor. After 30 minutes treatment with the different concentrations of inhibitor, the microglia were then treated with a final concentration of 15 μM Aβ(1-42) for 6 hours at 37 °C and 5% CO_2. The cellular medium was then collected and analyzed by ELISA for secreted IL-1β.

2.4 Inhibition of LPS-Induced Inflammation

Our lab collaborated with the Demchenko laboratory in hopes of developing a LPS antagonist that could be used to inhibit a systemic inflammatory response from a serious medical condition known as sepsis (Kaeothip et al., 2011). All compounds were prepared by the Demchenko laboratory and given to our lab as a solid powder. Compound 24 (Table 5.2) powder, 5 mg, was dissolved in 100 μL tetrahydrofuran (THF) in the cold room and quickly divided into 15 μL aliquots. The aliquots were then vacuum-centrifuged for one hour to allow evaporation of the THF. The compound was then stored at -80 °C until ready for an experiment.

These inhibition experiments were completed in human THP-1 monocytes which were differentiated into macrophages as described in 2.1.4. The THP-1 macrophages are a respectable cellular system when studying inflammation and they act as a model for peripheral macrophages by their response to bacterial infections (Kaeothip et al., 2011). Briefly, the THP-1 monocytes are centrifuged and resuspended in fresh growth medium at a cell density of 5×10^5 cells mL^{-1}. The monocytes were then plated in a 48-well sterile culture plate and differentiated into adherent macrophages by treatment with PMA. The cells were allowed to differentiate for 24 hours at 37 °C in 5% CO_2. After 24 hours the non-adherent cells were removed and the remaining adherent macrophages were

replenished with 293 μL assay medium containing 2% FBS. Before treating the cells, there were two wells set aside for calculating the percent differentiation. This was accomplished by washing the wells with PBS just before removing the adherent cells with 0.25% trypsin-EDTA and incubation at 37 °C for 7-10 minutes. Growth medium was then added to the wells to the stop trypsin reaction, and the cells were counted under a microscope with a hemocytometer. The remaining wells were pre-incubated with 2 μL of the LPS antagonist (compound 24) at different concentrations for 30 minutes before the treatment of 5μL ultrapure LPS from E. coli K12 (InvivoGen, San Diego, CA) at a final concentration of 10 ng mL^{-1}. The LPS antagonist was diluted in 100% DMSO and then into the microglia medium to make final concentrations of 0.55, 1.0, 3.0, 5.5, 10, 30, 55, and 100 μM, and 0.6% DMSO. DMSO at a final of 0.6% was also used as a control. The macrophages were then incubated at 37 °C in 5% CO_2 for 6 hours and then the cellular medium was collected and stored at -20 °C until ready for TNFα production analysis by ELISA. The ELISA data was then fit to a 3-parameter hyperbolic decay plot, using the equation $y = y_0 + \frac{a\,b}{b + x}$ (Kaeothip et al., 2011).

The actual concentrations of the compound were later calculated by measuring the absorbance of the Fluorenylmethyloxycarbonyl (Fmoc) group located on the compound at 301 nm. The compound was diluted to 180 μM in DMSO, and the absorbance was read at 301 nm after correcting the background absorbance for DMSO by itself. The absorbance was read on the UV-visible spectrophotometer Cary 50 (Agilent Technologies, Santa Clara, CA). After obtaining the absorbance the actual concentration of the compound was calculated using the extinction coefficient of the Fmoc group, 7800 M^{-1} cm^{-1}, which is for the piperidine-fluorenone adducts (Johansson et al., 2003,

Kaeothip et al., 2011). Once the actual concentration was calculated the percentage of inhibitor was then able to be calculated. Therefore the actual concentration of each dilution and final concentration was then obtained using the calculated percentage.

2.5 Cytokine Determination

Secreted and intracellular TNFα, IL-1β, and pro-IL-1β protein, and mRNA cytokines were determined using three different techniques: ELISA, Western blot, and reverse-transcriptase quantitative polymerase chain reaction (RT-qPCR). ELISA has become common technique for the detection and determination of cytokine levels in cultured medium. Both the detection and quantification of cytokines within the cell or secreted medium is important for evaluating inflammation. This method has an advantages of being highly specific and proficient when analyzing a large number of samples (Turner et al., 2004). Another protein analysis method that is widely used is Western blotting, or immunoblotting. This technique is also a sensitive technique for the detection and characterization of proteins. Western blotting uses the advantages of antibody recognition and their specificity towards an antigenic sequence in the protein of interest (Burnette, 1981). The last method that was used for the detection of cytokines was through the detection of mRNA in a technique known as RT-qPCR. This technology has become a mainstream research tool for three reasons: it does not need any post-PCR processing due to it being a homogeneous assay, the assay has a wide dynamic range and therefore allows comparisons between RNAs that are significantly quantitatively different, and because the method is both quantitative as well as qualitative (Bustin et al., 2005).

2.5.1 TNFα ELISA

Measuring the levels of secreted TNFα in the cellular condition medium was determined by ELISA as previously described (Udan et al., 2008). Udan et al., 2008 described the measurements of human TNFα, which was used for the human THP-1 monocytes and macrophages, while the protocol for the measurements in the mouse primary microglia and BV-2 microglia had to be modified slightly. Briefly, 96 well plates were coated overnight at room temperature with 0.4 μg/mL monoclonal anti-mouse TNFα capture antibody (stock aliquots were stored at -80 °C at 200 μg/mL in PBS). The next day the wells were washed with PBS containing 0.05% Tween 20, then blocked with for 1 hour at room temperature with PBS containing 1.0% BSA, 5.0% sucrose and 0.05% sodium azide (NaN_3), and again followed by a wash step. Successive treatments at room temperature with washing in between were completed with samples or standards for 2 hours, biotinylated polyclonal anti-mouse TNFα detection antibody for 2 hours, streptavidin-horseradish peroxidase (HRP) conjugate for 20 minutes, and equal volumes of HRP substrates 3,3',5,5'- tetramethylbenzidine (TMB) and hydrogen peroxide for 25 minutes. The mouse TNFα detection antibody was added to the wells at a final concentration of 0.2 μg/mL (stock aliquots stored at -80 °C at 50 μg/mL in detection antibody diluent) in 20 mM Tris with 150 mM NaCl and 0.1% BSA. The reaction was stopped by the addition of 1% H_2SO_4 solution. The SpectraMax 340 absorbance plate reader (Molecular Devices, Union City, CA) was used to read the optical density of each sample at 450 nm with a reference reading at 630 nm. The concentration of TNFα in the experimental samples was calculated from a TNFα standard curve of 15-2000 pg/mL. When necessary, the samples were diluted to fall within the standard curve. TNFα

concentrations for absorbance values below the lowest 15 pg/mL standard were determined by extrapolating of the standard curve regression line.

2.5.2 IL-1β ELISA

Measuring the levels of intracellular and extracellular IL-1β was determined by ELISA. This ELISA method was similar to TNFα ELISA method, as mentioned above, however, two changes were made. The two changes that had to be made for the mouse IL-1β specific ELISA were the capture and detection antibodies. To briefly explain, 96-well plates were again coated overnight at room temperature, but for this ELISA they were coated with 2.0 μg/mL monoclonal anti-mouse IL-1β capture antibody (stock aliquots were stored at -80 °C at 720 μg/mL in PBS). The detection antibody was also changed according to mouse IL-1β specificity. The biotinylated polyclonal anti-mouse IL-1β detection antibody was added to the wells at a final concentration of 0.5 μg/mL (stock aliquots stored at -80 °C at 180 μg/mL in detection antibody diluent) in 20 mM Tris with 150 mM NaCl and 0.1% BSA. The reaction was again stopped by the addition of 1% H_2SO_4 solution, and the optical density was read by the SpectraMax 340 absorbance plate reader (Molecular Devices, Union City, CA) for each sample at 450 nm with a reference reading at 630 nm. The concentration of IL-1β in the experimental samples was calculated from an IL-1β standard curve of 15-2000 pg/mL. Occasionally the samples were diluted to fall within the standard curve. IL-1β concentrations for absorbance values below the lowest 15 pg/mL standard were determined by extrapolating of the standard curve regression line.

Before being able to use this IL-1β ELISA on samples, the standard curve had to be optimized with the correct concentrations of IL-1β capture and detection antibodies. The recommended concentrations of the antibodies, by R & D Systems, were 4.0 μg/mL for capture antibody and 1.0 μg/mL for detection antibody. In order to optimize the standard curve, lower concentration of one or both IL-1β antibodies were investigated. Standard curves using the recommended concentrations given by R & D Systems were performed, along with 4 μg/mL and 0.5 μg/mL, 2 μg/mL and 1 μg/mL, and 2 μg/mL and 0.5 μg/mL capture and detection antibodies, respectively (Figure 2.1). All of the combinations of antibody concentrations gave similar standard curves with correlation coefficients of .9844 or better and slopes of 0.7914 to 0.8774. Due to the fact that all the standard curves were very similar, the standard curve that was chosen to calculate the sample concentrations was made using 2 μg/mL capture antibody and 0.5 μg/mL detection antibody. This decision was made because less material was used and very similar standard curves were received.

2.5.3 Pro-IL-1β ELISA

Measuring the levels of intracellular pro-IL-1β was determined by ELISA also. This ELISA method was similar to TNFα and IL-1β ELISA method as mentioned above; however, an ELISA kit was used. A kit was purchased from eBioscience and the protocol was followed. The kit contained capture and detection antibodies, standard pro-IL-1β protein, streptavidin-HRP, TMB substrate, assay diluent buffer, and coating buffer. The assay diluent buffer was used as the blocking buffer and to dilute the standard protein, detection antibody, and streptavidin-HRP, while the coating buffer was used to

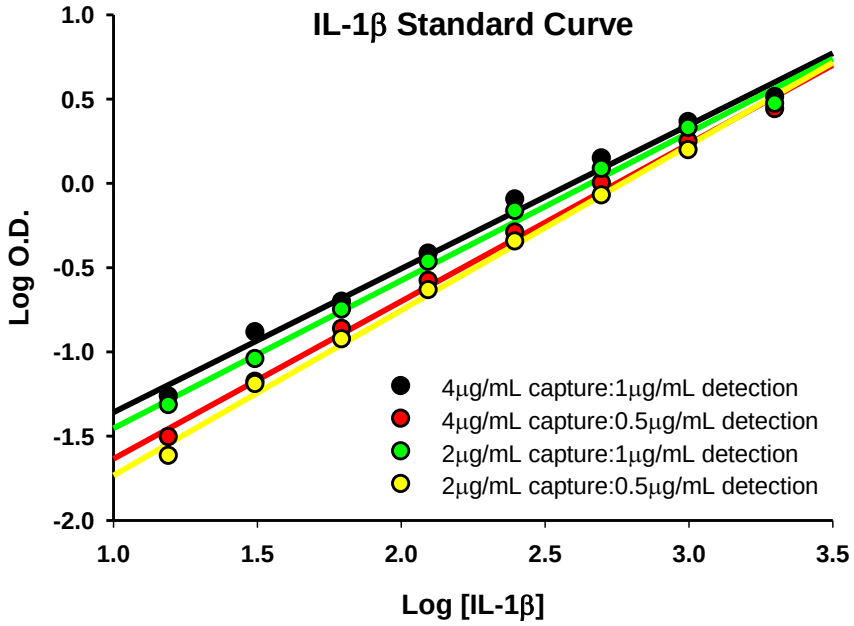

Figure 2.1. IL-1β standard curves. Optimization of the IL-1β ELISA was completed by varying the concentration of one or both of the capture and detection antibodies. The combination of capture and detection antibodies that were used was 4 μg/mL and 1 μg/mL, 4 μg/mL and 0.5 μg/mL, 2 μg/mL and 1 μg/mL, and 2 μg/mL and 0.5 μg/mL, respectively. The later concentrations were chosen as the optimal concentrations for determining the concentrations of the samples.

dilute the capture antibody. The materials that were not provided, such as the 96-well plates, wash buffer and stop solution, were used as mentioned above in the previous ELISAs. As far as the experimental procedure, it was very similar to the ELISA mentioned above. The protocol was followed by coating a 96-well plate with pro-IL-1β capture antibody overnight at 4 °C. The next day the wells were washed with wash buffer and then blocked with assay diluent buffer for 1 hour at room temperature and again followed by a wash step. Successive treatments at room temperature with washing in between were done with samples or standards for 2 hours, pro-IL-1β detection antibody for 2 hours, streptavidin-HRP conjugate for 30 minutes, and TMB substrate for 15 minutes. The reaction was stopped by the addition of the stop solution. The SpectraMax 340 absorbance plate reader (Molecular Devices, Union City, CA) was used to read the optical density of each sample at 450 nm with a reference reading at 630 nm. Again, the concentration of protein, pro-IL-1β, in the experimental samples were calculated from the pro-IL-1β standard curve of 15-2000 pg/mL. When necessary, the samples were diluted to fall within the standard curve. Pro-IL-1β concentrations for absorbance values below the lowest 15 pg/mL standard were determined by extrapolating the standard curve regression line.

The experimental procedure of this kit was verified, before being performed on experimental samples, by the trial of a pro-IL-1β standard curve (Figure 2.2). The specificity of the pro-IL-1β was also observed. This was completed by using both the capture and detection antibodies for recognition of the pro-IL-1β along with the addition of both the pro-IL-1β standard curve and the mature IL-1β standard curve. This confirmed the specificity by observing that the serial dilution of the mature IL-1β protein

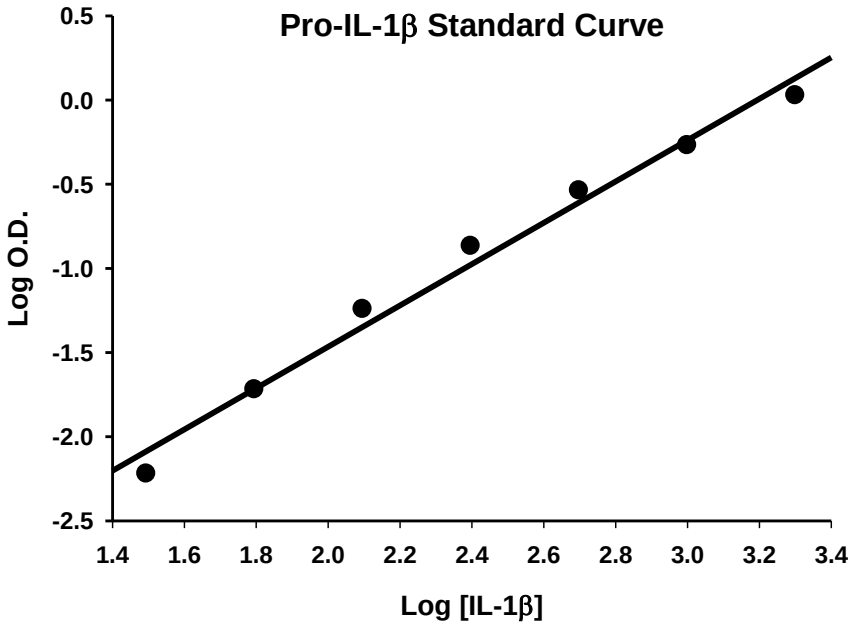

Figure 2.2. Pro-IL-1β standard curve. Optimization of the Pro-IL-1β ELISA was completed by varying all the materials that were supplied in the eBioscience Pro-IL-1β ELISA Kit, together with the materials that were not included and were supplied by our lab. The standard curve provided a correlation coefficient of 0.9852 and a slope of 1.2278.

standards was not detected by the pro-IL-1β-specific antibodies (Figure 2.3).

2.5.4 Western Blotting

Measuring the levels of intracellular Pro-IL-1β, IL-1β and α-tubulin was also determined by Western blotting. The primary microglial cells within a 96-well cell culture plate were lysed using RIPA buffer containing 150 mM NaCl, 20 mM Tris, 1 mM EDTA, 1% Triton X-100, 1% deoxycholic Acid, 0.1% SDS, and supplemented with 40x protease inhibitor cocktail (Sigma) before use. Similarly treated wells were added together to concentrate the sample and immediately placed on ice. Once the lysates were collected, they were centrifuged at 9,000 x *g* at 4 °C to remove cell debris. The samples were then diluted 2 fold with Laemmli sample buffer (Bio-Rad) containing 5% β-mercaptoethanol (Sigma), denatured at 95 °C for 5 minutes, and run on a 15% Tris-HCl Ready Gel (Bio-Rad). The gels were run in running buffer containing 25 mM tris, 192 mM glycine, 0.1% SDS at pH 7.8 using a Mini Protean 3 Cell (Bio-Rad) under 120V current at room temperature. The amount of time necessary to run the gel was between 1.5 and 2 hours or until the tracking dye was just above the bottom of the gel. The gel was then soaked in transfer buffer containing 0.025 M tris base, 0.192 M glycine, and 10% methanol at pH 8.3 for 15 minutes. The protein within the gel was transferred to polyvinylidene difluoride (PVDF) membrane (Milipore) in cold transfer buffer using a Tank Electroblotting system VEP-2 (Owl Separation systems). The PVDF membrane was prepared by being soaked in methanol for 15 seconds, water for 2 minutes and transfer buffer until ready for the actual transfer. The gel and membrane were arranged for the transfer by placing the black side of the transfer cassette down flat followed by a

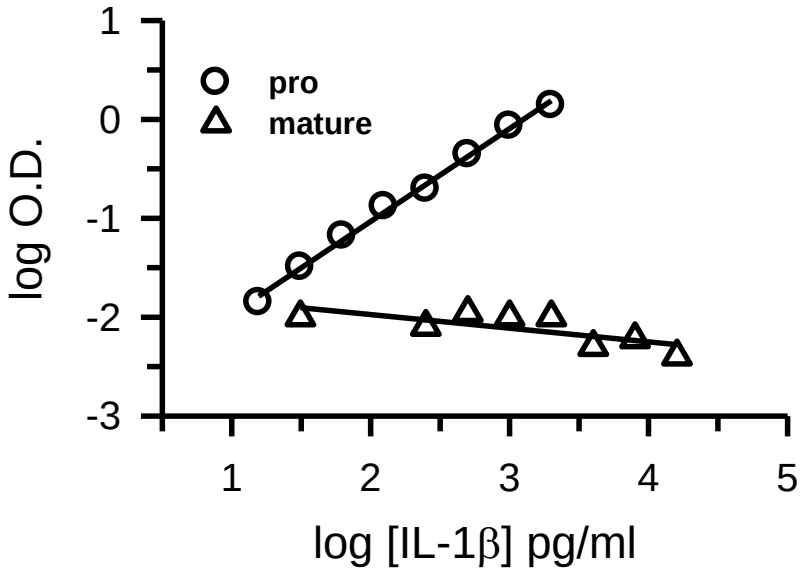

Figure 2.3. Pro-IL-1β standard curve specificity. Serial dilutions of pro-IL-1β (16-2,000 pg/ml, circles) and mature IL-1β (31-16,000 pg/ml, triangles) were prepared and analyzed using a pro-IL-1β ELISA (eBioscience).

support pad, filter paper, previously run SDS-PAGE gel, PVDF membrane, another filter paper, and support pad. The support pads and filter papers were also previously soaked in transfer buffer. The transfer system was placed in the cold room at 4 °C on a stir plate with a small magnetic stirrer. A current of 0.4 mA was applied to the system for 2 hours. After the proteins were transferred to the membrane, the membrane was blocked for 1 hour at room temperature with 5% nonfat dry milk and 0.1% Tween 20 in PBS with slow rotation and probed with 500x 3ZD monoclonal antibody (National Cancer Institute) or 200x IL-1β (H-153) (Santa Cruz Biotechnology) for both pro- and mature IL-1β in PBS with 1.0% milk and 0.1% Tween 20 for overnight incubation at 4 °C with slow rotation. The membranes were then washed in PBS containing 0.2% Tween and subjected to a secondary antibody, goat anti-mouse immunoglobulin (IgG)-HRP (R & D systems) and goat anti-rabbit IgG-HRP (R & D systems), respectively, which was diluted 1000x in PBS containing 1.0% milk and 0.1% Tween 20 for 1 hour at room temperature with slow rotation. The membrane was again washed and placed in equal amounts of enhanced chemiluminescence (ECL) Western Blotting Substrate Detection reagent 1 and 2 (Pierce) for 1 minute at room temperature with vigorous rotation. Lastly, the visual chemiluminescence of the blot was developed onto X-ray film (Kodak) by exposure of the membrane to the film for 1 minute in a metal film cassette. The film was then subjected to Kodak GBX developer for 15 seconds and fixer solution for 5 seconds. After development, the film was washed with water and hung to dry. To be sure that the same amount of protein was loaded into each lane of the gel, a loading control was used. To visualize the loading control, α-tubulin, the membrane was washed, after previous development, with PBS containing 0.2% Tween 3 times for 5 minutes each at room

temperature with slow rotation and stripped of the previous antibodies by 1x Restore western blot stripping buffer (Thermo Scientific) for 15 minutes at room temperature with slow rotation. The membrane was then blocked with 5% nonfat dry milk and 0.1% Tween 20 in PBS for 1 hour with slow rotation and re-probed over night at 4 °C with 200x α-tubulin (TU-02) (Santa Cruz Biotechnology) in 1.0% milk and 0.1% Tween 20 with slow rotation. The next day the membrane was again washed with PBS containing 0.2% Tween 3 times for 5 minutes each at room temperature with slow rotation and then the addition of 1000x goat anti-mouse IgG-HRP for 1 hour at room temperature in 1.0% milk and 0.1% Tween 20 with slow rotation. After the secondary antibody the membrane is again ready for development.

2.5.5 mRNA Quantitative Analysis

2.5.5.1 RNA Extraction

Measuring the levels of TNFα, IL-1β and β-Actin was also determined by RT-qPCR. First the total RNA was obtained using a GeneJET RNA purification kit (Fermentas). The procedure was completed by following the manufacturer's guidelines. Following treatment of primary microglial cells within a 96-well cell culture plate, the microglia were lysed using lysis buffer (Fermentas) supplemented with β-mercaptoethanol and 96-100% ethanol. The total contents were then collected and transferred to a spin column (Fermentas). The samples from similarly treated wells were added into the same spin column, up to 5 samples, to concentrate the amount of mRNA in each sample. Each sample was washed once with Buffer 1 (Fermentas) and twice with

Buffer 2 (Fermentas) with centrifugation for 1 minute at 12,000 x *g* between each wash. Lastly, nuclease free water was added to each spin column to elute the total RNA, centrifuged for 1 minute at 12,000 x *g*, and the flow through was collected. It was observed that if the elution was completed during two spin cycles that the mRNA elution from the column was more efficient. The total RNA concentration was then determined using the Epoch Nano-Drop (BioTek Instruments, Winooski, VT) absorbance at 260/280 nm ratio and the highest amount of total RNA available up to 1 µg was concentrated. The purified RNA was now ready for further downstream applications or can be stored at -20 °C for short time storage or -70 °C for longer storage.

2.5.5.2 Genomic DNA Removal

After determining the total RNA concentration and determining the total volume needed to obtain the same concentration for each sample, the volume of each sample was then reduced down to further concentrate the samples by vacuum-centrifugation. The genomic DNA was removed using a DNase I kit (Fermentas) and the procedure was followed according to the manufacture's protocol. Treatment consisted of the addition of 10x reaction buffer with $MgCl_2$ (Fermentas), DNase I (Fermentas), and 1 unit/µL RNase inhibitor (Fermentas), which was in addition to the kit but recommended by the DNase I manufacture, to each sample and an incubation at 37 ˚C for 30 minutes. The reaction was then stopped by the addition of 50 mM EDTA (Fermentas), incubation at 65 ˚C for 10 minutes, and placement on ice and ready for further downstream applications.

2.5.5.3 cDNA Synthesis

The synthesis of cDNA was also done according to the manufacturer's guidelines (RevertAid Kit, Fermentas). While the samples carried over from the genomic DNA removal step were on ice an oligo (dT)18 primer (Fermentas) was added. The samples were then mixed gently, centrifuged briefly, incubated at 65 ˚C for 5 minutes to open up any secondary structures and placed back on ice. The next step involved the addition of 5x reaction buffer (Fermentas), RiboLock RNase inhibitor (1 unit/μL) (Fermentas), and RevertAid M-MuLV Reverse Transcriptase (10 units/μL) (Fermentas) to each sample. The samples were then mixed, centrifuged, and incubated for 60 minutes at 42 ˚C. Lastly, the reaction was terminated by heating the samples to 70 ˚C for 5 minutes and then the samples were stored at -20 ˚C for one week or at -80 °C until ready for PCR applications.

2.5.5.4 RT-qPCR

Selected sequences of specific cytokines were amplified using RT-qPCR (C100 Thermocycler, BioRad, Hercules, CA). Each sample was prepared by adding Maxima SYBR Green qPCR Master Mix (Fermentas), forward (sense) primer, reverse (antisense) primer (Table 2.1), and template cDNA. RT-qPCR was run using Bio-Rad CFX Manager software. A three-step cycling protocol was set at an initial denaturation temperature of 95 ˚C for 3 minutes, 40 cycles of denaturation at 95 ˚C for 10 seconds, annealing at 55 ˚C for 10 seconds, and extension at 72 ˚C for 30 seconds. mRNA levels were then calculated and reported as relative quantities (RQ). The RQ was determined by the equation $RQ=E^{(Cq,\ control\ -\ Cq,\ stimulated)}$, where Cq is the quantification cycle value

Table 2.2. RT-qPCR primers.

Primer	Forward (5' to 3')	Reverse (5' to 3')
TNFα	**TTCCCAAATGGCCTCCCTCTCATC**	**TCCTCCACTTGGTGGTTTGCTAC**
IL-1β	**CCTGTGTAATGAAAGACGGCACAC**	**ATTGATTGGGATCCACACTCTCC**
B-Actin	**ACAGCTTCTTTGCAGCTCCTTCG**	**ATATCGTCATCCATGGCGAACTGG**

Forward and reverse primers for cytokines TNFα and IL-1β and for the control mRNA, β-Actin.

obtained by the fluorescence amplification plot and E is the efficiency with a value of 2. In numerous experiments β-actin was used as an internal control and did not vary significantly between samples regardless of microglia stimulation state.

2.6 Characterization of MyD88$^{-/-}$ Primary Murine Microglia

Primary microglia are known to express an assortment of TLRs (Cameron and Landreth, 2010). The WT microglia were characterized in Geeta Paranjape's dissertation. However, the characterization of the MyD88$^{-/-}$ primary microglia needed to be completed and compared to the WT microglia. In order to estimate and compare the proinflammatory response of the MyD88$^{-/-}$ microglia to the WT microglia various TLR ligands were used in the presence of both types of cells and analyzed by ELISA to quantify TNFα and IL-1β secretion. The TLR ligand experiments were carried out in dose-dependent manner for the known TLR ligands: LPS (TLR4 ligand), Pam_3CSK_4 (TLR 1 and 2 ligand) and FSL-1 (TLR 2 and 6 ligand). However, TLR ligands are not expected to induce IL-1β secretion unless a second stimulus is provided which activates the NLRP3 inflammasome. LPS and Pam_3CSK_4 were aliquotted at 600 μg/mL and FSL-1 at 60 μg/mL, stored at -20 °C and were further diluted to make the correct final concentrations for addition to the cells. Both WT and MyD88$^{-/-}$ primary microglia were harvested as mentioned above. The microglia were plated in fresh primary microglial growth medium at a volume of 100 μL and incubated at 37 °C and 5% CO_2 for 24 hours. The following day the growth medium was replaced with medium devoid of GM-CSF and FBS, and the ligands were added to the cells to make final concentrations of 3, 10, 30, and 100 ng/mL. After 6 hours of incubation at 37 °C and 5% CO_2, the cellular

medium was collected and analyzed by TNFα and IL-1β ELISAs, as described in Sections 2.2.1 and 2.2.2.

The TLR4 ligand, LPS, was able to produce a substantial TNFα response in the WT primary microglia with concentration dependence at the lower concentrations and plateauing at the higher concentrations. However, when knocking out both alleles of MyD88 in the MyD88$^{-/-}$ microglia the response was significantly reduced (Figure 2.4A). When measuring the cytokine IL-1β there was little to no amount of secreted IL-1β in both WT and the MyD88$^{-/-}$ microglia (Figure 2.4B). This response was due to the fact that the LPS was not able to activate the NLRP3 inflammasome which is needed in the production of mature IL-1β. Similar responses were seen during activation of the WT and MyD88$^{-/-}$ microglia with the TLR1 and -2 and TLR2 and -6 agonist, Pam_3CSK_4 (Figure 2.5A,B) and FSL-1 (Figure 2.6A,B), respectively. The only difference was in the TNFα concentration dependence in the WT microglia, where the Pam_3CSK_4 showed concentration dependence and the FSL-1 did not. The little to no IL-1β secretion by the Pam_3CSK_4 and FSL-1 was also due to not being able to activate the NLRP3 inflammasome.

2.7 Aβ Concentration Determinations

2.7.1 BCA Assay

Bicinchoninic acid (BCA), sodium salt, is a stable, water-soluble compound that complexes with cuprous ion (Cu^{1+}) in an alkaline environment and forms an intense purple color. The color produced increases in a proportional fashion with a broad range

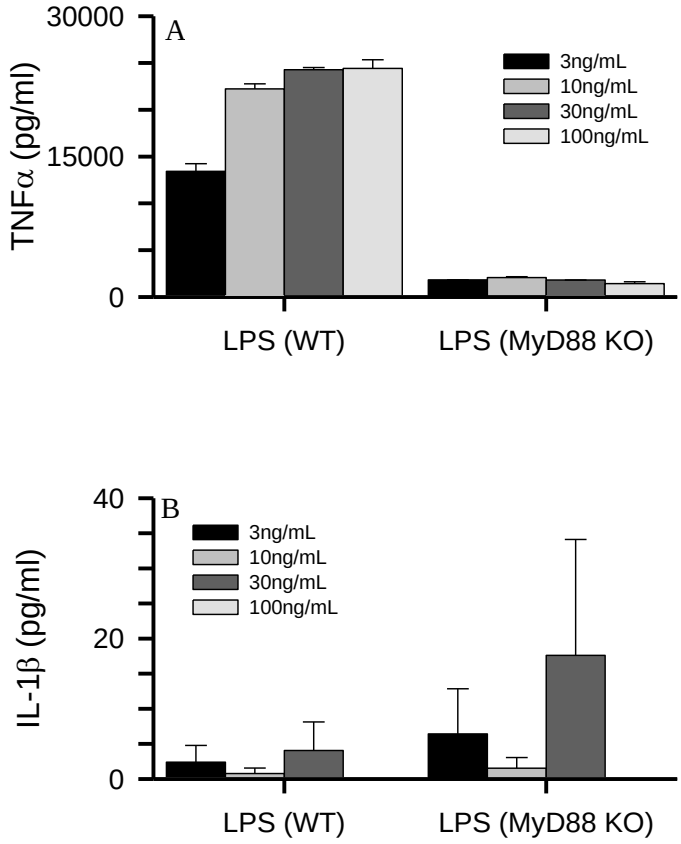

Figure 2.4. Concentration-dependence of LPS-induced TNFα and IL-1β response in primary WT and MyD88$^{-/-}$ microglia. WT and MyD88$^{-/-}$ microglia were plated for 24 hours in growth medium with FBS and GM-CSF and the next day replaced with assay medium without FBS and GM-CSF, treated with LPS at final concentrations of 3, 10, 30, and 100 ng/mL for 6 hours. The cellular medium was analyzed by ELISA for quantifying TNFα and IL-1β.

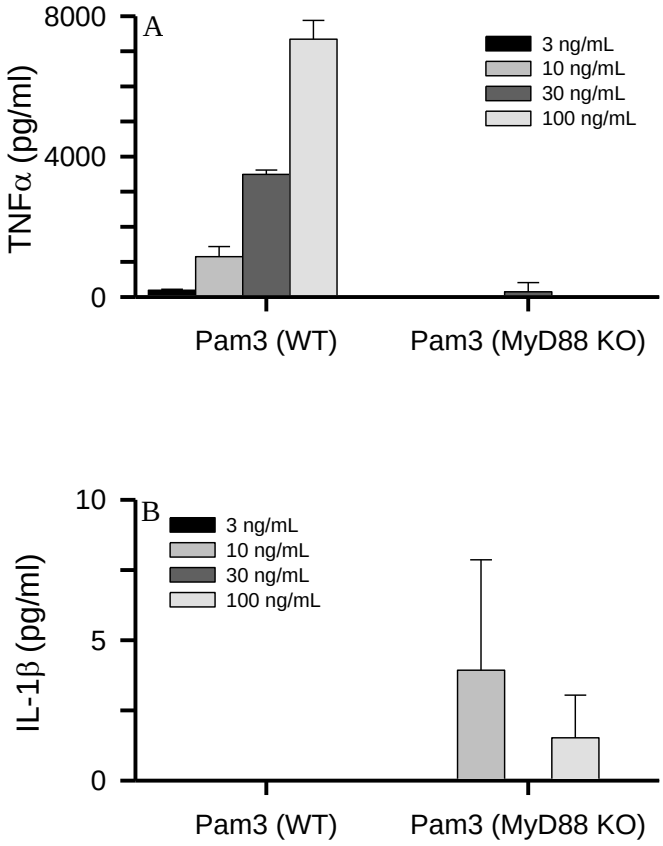

Figure 2.5. Concentration-dependence of Pam_3CSK_4-induced TNFα and IL-1β response in primary WT and MyD88$^{-/-}$ microglia. WT and MyD88$^{-/-}$ microglia were plated for 24 hours in growth medium with FBS and GM-CSF and the next day replaced with assay medium without FBS and GM-CSF, treated with Pam_3CSK_4 at final concentrations of 3, 10, 30, and 100 ng/mL for 6 hours. The cellular medium was analyzed by ELISA for quantifying TNFα and IL-1β.

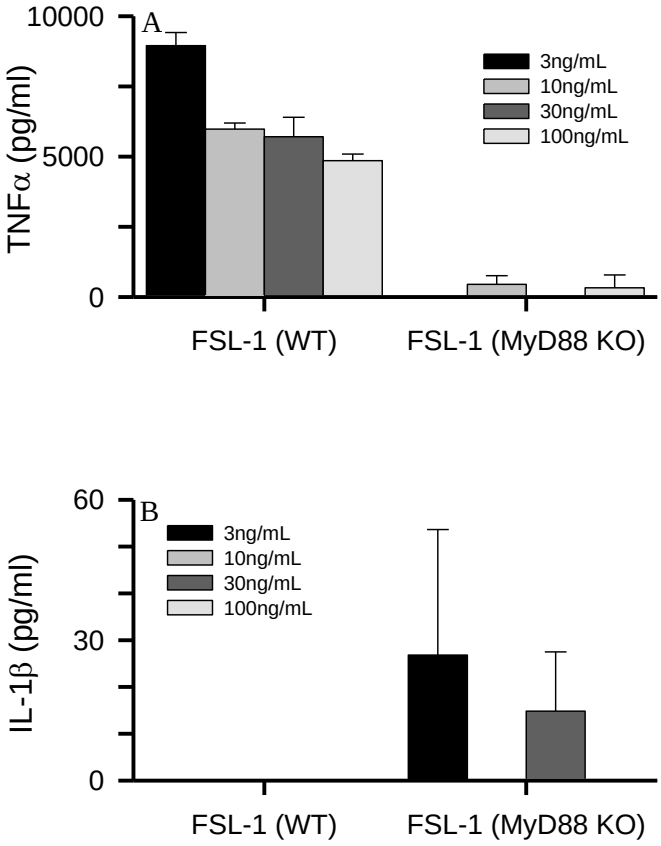

Figure 2.6. Concentration-dependence of FSL-1-induced TNFα and IL-1β response in primary WT and MyD88$^{-/-}$ microglia. WT and MyD88$^{-/-}$ microglia were plated for 24 hours in growth medium with FBS and GM-CSF and the next day replaced with assay medium without FBS and GM-CSF, treated with FSL-1 at final concentrations of 3, 10, 30, and 100 ng/mL for 6 hours. The cellular medium was analyzed by ELISA for quantifying TNFα and IL-1β.

of increasing concentrations. The previous method used to measure protein concentration, known as the Lowry method, used Folin-Ciocalteu reagent to enhance the sensitivity of the Biuret reaction, while this assay uses the bicinchoninic Acid to enhance the sensitivity of the Biuret reaction. The Biuret reaction results in the formation of a light blue complex by the chelation of copper with protein in an alkaline environment. The intense purple color is then formed when two bicinchoninic acid molecules reacts with one reduced cuprous cation. The BCA assay is known to have a greater tolerance toward commonly encountered interferences, such as nonionic detergents and simple buffer salts and can be strongly influenced by amino acids such as cysteine, tyrosine, and tryptophan. The stability of this method and its resulting chromophore allows for a more simplified technique and one-step analysis (Smith et al., 1985).

In addition to in-line UV absorbance, the BCA assay was also utilized to measure Aβ concentrations. A standard curve was constructed using SEC-purified Aβ(1-40) monomer diluted in aCSF typically in the concentration range of 5 μM to 80 μM. Aβ(1-40) standards or Aβ(1-42) samples (10 μL) were added to 100 μL of 50:1 mixture of BCA Reagent A to Reagent B (Thermo Fisher Scientific) and mixed thoroughly in individual wells of a 96-well plate. Reagent A contains sodium carbonate, sodium bicarbonate, bicinchoninic Acid detection reagent and sodium tartrate in 0.1N sodium hydroxide, while Reagent B contains an oxidized copper reagent. The plate was then covered and incubated for 30 minutes at 37 °C followed by cooling for an additional 15 minutes. Absorbance was then determined for each well at a wavelength of 562 nm.

2.7.2 Bradford Assay

The Bradford assay is also a method for determining protein concentration and involves the binding of Coomassie Brilliant Blue G-250 to protein. The binding causes a shift in the absorption maximum of the dye from 465 to 595 nm. This method has shown to be very reproducible, rapid and stable. There have been little to no interferences reported other than a small color change in the presence of strong alkaline buffers or detergents such as sodium dodecyl sulfate, Triton X-100, and commercial glassware detergents, however, the assay is reliable if the correct buffer controls are used (Bradford, 1976).

Aβ(1-40) standard curves were also evaluated using the Bradford method (Bradford, 1976) to determine Aβ protein concentrations. Briefly, 10 μL from Aβ(1-40) standard solutions ranging from 20-60 μM were placed on the bottom of a polystyrene semi-micro disposal cuvette (Perfector Scientific), 1.5 ml 1x Bradford reagent (BioRad) was then added, the cuvette was then inverted several times and incubated for 10 minutes at room temperature. After the incubation, the absorbance was determined at 595 nm.

2.7.3 Aβ C-terminal Selective ELISA

Even though the ratios formed, as described in the methods above 2.4, obtained a specific amount of Aβ(1-42) and a specific amount of Aβ(1-40), it was unclear how much of each peptide populated the SEC-isolated protofibrils and monomers. Therefore our lab established an Aβ C-terminal selective ELISA in an attempt to observe how much Aβ(1-42) and Aβ(1-40) was incorporated into each SEC-isolated species.

The Aβ antibodies used were received as a generous gift from Mayo Clinic. C-terminal selective antibodies Ab2.1.3 (Aβ42 specific) and Ab13.1.1 (Aβ40 specific) were employed as capture antibodies, while the detection antibody used, Ab5, recognized both Aβ peptides (Chakrabarty et al., 2010). For this purpose Ab5 was conjugated to HRP, based on the method from Wisdom et al., 2005 (Wisdom, 2005), and performed by Ben Colvin.

Measuring the levels of Aβ(1-42) and Aβ(1-40) in each SEC-isolated Aβ(1-42):Aβ(1-40) protofibril and monomer fraction was determined by ELISA. While this protocol was based on the protocols used for the measuring cellular cytokines as mentioned above and in our laboratories previous publications (Paranjape et al., 2013), this protocol had to be modified slightly. Briefly, a 96-well plate was coated overnight at room temperature with 5.0 μg/mL Ab2.1.3 (Aβ42 specific) or Ab13.1.1 (Aβ40 specific) capture antibodies (stock aliquots were stored at -20 °C at 1.6 mg/mL determined by Ben Colvin). The next day the wells were washed with PBS containing 0.05% Tween 20, then blocked with for 1 hour at room temperature with PBS containing 1.0% BSA, 5.0% sucrose and 0.05% NaN_3 and again followed by a wash step. Successive treatments at room temperature with washing in between were done with samples or standards for 2 hours, HRP-Ab5 detection antibody for 2 hours, and equal volumes of HRP substrates TMB and hydrogen peroxide for 25 minutes. The Ab5 detection antibody-HRP conjugate was added to the wells at a final concentration of 0.12 μg/mL, determined by Ben Colvin (stock aliquots stored at -20 °C at concentrations determined by SEC purification: SEC fraction 13 is 0.0572 mg/mL, SEC fraction 14 is 0.2467 mg/mL and fraction 15 is 0.1461 mg/mL) in 20 mM Tris with 150 mM NaCl and 0.1% BSA. The

reaction was stopped by the addition of 1% H_2SO_4 solution. The SpectraMax 340 absorbance plate reader (Molecular Devices, Union City, CA) was used to read the optical density of each sample at 450 nm with a reference reading at 630 nm. The concentrations of Aβ(1-42) and Aβ(1-40) were calculated from a SEC-isolated Aβ(1-42) or Aβ(1-40) monomeric standard curve of 1000-10000 pg/mL. The standards were produced using the Aβ monomer preparation mentioned in the methods 2.4.2 and then stored at 4 °C. The samples were diluted to fall within the standard curve.

When optimizing this method it was observed that the Aβ(1-42) standard curve was gradually producing a smaller absorbance range over the same Aβ concentrations. Due to the known fact that Aβ(1-42) aggregates faster than Aβ(1-40) the reduction in absorbance was hypothesized to be caused by aggregation. To confirm this hypothesis SEC-freshly purified Aβ(1-42) monomer was diluted into three different concentrations, 10, 1.0 and 0.1 μM, because the rate of aggregation is also known to be slowed at lower Aβ concentrations. Therefore if the different concentrations were used to perform multiple standard curves over time, it could then be observed whether aggregation plays a role in the reduced absorbance readings. The hypothesis was confirmed by measuring the 10 μM Aβ(1-42) monomer over a 32 day time period. It was observed that as the incubation time increased the absorbance range decreased (Figure 2.7A), however the observed slopes varied only minimally. Once it became obvious that the absorbance was decreasing for the standard curve from the 10 μM stock, the lower concentrations were tested (1 and 0.1 μM) after 17 days of incubation at 4 °C (Figure 2.7B). It was detected that the 1.0 μM stock Aβ(1-42) monomer showed a greater absorbance range indicating that aggregation does affect the standard curve absorbance and possibly plays a role in

detection by the Aβ antibodies. It was also observed that the lowest stock concentration (0.1 μM) showed little to no absorbance; these low absorbance readings were attributed to the possible loss of a small amount of Aβ during incubation, due to the stickiness of the Aβ and its adherence to the microcentrifuge tube. Another way to conclude that aggregation affects the absorbance reading during the Aβ ELISA is to dilute the aggregated Aβ in a denaturant to break up some of the aggregated species. This method was performed by the use of GuHCl. To test this the standard curve of the 10 μM Aβ(1-42) monomer stock after 32 days of incubation was compared to the same stock monomer but diluted first in GuHCl (Figure 2.7C). The GuHCl also showed that aggregation does play a role in the reduction of the standard curve optical densities. Taking into account the data presented here (Figure 2.7) the standards for both the Aβ(1-42) and Aβ(1-40) ELISA along with the unknown ratio samples were first diluted into GuHCl to reduce the amount of aggregation and increase the absorbance and possibly the efficiency of the Aβ antibodies. Ben Colvin also examined the selectivity of the antibodies by performing an Aβ(1-42) standard curve with the Aβ(x-40) selective antibody and an Aβ(1-40) standard curve with the Aβ(x-42) selective antibody. The absence of an increase in absorbance confirmed that both antibodies were selective for their own antigen (unpublished).

2.8 Viability and Proliferation of cells After Treatment

2.8.1 XTT Cell Viability Assay

Viability of the BV-2 microglia and THP-1 macrophages were monitored using the XTT [2,3-bis(2-methoxy-4-nitro-5-sulfophenyl)-2H-tetrazolium-5-carboxanilide]

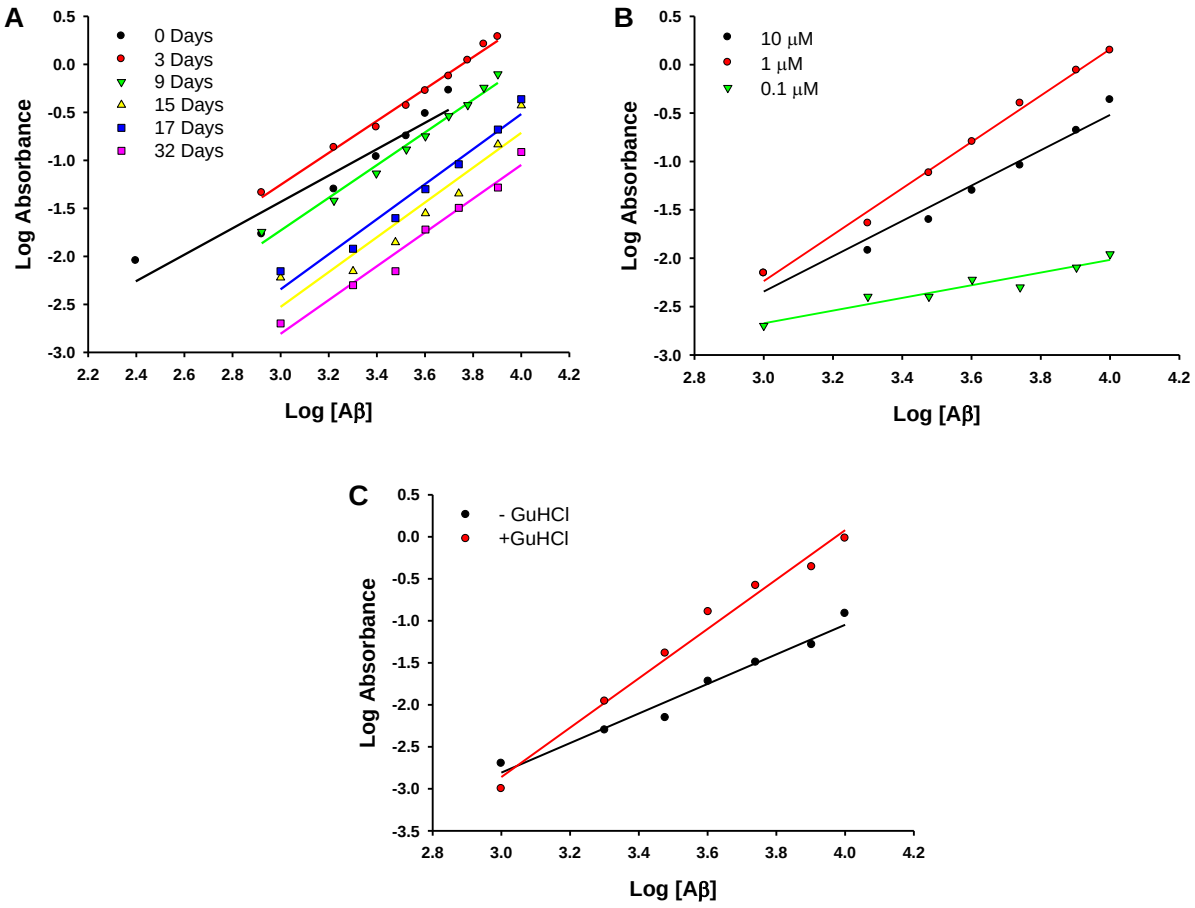

Figure 2.7. Optimization of Aβ C-terminal selective ELISA. Panel A. A log-log plot of the 10 µM SEC-isolated Aβ(1-42) monomer standard curve over time. The Aβ(1-42) monomer was incubated at 4 °C over a 32 day period and a standard curve was performed on various separate days. Panel B. A log-log plot of standard curves from SEC-isolated Aβ(1-42) monomer that have been incubated at 4 °C for 17 days at 10, 1, and 0.1 µM. Panel C. A log-log standard curve plot of SEC-isolated Aβ(1-42) monomer that has been incubated for 32 days at 4 °C at 10 µM. One standard curve the Aβ(1-42) was diluted normally in standard diluent and the second standard curve the Aβ(1-42) was first diluted into GuHCl and then further diluted into standard diluent.

assay. XTT is a tetrazolium dye that can be monitored by the absorbance of its reduced form. XTT can be reduced by the mitochondrial electron transport chain in the presence of phenazine methosulfate (PMS, Acros, Morris Plains, NJ), which forms a water-soluble formazan product, and is an indicator of cellular health (Scudiero et al., 1988).

XTT arrived as a yellow colored solid, which was divided into ~15 mg aliquots and stored at -20 °C in 15 mL conical tubes. For an experiment, the solid in one aliquot was resuspended under aseptic conditions in sterile RPMI-1640 medium without phenol red at a concentration of 1 mg/mL. The 1 mg/mL XTT solution was then aliquotted into 0.5 mL aliquots and stored at -20 °C. The PMS was also dissolved in aseptic conditions at a concentration of 5 mM in sterile water, and aliquots were stored at -20 °C. In both BV-2 microglia and THP-1 macrophage experiments, the cells that were exposed to treatment of any kind for 6 hours were further incubated with 0.33 mg/mL XTT diluted in RPMI-1640 without phenol red and 8.3 μM PMS for 2 hours at 37 °C and 5% CO_2. The viability of the cells was measured by the extent of XTT reduction. The absorbance of the reduced form of XTT was measured at 467 nm.

The viability of an Aβ solution can also be measured by XTT in a method known as cell-free XTT assay. This technique was completed to make sure there was no bacterial contamination within the Aβ solution. The cell free XTT was done in a similar manner as the above cellular XTT, except the Aβ sample was incubated with a solution containing 0.33 mg/mL XTT and 8.3 μM PMS without any cells at a final Aβ concentration of 15 μM for 6 hours. After the incubation period, the reduced form of XTT was again measured by absorbance at 467 nm.

2.8.2 LDH Release Assay

An alternative to XTT of cell viability is the lactate dehydrogenase (LDH) release assay. This assay was used with the BV-2 microglia to verify the XTT analysis. This technique measures the amount of LDH released into the cellular medium to assess the viability of the cells, because the release of LDH is an indicator of leakage from the microglia due to disruption or damage to the cellular membrane (Tan et al., 2014). This assay involves LDH-mediated reduction of nicotinamide adenine dinucleotide (NAD^+), and is coupled to XTT reduction to enhance the assay's sensitivity. This procedure was modified slightly from Korzeniewski et al., 1983 (Korzeniewski and Callewaert, 1983).

Following stimulation of the BV-2 microglia with LPS for 24 hours, the cellular medium was removed and centrifuged to remove any of the detached microglia. The sample medium (25 μL) was added to a 2:1 ratio of LDH reaction cocktail containing 150 mM CAPS buffer at pH 10.0 in water, 6 mM NAD^+ in water, and 150 mM lactate in water (all from Sigma Aldrich, St. Louis, MO), to XTT/PMS, containing 0.33 mg mL^{-1} XTT and 8.3 μM PMS. The amount of LDH release was measured by the change in absorbance of reduced XTT at 467 nm over a linear time course of 5 minutes. These samples were also compared to a positive control, where the BV-2 microglia were treated with saponin, a known cellular toxin. Saponin causes significant LDH release from microglia by removing cholesterol and disrupting the membrane integrity (Tan et al., 2014).

2.8.3 Cell Adhesion and Growth

Cell adhesion of adherent cells and cell proliferation are also ways to observe the viability of a cellular culture. The cell adhesion and proliferation observations were conducted in BV-2 microglia. The microglia were removed from the culture flask, centrifuged, and resuspended in fresh growth medium as mentioned above in 2.5. However, in these experiments, 300 μL of the microglia were plated at 5 x 10^5 cells mL^{-1} and incubated overnight at 37 °C and 5% CO_2. The next day the microglia were replenished with fresh growth medium and treated with LPS for 24 hours or longer. After 24 hours the medium was removed and the cells in the medium were counted using a Cellometer Auto T4 Plus SK-150 cell counter (Nexcelom Bioscience LLC, Lawrence, MA, USA). The number of counted cells in the medium was then divided by the total number of cells plated to determine the percentage of detached cells. The magnitude of microglia proliferation was determined by directly counting the number of adherent microglia over time (24, 48, and 72 hours). After each incubation time point, the cellular medium was removed and the adherent cells were detached the same way as they were detached from the culture flask, 0.25% trypsin. The number of adherent cells was then counted using the same Cellometer, as mentioned above, along with the same calculation to calculate the percent of attached cells.

2.9 ThT Measurements

Thioflavin-T Fluorescence (ThT) is a benzothiazole dye, which shows increased fluorescence when bound to amyloid fibrils (Khurana et al., 2005) specifically binding to the β-sheet secondary structure of aggregated Aβ. This dye has been extensively used

for characterization of amyloid fibril presence and their rate of formation (Krebs et al., 2005). Freshly purified Aβ(1-42), Aβ(1-40), and ratios of Aβ(1-42)/Aβ(1-40) monomer and protofibrils solutions were monitored by ThT-fluorescence. For the experiment, the Aβ solution was diluted to a final concentration of 5 μM in a final ThT concentration of 5 μM prepared in 50 mM Tris-HCl buffer (pH 8.0) to make a total volume of 100 μL. Using a Cary Eclipse Fluorescence spectrophotometer, the ThT fluorescence emission scans (460-520 nm) were carried out at an excitation wavelength of 450 nm. The actual ThT fluorescence values were generated by integrating the emission scan between 470-500 nm. The vehicle buffer control, aCSF, showed little to no ThT fluorescence when used as a negative control in the absence of Aβ.

2.10 TEM

Transmission Electron Microscopy (TEM) was used to examine SEC-purified Aβ(1-42), Aβ(1-40) and ratios of Aβ(1-42):Aβ(1-40) protofibrils and monomer after aggregation. The samples were diluted to 20 μM in water and 10 μL were applied to a 200-mesh formvar-coated copper grid, the red side of the grid (Ted Pella Inc.). The samples were allowed to incubate at room temperature for 10 minutes and then the excess Aβ solution was removed by a Kimwipe. The grids were then washed three times by being placed Aβ side down on a droplet of water. Heavy metal staining was performed next by a 5 minute incubation of the grid, Aβ side down, on a droplet of 2 % uranyl acetate (Electron Microscopy Sciences, Hatfield, PA). Lastly, the excess stain was removed by a Kimwipe and the grid was allowed to air dry under a petri dish lid to avoid

accumulation of dust particles. The affixed samples were visualized with a Philips EM 430 TEM at 300 kEv (courtesy of David C. Osborn).

2.11 DLS

Dynamic Light Scattering (DLS) was the technique used to assess the R_H measurements of Aβ(1-42):Aβ(1-40) ratios. The measurements were made at room temperature with a DynaPro Titan instrument (Wyatt Technology, Santa Barbara, CA). For each measurement, 30 μL of each sample was placed directly into a quartz cuvette and light scattering intensity was collected at a 90° angle using a 10-second acquisition time. Auto-corrected light intensity data was used to calculate particle diffusion coefficients and converted to R_H with the use of the Stokes-Einstein equation. Dynamics software (version 6.7.1) was used to generate average R_H values and to show histograms of percent intensity vs. R_H by data regulation and intensity-weighted mean R_H values. All DLS measurements were made and analyzed by Dr. Michael R. Nichols.

CHAPTER 3

Aβ(1-42) PROTOFIBIRLS REGULATE IL-1β LEVELS AT MULTIPLE SITES IN MICROGLIA

3.1 Introduction

AD is the most prevalent form of late-life dementia amidst the different neurodegenerative disorders and has been defined by the presence of two pathological hallmarks, NFTs and senile (amyloid) plaques. The NFTs are intracellular lesions of insoluble, highly stable filamentous aggregates of the microtubule associated protein, tau, whereas the senile plaques are extracellular lesions of insoluble, amyloid fibrils that are polymers of the Aβ protein (Dickson, 2004, Selkoe, 2001). Recent data has shown that the toxicity of Aβ actually lies within the soluble oligomeric intermediates found in the AD brain and CSF, rather than the insoluble fibrils (Haass and Selkoe, 2007, Kayed et al., 2003). These soluble oligomeric forms of Aβ have shown to contribute to the onset of AD and induce neuronal and/or synaptic dysfunction (Haass and Selkoe, 2007, Lee et al., 2006).

There has been an array of different aggregate morphologies of Aβ found within the AD brain (Selkoe, 2004). The core of the Aβ plaques is primarily composed of the 42-amino acid Aβ fragment, Aβ(1-42). However, Aβ(1-40) has also been found colocalized with the Aβ(1-42) (Selkoe, 2001). *In vitro*, the Aβ monomer undergoes the self-assembly by non-covalent interactions to form polydisperse mixtures of soluble

oligomers (Kayed et al., 2003) and protofibrils (Harper et al., 1997, Walsh et al., 1997). These soluble aggregates go through a conformational transition from predominately random coil to increasing amounts of β-sheet structure and ultimately produce insoluble fibrils (Harper et al., 1999, Walsh et al., 1999). As a precursor to mature fibrils, protofibrils have been characterized fairly well and have been shown to alter the normal physiology of cultured neurons (Hartley et al., 1999), disrupt ion channels (Ye et al., 2003), block LTP, inhibit synapse remodeling and impair memory consolidation (O'Nuallain et al.).

A prominent component of AD pathology is the neuroinflammation found in the affected areas of the AD brain. The evidence of inflammation, such as activated microglia and proinflammatory cytokines, is most predominantly observed surrounding the Aβ lesions within the AD brain (McGeer et al., 1987). The exact sequence of events leading to AD is still unknown; however, it is thought that the accumulation of the Aβ protein initiates a pathological cascade of events leading to neuronal dysfunction and ultimately dementia. One downstream event of the pathological cascade is an inflammatory response involving the activation and proliferation of microglia and astrocytes which leads to an increase of inflammation associated proteins and markers of oxidative stress (Golde, 2002). If the inflammation persists, it can lead to a chronic inflammatory state, which has been suggested to be one of the underlying mechanism causing progressive neurodegeneration (Golde, 2002, McGeer and McGeer, 1998).

The innate immune system protects the organism by recognizing invading pathogens using PRRs. Both microglia and astrocytes express TLRs, which are a family member of the PRRs and act by allowing the recognition of PAMPs of bacteria, fungi,

and viruses. When activated, the TLR family, with the exception of TLR3, leads to the recruitment of the adaptor protein myeloid differentiation protein 88 (MyD88), the activation of the transcription factor nuclear factor-κB (NF-κB) and the expression of a variety of genes involved in immune response, such as TNFα and pro-IL-1β (Kielian, 2006). However, the mechanism by which Aβ evokes a proinflammatory response is very complex and many TLRs and accessory proteins have been shown to play a role in the Aβ-induced proinflammatory response in monocytes/macrophages and microglia including CD36, TLR4 and TLR6 (Stewart et al., 2010), and CD14, TLR2 and TLR4 (Fassbender et al., 2004, Reed-Geaghan et al., 2009, Udan et al., 2008). Studies have also shown that a multireceptor complex comprised of SR class B (SR-B), CD36, α6β1-integrin and the integrin associated protein CD47 interacts with Aβ and initiates an inflammatory response (Bamberger et al., 2003).

Extracellular recognition of PAMPs by TLRs and downstream signaling events can trigger oligomerization of cytoplasmic NLRs to form a multisubunit inflammasome complex (Kersse et al., 2011). Different NLR family members vary in their N-terminal protein-protein interaction region. For example, NLRP3 contains a pyrin domain, which is responsible for complexation with ASC, the adaptor molecule containing CARD (Latz et al., 2013). An important aspect of TLR signaling is the production of IL-1β mRNA and the pro-form of IL-1β protein (pro-IL-1β). This event is considered "priming" of the inflammasome and represents Signal 1 of a 2-stage process (Hanamsagar et al., 2012). Many molecules, including the classical TLR4 agonist LPS, are known to stimulate priming of the inflammasome (Signal 1) but not activation (Signal 2). Inflammasome assembly via a CARD-CARD interaction brings caspase-1 to the complex and activation

of the complex triggers caspase-1-catalyzed proteolytic cleavage of pro-IL-1β to mature IL-1β (Schroder and Tschopp, 2010). A second signal is required for the inflammasome activation step and subsequent production of mature IL-1β. Signal 2 may be provided by a growing number of endogenous human molecules, referred to as DAMPs. These molecules include certain pore-forming toxins, ATP, K^+ efflux, and crystalline particles such as silica and uric acid crystals (Hanamsagar et al., 2012).

Increasing data has demonstrated a significant role for the NLRP3 inflammasome in AD (reviewed in (Tan et al., 2013)). Double transgenic mice that overexpress human APP with familial AD mutations and have a deficiency in the NLRP3 inflammasome showed a reduction in AD pathology and were protected from the ensuing cognitive defects (Heneka et al., 2013). Earlier *in vitro* studies demonstrated that fibrillar Aβ stimulated NLRP3 inflammasome activation and IL-1β production in microglia and this process was shown to involve phagocytosis, lysosomal damage, and release of cathepsin B (Halle et al., 2008). Another report confirmed fibrillar Aβ-stimulated inflammasome activation but demonstrated that pre-priming of the inflammasome was required (Wu et al., 2013). However, it was recently shown that Aβ may be able to provide both priming and activation signals (Sheedy et al., 2013).

3.2 MyD88-Dependent Microglia Aβ(1-42) Protofibril-Induced Stimulation and Priming of the NLRP3 Inflammasome

Aβ(1-42) protofibrils were prepared as mentioned in the methods and isolated by SEC (Paranjape et al., 2013, Walsh et al., 1997). We have previously shown that this protofibril preparation produces a Superdex 75 void-volume fraction containing Aβ protofibrils characterized as curvilinear structures less than 100 nm in length with a R_H

range of 10-40 nm and an average R_H of 21 nm (Paranjape et al., 2013). Our SEC-isolated soluble protofibrils have also shown to bind and enhance ThT fluorescence emission at 480 nm compared to the SEC-isolated monomer, which elutes in the included volume and did not show enhanced ThT fluorescence (Paranjape et al., 2012, Paranjape et al., 2013). We have also previously demonstrated that Aβ(1-42) protofibrils, but not Aβ(1-42) fibrils, are activators of microglia (Paranjape et al., 2012, Paranjape et al., 2013) and that these soluble fibrillar precursors are able to trigger a proinflammatory response via TLRs (Udan et al., 2008).

In this investigation, the role of MyD88 in Aβ(1-42) protofibril-induced cytokine production, NLRP3 inflammasome activation and IL-1β production and secretion was examined. During this investigation, I identified multiple points of regulation by Aβ protofibrils including new insights into the IL-1β secretion process. The first observation was of the mRNA levels of proinflammatory cytokines, TNFα and IL-1β. Primary murine microglia were treated with SEC-isolated Aβ(1-42) protofibrils at different incubation times and the mRNA levels were quantified. Protofibrils showed to significantly increase the TNFα (Figure 3.1A) and IL-1β (Figure 3.1B) mRNA levels by 2 hours followed by a rapid drop of the transcript at the 4 and 6 hour time points.

Several TLRs have been demonstrated to recognize extracellular Aβ and initiate a proinflammatory event in monocytes/macrophages and microglia (Fassbender et al., 2004, Jana et al., 2008, Liu et al., 2012, Reed-Geaghan et al., 2009, Stewart et al., 2010, Udan et al., 2008). One cytoplasmic mediator following signal transduction of TLR stimulation and prior to NFκB activation is MyD88 (Kielian, 2006). Microglia isolated from either WT or $MyD88^{-/-}$ mice were used to assess the contribution of TLR/MyD88

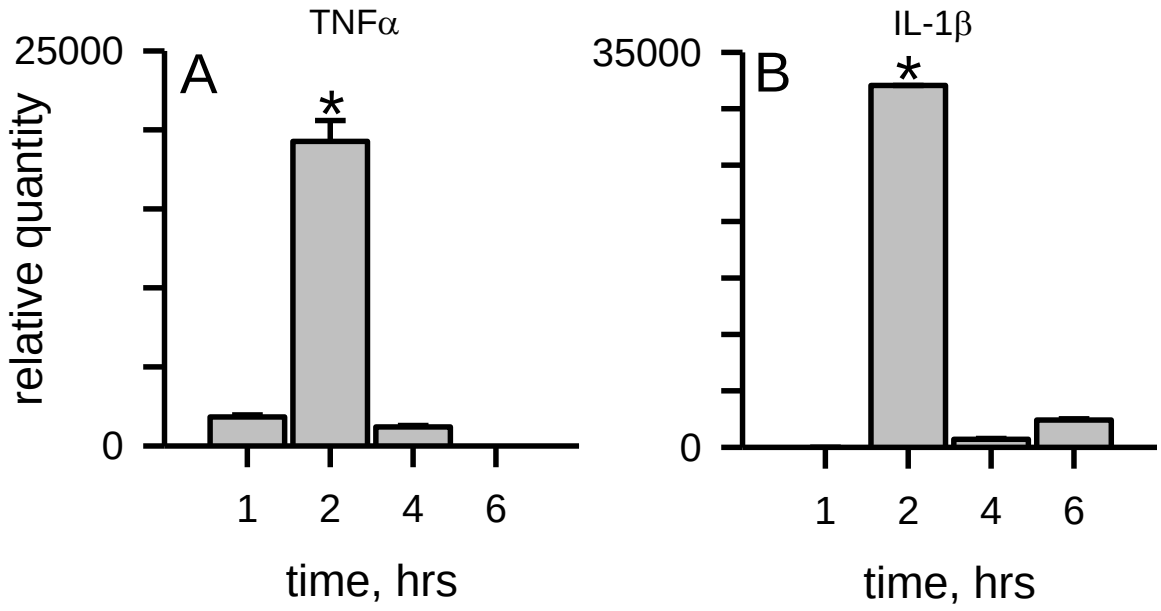

Figure 3.1. Aβ(1-42) protofibrils formed and isolated in aCSF are significant stimulators of TNFα and IL-1β transcription. SEC-isolated Aβ(1-42) protofibrils in aCSF were incubated with WT primary microglia at a final concentration of 15 μM for 1, 2, 4, and 6 hours in serum-free medium. At each time point the cells were lysed for total RNA extraction. TNFα (Panel A) and IL-1β (Panel A) mRNA levels were measured by qPCR as described in Chapter 2, section 2.5.5.4. The term relative quantity is described in Chapter 2, section 2.5.5.4 and represents the mRNA comparison between microglia treated with Aβ(1-42) protofibrils and those treated with buffer control. β-actin was used as an internal control in separate experiments and did not vary significantly between samples. Data bars represent the mean ± standard error of n=8 qPCR trials. TNFα and IL-1β mRNA levels at 2 hours were significantly different than any other time point (*$p<0.001$).

signaling in the Aβ protofibril-induced cytokine mRNA upregulation. WT microglia again showed increase responsiveness at 2 hours in both TNFα and IL-1β mRNA to Aβ(1-42) protofibrils (Figure 3.2). However, this responsiveness was significantly diminished in MyD88$^{-/-}$ microglia compared to WT microglia. In the MyD88$^{-/-}$ microglia, the TNFα and IL-1β levels were comparative to the buffer controls (Figure 3.2). This data revealed that the transcriptional activation-induced by Aβ(1-42) protofibrils is TLR/MyD88-dependent.

The next step along this pathway is the translation of the IL-1β mRNA to pro-IL-1β, which was explored further by measuring the amount of intracellular pro-IL-1β using an ELISA specific for the pro-form of IL-1β. The specificity of the pro-IL-1β ELISA was confirmed by the observation that a mature IL-1β standard curve was not detected by the pro-IL-1β specific antibodies, as seen in Chapter 2, Figure 2.4. After treatment of the microglia with Aβ protofibrils, the conditioned medium was removed, the cells were washed and lysed, the extract was analyzed and several observations were made. One observation was the presence of existing stores of pro-IL-1β in the unstimulated WT and MyD88$^{-/-}$ microglia after 6 hours (Figure 3.3). These stores indicate some level of underlying basal NLRP3 inflammasome priming in the isolated primary microglia. This may be unintentionally caused by the isolation and culturing process or intentionally caused by the cells as an intracellular reservoir in order to induce a rapid microglial response to potential stimuli. The second observation was the significant increase in the pro-IL-1β levels in the WT microglia-induced by Aβ(1-42) protofibrils compared to the control treatment after 4 ($P<0.005$, one-way ANOVA) and 6 hours ($P<0.005$) (Figure 3.3A). However, this same analysis did not show a significant difference in the MyD88$^{-/-}$

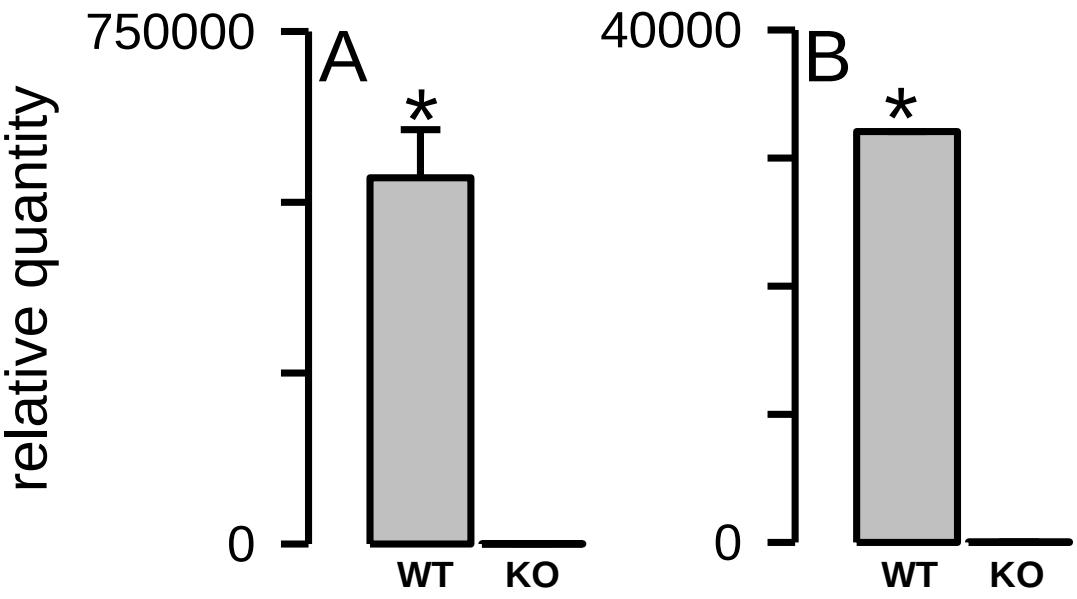

Figure 3.2. TNFα and IL-1β mRNA production is reduced in the MyD88$^{-/-}$ microglia in response to protofibrils. SEC-isolated Aβ(1-42) protofibrils were incubated with WT primary microglia and MyD88$^{-/-}$ (KO) microglia at a final concentration of 15 μM for 2 hours in serum-free medium. After 2 hours the total RNA was collected and TNFα (Panel A) and IL-1β (Panel B) mRNA levels were quantified by qPCR as described in Figure 3.1 legend. Data bars represent the mean ± standard error of n=8 qPCR trials. Absolute relative quantity values fluctuated between experiments (e.g. TNFα mRNA Figure 3.1A and 3.2A) due to the exponential in the calculation which is sensitive to small changes in raw data. Protofibril-treated microglia were compared to aCSF-treated microglia to determine relative quantity. When comparing WT and MyD88$^{-/-}$ microglia, experiments were always done on the same day. Statistical analysis confirmed a significant difference (*$p<0.001$) between the WT and MyD88$^{-/-}$ microglial TNFα and IL-1β mRNA response.

microglia (P>0.05) (Figure 3.3B). These data points were examined further by univariate ANOVA considering both Aβ(1-42) protofibril-induced and vehicle control in both WT and MyD88$^{-/-}$ microglia. This comparison showed a lesser, but still significant difference (P<0.05) between the WT and MyD88$^{-/-}$ microglial response at the 6 hour time point. The time-dependence production of pro-IL-1β was somewhat variable and difficult to quantitate due to the observation that the protofibrils may have the ability to activate the NLRP3 inflammasome, creating a dynamic pool of pro-IL-1β with a balance between production and conversion to mature IL-1β.

3.3 Production of Intracellular Mature-IL-1β Induced by Aβ(1-42) Protofibrils in Primary Microglia

Recent observations have demonstrated a role for Aβ in the activation of the NLRP3 inflammasome (Halle et al., 2008, Heneka et al., 2013, Sheedy et al., 2013, Wu et al., 2013). The activation of the NLRP3 inflammasome results in caspase-1 mediated proteolytic cleavage of pro-IL-1β (31 kD) to the mature form of IL-1β (17 kD). When studying the intracellular inflammasome processing of pro-IL-1β to mature IL-1β by Aβ(1-42) protofibrils in WT microglia, both immunoblots and ELISA were used to evaluate the intracellular pro- and mature IL-1β. Primary WT microglia were treated for increasing times with SEC-isolated Aβ(1-42) protofibrils and the cells were lysed to access intracellular IL-1β levels. Western blots were performed using 3ZD antibody, which recognizes both pro- and mature IL-1β. The analysis showed a consistent pool of pro-IL-1β throughout the time course of both the Aβ(1-42) protofibril induced and vehicle control treated microglia (Figure 3.4A). In the same blot, significant levels of intracellular mature IL-1β was observed after 4 and 6 hours of Aβ(1-42) protofibril

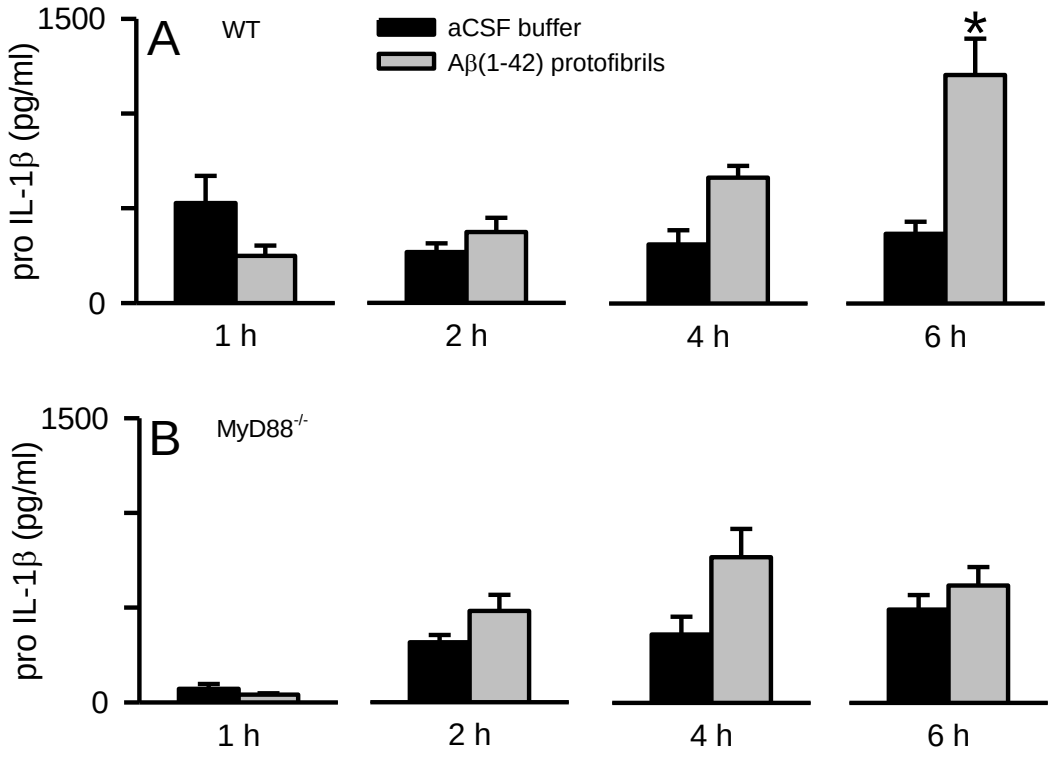

Figure 3.3 Aβ(1-42) protofibrils stimulate intracellular pro-IL-1β production in microglia. SEC-isolated Aβ(1-42) protofibrils in aCSF (gray bars) or aCSF buffer alone (black bars) were incubated with WT (Panel A) and MyD88$^{-/-}$ (Panel B) primary microglia at a final concentration of 15 μM for 1, 2, 4, and 6 hours in serum-free medium. After each time point the conditioned medium was removed, the cells were lysed and the extract was collected to measure intracellular pro-IL-1β protein by ELISA. Data bars represent the average ± standard error of n=5 trials. One-way ANOVA looking at each time point individually showed a significant difference between control and protofibril-stimulated WT microglia at 4 and 6 hours (both $p<0.005$) with no statistical difference at 1 and 2 hours in WT microglia and at any time point in MyD88$^{-/-}$ microglia. Univariate ANOVA considering both treatment and the presence of MyD88 showed a lesser, but still significant, difference (*$p<0.05$) between the WT and KO microglial response at only the 6 hour time point.

treatment where no mature IL-1β was observed at 1 and 2 hours (Figure 3.4A). ELISA-based IL-1β measurements were also conducted on the same samples, showing the same time-dependent production of intracellular mature IL-1β with significant increases at 4 and 6 hours (Figure 3.4C). It is possible that the IL-1β ELISA antibodies detect both the pro- and mature IL-1β forms of the protein, however, the large increase in the IL-1β levels measured by the ELISA (Figure 3.4C) corresponded with the increases observed in the Western blot (Figure 3.4A). This suggests that the increase in the ELISA was mature IL-1β protein. The intracellular mature IL-1β levels appear high due to the combination of multiple wells (n=5) to prepare cell extracts in a small volume to increase detection levels in the Western blot. A longer time course was also conducted at different incubation times of the Aβ(1-42) protofibrils-induced primary microglia up to 24 hours (Figure 3.4B and D). Both the Western blot and ELISA confirmed that the intracellular mature IL-β levels continued to increase after the microglia were stimulated with Aβ(1-42) protofibrils.

So far, the time course data has shown that Aβ triggers the TLR/MyD88 pathway leading to the transcription of IL-1β mRNA, synthesis of pro-IL-1β, and conversion of pro- to mature IL-1β. Experiments were also completed to test this model by comparing the intracellular mature IL-1β levels between WT and MyD88$^{-/-}$ microglia after treatment with Aβ(1-42) protofibrils. WT microglia produced significant levels of intracellular IL-1β while the MyD88$^{-/-}$ microglia were severely diminished in their ability to produce intracellular mature IL-1β (Figure 3.4E). After a 6 hour incubation in the MyD88$^{-/-}$, microglia mature IL-1β levels were only 8% of the WT microglia, while no mature IL-1β above the control was produced at 24 or 48 hours in the MyD88$^{-/-}$ microglia after with

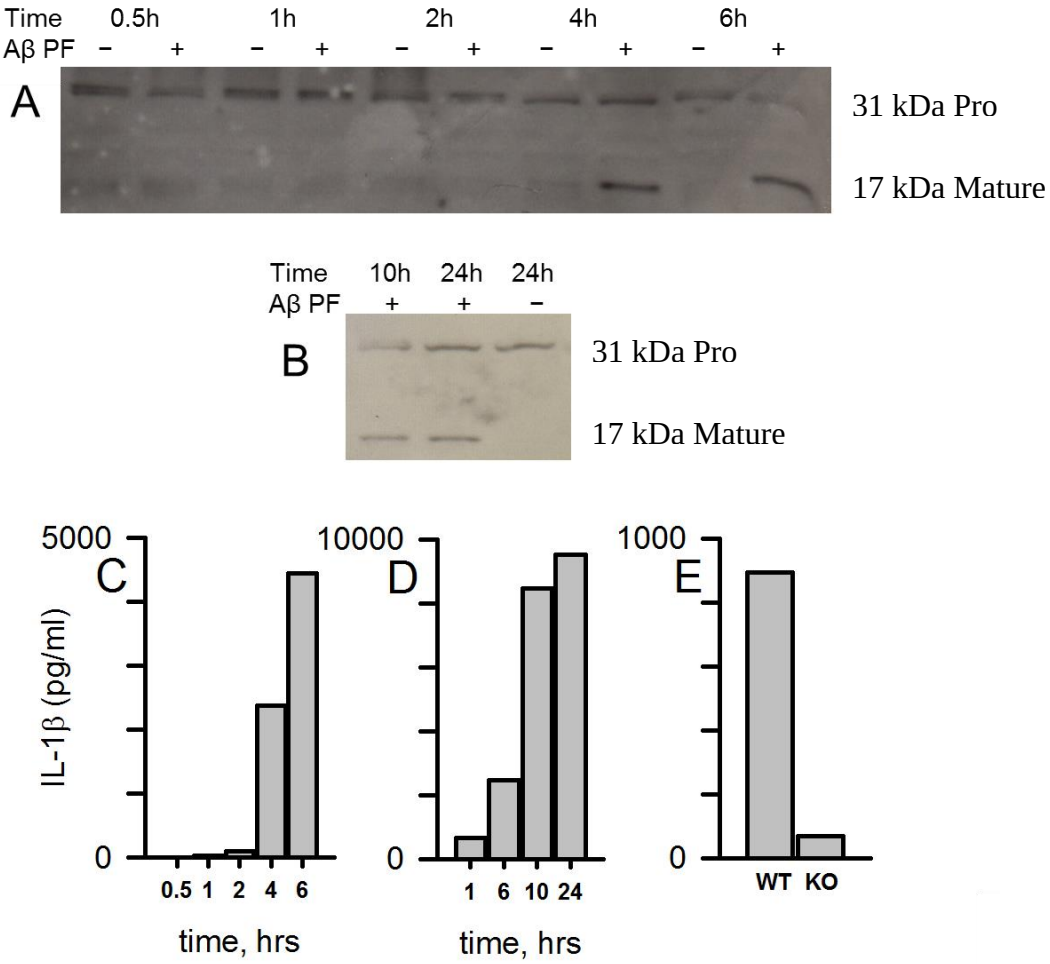

Figure 3.4. Aβ(1-42) protofibrils stimulate time- and MyD88-dependent intracellular mature IL-1β accumulation in microglia. Panel A and C. WT primary microglia were treated with SEC-isolated Aβ(1-42) protofibrils (15 μM) in aCSF (+) or just aCSF buffer (−) and incubated for 0.5, 1, 2, 4, and 6 hours in serum-free medium at 37 °C. At each time point the cells were lysed and extracts prepared for intracellular IL-1β Western blot (Panel A) and ELISA (Panel C) analysis. A separate, but similar experiment was done over a longer time course with the same analysis (Panel B Western blot, Panel D ELISA). Each cell extract sample for all panels was obtained from five replicate wells in a 96-well plate and the band or data bar is representative of the 5-well extract pool. Panel E. Intracellular mature IL-1β was measured by ELISA after treatment of WT and MyD88$^{-/-}$ primary microglia (KO) with Aβ(1-42) protofibrils (15 μM) for 6 hours in serum-free medium. Extracts were prepared as above. Control treatments with an equal volume of aCSF were subtracted from Aβ-stimulated samples and averaged 10% for intracellular IL-1β.

Aβ(1-42) protofibrils.

3.4 Time-Dependent Sequence of Aβ(1-42) Protofibril-Induced Microglia TNFα and IL-1β Protein Secretion

Primary microglia were treated with SEC-isolated Aβ(1-42) protofibrils for different lengths of time and the amount of secreted proinflammatory cytokines TNFα and IL-1β were quantified from within the conditioned medium. The protofibrils were able to induce a steady increase in the amount of secreted TNFα protein over a 6 hour incubation (Figure 3.5A). The TNFα protein was in-line with the observed TNFα mRNA seen in Figure 3.1A, where most of the protein was secreted after the majority of the mRNA was transcribe. The Aβ(1-42) protofibril-induced IL-1β secretion time course was significantly different than what was observed for TNFα. The maximal level of secreted mature IL-1β was unexpectedly observed after a 1 hour incubation time and was maintain at the same level through 6 hours (Figure 3.5B). This observation was unexpected due to the maximal IL-1β protein secretion induced by Aβ(1-42) protofibrils being observed prior to the induction of the maximal IL-1β mRNA transcription (Figure 3.1B). Additional experiments were performed and found that maximal levels of secreted IL-1β protein were observed as early as 15 minutes, which was the earliest time point tested. The amount of IL-1β produced by the microglia after overnight plating was also observed and showed that there was no IL-1β secreted during overnight plating. This data made it apparent that the microglia secrete a rapid quantum of mature IL-1β after Aβ(1-42) protofibril stimulation and that the time point in which the conditioned medium was collected was irrelevant. This rapid IL-1β secretion pattern was observed multiple times. In fact, during the intracellular experiments presented in Figure 3.4A-D, secreted

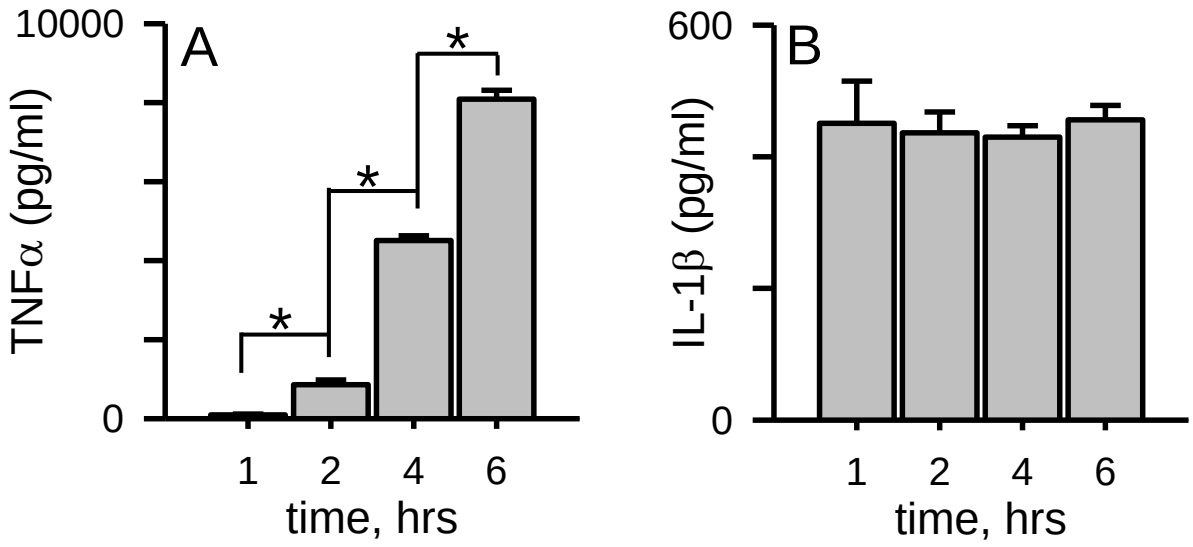

Figure 3.5. Aβ(1-42) protofibrils stimulate rapid IL-1β secretion but a slower time-dependent TNFα secretion. SEC-isolated Aβ(1-42) protofibrils in aCSF were incubated with WT primary microglia at a final concentration of 15 μM for 1, 2, 4, and 6 hours in serum-free medium. At each time point the conditioned microglial medium was collected for TNFα and IL-1β protein determination by ELISA. Panel A. TNFα protein levels were determined from the supernatant of individually treated wells. Data bars represent the mean ± standard error of n=5 trials at each time point. Control treatments with an equal volume of aCSF produced very low TNFα levels compared to protofibrils ranging from 36-290 pg/ml (<4%) at the different time points and were subtracted from Aβ-stimulated samples. TNFα levels at each successive time point are statistically different than the preceding time point ($p<0.001$). Panel B. IL-1β protein levels were measured in the same manner as for TNFα. Control treatments with an equal volume of aCSF produced IL-1β levels of 1 pg/ml and were subtracted from Aβ-stimulated samples. The length of incubation time had no statistical difference on the amount of secreted IL-1β ($p>0.05$).

IL-1β was also measured in the conditioned medium, which was collected prior to the cell lysate preparation. The samples collected at 0.25, 1, 2, 4, 6, or 24 hours had a similar quantum of secreted mature IL-1β within the conditioned medium (Figure 3.6), again showing the collection time point did not matter. Measuring both the secreted and intracellular mature IL-1β from the same cells provided even stronger evidence that the rapid IL-1β secretion stimulated by the Aβ(1-42) protofibrils was temporally distinct from, and not entirely dependent on, the Aβ-triggered intracellular mature IL-1β accumulation. The time-dependent studies presented have revealed several interesting findings: (1) the presence of a small amount of pre-existing pro-IL-1β in the isolated primary microglia, (2) that the activation of the NLRP3 inflammasome-induced by Aβ(1-42) protofibrils occurs much faster than the activation of the TLR/MyD88 pathway and cytokine transcription/translation-induced by Aβ(1-42) protofibrils, and (3) the intracellular build-up of mature IL-1β does not necessarily translate into an increase in the IL-1β secretion. This data also again shows that Aβ(1-42) protofibrils are able to produce mature IL-1β without an additional stimulus, as is the case with LPS and ATP (Kielian, 2006).

3.5 The Impact of MyD88 on the Aβ(1-42) Protofibrils-Induced Microglial TNFα and IL-1β Protein Secretion

Secretion of the TNFα protein was compared in the WT and MyD88$^{-/-}$ microglia after being stimulated with three known TLR ligands: LPS (TLR4), PAM_3CSK_4 (TLR2/1) and FSL-1 (TLR2/6). The levels of TNFα were significantly decreased in the MyD88$^{-/-}$ microglia compared to the WT in response to LPS (93.5% reduction), due to the MyD88$^{-/-}$ microglia response not being completely diminished confirms both MyD88-

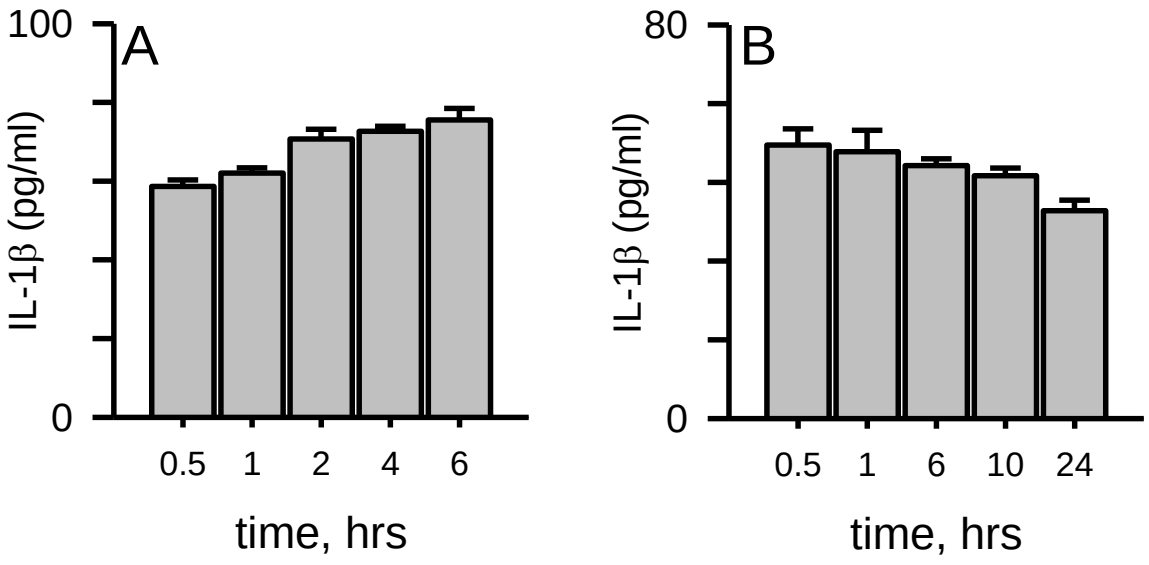

Figure 3.6. Correlation of IL-1β secretion with intracellular IL-1β production in primary microglia after stimulation with Aβ(1-42) protofibrils. The conditioned medium (Aβ protofibril-treated) from the samples presented in Figure 3.4 was removed and secreted IL-1β was measured by ELISA. Data bars represent the average ± standard error of n=5 trials. Secreted IL-1β in panels A and B was determined from the conditioned medium collected from the same samples used for lysate preparation and intracellular IL-1β measurement in Figure 3.4 C and D, respectively.

dependent and independent pathways (Figure 3.7A). However, this was not the case for PAM_3CSK_4 and FSL-1, where the absence of MyD88 completely eliminated the TNFα secretion (Figure 3.7A). These results were obtained using a ligand concentration of 100 ng/mL; however, similar responses were seen in additional experiments using 10 ng/mL (Figure 3.7B). The microglial TNFα response to Aβ(1-42) protofibrils was significantly lowered in the absence of MyD88 (88% reduction), demonstrating a significant role for the adaptor protein in mediating an Aβ(1-42) protofibril-induced TNFα secreted response. The remaining response indicates the possibility of additional pathways for mediating TNFα secretion that are independent of MyD88 (Figure 3.7A).

The levels of secreted mature IL-1β protein were also observed in the WT and $MyD88^{-/-}$ microglia conditioned medium after treatment with the three different TLR ligands and Aβ(1-42) protofibrils. Neither LPS, PAM_3CSK_4, nor FSL-1 alone were able to induce the secretion of mature IL-1β protein in WT nor $MyD88^{-/-}$ microglia (Figure 3.8A), confirming that these TLR ligands do not activate the NLRP3 inflammasome without the addition of a second stimulus. SEC-isolated Aβ(1-42) protofibrils, however, induced similar levels of secreted IL-1β protein in both WT and $MyD88^{-/-}$ microglia conditioned medium collected after 1, 2, 4, and 6 hours of stimulation (Figure 3.8B). The observation that the absence of MyD88 did not decrease the Aβ(1-42) protofibril induced IL-1β protein secretion, but does significantly decrease the IL-1β mRNA (Figure 3.2), was the second piece of evidence suggesting a potential intracellular reservoir of pro- or mature IL-1β within the cell that was produced prior to stimulation with Aβ(1-42) protofibrils.

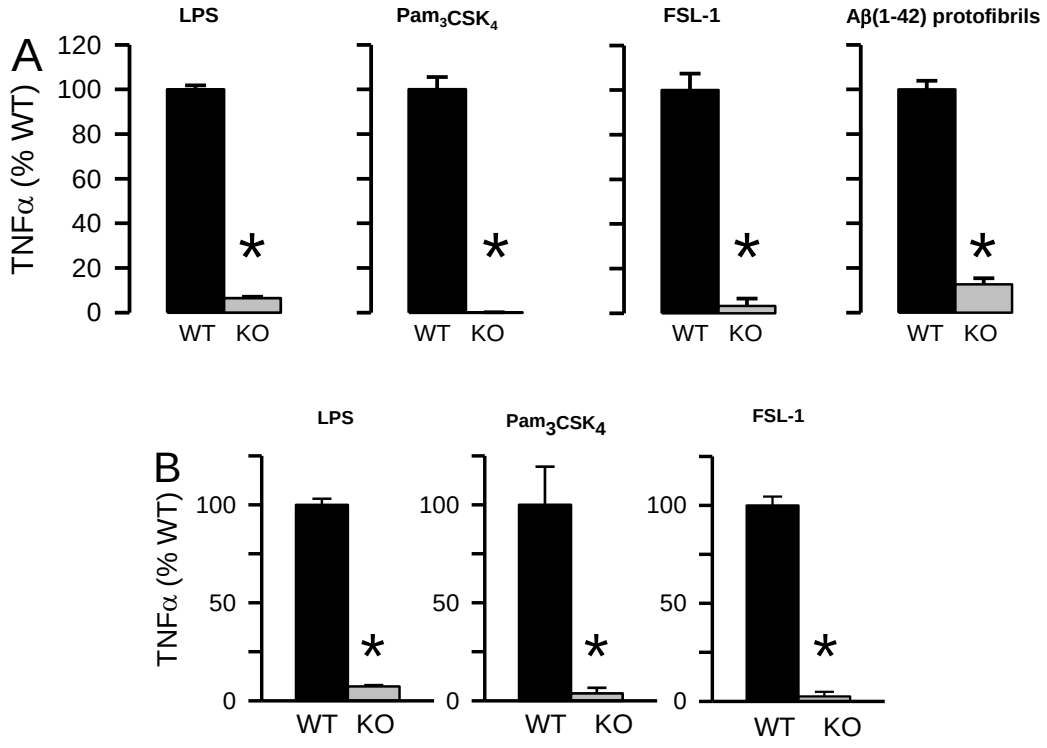

Figure 3.7. Aβ(1-42) protofibril-induced TNFα secretion is dependent on MyD88. Panel A. TLR4 ligand LPS, TLR1/2 ligand Pam_3CSK_4, TLR2/6 ligand FSL-1, and SEC-isolated Aβ(1-42) protofibrils were incubated with WT and MyD88$^{-/-}$ (KO) primary microglia at a final concentration of 100 ng/ml for all TLR ligands and 15 μM for Aβ for 6 hours in serum-free medium. Secreted TNFα was measured by ELISA in the conditioned medium. Data bars represent the average ± standard error of n=3 trials for LPS, Pam_3CSK_4, and FSL-1, and n=6 trials for Aβ(1-42) protofibrils. Data is presented as % WT response. Actual TNFα levels were 28467, 5480, 2556, and 12652 pg/ml were LPS, Pam_3CSK_4, FSL-1, and Aβ(1-42) protofibrils, respectively. Panel B. TLR4 ligand LPS, TLR1/2 ligand Pam_3CSK_4, and TLR2/6 ligand FSL-1 were incubated with WT and MyD88$^{-/-}$ (KO) primary microglia at a final concentration of 10 ng/ml for all TLR ligands in serum-free medium. Secreted TNFα was measured by ELISA in the conditioned medium. Data bars represent the average ± standard error of n=9 trials for WT and n=12 trials for MyD88$^{-/-}$. Data is presented as % WT response. Actual TNFα levels were 16112, 1098, and 3874 pg/ml were LPS, Pam_3CSK_4, and FSL-1, respectively. Control treatments with an equal volume of H_2O or aCSF were less than 3% of the TNFα response and were subtracted from TLR ligand- or Aβ-stimulated samples. Statistical analysis showed a significant difference ($p<0.005$) between the WT and MyD88$^{-/-}$ results for all treatments.

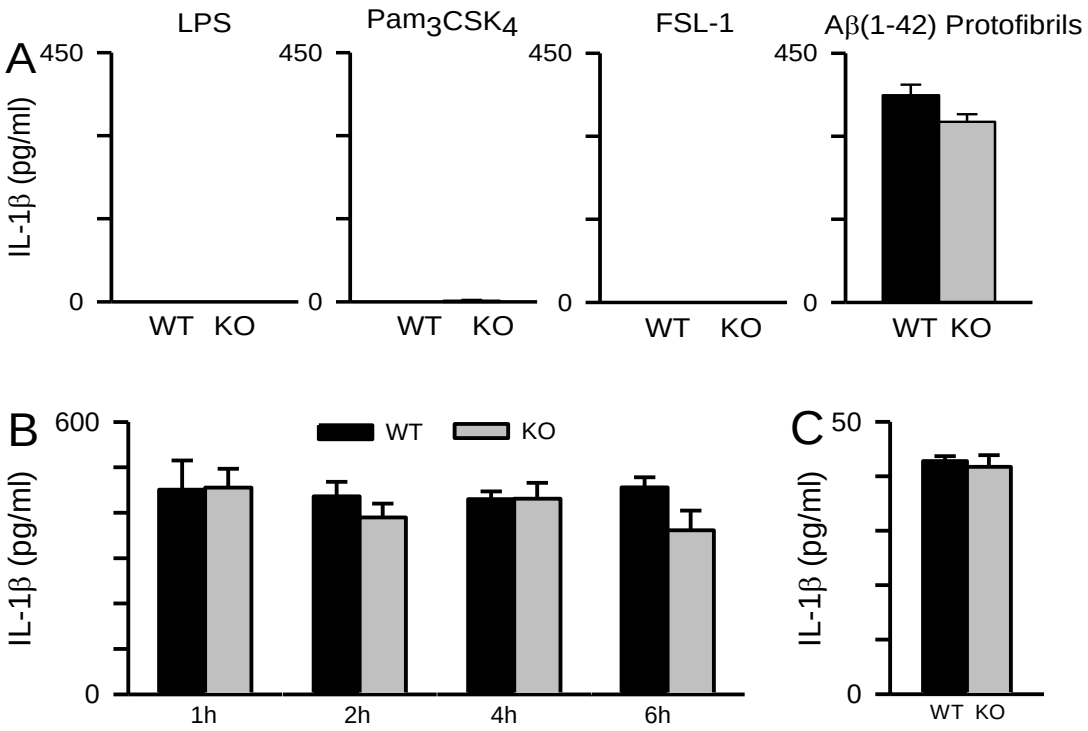

Figure 3.8. Aβ(1-42) protofibril-induced rapid IL-1β secretion is not dependent on MyD88. Panel A. TLR4 ligand LPS, TLR1/2 ligand Pam_3CSK_4, TLR2/6 ligand FSL-1, and SEC-isolated Aβ(1-42) protofibrils were incubated with WT and MyD88$^{-/-}$ (KO) primary microglia at a final concentration of 100 ng/ml for all TLR ligands and 15 μM for Aβ for 6 hours in serum-free medium. Secreted IL-1β was measured by ELISA in the conditioned medium. Data bars represent the average ± standard error of n=3 trials for LPS, Pam_3CSK_4, FSL-1, and Aβ(1-42) protofibrils. Panel B. SEC-isolated Aβ(1-42) protofibrils were incubated with WT primary microglia and MyD88$^{-/-}$ (KO) microglia at a final concentration of 15 μM for 1, 2, 4, and 6 hours in serum-free medium. Secreted IL-1β was measured by ELISA in the conditioned medium. Data bars represent the average ± standard error of n=5 trials. Control treatments with an equal volume of aCSF produced 1 pg/ml IL-1β at all time points for both the WT microglia and the MyD88$^{-/-}$ microglia and were subtracted from Aβ-stimulated samples. Statistical analysis showed no significant difference between the WT and MyD88$^{-/-}$ results at any time point ($p>0.05$). Panel C. Secreted IL-1β was measured by ELISA after treatment of WT and MyD88$^{-/-}$ primary microglia (KO) with Aβ(1-42) protofibrils (15 μM) for 6 hours in serum-free medium. Conditioned medium was collected and secreted IL-1β was measured by ELISA. The secreted data bars are the average ± standard error for n=5 trials. Control treatments with an equal volume of aCSF were subtracted from Aβ-stimulated samples and averaged 0.4%. No statistical difference was observed between the WT and MyD88$^{-/-}$ response ($p>0.05$).

3.6 Possible Mechanisms of Aβ(1-42) Protofibril-Induced IL-1β Secretion

There are two possible explanations for the disconnection between TLR/MyD88-mediated IL-1β mRNA production and secretion of mature IL-1β. The probable options are that the rapid Aβ(1-42) protofibril-induced microglia secretion is from an existing mature IL-1β reservoirs, or that there is rapid activation of the NLRP3 inflammasome by Aβ(1-42) protofibrils, activating caspase-1 which would then cleave an existing pool of pro-IL-1β to mature IL-1β that can then be secreted. Both likely scenarios would presumably occur prior to the TLR/MyD88-induced IL-1β transcription and translation to pro-IL-1β protein. To explore these two potential hypotheses, we further examined the rapid secretion process. First, the microglia were treated with a concentration range of Aβ(1-42) protofibrils, which showed a dose-depended effect on the secreted mature IL-1β levels; however, the secreted IL-1β levels were not affected by time (Figure 3.9A). This indicated that the level of secreted mature IL-1β initially triggered by Aβ(1-42) protofibrils correlated with the magnitude or concentration of the Aβ(1-42) protofibril stimulus. Secondly, the amount of secreted IL-1β-mediated by Aβ(1-42) protofibrils was reduced in a dose-dependent manner by a caspase-1 inhibitor z-YVAD-fmk (Figure 3.9B). The ability of a caspase-1 inhibitor to reduce the amount of secreted mature IL-1β supports the second scenerio in which the rapid secretion of IL-1β originated from existing reserviors of pro-IL-1β.

In all the previous experiments, and in most cases within the literature, the microglia were treated once with the Aβ(1-42) protofibrils and then the secreted cytokines were ananlyzed by collecting the conditioned medium after different incubation times. This method is common, but it allows for the possiblity that the cytokine, or in

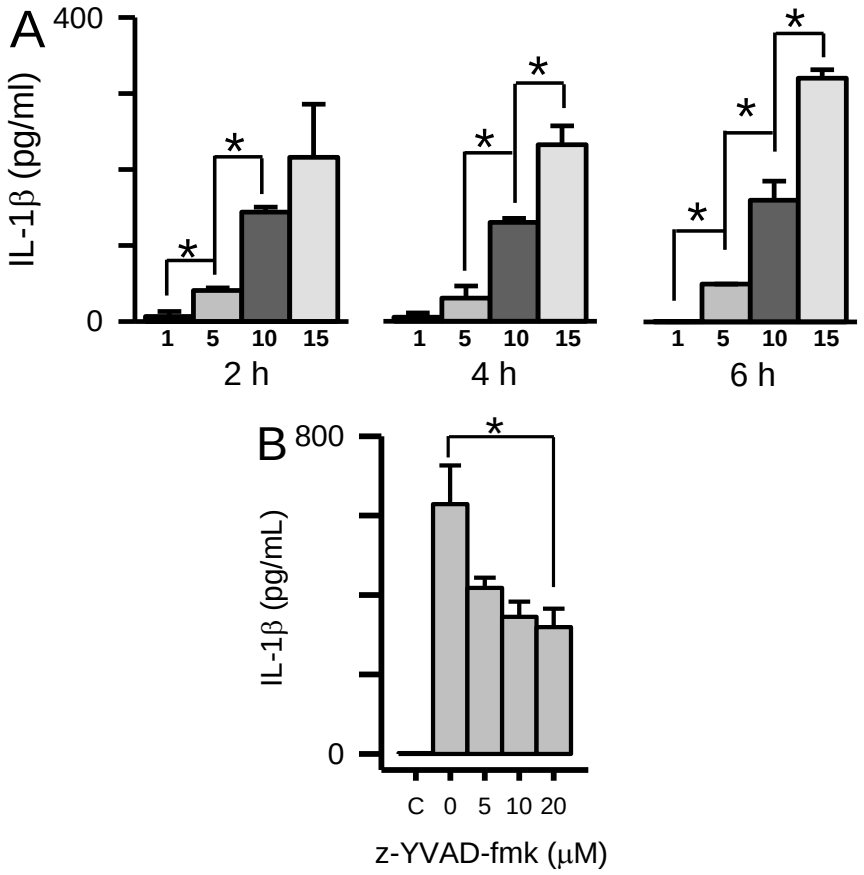

Figure 3.9. Dose-dependent IL-1β secretion in primary microglia induced by Aβ(1-42) protofibrils. Panel A. Primary microglia were treated with SEC-isolated Aβ(1-42) protofibrils (1, 5, 10, and 15 μM) and incubated for 2, 4, and 6 hours. Secreted IL-1β levels were measured in the conditioned medium by ELISA. Data bars represent the average ± standard error of n=3 trials for each condition. Statistical differences ($p<0.05$) in secreted IL-1β elicited by each Aβ protofibril concentration are denoted with an asterisk. No statistically significant differences were noted in the time dependence for each Aβ(1-42) protofibril concentration. Panel B. Primary microglia were treated with final concentrations of 0 μM, 5 μM, 10 μM, and 20 μM caspase-1 inhibition (Z-YVAD-FMK) for 30 minutes and then treated with SEC-isolated Aβ(1-42) protofibrils at a final concentration of 15 μM and incubated for 6 hours. Secreted IL-1β levels were measured in the conditioned medium by ELISA. Data bars represent the average ± standard error of n=3 trials for each condition. Statistical differences ($p<0.05$) in secreted IL-1β elicited by each Aβ protofibril concentration are denoted with an asterisk.

this case IL-1β, was secreted early during the incubation and that the collection time does not matter. In order to examine whether the microglia produced a sustained response to the initial Aβ(1-42) protofibril stimulus, we conducted experiments where the microglia were treated with Aβ(1-42) protofibrils and then the conditioned cellular medium was collected, replaced, and collected again at increasing times. Using this methodology, secreted IL-1β was only observed after the first collection of conditioned medium (Figure 3.10A), indicating that the Aβ(1-42) protofibril-induced secretion occurred shortly after stimulation and was not sustained over time. Next, the same procedure was used but with repeated stimulation of the same microglia with Aβ(1-42) protofibrils. This treatment produced a similar quantum of secreted IL-1β with each subsequent treatment (Figure 3.10B). This data revealed that the microglial IL-1β secretion mechanism was not desensitized nor depleted by the Aβ(1-42) protofibrils. These same findings were obtained in the MyD88$^{-/-}$ microglia (Figure 3.11), again providing evidence of MyD88-independent reservoirs of pro or mature IL-1β.

In Figures 3.4 and 3.6, it was observed that Aβ(1-42) protofibrils were able to induce an accumulation of intracellular IL-1β at longer time points (6, 10 and 24 hours), but that accumulation did not result in a corresponding increase of secreted mature IL-1β protein. This observation, along with results from Figure 3.10, suggested that an additional Aβ stimulus may be needed to trigger the release of the accumulated intracellular mature IL-1β. To test this hypothesis, the primary microglia were treated with Aβ(1-42) protofibrils for 6 hours to allow the accumulation of intracellular mature IL-1β and then treated a second time with Aβ(1-42) protofibrils. However, this did not result in a substantial increase in secreted mature IL-1β (Figure 3.12A), even though the

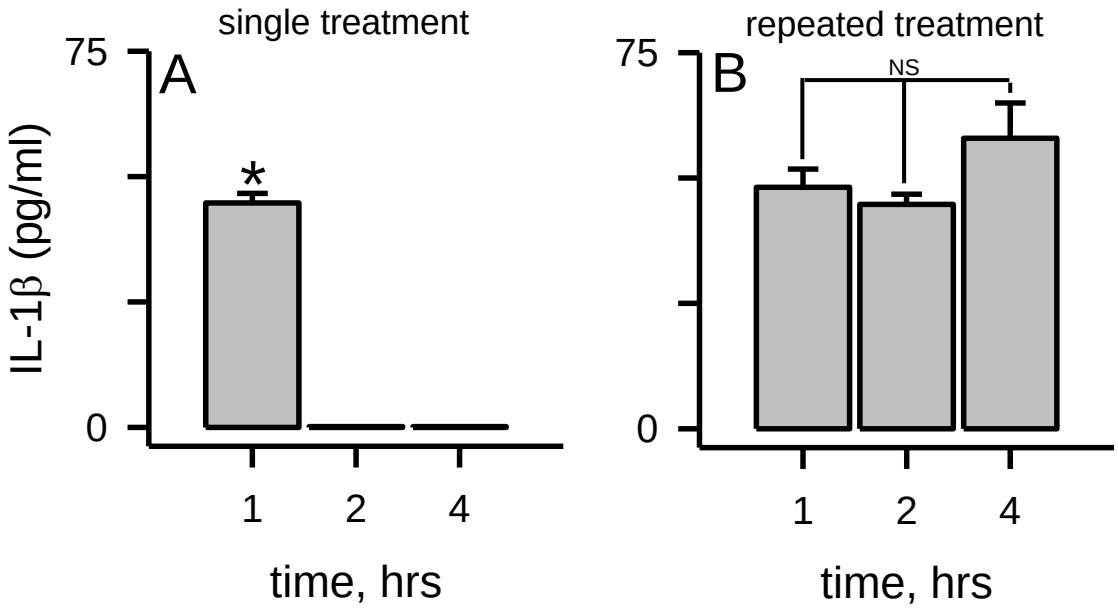

Figure 3.10. Aβ protofibril-induced rapid IL-1β secretion is not sustained but is repeatable. Panel A. Primary microglia were exposed to SEC-isolated Aβ(1-42) protofibrils (15 μM) and allowed to incubate at 37 °C for 1 hour. The conditioned medium was then removed, fresh medium applied, and collected at 2 hours. This process was repeated again for the 4 hour analysis. No further IL-1β was secreted compared to the 1 hour time point ($p<0.001$). Panel B. Experiments were conducted as described in Panel A, although Aβ(1-42) protofibrils (15 μM) were added with the fresh medium at 1 and 2 hours. Data bars represent the average ± standard error of n=5 trials. No statistical difference (NS) was noted in the amount of secreted IL-1β elicited by each successive Aβ(1-42) profibril treatment ($p>0.05$).

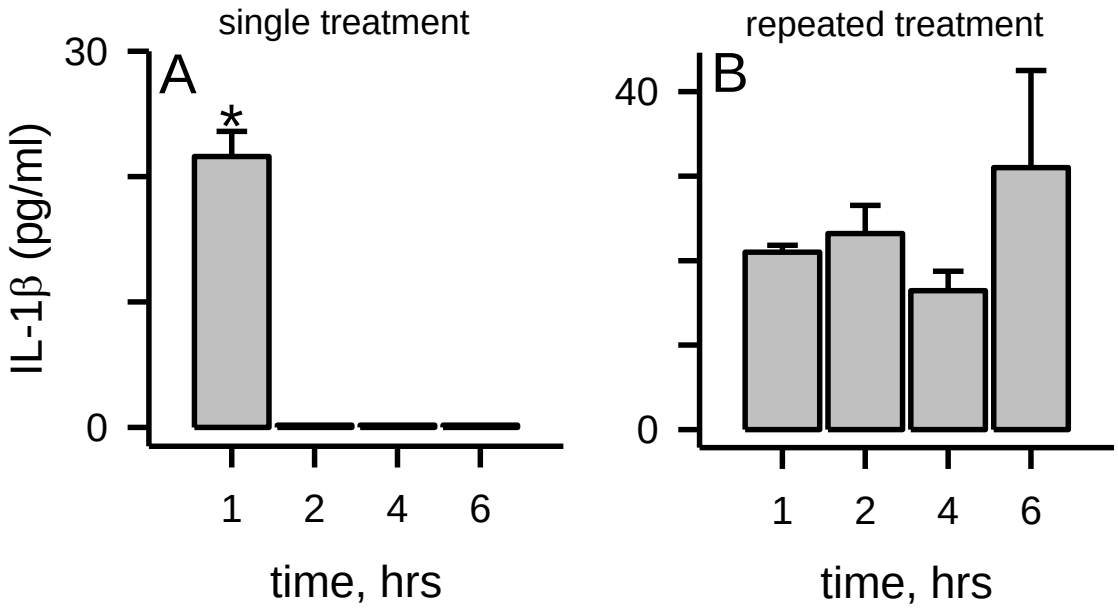

Figure 3.11. Aβ protofibril-induced rapid IL-1β secretion is not sustained but is repeatable in MyD88$^{-/-}$ microglia. Experiments were conducted in the same manner as described in Figure 3.10 legend but with the addition of a 6 hour time point. Panel A. One initial treatment of primary microglia with Aβ(1-42) protofibrils (15 μM). A statistically significant difference in secreted IL-1β was observed at 1 hour compared to subsequent time points ($p<0.001$). Panel B. Repeated treatments with Aβ(1-42) protofibrils did not significantly change the amount of secreted IL-1β ($p>0.05$). Data bars represent the average ± standard error of n=3 trials.

intracellular IL-1β was significantly increased during the initial 6 hour incubation with Aβ(1-42) protofibrils (Figure 3.12B). The secreted results were similar to what was observed in Figure 3.10 where the additional Aβ(1-42) protofibril treatments triggered the same quantum of secreted mature IL-1β as the initial stimulus; however, this data shows that the quantum was the same despite the substantial increase in the intracellular IL-1β.

3.7 Discussion

Aggregated Aβ has been recognized as a DAMP, which has similar qualities as PAMPs, but are endogneous instead of external pathogens. As the Aβ monomer self-assembles into small, soluble oligomers and ultimately insoluble fibrils, their unique structural character gives rise to proinflammatory properties. TLRs are the primary recognition molecules in the innate immune system and a few of them, such as TLR4 and TLR2 (Fassbender et al., 2004, Jana et al., 2008, Liu et al., 2012, Reed-Geaghan et al., 2009, Udan et al., 2008) and TLR4 and TLR6 (Stewart et al., 2010) have been shown to be major mediators of Aβ-triggered inflammation and cytokine production by monocytes/macrophages and microglial cells. The adaptor protein, MyD88, has also been implicated in an Aβ-induced inflammatory response within microglia (Lim et al., 2012).

The TLRs and the NLRP3 inflammasome are connected through a well-accepted 2-signal model (Hanamsagar et al., 2012). The model is initiated in the first step, which is "priming" of the immune cell, where the activation of the TLR causes MyD88 signaling and transcriptional activation resulting in mRNA and protein production. For the protein production of IL-1β, the priming process results in the pro-form of the protein.

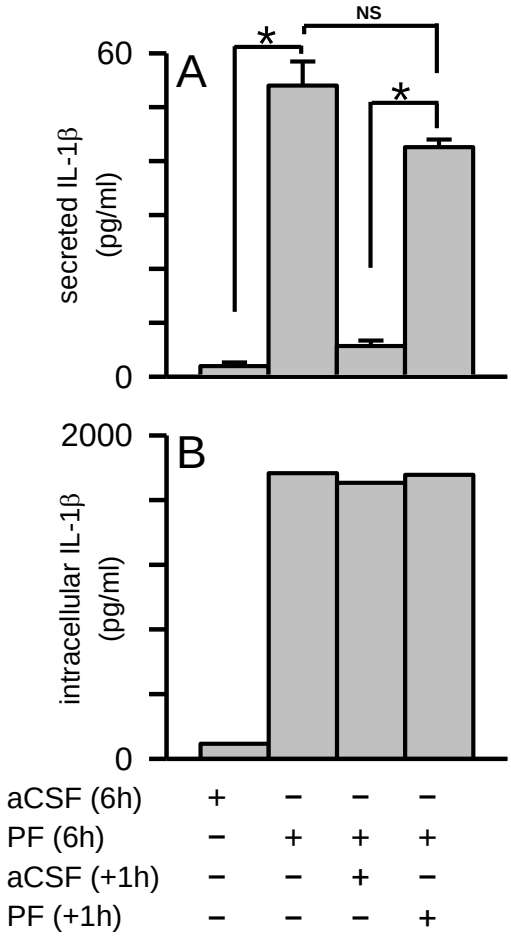

Figure 3.12. A second stimulus of microglia with Aβ protofibrils secretion does not release accumulated intracellular IL-1β. Primary microglia were exposed to SEC-isolated Aβ(1-42) protofibrils (15 μM) or aCSF buffer alone and allowed to incubate at 37 °C for 6 hrs. The conditioned medium was then removed and one cell extract was prepared for each condition (combination of five wells in 20 μL of lysis buffer). For the remaining cells, fresh medium was applied along with a second protofibril (n=5 wells or replicates) or buffer treatment (n=5 replicates). After an additional 1 hr incubation, the conditioned medium from each well was removed separately and one cell extract was again prepared for each condition. Secreted (Panel A) and intracellular (panel B) IL-1β was determined by ELISA. IL-1β data bars represent the average ± std error of n=5 replicates for secreted and one intracellular extract for each condition. Statistically significant differences between treatments are denoted with an asterisk ($p<0.001$). No statistical difference (NS) was found between the microglial IL-1β response when treated with Aβ(1-42) protofibrils for 6 hr and again for 1 hr ($p>0.05$).

The second step is signaled by endogneous molecules such as ATP and K^+ efflux, which triggers the activation of the inflammasome and cleavage of the pro-IL-1β into the mature form of IL-1β. Over the last five years, Aβ has been observed in the stimulation of many different innate immune pathways, including playing a role in the activation of the inflammasome (Halle et al., 2008, Heneka et al., 2013, Sheedy et al., 2013, Wu et al., 2013). Some of the reports studying Aβ and the NLRP3 inflammasome have used LPS as TLR/MyD88 priming stimulus to produce the pro-IL-1β, therefore priming the inflammasome (Halle et al., 2008). However, it has also been observed that Aβ alone is able to stimulate both the priming (Stewart et al., 2010) and the activation of the inflammasome. The studies shown in Chapter 3 clearly show that Aβ is able to provide both signals needed to elicit the production and secretion of mature IL-1β; however, it is likely that there are other mechanisms following the production of mature IL-1β in microglia and its secretion. Recently, Savage and colleagues reported differences between intracellular and secreted mature IL-1β in microglia stimulated with LPS (Savage et al., 2012). The data presented here, along with others, have shown that LPS alone does not induce IL-1β secretion; however, Savage et al., 2012 showed that LPS alone did induce the production of intracellular mature IL-1β. This suggests the possibility of additional sites for the regulation of IL-1β metablolism and/or trafficking.

While piecing together a representative model, the original 2-signal model of linking TLRs to the NLRP3 inflammasome was applied, but specifically connected it to Aβ(1-42) protofibrils and their ablility to effect multiple innate immune pathways (Figure 3.13). In the model (depicted from the analysis of the above data), the Aβ(1-42) protofibrils are able to trigger two, possibly, three signals. The first signal is the

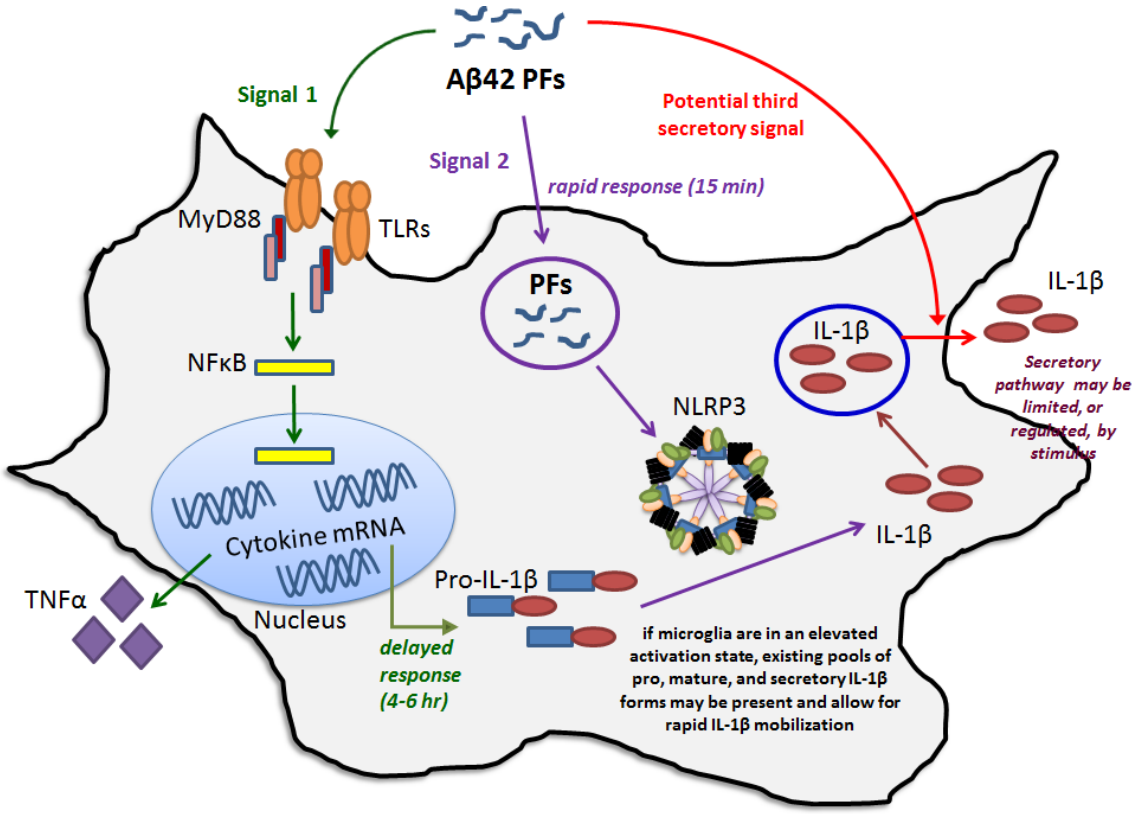

Figure 3.13 Proposed model of Aβ(1-42) protofibril stimulation of the TLR/MyD88 and NLRP3 inflammasome pathways. This model fuses together the original two signal model along with the new information obtained for the studies presented above.

activation of the TLR/MyD88 pathway, representing Signal 1 of the original model. During the first signal, the Aβ(1-42) protofibrils significantly upregulated IL-1β and TNFα mRNA and pro-IL-1β protein, which were highly dependent on the TLR/MyD88 pathway. The Aβ(1-42) protofibrils were also able to provide Signal 2, which activated the NLRP3 inflammasome resulting in the cleavage of pro-IL-1β to mature IL-1β. The production of intracellular mature IL-1β induced by the Aβ(1-42) protofibrils was time-dependent and signficantly reduced in the absecne of MyD88, likely due to the diminished priming of the inflammasome. Fibrillar Aβ has previously been shown to activate the inflammasome via a phagocytosis/lysosomal-leakage mechanism (Halle et al., 2008, Sheedy et al., 2013, Wu et al., 2013), which was incorporated in this model (Figure 3.13). In the original 2-signal model, the TLR/MyD88 engagement is accepted as Signal 1; however, the first reponse that was observed through our analysis was the rapid secretion of mature IL-1β (<15 minutes). This observed novel rapid secretion process is not dependent on Aβ protofibril-induced, MyD88-mediated, priming of the microglia, which occurred over longer periods of time. Throughout the investigation, low basal-levels of pro-IL-1β were observed by Western blot and ELISA and very low basal-levels of mature IL-1β detected only by ELISA. Existing pools of pro-IL-1β in primary microglia cultures have been previosly observed by Western blot in several studies (Takenouchi et al., 2011, Terada et al., 2010, Wu et al., 2013). The basal level of inflammasome priming in unstimulated microglia may produce a pool of pro-IL-1β poised for rapid caspase-1 cleavage or mature IL-1β pre-packaged in secretory vesicles and available for rapid secretion. *In vivo*, these reserviors of pre- or mature IL-1β may not be present unless

primed by a separate event preparing the microglia for rapid IL-1β secretion in repsone to Aβ.

The novel Aβ(1-42) protofibril-induced rapid IL-1β secretion was very reproducible and appears to be secreted as a quantum of IL-1β. The quantum could be repeatedly secreted by additional Aβ(1-42) protofibril treatments and the magnitude of the IL-1β secretion was dependent on the concentration of the Aβ(1-42) protofibrils. A recent review has suggested five different possible mechanisms for the secretion of IL-1β: (1) exocytosis of the IL-1β-containing secretory lysosomes, (2) release of IL-1β from shed plasma membrane microvesicles, (3) fusion of multivesicular bodies with the plasma membrane and subsequent release of the IL-1β containing exosome, (4) export of IL-1β through the plasma membrane using specific membrane transporters, and (5) release of the IL-1β upon cell lysis (Lopez-Castejon and Brough, 2011). The last mechanism is unlikely since we have previously shown that the Aβ(1-42) protofibrils are not toxic to the microglia (Paranjape et al., 2012) and because the IL-1β secretion was not sustained, and could be re-evoked by additional treatments of the same cells (Figures 3.10-3.12). A possible hypothesis is that the Aβ(1-42) protofibrils are able to trigger rapid secretion of IL-1β from microglia that have previously attained a basal level of activation and can either modulate the mature IL-1β secretion process or can rapidly stimulate the NLRP3 inflammasome and mediate the cleavage of pro-IL-1β to mature IL-1β, which can then be secreted.

From the above data, it was concluded that the Aβ(1-42) protofibrils are able to stimulate both a time- and MyD88-dependent accumulation of intracellular mature IL-1β and secretion of TNFα in the microglia. However, the Aβ(1-42) protofibril-induced pro-

IL-1β and accumulation of intracellular mature IL-1β did not translate into increased secreted IL-1β. Instead, the protofibrils secreted a rapid quantum of IL-1β that was seen at earlier time points than the upregulation of the intracellular pathway. This secretion was also limited or possibly highly regulated in its response. These findings allowed further insight into the mechanisms by which Aβ(1-42) protofibrils are able to prime and activate the NLRP3 inflammasome and highligthted differences between the Aβ(1-42) protofibrils and other TLR ligands and NLRP3 inflammasome activators.

CHAPTER 4

AGGREGATION PROPERTIES OF MIXED Aβ(1-42) AND Aβ(1-40) SOLUTIONS

4.1 Introduction

In the past it was thought that the insoluble fibrillar Aβ was the species which caused the most damage in AD, including cytokine production (Meda et al., 1995, Yates et al., 2000), interaction with proinflammatory receptors (Bamberger et al., 2003, Fassbender et al., 2004, Stewart et al., 2010), and interaction with proinflammatory pathways (Bianca et al., 1999, McDonald et al., 1998). However, more recent findings have shown that the more diffuse soluble oligomeric Aβ intermediates found in the brain and CSF are the more damage-causing species (Haass and Selkoe, 2007, Kayed et al., 2003, Paranjape et al., 2012).

Within the brain of AD patients several different aggregate morphologies have been identified (Selkoe, 2004). In normal physiological conditions the Aβ monomer peptide is highly soluble, but through mechanisms that are not completely understood the Aβ peptide aggregates to form Aβ plaques within the brain (Jarrett et al., 1993). *In vitro* aggregation studies have shown that synthetic Aβ peptides are able to form fibrils which are indistinguishable from fibrils isolated from AD patients' brains (Halverson et al., 1990, Hilbich et al., 1991, Kirschner et al., 1987). These studies show that the Aβ monomer self-assembles through non-covalent interactions to form polydisperse soluble

oligomers (Kayed et al., 2003) and protofibrils (Harper et al., 1997, Walsh et al., 1997) and eventually produce insoluble fibrils (Harper et al., 1999, Walsh et al., 1999).

The Aβ peptide is formed by the proteolytic cleavage of APP by β- and γ-secretase resulting in Aβ fragments that are 39-42 amino acids in length (Nixon, 2007, Selkoe, 2001). The two fragments that are most commonly produced are Aβ(1-40) and Aβ(1-42) (Selkoe, 2001). Even though these two isoforms have similar chemical structures their structural and biophysical properties are very different. Aβ(1-42) is widely known as the isoform that is more fibrillogenic and aggregation prone, compared to Aβ(1-40) (Pauwels et al., 2012). Mutations in the APP gene surrounding the γ-secretase cleavage site alter the production of Aβ(1-40) and Aβ(1-42) by increasing the total Aβ amount within the AD brain and by increasing the ratio of Aβ(1-42):Aβ(1-40) (Scheuner et al., 1996).

Initial characterization of the Aβ plaques led to the conclusion that the plaques mostly consisted of the Aβ(1-40) peptide (Mori et al., 1992). However, more recent data supports the predominance of Aβ(1-42) (Roher et al., 1993). Different ratios of Aβ(1-42):Aβ(1-40) were found when examining Aβ plaques from different regions of the diseased brain. For example, Roher et al., 1993 showed that plaques within the leptomeningeal vessels had an average ratio of 58:42 Aβ(1-42):Aβ(1-40), while plaques within the parenchymal vessels had an average ratio of 75:25 Aβ(1-42):Aβ(1-40) (Roher et al., 1993). *In vivo* mouse studies provided evidence that the ratio of Aβ(1-42):Aβ(1-40) plays a more significant role in the Aβ plaque load compared to the total amount of Aβ (Yin et al., 2007). In an attempt to identify a biomarker for cognitively normal patients who have an increased risk for developing AD, it was found that patients with

low Aβ(1-42):Aβ(1-40) ratio levels in their plasma and CSF have a significantly greater risk of developing AD. The reduction in the Aβ(1-42):Aβ(1-40) ratio within the plasma and CSF is thought to be due to the aggregation and deposition of Aβ(1-42) in the brain preceding the onset of AD symptoms (Fagan et al., 2000, Graff-Radford et al., 2007).

In vivo studies have established that the ratio of Aβ(1-42):Aβ(1-40) is an important factor in the pathology of AD. The literature provides numerous studies examining the aggregation and molecular mechanisms of the individual Aβ peptides, but it is more physiologically relevant to understand the molecular basis and the consequences associated with different ratios of Aβ(1-42):Aβ(1-40). *In vitro* studies observing the aggregation, toxicity and influence of mixed Aβ in AD pathology have identified many different effects Aβ(1-40) has on Aβ(1-42). Monomeric Aβ(1-40) was shown to alter the kinetic stability, solubility, and morphological properties of Aβ(1-42) aggregates. Equimolar ratios of Aβ(1-42):Aβ(1-40) (1:1) showed greater than 50% inhibition of fibrillar formation by monomeric Aβ(1-42) (Jan et al., 2008) as well as the formation of spherical oligomers (Chang and Chen, 2014). It was also found that protofibrillar Aβ(1-42) fibrillogenesis was inhibited at even higher ratios of Aβ(1-42):Aβ(1-40) (10:1) (Jan et al., 2008). Aβ(1-40) was thought to inhibits Aβ(1-42) aggregation by preferentially binding to the Aβ(1-42) protofibril (Pauwels et al., 2012, Yin et al., 2007). Different levels of neurotoxicity were also found when observing different ratios of Aβ(1-42):Aβ(1-40) (Chang and Chen, 2014, Kuperstein et al., 2010).

The current study was designed to learn more about the effect Aβ(1-40) has on Aβ(1-42) aggregation. In order to be certain that the experiments started with unaggregated dry Aβ peptides, individual Aβ peptides were treated with HFIP, mixed at

the designed ratios and dried. Each ratio was separated by SEC and the amount of protofibril formation and protofibril/monomer distributions were quantified. The data showed that as the ratio of Aβ(1-42):Aβ(1-40) decreased in the original mixed Aβ samples there was a corresponding decrease in the amount of protofibril formation and increase in the monomer pool. The DLS and ThT fluorescence measurements of the SEC-isolated protofibrils also decreased with a decrease in the Aβ ratio. Measurements of ThT fluorescence of the SEC-isolated monomers were also observed over time demonstrating a significant increase in the lag phase and aggregation time. Finally the actual amounts of each peptide within the protofibril and monomer peaks were assessed, by an Aβ C-terminal selective ELISA. These results suggested that Aβ(1-40) may have very little interaction with Aβ(1-42) during protofibril formation.

4.2 Characterization of SEC-Isolated Aβ(1-42):Aβ(1-40) Protofibrils

Different ratios of Aβ(1-42):Aβ(1-40) have been observed in Aβ plaques throughout different regions of the AD brain (Roher et al., 1993), indicating the pathophysiological significance of both peptides. The majority of the biophysical studies examining the molecular basis of Aβ peptide aggregation have been performed on the individual isoforms, however, *in vivo* analysis has indicated that the ratio of Aβ(1-42):Aβ(1-40) is more physiologically relevant. The following study focuses on examining the effect that the Aβ(1-40) isoform has on the protofibril formation and aggregation of the Aβ(1-42) isoform. The different ratios were prepared from individual lyophilized Aβ(1-42) and Aβ(1-40) peptides. The individual peptides were dissolved in HFIP, then the Aβ/HFIP solutions were mixed at the selected molar ratios of 5:0, 4:1, 1:1,

1:4, and 0:5 Aβ(1-42):Aβ(1-40) (Table 4.1 and Table 2.1), followed by evaporation and vacuum-centrifugation to remove the residual HFIP. The molar ratios used were chosen based on the desire to have a total Aβ concentration of 200 μM, suitable for SEC-insolation (Table 4.1). The dry ratio peptides were brought into solution using the protofibril preparation as described in Chapter 2, section 2.2.1 (Paranjape et al., 2013). Reconstitution of the HFIP-treated and lyophilized Aβ(1-42):Aβ(1-40) ratios in NaOH followed by dilution into aCSF at an overall Aβ concentration of 200 μM resulted in the formation of protofibrils which were then isolated by SEC on a Superdex 75 column (Figure 4.1A). This protofibril preparation and SEC-elution profile produced a void-volume similar to what was previously observed by the Aβ(1-42) isoform alone (Paranjape et al., 2013), however, the distribution of protofibrils to monomers decreased as the ratio of Aβ(1-42):Aβ(1-40) decreased (Figure 4.1B and Table 4.1). The SEC-elution profile of 5:0 Aβ(1-42):Aβ(1-40) produced approximately equivalent amounts of protofibrils and monomers, 56% and 44%, respectively (Figure 4.1A blue line, Figure 4.1B, and Table 4.1). As the ratio of Aβ(1-42):Aβ(1-40) increased, the distribution shifted to a greater abundance of monomers, compared to protofibrils (Figure 4.1B and Table 4.1).

DLS analysis was conducted on the Aβ(1-42):Aβ(1-40) ratio protofibril peaks from Figure 4.1A and the R_H was determined. A histogram (Figure 4.2 ratio 5:0, other ratio histograms not shown) for each ratio was generated from the autocorrelation data and the R_H values were measured to be 21 nm for 5:0, 16 nm for 4:1, 15 nm for 1:1, and 14 nm for 1:1 (Table 4.2). The R_H for 0:5 was undetermined. The DLS data showed that the R_H of the SEC-isolated Aβ(1-42):Aβ(1-40) protofibrils slightly decreases as the

Table 4.1. Ratios of Aβ(1-42):Aβ(1-40).

Ratios	[Aβ1-40] μM	[Aβ1-42] μM	% Protofibril	% Monomer
5:0	200	0	56	44
4:1	160	40	39	61
1:1	100	100	31	69
1:4	40	160	11	89
0:5	0	200	10	90

This table gives the concentrations of each peptide for each ratio prior to SEC-purification, along with the percentage of protofibrils and monomers formed for each ratio.

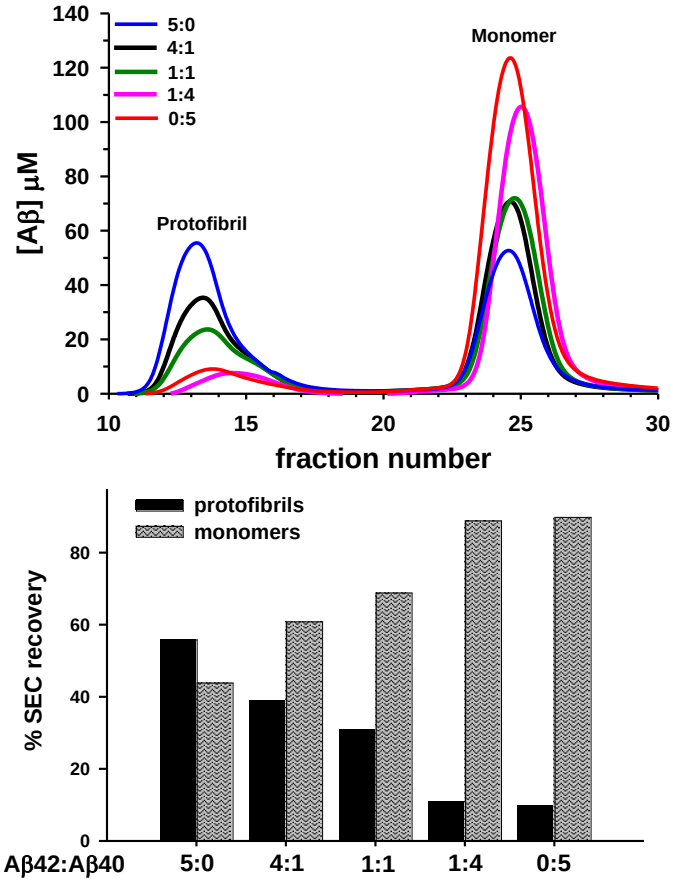

Figure 4.1. SEC-isolated Aβ(1-42):Aβ(1-40) protofibrils formed and isolated in aCSF. Panel A. SEC-isolated Aβ(1-42):Aβ(1-40) protofibrils formed and isolated in aCSF decreases as monomer increases when the ratio of Aβ(1-42):Aβ(1-40) decreases. Lyophilized Aβ(1-42):Aβ(1-40) ratios were brought into solution with NaOH followed by dilution into aCSF at a final concentration of 200 μM. The supernatant after centrifugation was eluted from a Superdex 75 column and 0.5 ml fractions were collected. UV absorbance at 280 nm was monitored during the elution. The protofibrils eluted in the void volume while the monomer eluted in the included peak. The blue line indicates Aβ(1-42) by itself and the red line indicates Aβ(1-40) by itself, while the black, green and pink lines indicate the 4:1, 1:1, and the 1:4 Aβ(1-42):Aβ(1-40) ratios, respectively. Panel B. Percent SEC recovery of Aβ(1-42)/Aβ(1-40) protofibril decreases as the Aβ(1-42) concentration decreases. The graph indicates the percent of protofibril and monomer from each SEC purified Aβ(1-42):Aβ(1-40) ratio. The black bars indicate the percent of protofibril and the grey bars indicate the percent of monomer. Percent was calculated by dividing the concentration of either the eluted protofibril or monomer by the total eluted SEC-Aβ concentration and then multiplied by 100. Aβ(1-42):Aβ(1-40) ratio decreases.

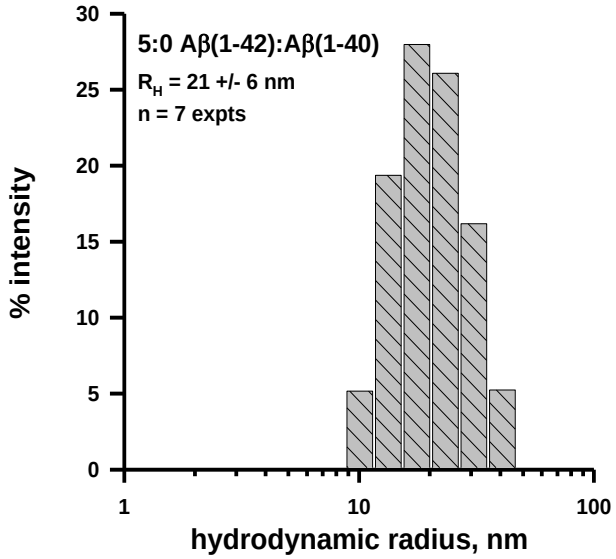

Figure 4.2. DLS of SEC-isolated Aβ(1-42):Aβ(1-40) protofibrils. Aβ(1-42):Aβ(1-40) protofibrils R_H slightly decreased as the concentration of Aβ(1-42) decreased. Aβ(1-42):Aβ(1-40) protofibrils were analyzed immediately after SEC-isolation by DLS and a representative regularized histogram of percent intensity versus R_H is shown of the Aβ(1-42):Aβ(1-40) 5:0 ratio. Intensity-weighted mean R_H values were derived from the regularized histograms. The table indicates the R_H for the other Aβ(1-42):Aβ(1-40) ratios.

Table 4.2. R_H measurements of SEC-isolated Aβ(1-42):Aβ(1-40) protofibrils.

Ratio	[Aβ(1-42)] μM	[Aβ(1-40)] μM	R_H (nm)
5:0	200	0	21
4:1	160	40	16
1:1	100	100	15
1:4	40	160	14
0:5	0	200	ND

original Aβ(1-42):Aβ(1-40) ratio decreased.

ThT is a benzothiazole dye, which shows increased fluorescence when bound to amyloid fibrils (Khurana et al., 2005), specifically when bound to the β-sheet secondary structure of aggregated Aβ (Krebs et al., 2005). The ThT technique has previously been used as an indirect way to measure the extent of β-sheet structure within the soluble Aβ protofibril species (Paranjape et al., 2013, Walsh et al., 1999). Here, ThT fluorescence was used to characterize the SEC-isolated Aβ(1-42):Aβ(1-40) protofibrils from each of the different Aβ(1-42):Aβ(1-40) ratios. For all ThT measurements, the SEC-isolated Aβ(1-42):Aβ(1-40) protofibrils were diluted to 5 μM Aβ. Analysis of the SEC-peak of the Aβ(1-42):Aβ(1-40) protofibril fractions after aggregation and elution in aCSF revealed that the extent of ThT binding and fluorescence decreased as the ratio of Aβ(1-42):Aβ(1-40) decreased (Figure 4.3). These findings suggest that the amount of β-sheet secondary structure decreased in the Aβ(1-42):Aβ(1-40) protofibrils as the ratio of Aβ(1-42):Aβ(1-40) decreased. However, the decreases observed in the amount of protofibrils formed and in the protofibril R_H and ThT fluorescence could be caused by the overall decrease in the Aβ(1-42) concentration.

4.3 SEC-Purification of Aβ(1-42):Aβ(1-40) Ratios While Holding [Aβ(1-42)] Constant

In an attempt to identify whether or not the Aβ(1-40) peptide is intermingling with the Aβ(1-42) peptide to form the SEC-isolated protofibrils, two Aβ(1-42):Aβ(1-40) ratios where the Aβ(1-42) concentration was held constant while increasing Aβ(1-40) were examined. The ratios were again prepared from individual lyophilized Aβ(1-42) and Aβ(1-40) peptides, however this time the preferred molar ratios were 5:0 and 4:1

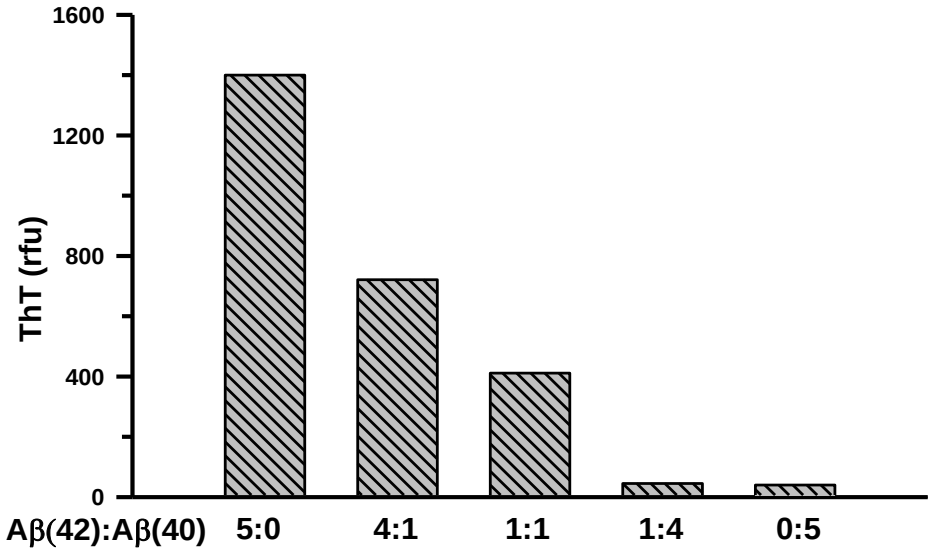

Figure 4.3. ThT fluorescence of SEC-isolated Aβ(1-42):Aβ(1-40) protofibrils. Freshly isolated Aβ(1-42):Aβ(1-40) protofibrils ThT fluorescence decreases as the concentration of Aβ(1-42) decreases. Aβ(1-42):Aβ(1-40) protofibrils eluted from a Superdex 75 SEC column in aCSF were diluted to 5 μM in aCSF containing 5 μM ThT and the fluorescence emission was measured as described in the Chapter 2, section 2.9.

with an Aβ(1-42) concentration of 200 μM in both ratios. The constant concentration of the Aβ(1-42) peptide in this set of Aβ(1-42):Aβ(1-40) ratios caused the overall total Aβ concentrations to be different for each ratio, 200 μM for the 5:0 and 250 μM for the 4:1. The dry ratio peptides were again brought into solution using the protofibril preparation as mentioned in Chapter 2, section 2.2.1, and then the aggregate species were isolated by SEC. The SEC-elution profile for the 5:0 Aβ(1-42):Aβ(1-40) ratio was the same as seen in Figure 4.1A. The SEC-elution profile of the 4:1 Aβ(1-42):Aβ(1-40) protofibril peak was very similar to the protofibril peak of the 5:0 Aβ(1-42):Aβ(1-40) ratio, however the monomer peak of the 4:1 Aβ(1-42):Aβ(1-40) indicates significantly more monomer compared to the 5:0 Aβ(1-42):Aβ(1-40) monomer peak (Figure 4.4). Comparing the SEC-profiles of the 5:0 and 4:1 Aβ(1-42):Aβ(1-40) ratios with constant Aβ(1-42) concentrations suggested that the Aβ(1-40) peptide does not play a significant role in the formation of the Aβ(1-42) protofibrils.

4.4 BV-2 Microglia Inflammatory Response Induced by Aβ(1-42):Aβ(1-40) Protofibrils

Aβ(1-42) protofibrils formed and isolated by SEC have previously been shown to be effective stimulators of TNFα production in BV-2 microglia (Paranjape et al., 2013). Similarly the SEC-isolated 5:0 Aβ(1-42):Aβ(1-40) protofibrils were able to stimulate the BV-2 microglia at a final concentration of 15 μM. However when treating the BV-2 microglia with the same final concentration of both SEC-isolated 4:1 and 1:1 Aβ(1-42):Aβ(1-40) protofibrils their ability to stimulate the microglia decreased (Figure 4.5). Treatment of the BV-2 microglia could not be completed for either the SEC-isolated 1:4 or 0:5 Aβ(1-42):Aβ(1-40) protofibrils due to the SEC in-line UV-determined

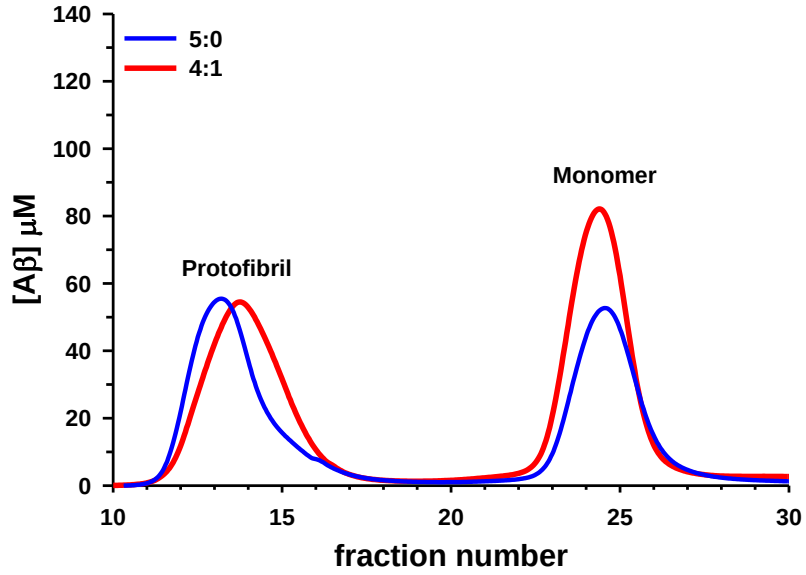

Figure 4.4. SEC-purification profile of 5:0 and 4:1 Aβ(1-42):Aβ(1-40) ratios while leaving the Aβ(1-42) concentration constant. SEC comparison of Aβ(1-42):Aβ(1-40) ratios of 5:0 and 4:1 while leaving the Aβ(1-42) concentration constant shows an equivalent amount of protofibrils and an increase in monomer. Lyophilized Aβ(1-42):Aβ(1-40) ratios were brought into solution with NaOH followed by dilution into aCSF at a final concentration of 200 μM for Aβ(1-42) by itself and 250 μM for Aβ(1-42):Aβ(1-40) ratio at 4:1. The supernatant after centrifugation was eluted from a Superdex 75 column and 0.5 ml fractions were collected. UV absorbance at 280 nm was monitored during the elution. The blue line indicates Aβ(1-42) by itself and the red line indicates Aβ(1-42):Aβ(1-40) ratio at 4:1.

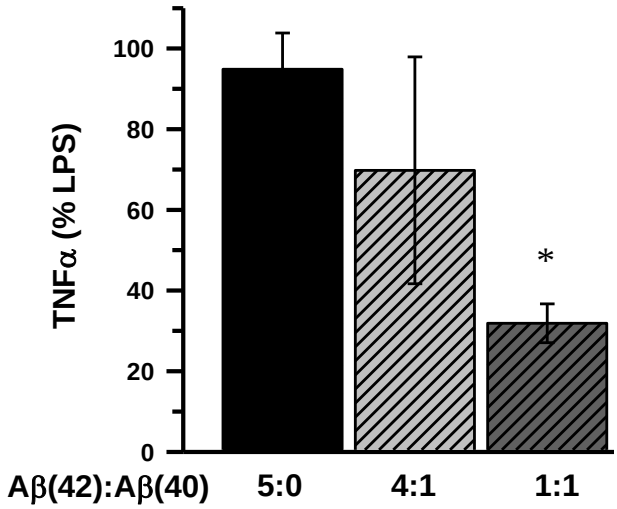

Figure 4.5. Stimulation of BV-2 microglia by SEC-isolated Aβ(1-42):Aβ(1-40) protofibrils. Aβ(1-42):Aβ(1-40) protofibrils formed and isolated in aCSF decrease in their ability to stimulate the microglia as the amount of Aβ(1-42) decreases. SEC-isolated protofibrils from Aβ(1-42):Aβ(1-40) ratios of 5:0, 4:1, and 1:1 in aCSF were incubated with BV-2 microglia at a final concentration of 15 μM (UV absorbance-determined) for 6 hours in serum-free medium. Secreted TNFα was measured by ELISA in the conditioned medium. Control treatments with an equal volume of aCSF were subtracted from Aβ-stimulated samples. Due to the measurements being on separate days and the variability of the cells the TNFα stimulated by the Aβ(1-42):Aβ(1-40) protofibrils is expressed as a percentage of that day's LPS TNFα response. 5:0 n=2 replicates, 4:1 n=5 replicates and 1:1 n=6 replicates. Statistics were compared to 5:0 SEC-isolated Aβ(1-42):Aβ(1-40) protofibril treatment (* $p < 0.005$).

concentrations being inadequate to obtain a final Aβ treatment concentration of 15 μM. However, previous data from our lab has shown that SEC-isolated Aβ(1-40) protofibrils are not able to stimulate microglia as well as SEC-isolated Aβ(1-42) protofibrils (Paranjape et al., 2012). Due to the experiments being performed on separate days the data was normalized to the % of the positive LPS control. This data shows that the decrease in Aβ(1-42):Aβ(1-40) ratio resulted in a decrease in effective stimulation of TNFα production in BV-2 microglia.

4.5 Aggregation of SEC-Isolated Aβ(1-42):Aβ(1-40) Monomer

A second set of the original Aβ(1-42):Aβ(1-40) ratios (Table 4.1) were SEC-isolated in order to study the aggregation of the SEC-isolated Aβ(1-42):Aβ(1-40) monomer. These Aβ(1-42):Aβ(1-40) ratio preparations were incubated for 4 hours before centrifugation and SEC-purification. Even though the incubation time was longer for the second set of Aβ(1-42):Aβ(1-40) ratios, each ratio still produced similar SEC-profiles as seen in Figure 4.1A.

ThT fluorescence was used to observe the increasing amount of β-sheet structure within each Aβ(1-42):Aβ(1-40) ratio monomer fraction over time, which is an indirect measure of aggregation. When measuring the ThT fluorescence of the SEC-isolated Aβ(1-42):Aβ(1-40) monomers, each sample was diluted to 40 μM in aCSF with 0.05% sodium azide, to prevent contamination, incubated at room temperature for 26 days and measured for ThT fluorescence every 1-2 days. The SEC-isolated 5:0 and 4:1 Aβ(1-42):Aβ(1-40) monomers showed a very rapid initial aggregation with no lag phase, whereas the SEC-isolated 1:1 Aβ(1-42):Aβ(1-40) monomer had a lag phase of 1 day,

compared to the SEC-isolated 1:4 and 0:5 Aβ(1-42):Aβ(1-40) monomers whose aggregation was much slower and had an obvious lag phase of 3 days. There was also an observable difference in the intensity of the ThT fluorescence/binding of the SEC-isolated Aβ(1-42):Aβ(1-40) monomers over time. The SEC-isolated 5:0 Aβ(1-42):Aβ(1-40) monomer produced the greatest amount of ThT fluorescence/binding, followed by the SEC-isolated 4:1 Aβ(1-42):Aβ(1-40) monomer and then the SEC-isolated 1:1 Aβ(1-42):Aβ(1-40) monomer. These three Aβ(1-42):Aβ(1-40) monomer ratios also showed a similar trend in their aggregation profile; after aggregation into the species with the greatest ThT binding, there was an observable decrease in the ThT fluorescence followed by stabilization over a period of several days. The SEC-isolated 1:4 and 0:5 Aβ(1-42):Aβ(1-40) monomer both showed similar aggregation trends and ThT fluorescence/binding intensities, eventually reaching a plateau that was lower than those found for the 5:0, 4:1, and 1:1 Aβ(1-42):Aβ(1-40) (Figure 4.6). Together this data shows that as the ratio of Aβ(1-42):Aβ(1-40) decreases the lag phase increases and the overall ThT fluorescence/binding decreases. The observations of increased lag-phase and reduced aggregation in these studies may be caused by either the combination of Aβ(1-40) monomer within the Aβ(1-42) monomer, or the overall reduction in Aβ(1-42) within the SEC monomer peak.

4.6 Aβ C-Terminal Selective ELISA of the SEC-Isolated Aβ(1-42):Aβ(1-40) Protofibrils and Monomers

Even though the original ratios contained a specific amount of Aβ(1-42) and Aβ(1-40), it was not entirely clear how much of each peptide populated the SEC-isolated protofibrils and monomers. In an attempt to observe how much Aβ(1-42) and Aβ(1-40)

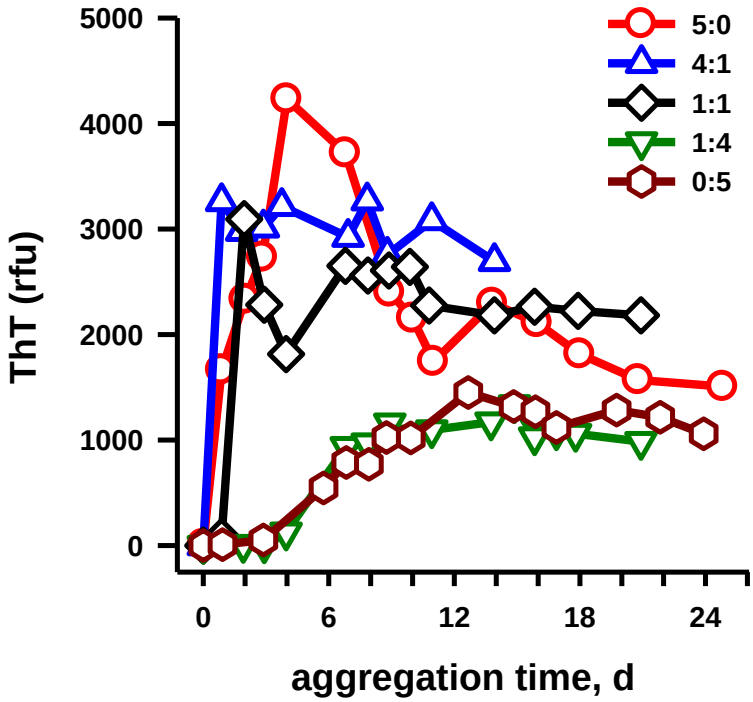

Figure 4.6. Aggregation of SEC freshly isolated Aβ(1-42):Aβ(1-40) monomer. Freshly isolated Aβ(1-42):Aβ(1-40) monomer aggregates faster and with a higher ThT fluorescence as the ratio of Aβ(1-42):Aβ(1-40) increases. The Aβ(1-42):Aβ(1-40) monomer peak fractions were diluted to 40 μM in aCSF with 0.05% NaN3. The Aβ(1-42):Aβ(1-40) monomer samples were allowed to incubate at room temperature for 14-26 days. At different time points each Aβ(1-42):Aβ(1-40) monomer sample was diluted to 5 μM in aCSF containing 5 μM ThT and fluorescence emission was measured as described in the Chapter 2, section 2.9.

were incorporated into each SEC-isolated Aβ(1-42):Aβ(1-40) protofibril and monomer peak, an Aβ C-terminal selective ELISA was designed. The Aβ ELISA was designed to distinguish the difference between the C-terminus of Aβ(1-40) and Aβ(1-42), with the difference being the addition of two amino acids, isoleucine and alanine, at the C-terminus of Aβ(1-42), within a single mixed Aβ sample. The ELISA was performed like a standard sandwich ELISA, expect the capture antibodies were selective for either Aβ(1-42) or Aβ(1-40) and the detection antibody, Ab5, which recognizes all Aβ, was conjugated to HRP.

SEC-peak fractions (monomer and protofibril) of the mixed Aβ samples were analyzed by the C-terminal selective ELISA to directly measure the actual ratio of Aβ(1-42):Aβ(1-40) contained in each sample. Also both set of SEC-purified Aβ(1-42):Aβ(1-40) were examined and produced similar observations. As expected both the monomer and the protofibril of the 5:0 Aβ(1-42):Aβ(1-40) ratio was only detected by the Aβ(1-42) ELISA (Table 4.3). The 4:1 Aβ(1-42):Aβ(1-40) ratio showed that the SEC-protofibrils only contained Aβ(1-42), while the monomer contained a lower ratio of Aβ(1-42):Aβ(1-40) (1.56) than the protofibrils, but still contain more Aβ(1-42) than Aβ(1-40) (Table 4.3). The 1:1 Aβ(1-42):Aβ(1-40) ratio displayed only trace amounts of Aβ(1-40) compared to Aβ(1-42) in the SEC-isolated protofibrils, while the monomer had a much lower ratio of Aβ(1-42):Aβ(1-40) (0.57) and actually contained more Aβ(1-40) than Aβ(1-42) (Table 4.3). The SEC-isolated monomer of the 1:4 Aβ(1-42):Aβ(1-40) ratio exhibited an even smaller ratio of Aβ(1-42):Aβ(1-40), again showing that the monomer contained much more Aβ(1-40) than Aβ(1-42) (Table 4.3). While the protofibril of the 1:4 Aβ(1-42):Aβ(1-40) ratio and the 0:5 Aβ(1-42):Aβ(1-40) protofibril and monomer

Table 4.3. Measured Aβ(1-42):Aβ(1-40) ratios in protofibril and monomer SEC peaks.

Dry Aβ(1-42):Aβ(1-40)	Protofibril Peak	Monomer Peak
5:0	>10[a]	>10[a]
4:1	>10[a]	1.56
1:1	>10[b]	0.57
1:4	ND	0.18
0:5	ND	ND
a = no Aβ(1-40) detected	b = trace Aβ(1-42) detected	c = no Aβ(1-42) detected

samples remain to be analyzed, the current C-terminal selective ELISA aids in explaining some of the observed characteristics of the SEC-isolated protofibrils and monomers displayed in Figures 4.1-4.6. This data also further suggests that the Aβ(1-40) does not have a significant role in the formation of Aβ(1-42) protofibrils, due to the majority of the Aβ(1-40) remaining in the monomer SEC-peak fractions.

4.7 Discussion

The current report examined different ratios of Aβ(1-42):Aβ(1-40) in order to explore the effect of Aβ(1-40) on Aβ(1-42) aggregation. *In vivo* analysis has proven that it is more physiologically relevant to fully understand the mechanistic details of Aβ(1-42):Aβ(1-40) ratios rather than one peptide by itself. The brain of AD patients contains several different aggregate morphologies, including oligomers, protofibril and fibrils, consisting of Aβ(1-40) co-localized with Aβ(1-42) (Harper and Lansbury, 1997, Harper et al., 1999, Kayed et al., 2003, Selkoe, 2001, Selkoe, 2004, Walsh et al., 1997, Walsh et al., 1999). Both peptides are commonly produced and are present in all individuals (Selkoe, 1998, Selkoe, 2001) and their chemical structures are very similar, differing only by two amino acids, isoleucine and alanine. However, Aβ(1-42) is known to be more fibrillogenic and aggregation-prone, compared to Aβ(1-40) (Pauwels et al., 2012).

The studies presented here showed that reconstitution of dry Aβ(1-42):Aβ(1-40) peptide mixtures at different ratios resulted in immediate protofibril formation. However, SEC-purification of the mixed solutions indicated that as the ratio of Aβ(1-42):Aβ(1-40) decreased, the amount of SEC-isolated protofibrils decreased and the monomer increased

(Figure 4. 1 and Table 4.1). Similar results were observed in previous studies, in our laboratory, when observing the SEC-purification profiles of the individual peptides (Paranjape et al., 2012). Subsequent SEC studies showed that if the Aβ(1-42) concentration was held constant while increasing the Aβ(1-40) concentration, there was no change in the amount of SEC-isolated protofibrils formed, while monomer increased (Figure 4.4). Other than Jan et al., 2008, to my knowledge this report is one of the only studies that observe the difference between Aβ(1-42):Aβ(1-40) ratios, where one peptide was held constant while the other peptide and the total Aβ concentration were variable. Jan and colleagues similarly suggested that Aβ(1-40) monomer does not interfere with Aβ(1-42) ability to form higher order prefibrillar aggregates, however it does interfere with Aβ(1-42) ability to form mature fibrils (Jan et al., 2008). In general, Aβ(1-40) has been shown to effect Aβ(1-42) fibril formation, including kinetic stability, solubility, and morphological properties and its induced neurotoxicity (Chang and Chen, 2014, Jan et al., 2008). Even though some earlier studies show that Aβ(1-40) inhibits Aβ(1-42) aggregation by preferentially binding to the Aβ(1-42) protofibril (Yin et al., 2007), the protofibril formation and SEC-purification data in this report, suggests that Aβ(1-40) has very little contact with Aβ(1-42) during protofibril formation, while others have suggested that the two peptides interact, but prefer interactions with the same peptide over interactions between different ones (Pauwels et al., 2012).

Other experiments were conducted during this study to examine the biophysical properties of the formed and SEC-isolated Aβ(1-42):Aβ(1-40) ratio protofibrils. During these biophysical studies, DLS and ThT fluorescence were used to observe the protofibrils' R_H and β-sheet formation. The R_H measurement for the SEC-isolated 5:0

Aβ(1-42):Aβ(1-40) protofibrils (21 nm) was similar to that measured previously of the Aβ(1-42) protofibrils (21.9 ± 4.0 std nm for n-5 SEC-purifications) (Paranjape et al., 2013). However, the R_H slightly decreased as the ratio of Aβ(1-42):Aβ(1-40) decreased (Figure 4.2 and Table 4.2). A more distinct decrease was observed in the amount of ThT fluorescence (Figure 4.3). Due to the conclusions drawn from the SEC-purification profile comparisons and the C-terminal selective ELISA, it is likely that the slight decrease observed by the DLS and the decrease in ThT fluorescence measurements are caused by the overall decrease in the Aβ(1-42) concentration. However, Jan et al., 2008 attributed the decrease of ThT fluorescence to the Aβ(1-40) reducing the ability Aβ(1-42) to form mature fibrils (Jan et al., 2008).

Early data examining cellular damage caused by Aβ indicated that the insoluble fibrillar Aβ species caused the most damage, including cytokine production (Meda et al., 1995, Yates et al., 2000) and interaction with proinflammatory receptors and pathways (Bamberger et al., 2003, Bianca et al., 1999, Fassbender et al., 2004, McDonald et al., 1998, Stewart et al., 2010). However, recently it has been found that the more diffuse soluble oligomeric Aβ intermediates actually cause the most damage in AD by causing neuronal and/or synaptic dysfunction (Haass and Selkoe, 2007, Kayed et al., 2003, Lee et al., 2006). We have also recently confirmed that the Aβ(1-42) protofibrils, but not the Aβ(1-42) fibrils, are robust activators of microglia (Paranjape et al., 2012). This present study again shows that the Aβ protofibrils are able to significantly stimulate microglia, however the extent of activation decreases as the ratio of Aβ(1-42):Aβ(1-40) decreases (Figure 4.5).

Several groups have used the technique of ThT fluorescence as a way to observe Aβ aggregation, typically displaying a sigmoidal curve, which is characteristic for aggregating proteins (Harper and Lansbury, 1997). Our lab has previously shown a ThT fluorescent profile of SEC-isolated Aβ(1-42) monomer, which showed a lag phase of 14 days and aggregation over 3 days (Coalier et al., 2013). This technique has also been used for comparing the aggregation properties of the different mixed Aβ(1-42):Aβ(1-40). However my studies were constructed differently than other published studies by using SEC-isolated Aβ(1-42):Aβ(1-40) monomer compared to freshly reconstituted Aβ(1-42):Aβ(1-40), which could contain a polydisperse mixture of Aβ spices. The studies using freshly reconstituted Aβ(1-42):Aβ(1-40) concluded that equally mixing Aβ(1-42) and Aβ(1-40) had the lowest ThT fluorescence even compared to an all Aβ(1-40) preparation (Chang and Chen, 2014), while another study showed that lower ratios of Aβ(1-42):Aβ(1-40) had longer lag phases, but increased elongation rates (Kuperstein et al., 2010). However, the aggregation studies of SEC-isolated Aβ(1-42):Aβ(1-40) monomer presented here indicate that as the ratio of Aβ(1-42):Aβ(1-40) decreased, meaning the amount of Aβ(1-40) increases in the dry peptide ratio, the lag phase and aggregation time increased (Figure 4.6). If the specific ratio of Aβ(1-42):Aβ(1-40) dictates the amount of damage within the brains of AD patients then these observations may have important implications toward a potential therapeutic target.

The Aβ C-terminal selective ELISA aided in explaining the results observed by the SEC-purification, biophysical analysis and ThT aggregation of the monomer. The ELISA indicated that the Aβ(1-40) may not have much interaction with the Aβ(1-42)

during protofibril formation. This conclusion is suggested by a minimal amount of Aβ(1-40) observed in the SEC-purified protofibrils and a decrease in the

ratio of Aβ(1-42):Aβ(1-40) in the SEC-isolated monomers.

Overall, the data presented here has shown that the reconstitution of dry Aβ(1-42):Aβ(1-40) peptide mixtures at different ratios resulted in immediate protofibril formation. However, SEC-purification of the mixed Aβ(1-42) and Aβ(1-40) peptides showed that as the ratio of Aβ(1-42):Aβ(1-40) decreased, the amount of SEC-isolated protofibrils decreased and monomer increased. While a second SEC comparison experiment revealed that if the Aβ(1-42) concentration was held constant while increasing the Aβ(1-40) concentration the amount of SEC-isolated protofibrils formed would remain the same, while monomer increased. The Aβ C-terminal-selective ELISA in combination with the SEC-profiles as well as other biological and biophysical studies suggested that Aβ(1-40) may not significantly interact with Aβ(1-42) during protofibril formation. The observations made from data presented here could assist in the development of a more physiological relevant therapeutic target against mixed Aβ ratios.

CHAPTER 5

THE EFFECT OF GOLD TEXTURED SURFACES AND AN LPS ANTAGONIST ON CELLULAR PROCESSES

5.1 Introduction

Recently, significant efforts have focused on the development of new biomaterials or biomembrane-mimicking substrates/interfaces, with the ability to monitor, investigate, and modulate biological behavior. This effort may improve our ability to repair damaged tissues due to trauma, disease, or congenital abnormalities. However, these interfaces must be assessed for biocompatibility properties including *in vivo* stability, stimulation of the host immune response and active interaction with living cells (Zhong and Bellamkonda, 2008). Gold has been investigated for many years as a potential biomaterial in biomedical devices and as a cell culture substrate. The advantages of gold comes from its chemical stability, high conductivity (Shulga et al., 2007) and the advances in gold-thiol chemistry for presenting ligands or immobilizing proteins for cell adhesion studies (Mrksich, 2009, Mrksich and Whitesides, 1996, Tan et al., 2008, Tan et al., 2011). Numerous examples of cellular studies on gold or chemically-modified gold substrates have been reported and these studies demonstrate that cell adhesion is influenced by the size and shape of the gold surface along with the chemical and protein composition and the mechanical properties (Nikkhah et al., 2012, Park and Shuler, 2003) of the nanoparticles (Hutter et al., 2010).

Nanoporous gold is a member of the mesoporous metals that have pores and ligaments ranging from tens to hundreds of nanometers in scale. These features are of interest due to the potential applications of the nanoporous gold in biosensors (Pandey et al., 2012, Shulga et al., 2007), catalysis (Wittstock et al., 2010) and cell culture platforms. Due to nanoporous gold being resistant to corrosion and oxidation along with its porosity makes it a unique material and a good candidate for being used as a potential platform for cellular adhesion and drug delivery (Seker et al., 2012).

In the following studies, four substrates, including glass, ultra-flat gold (UF-Au), ultra-thin nanoporous gold (UT np-Au) and nanoporous gold monolith (np-Au) (all produced by Dr. Y.H. Tan), were evaluated for their ability to support microglial survival, growth and functional cytokine production upon stimulation in the presence and absence of LPS. LPS is a vital component of the outer membrane of gram-negative bacteria (Kaeothip et al., 2011) and is a potent immune system stimulant commonly used for inducing microglial activation (Hanisch and Kettenmann, 2007, Kloss et al., 2001, Paranjape et al., 2012). During the duration of this project, Dr. Y.H. Tan produced all surfaces necessary and performed all the imaging techniques, while I performed all cellular plating and further biocompatibility studies.

Scanning electron microscopy (SEM), performed by Dr. Y.H. Tan, was also used to evaluate whether microglia morphology is disturbed by the varied surfaces tested. UF-Au substrate was generated using a well-known gold deposition technique, which results in a 200 nm thick layer of gold on mica that can be subsequently glued to a glass coverslip (Pandey et al., 2012). As a control, the glass coverslip was used in these experiments. Since glass is a poor conductor, about 10 nm of gold was splattered on one

side of the glass coverslip in order to enable SEM characterization. The porous metals, UT np-Au and np-Au, were formed by dealloying to exhibit a completely irregular morphology for both the ligaments and pore channels of the two metallic gold surfaces. The average pore diameter and ligament dimension for UT np-Au was 54.3 ± 22 nm and 57.5 ± 20 nm, respectively; whereas the np-Au monolith plate had an average pore diameter and ligament dimension of 35.3 ± 19 nm and 45.1 ± 26 nm, respectively.

Due to the fact that the nanoporous gold substrates were prepared by acid dealloying allows for the possibility of residual less noble metals to form metal oxides and disrupt normal cellular biology. This could cause toxicity to the cells by interfering with metabolic processes or by causing oxidative stress via metal-induced ROS (Ercal et al., 2001, Wataha et al., 1994). To rule out the presence of high amounts of residual metals remaining after the acid dealloying process, energy dispersive X-ray spectroscopy (EDS) analysis was performed by Dr. Y.H. Tan to determine the composition of metals, such as gold, copper and silver on the gold or nanoporous gold substrates. Based on the four EDS collected by Dr. Y.H. Tan, various small amounts of residual metals were present on these substrate surfaces. The EDS peaks for copper (0.93 and 8.04 keV) and silver (2.98 keV) were relatively insignificant compared to gold. Therefore, the potential for silver or copper oxide toxicity or oxidative stress that may damage the cells is minimal. The knowledge obtained by these studies may have implications for the production of nanoelectronic devices to aid in the improvement of cell adhesion and drug discovery.

Separate studies were also completed in an effort to explore molecules that antagonize LPS signaling without activating an inflammatory cascade. This was

accomplished by the design of simplified Lipid A analogs by the Demchenko laboratory. The synthesis of these compounds enabled inhibition and toxicity studies to be completed in order to test different methyl glucopyranoside-amino acid conjugates. This project was a collaborative project among many different people. The Demchenko laboratory produced all necessary compounds, while the Nichols laboratory performed all cellular studies. Previous Nichols' research assistants started all the cellular assays on the first five compounds, while all my work was completed on the last compound (compound 24) and the positive control (Table 5.1).

5.2 Adherence of Microglia to Gold Substrate Surfaces

The ability of BV-2 microglia to adhere to glass and the different gold substrates was determined by quantifying the number of adherent microglia after plating of the cells and overnight incubation at 37 °C in 5% CO_2. Microglia adherence was exceptional for UF-Au, and UT np-Au (>94% adherent cells), but slightly lower for np-Au (83% adherent cells) compared to the control glass surface (Figure 5.1).

5.3 Viability of BV-2 Microglia Adhered to Different Gold Surfaces

In order to conclude whether or not the gold substrates were toxic to the BV-2 microglia, an XTT assay was performed to determine the cell viability. The standard XTT assay relies on mitochondrial-mediated reduction of XTT by nicotinamide adenine dinucleotide (NADH) (Berridge et al., 2005). This method generates a water-soluble, orange-colored reduced formazan product. Since this conversion only occurs in viable cells, the reduced orange formazan solution can be quantified spectrophotometrically at

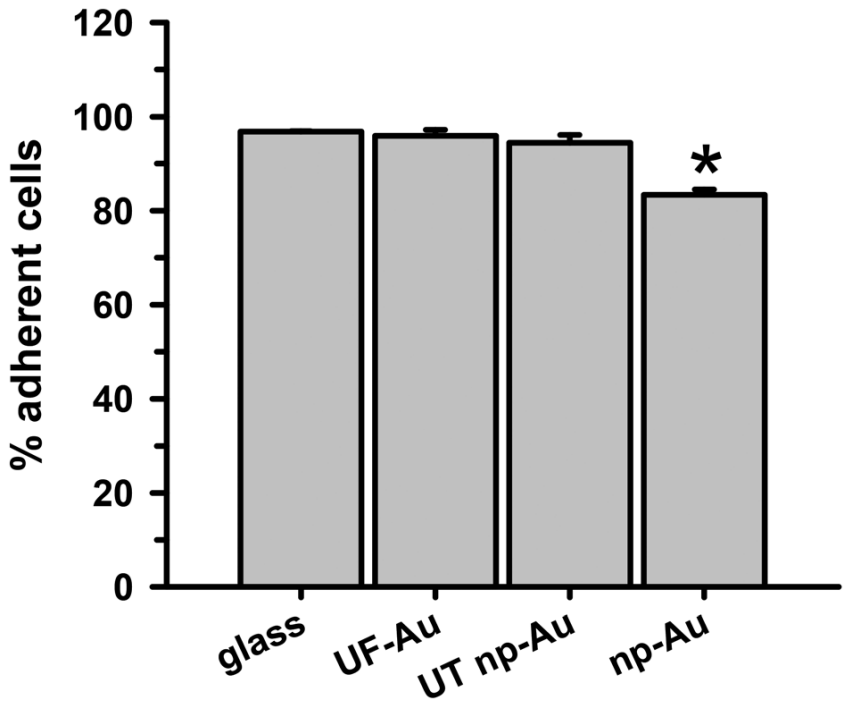

Figure 5.1. Ability of microglia to adhere to different substrates. BV-2 microglia (2 x 10^5 cells) were plated on different substrates (n=4 for each surface) and incubated overnight at 37 °C and 5% CO_2 to allow for cell adherence. The number of adherent cells was determined as described in Chapter 2, section 2.8.3. Data and error bars represent the mean and standard error for the 4 trials in one experiment. A statistically significant difference, using a student t-test, was found in microglia adherence between glass and np-Au (*$p < 0.001$).

an absorbance of 467 nm. Microglia attached to glass, UF-Au, and UT np-AU produced significant amounts of reduced XTT (Figure 5.2, black bars); meaning very little toxicity was observed. However, the amount of reduced XTT produced by the cells incubated on np-Au was significantly less compared to the other surfaces. Control wells, which were cell-free, but contained each substrate and XTT, were also tested and showed very little background levels of reduced XTT for each surface (Figure 5.2, gray bars). This was expected, as the blank substrates used in this investigation are not known to react or cause reduction of XTT. The low absorbance observed for the microglia on np-Au monolith was rather unexpected since the np-Au monolith contains a similar porous morphology as the UT np-Au substrate. The cell viability data indicated that the microglia on np-Au monolith were metabolically compromised despite looking morphologically normal by SEM and having similar adherence properties to the other substrates. A second possibility was that the thickness of the np-Au monolith interfered with the production or detection of reduced XTT. Although gold is known for its inertness, either flat or in the presence of variable porosity, this scenario was possible due to the lower background levels of reduced XTT observed for the np-Au control compared to the other substrates (Figure 5.2).

Due to the potential interference of the np-Au monolith substrate with the XTT assay, an alternative method of cell viability was used to test the viability of microglia on the substrates. The alternative method was an LDH release assay, where the presence of LDH in the medium indicates the leakage of intracellular LDH from the cells due to disruption or damage of the membrane. Following incubation of microglia with the various substrates, the cell culture media was collected and centrifuged and then the cell-

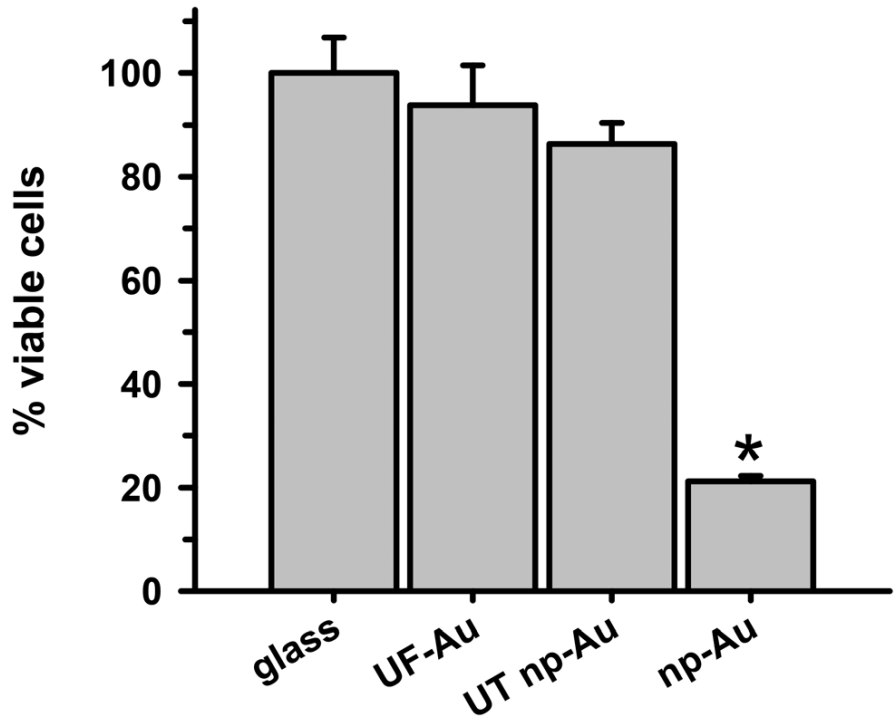

Figure 5.2. Analysis of microglia viability by XTT assay. BV-2 microglia were plated overnight to allow cell adherence followed by incubation for 24 hour at 37 °C in 5% CO_2, the medium was removed and cell viability was assessed using a XTT assay as described in Chapter 2, section 2.8.1. Reduced XTT absorbance was measured at 467 nm. % cell viability was determined by comparing metabolism of reduced XTT by microglia on UR-Au, UT np-Au, and np-Au to microglia on glass. Data and error bars represent the mean and standard error for 12 measurements for each condition over two separate experiments. A statistically significant difference was found in microglia viability between glass and np-Au (*$p < 0.001$). The other data points were not statistically different from each other.

free supernatant was examined for LDH activity (Figure 5.3). Minimal LDH activity was observed in the microglia medium after incubation of all four substrates (Figure 5.3). In particular, the np-Au monolith substrate did not elicit LDH release from the adherent microglia indicating that the np-Au monolith was not toxic to microglia. Saponin, a known cellular toxin via cholesterol removal and membrane disruption, caused significant LDH release from the microglia cultured on glass and served as a positive toxic control in these experiments (Figure 5.3).

5.4 Microglial Proliferation on Gold Substrate Surfaces

Cell survival and proliferation are important criteria for substrate biocompatibility. In addition to morphology and toxicity, the four substrates used in this investigation were evaluated for their ability to support cell growth and proliferation. Time dependent studies of microglia seeded onto the four substrate surfaces were carried out at 24, 48 and 72 hours (Figure 5.4). Quantification of cell density on these surfaces over time indicated that the number of adherent microglia progressively increased on the flat substrate surfaces, as observed by glass and UF-Au. Microglia density more than doubled from the initial number of seeded cells on the flat surfaces (circles, triangles, Figure 5.4). An increase in microglia density was also observed on the UT np-Au substrate (squares, Figure 5.4) at the 48 hour time point; however, microglia density leveled off after that. The density of microglia cultured on the np-Au monolith (diamonds, Figure 5.4) after 24 hours of seeding was slightly less than the number of cells plated and did not increase or decrease over time. The difference in microglia growth was particularly striking at 48 hours between np-Au monolith and the other

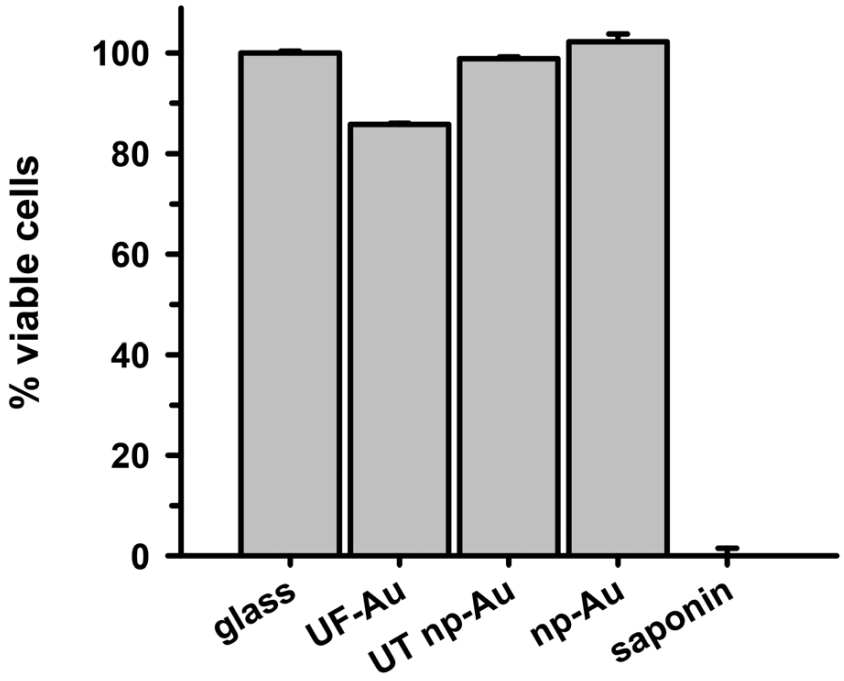

Figure 5.3. Cell cytotoxicity determined by LDH release assay. BV-2 microglia were plated overnight on the four substrate surfaces to allow adherence and then incubated for 24 hours as described in Chapter 2, section 2.8.2. Conditioned medium was collected for each sample and analyzed for LDH activity by measuring absorbance/min. The levels of LDH activity in the conditioned medium from untreated or saponin-treated microglia on glass were used as 100% or 0% viability controls, respectively. % cell viability for other samples was determined by comparing LDH activity to the controls. Data and error bars represent the mean and standard error for n=3 measurements in one experiment for all conditions.

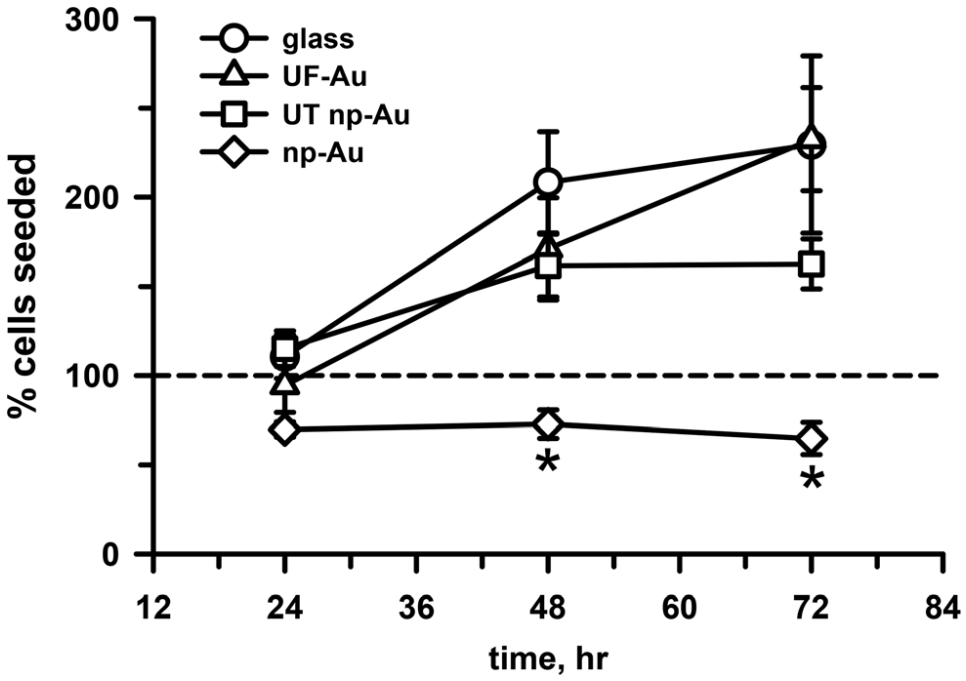

Figure 5.4. Microglial proliferation on different substrate surfaces. BV-2 microglia (2×10^5 cells, dashed line) were plated and allowed to grow at 37 °C and 5% CO_2 on glass (circles), UF-Au (triangles), UT np-Au (squares), and np-Au (diamonds) substrates. Cell number was quantified as described in Chapter 2, section 2.8.3 at 24, 48, and 72 hours. Data points and error bars represent the mean and standard error for n=7 measurements for each condition and time point from two separate experiments. Statistical analysis was performed using a student t-test and significant differences in microglia density were observed between np-Au and the other samples at both 48 and 72 hours (*$p < 0.001$). The other data points were not statistically different from each other.

substrates. The additional observation that continued growth on UT np-Au was also hindered suggested that the texture had a negative effect on the process of cell division. To ensure consistency in the given experiment, all microglial proliferation studies were carried out simultaneously and similar observation were reached with repeated experiments. The inability of the microglia to grow or proliferate on the texturized np-Au surface helped to explain the contradiction between the earlier XTT and LDH release toxicity results. Since the XTT assay was conducted after overnight plating along with an additional 24 hour treatment incubation, the number of microglia at the analysis time point showed to be significantly lower on the np-Au compared to the other substrates. The difference in microglia cell number could explain the noticeably lower reduced XTT absorbance values for np-Au in Figure 5.2.

5.5 Microglia Morphology upon LPS Stimulation

All of the above data has been in the absence of LPS to specifically show the effect of the different gold surfaces on BV-2 microglia; however, at the same time as the above experiments, samples in the presence of LPS were also observed. A time-dependent morphological examination of LPS-stimulated microglia on glass and gold surfaces was completed. The microglia were immobilized onto glass, UF-Au, UT np-Au, and np-Au, stimulated with 10 ng/mL LPS or vehicle control and imaged using SEM by Dr. Y.H. Tan at 0, 2, 6, 10 and 24 hour time points (Figure 5.5). Data for 2 and 10 hour time points are not shown. Supported by numerous experimental trials, the morphology of the microglia after LPS stimulation did not appear dramatically different compared to unstimulated microglia under the same culture conditions. The shapes of the cells were

observed by eye and it was found that the most frequently detected morphologies included rounded, elongated, unipolar and bipolar shapes. Most of the microglia contained many long and short processes (5 μm to 30 μm in length) projecting out of the cell body. Additionally, some cells contained a major process extending from one end of the microglial pole (unipolar), while other microglia had two major processes extending or stretching from two opposite ends of the microglial poles (bipolar) (Figure 5.5). The length of these major processes varied from cell to cell with some of the longest axes extending 20 μm or more. Another interesting observation observed during SEM analysis was the direct interactions between extended major and minor processes of neighboring microglia. These connecting microglia processes appeared to form conjoining junctions.

Additional studies were done to assess the adherence and viability of LPS-stimulated microglia on glass and gold substrate surfaces. These experiments were conducted in a similar manner to those presented in Figures 5.1-5.3 using adherence, XTT and LDH release assays. No differences were observed in microglia adherence or viability on the glass and gold surfaces between unstimulated and LPS-stimulated microglia (Figure 5.6).

5.6 Cytokine Release from Microglia Adhered to Substrate Surfaces

TNFα is a well-documented proinflammatory cytokine that is routinely monitored to reflect microglial activation. Therefore, the level of microglial activation can be assessed based on the amount of secreted TNFα (Paranjape et al., 2012, Syed et al., 2007). In order to determine if microglia adherence to texturized gold surfaces has an

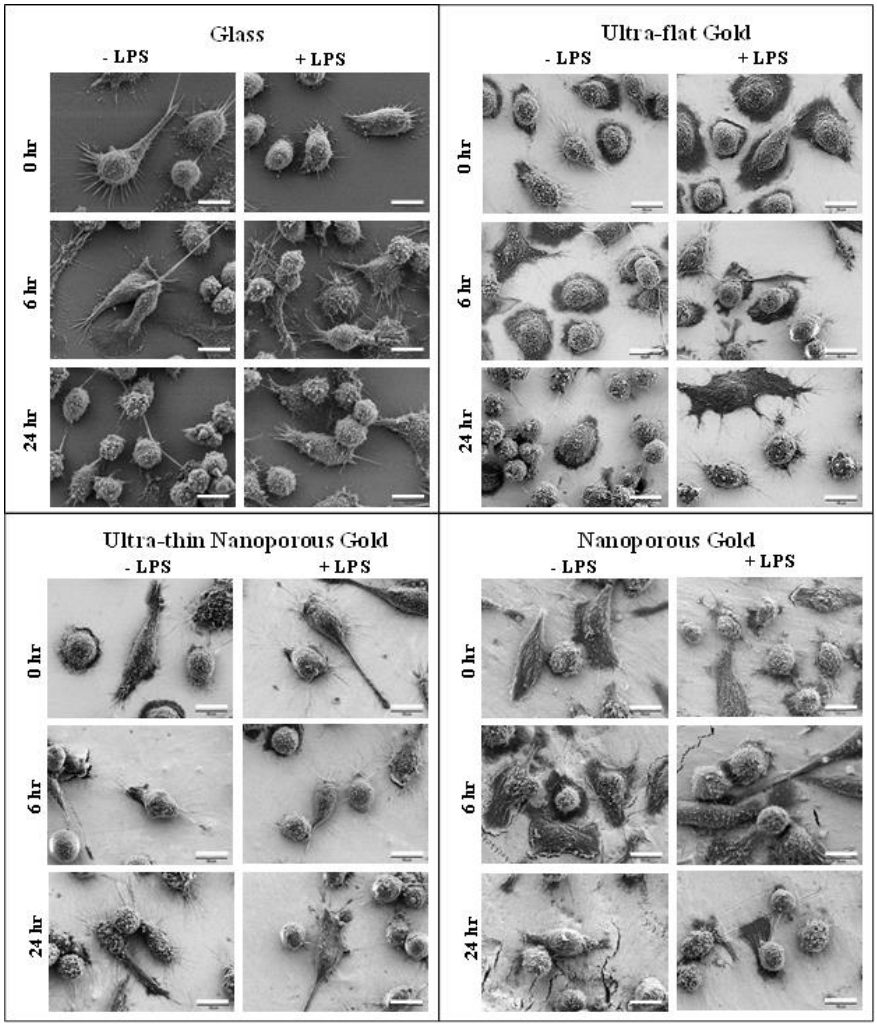

Figure 5.5. Microglia morphology on different substrate surfaces with and without challenge by LPS. BV-2 microglia were allowed to adhere to glass, UF-Au, UT np-Au and np-Au monolith followed by LPS (10 ng/ml) exposure for 0, 2, 6, 10 and 24 hours. At each time point the samples were prepared for SEM imaging. Images were captured at an accelerating voltage of 5 kV. Data for 2 and 10 hour time points are not shown for space reasons. All images are 58 μm × 43 μm in size. Scale bar equal to 10 μm.

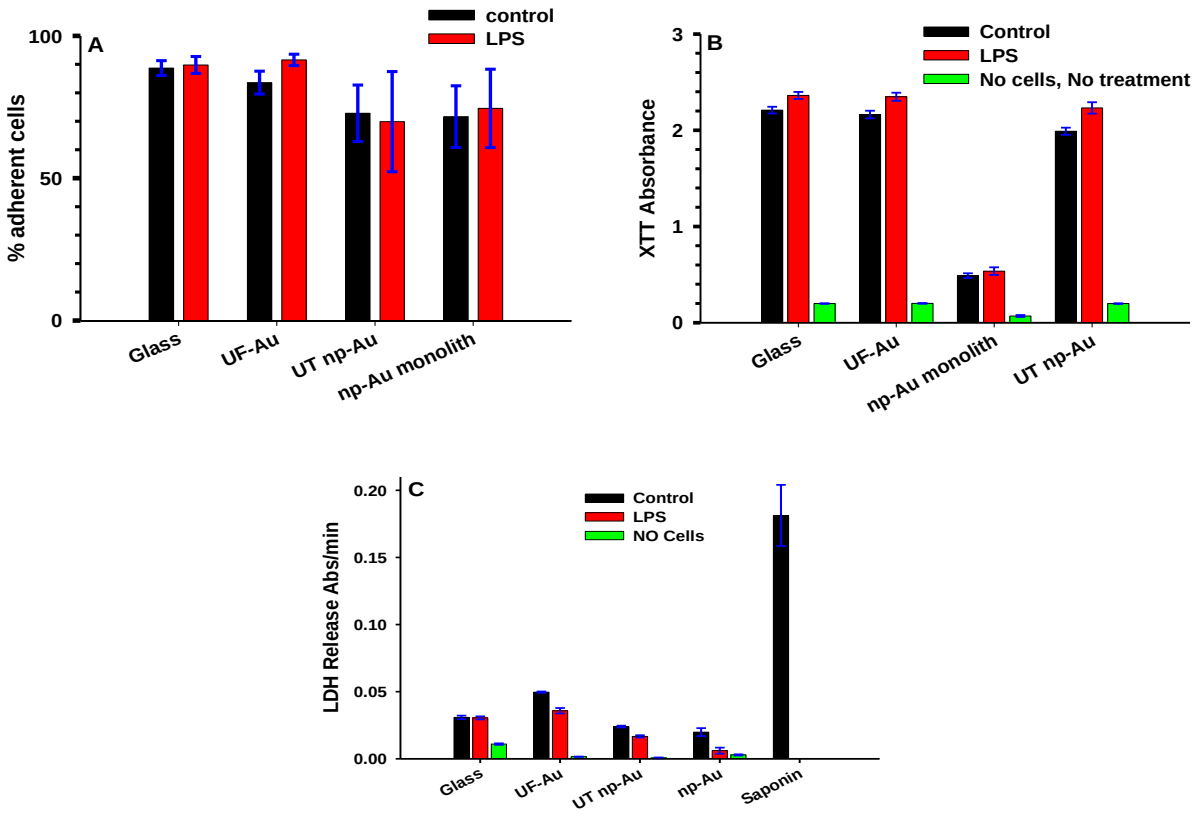

Figure 5.6. Adherence and viability of LPS-stimulated microglia on glass and gold substrate surfaces. BV-2 microglia (2 x 10^5 cells) were plated on different substrates, incubated overnight at 37 °C and 5% CO_2 to allow for cell adherence, treated with either control-water (black bars) or LPS (red bars) incubated again for 24 hours. Substrates alone were also tested in the absence of cells and treatment (green bars). Panel A. The number of adherent cells were determined as described in Chapter 2, section 2.8.3. Data and error bars represent the mean and standard error for n=3 and 2 for each surface during two separate experiments. Panel B. Cellular viability was assessed by removing the medium and preforming the XTT assay as described in Chapter 2, section 2.8.1. Reduced XTT absorbance was measured at 467 nm. Data and error bars represent the mean and standard error for 12 measurements (6 from two different experiments) for each condition. Panel C. Conditioned medium was collected for each sample and analyzed for LDH activity (absorbance/min) as described in Chapter 2, section 2.8.2. Data and error bars represent the mean and standard error for n=4 measurements for glass and n=3 for the other conditions.

impact on microglia inflammatory pathways, the microglia were seeded and adhered to glass, UF-Au, UT np-Au and np-Au substrates, stimulated with LPS (10 ng/mL) for 24 hours and then the levels of secreted TNFα were measured. This analysis revealed comparable levels of TNFα production by microglia among the four studied substrate surfaces (Figure 5.7). The findings indicated that these surfaces did not markedly alter microglial cytokine production and were biocompatible with microglia proinflammatory studies. There was only a small amount of TNFα production by the unstimulated microglia demonstrating that the substrates alone do not elicit a microglial response (Figure 5.7). Therefore, the TNFα production is solely caused by the LPS stimulation of the microglia without any interference from the substrates themselves. The ability of microglia to retain their normal specific response to LPS stimulation on glass and both flat and texturized gold surfaces was a good indicator of biocompatibility for functional microglial assays.

5.7 Biological Activity of LPS Antagonistic Compounds

One disease in which a drug delivery candidate has been studied in separate experiments by our laboratory in conjunction with the Demchenko laboratory is Septicemia. Septicemia is a world-wide health problem that is associated with mortality rates of 40-60%. It has been well-established that septic shock is initiated by the introduction of bacterial endotoxins, such as LPS, into the blood stream. In return, this causes cardiovascular problems like myocardial dysfunction, vascular tone and permeability abnormalities, as well as abnormal oxygen delivery and metabolism resulting in brain, heart, kidney and liver failure (Kaeothip et al., 2011).

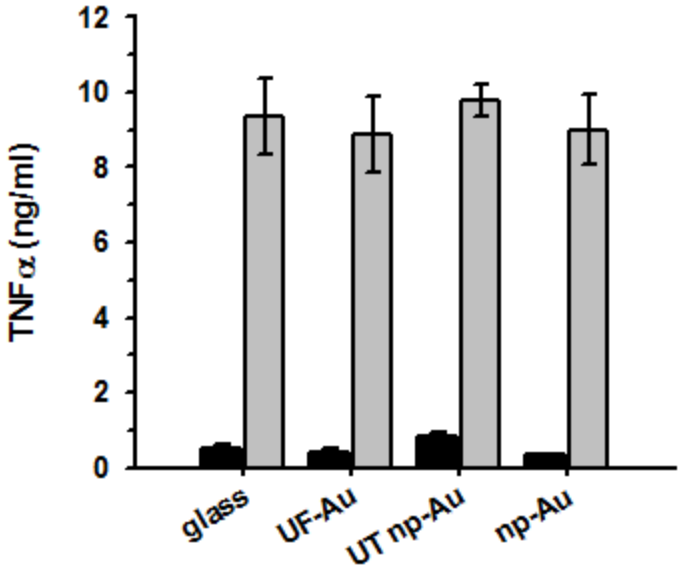

Figure 5.7. Microglial inflammatory response upon LPS stimulation. BV-2 microglia were allowed to adhere to the substrate surfaces overnight, treated with 10 ng/mL final concentration of LPS or the same volume of sterile water and incubated for 24 hours at 37 °C and 5% CO_2. The supernatant was then collected and analyzed for secreted TNFα by ELISA. The black bars represent unstimulated control microglia and the gray bars represent microglia stimulated with LPS. Values and error bars represent the mean and standard error for n=6 measurements for each condition over two separate experiments.

LPS is comprised of three structural regions (Figure 5.8). One region is known as the Lipid A region, which consist of a polyacrylated glucosamine disaccharide and is largely responsible for the toxic activity (Kaeothip et al., 2011). The effects of LPS are exerted through its interaction with LBP (LPS-binding protein). The LPS-LBP complex then interacts with CD14, followed by additional interactions with TLR4 and MD-2. As mention in Chapter 1, section 1.13.1, TLR4 is an integral membrane protein that transmits the activation signal into the cell and initiates an immune response resulting in the production of proinflammatory cytokines, such as TNFα (Kielian, 2006, Salminen et al., 2009).

The driving force of the experiments with LPS antagonists was to investigate the effect of the different synthetic manipulations within the LPS-antagonist compounds. The inhibitory activity for these compounds on the LPS-induced TNFα production were investigated by *in vitro* studies using THP-1 macrophages prepared as described in Chapter 2, section 2.1.4. These compounds were also tested in the absence of LPS to determine if the compounds alone showed any agonistic activity. Lastly, the compounds were examined for their toxicity to the macrophages by the use of the XTT assay. Together these measurements allowed for the explanation of whether the compounds are actually inhibiting the LPS- induced activity or if the pseudo-inhibition was actually caused by the toxicity of the compound to the cells.

The first compounds that were synthesized by the Demchenko lab and observed for its antagonistic, toxicity, and agonistic properties were compounds 10, 12 and 13 (Table 5.1). These three initial compounds showed no LPS-induced TNFα production inhibition, no toxicity and no agonistic activity in the concentration range of 0.1 nM to

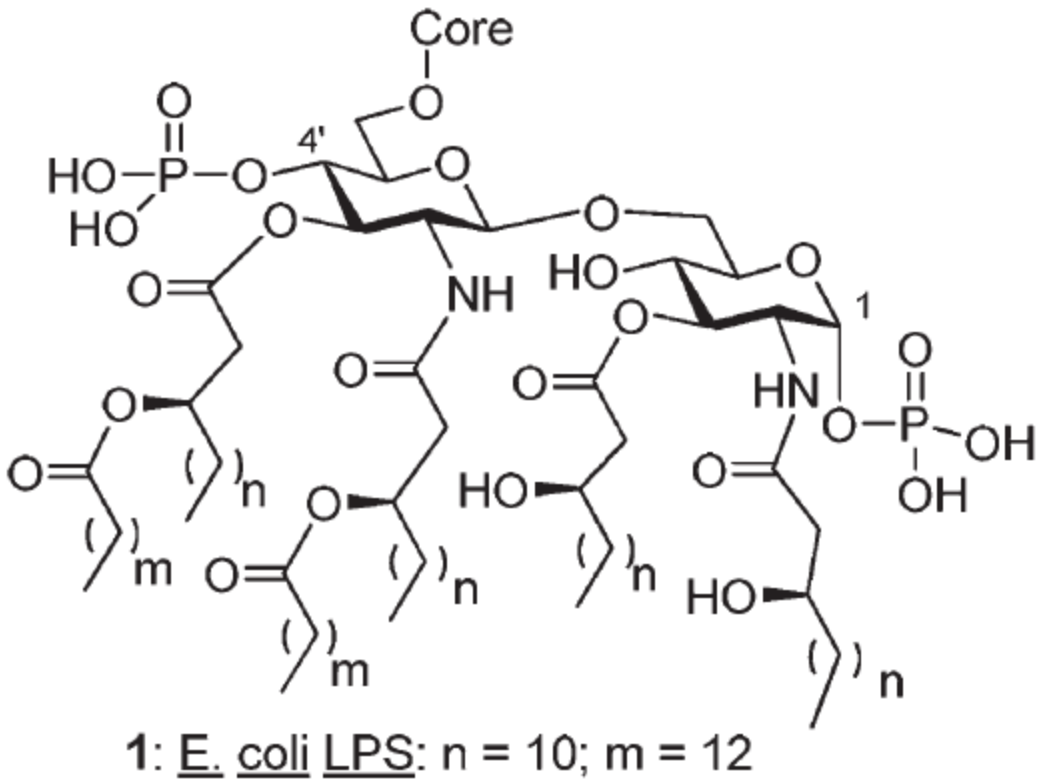

Figure 5.8. Structure of the Lipid A region of *E. coli* LPS (Kaeothip et al., 2011). Possible structural elements responsible for the endotoxic activity of Lipid A are the number and chain length of the fatty acid (lipids), the disaccharide core, and the 1, 4'-diphosphate groups (Kaeothip et al., 2011).

10 μM (Table 5.2). The key construct, compound 10, was slightly changed to obtain a free carboxylic group (compound 11, Table 5.1) and was then able to significantly inhibit the LPS-induced TNFα production at concentrations greater than 10 μM; however, the compound showed toxic effects toward the macrophages at concentrations greater than 30 μM (Table 5.2), therefore it was suggested that most of the antagonistic activity was related to the toxicity of the compound. After observing the antagonistic effects compound 11, two new compounds were synthesized, which were lipidated (compound 19, Table 5.1) and alkylated (compound 24, Table 5.1) analogs of compound 11. In addition to the above compounds, a standard positive control compound was also synthesized (compound 4, Table 5.1), as described by Peri et al., 2007 (Peri et al., 2007). For compound 19, the inhibition of the LPS-induced TNFα production was greatly enhanced and began at 550 nM. At the concentration of 5 μM, the inhibition was ~80% with no observed toxicity; however, the viability of the cells began to be compromised at higher concentrations and small amounts of agonistic activity was observed in the 10-30 μM range. Compound 24, on the other hand, was found to be a very effective inhibitor of the TNFα production induced by LPS (Figure 5.9). At 1 μM, the compound inhibited 70% of the LPS-induced TNFα production and eventually reached 90% inhibition by 40 μM. This particular compound also showed no toxicity towards the macrophages or agonistic properties in the concentration range of 0.2 to 40 μM. After curve fitting, the inhibition data it was observed that the IC_{50} of compound 24 was 470 nM. The results observed by compound 24 were superior to the results observed by the positive control (compound 4), which had an inhibition range of 3-10 μM, agonistic properties at concentrations greater than 10 μM and caused toxicity to the macrophages at

Table 5.1. Structure of Lipid A mimicking LPS antagonists.

Compound	Structure	Compound	Structure
10	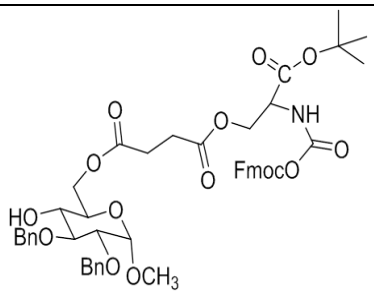	12	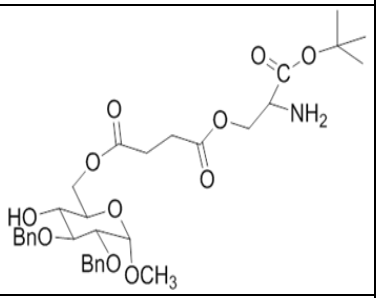
13	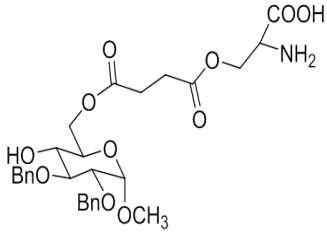	11	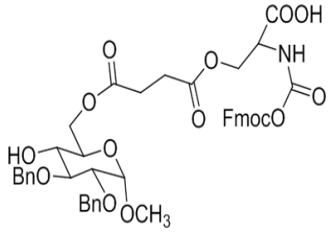
19	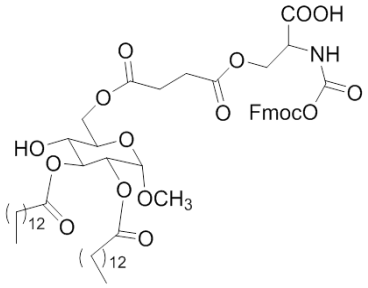	24	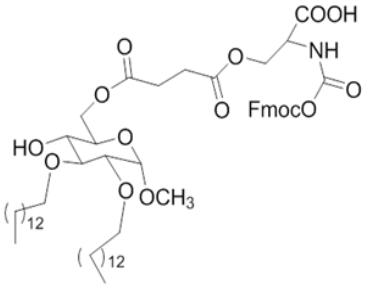
4	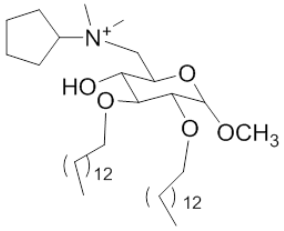	Benzyl ring -Bn	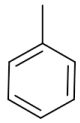
Fluorenylmethyloxycarbonyl -Fmoc			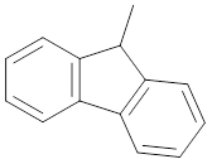

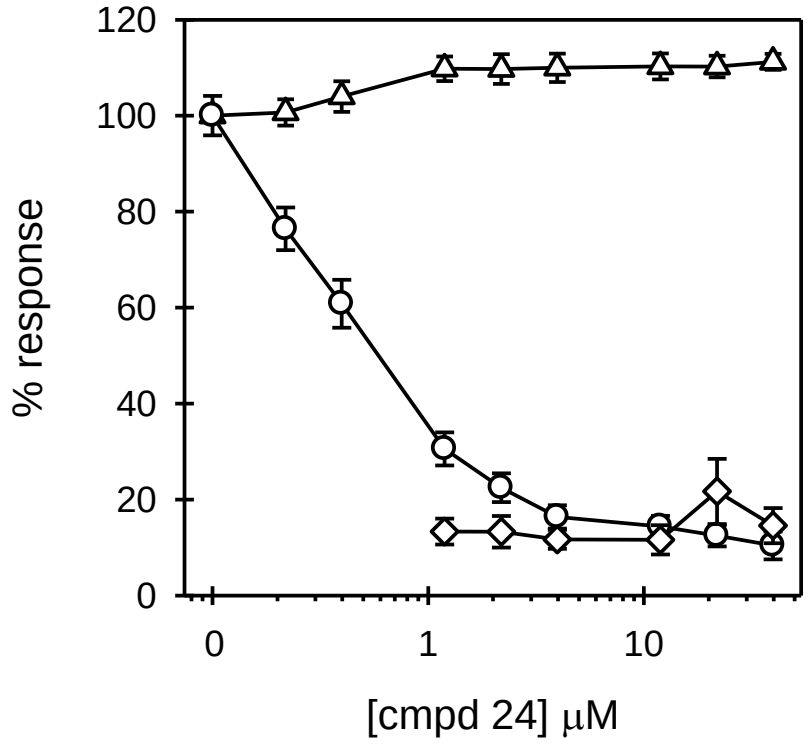

Figure 5.9. Compound 24 shows significant LPS-induced antagonistic activity without inducing toxicity to the macrophage cells. THP-1 macrophages were treated in 4 separate experiments, as described in Chapter 2, section 2.4, with increasing concentrations of Compound 24. Secreted TNFα levels were determined in the presence (circles, n=12) and absence (diamonds, n=8) of LPS. Cell viability (triangles, n=12) was also observed as described in Chapter 2, section 2.8.1.

concentrations greater than 30μM. Due to the inhibition qualities of compound 24 along with its nontoxic effects this compound proves to be a potential therapeutic option (Table 5.2).

The knowledge gained from the monosaccharide-based compounds described in these experiments adds to the work that has previously been published with disaccharide-based derivatives of Lipid A, however the monosaccharide-based compound, compound 24, is more potent than other published monosaccharide-based LPS inhibitors, but not quite as potent as some of the best disaccharide compounds (Kaeothip et al., 2011) . The noticeable increase in inhibition between compounds 19 and 24 compared to compounds 10, 12, 13, and 11 is likely caused by replacing the benzyl groups with acyl and alkyl fatty acid chains. By removing the benzyl groups and adding the acyl and alkyl fatty acids it may allow for less steric hindrance and more symmetrical similarities to the fatty acid chains located on the Lipid A region of LPS. The lipid portions of compounds 19 and 24 likely makes them better inhibitors due to their similarities to the lipid chains on Lipid A region of LPS and its known binding properties to CD14, where the lipid portion of the LPS binds in the hydrophobic pocket of CD14 (Kim et al., 2005). The noticeable increase in potency and decrease in toxicity by compound 24 with the alkyl chains (ether, R-O-R) compared to compound 19 with the fatty acyl chains (ester, R-COO-R) is a little less evident. The data suggests that the additional modifications further enhance the activity of the compound (Kaeothip et al., 2011). Even though the structural differences between compound 19 and 24 may be minimal, the differences in the activity/inhibition could be due to polarity. The ester linkage of compound 19 is slightly more polar then that of the ether linkage of compound 24. This additional element of hydrophobicity may

Table 5.2. Summary of biological activity in human macrophage cells.

Compound	TNFα inhibition (IC_{50})	Toxicity	Agonist activity
10, 12, 13	None observed	None observed	None observed
11	46 μM	>10 μM	None observed
19	3 μM	>10 μM	10-30 μM
24	0.5 μM	None observed	None observed
4	6 μM	>30 μM	30-100 μM

explain the increased potency of compound 24.

We are currently investigating the potential therapeutic and mechanistic properties of compound 24. *In vivo* inhibition studies of LPS-induced inflammation (TNFα production) in mouse peritoneal cavities were conducted externally at Washington Biotech. In preparation for these studies, the solubility and stability of compound 24 was ascertained. In order to prepare compound 24 for these studies, the compound was initially resuspended in 100% DMSO and then diluted further in PBS to make a final concentration of 10% DMSO. The 10% DMSO was recommended by Washington Biotech due to past observation of DMSO having anti-inflammatory properties (Repine et al., 1979). Because all of the above studies for compound 24 were performed at 100% DMSO until the addition into the cellular medium (0.67% DMSO), stability studies were executed on compound 24 in 10% DMSO over a 14 day period (Figure 5.10). The stability study provided evidence that compound 24 was stable in 10% DMSO by remaining in solution. The compound was then able to be sent to Washington Biotech for the *in vivo* studies (data not yet received). These studies will eventually be followed by mechanistic studies observing the inhibition of Pam_3CSK_4 and FSL-1, which are known TLR2/TLR1 and TLR2/TLR6 ligands, respectively, in human THP-1 macrophages, followed by mouse microglia.

5.8 Discussion

The above studies describe the general morphology of BV-2 murine microglia cultured on different gold substrate surfaces, along with the inhibition of LPS-induced TNFα production in THP-1 macrophages. The gold surface studies used UF-Au, UT np-

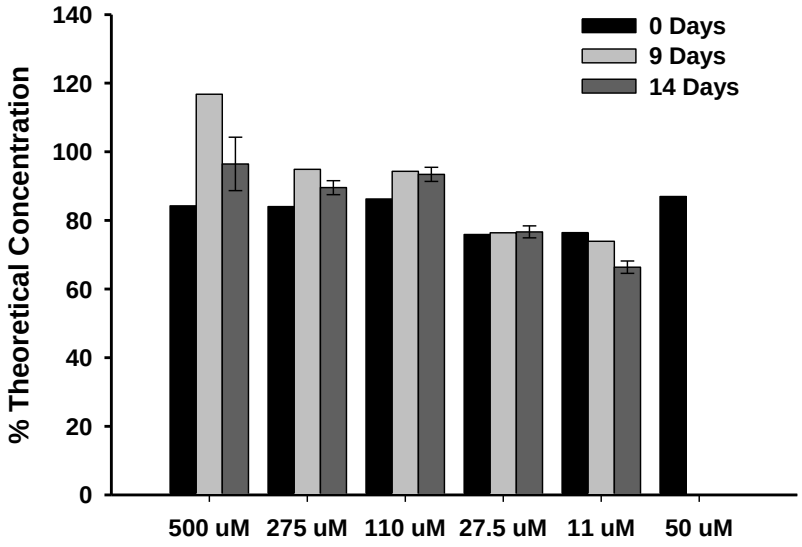

Figure 5.10. Stability of Compound 24 in 10% DMSO. Compound 24 was resuspended first in 100% DMSO and then further diluted by PBS for the final Compound 24 concentrations in 10% DMSO. The absorbance of Compound 24 (Fmoc group) at the indicated concentrations in 10% DMSO was measured at a wavelength of 301 nm three separate times over a 14 day time period.

Au, and np-Au substrates to investigate their biocompatibility with microglia. SEM provided high resolution images of microglia morphologies, while the *in vitro* studies demonstrated that microglia were able to adhere to flat glass and gold surfaces as well as texturized gold surfaces, although slightly less to the np-Au. The gold surfaces, even the highly grooved UF np-Au and np-Au monolith, were not toxic to microglia and did not interfere with LPS-induced TNFα production, suggesting good biocompatibility for microglial functional and morphological studies.

The use of flat gold as a substrate platform for cell culture has been widely reported in the literature due to its known biocompatibility (Voskerician et al., 2003, Wegener et al., 2000) and ease of modification for controlling protein adsorption and cell adhesion (Mrksich and Whitesides, 1996, Tan et al., 2008). Furthermore, a variety of gold-based compounds have been investigated for their interaction with immune cells and demonstrated the uptake of gold nanoparticles and microglial activation *in vivo*, via bioluminescence imaging (Hutter et al., 2010). In 2012, Seker et al., 2012 presented the first effort to utilize the high surface-to-volume ratio of np-Au compared to flat gold as a potential platform for culturing adherent astrocytes and investigate its feasibility for application as a drug delivery platform. Their results indicated that the porous surfaces were only minimally effected by either the adherent astrocytes or the cell culture media, making the porous surface a prospective material favorable for sustained drug delivery (Seker et al., 2012).

Microglia are known to respond to many signals in their physical environment, such as temperature, pressure and stiffness property of the substrate. Many of these signals induce microglial migration towards site of damage or injury in the CNS. A

recent study by Persheyev et al., 2011 indicated that BV-2 microglial morphology can be greatly impacted upon interaction with nanoparticles that possess micro-protrusions in the form of either sharp, homogeneous cones or spikes. The protrusions greatly impacted the overall cell morphology and the actin cytoskeleton (Persheyev et al., 2011). Yarmush and colleagues found that shorter processes were observed when astrocytes were cultured on porous gold surfaces (Seker et al., 2012). They suggested that the presence of "nanopits" in the nanoporous gold substrate may accommodate only a limited number of focal adhesion sites compared to the non-porous gold substrates, thereby reducing cellular spreading. The low impact of the flat and texturized gold surfaces on microglia morphology in the studies above may be because the gold pores and ligaments are significantly smaller than the reported dimensions in Persheyev et al., 2011; however, the presence of pores and the discontinuous gold area may hinder the formation of the focal adhesion sites needed for cell adhesion.

The use of SEM, performed by Dr. Y.H. Tan, at high resolution revealed very little distinction in microglia morphology, whether they were cultured on UF-Au, UT np-Au or np-Au. These observations may be due to minimal disruption of integrin clustering. It has been reported that nanotopography can greatly impact the focal adhesion of cells on the surface (Huang and Ding, 2010, Persheyev et al., 2011). The ideal spacing of ~70 nm between the neighboring features or ligands can promote integrin clustering, leading to an increase of focal adhesion complexes and an F-actin network. Larger separation distances between neighboring features or ligands tend to disrupt the integrin clustering and dramatically influence cell adhesion quality and dynamic cell behaviors (Huang and Ding, 2010). In the case of the np-Au substrate, the

ridged surface contains both irregular ligaments and pores; therefore, lacking a continuous smooth surface along with the presence of gold surface features (pores and ligaments) may not impact the exterior morphology of the microglia, but might directly affect the quality of focal adhesion or the number of focal adhesion sites. However, microglia adhesion to UT np-Au was not hampered and only slightly affected by np-Au (~14%).

The UT np-Au and np-Au substrates were biocompatible with cultured microglia in most of our assays except for cell growth or proliferation. UT np-Au was supportive of microglia proliferation during the first 48 hours, but did not sustain growth at later time points. Microglial growth was completely absent on the texturized np-Au surface, which is consistent with a previous reports using antiserum against CD11b to label endogenous microglia and macrophages from the retrieved implanted electrode from rats' brains. The study resulted in a higher number of adherent microglia observed on the smooth side of the electrode compared to the side which was composed of grooved structures, along with a reduction of cells as the implantation time increased (Leung et al., 2008).

The findings from these studies demonstrated that np-Au as a microglial cell culture platform was metabolically non-toxic, non-disruptive to the cellular membranes and compatible with microglia functional assays, but did not support microglial growth. UT np-Au, however, did support microglia growth and matched the other characteristics of np-Au. These materials may have potential as effective substrates for coating or constructing nanoelectronic devices, biosensors and functional biomaterial coatings for drug delivery.

The studies involving the LPS-antagonists provided new information about the structure-activity relationship of a novel class of compounds that mimic the Lipid A portion of LPS, which will have an impact on the treatment of patients diagnosed with septicemia. As a result, we have developed a plan to investigate the molecular mechanisms underlying the antagonistic actions of the synthetic Lipid A analogs.

BIBLOGRAPHY

Akiyama, H., Barger, S., Barnum, S., Bradt, B., Bauer, J., Cole, G. M., Cooper, N. R., Eikelenboom, P., Emmerling, M., Fiebich, B. L., Finch, C. E., Frautschy, S., Griffin, W. S., Hampel, H., Hull, M., Landreth, G., Lue, L., Mrak, R., Mackenzie, I. R., McGeer, P. L., O'Banion, M. K., Pachter, J., Pasinetti, G., Plata-Salaman, C., Rogers, J., Rydel, R., Shen, Y., Streit, W., Strohmeyer, R., Tooyoma, I., Van Muiswinkel, F. L., Veerhuis, R., Walker, D., Webster, S., Wegrzyniak, B., Wenk, G., and Wyss-Coray, T. (2000) Inflammation and Alzheimer's disease. *Neurobiology of aging* **21**, 383-421

Antzutkin, O. N., Leapman, R. D., Balbach, J. J., and Tycko, R. (2002) Supramolecular structural constraints on Alzheimer's b-amyloid fibrils from electron microscopy and solid-state nuclear magnetic resonance. *Biochemistry* **41**, 15436-15450

Antzutkin, O. N., Balbach, J. J., Leapman, R. D., Rizzo, N. W., Reed, J., and Tycko, R. (2000) Multiple quantum solid-state NMR indicates a parallel, not antiparallel, organization of b-sheets in Alzheimer's b-amyloid fibrils. *Proceedings of the National Academy of Sciences of the United States of America* **97**, 13045-13050

Arai, K., Nishida, J., Hayashida, K., Hatake, K., Kitamura, T., Miyajima, A., Arai, N., and Yokota, T. (1990) [Coordinate regulation of immune and inflammatory responses by cytokines]. *Rinsho byori. The Japanese journal of clinical pathology* **38**, 347-353

Balbach, J. J., Petkova, A. T., Oyler, N. A., Antzutkin, O. N., Gordon, D. J., Meredith, S. C., and Tycko, R. (2002) Supramolecular structure in full-length Alzheimer's b-amyloid fibrils: evidence for a parallel b-sheet organization from solid-state nuclear magnetic resonance. *Biophysical journal* **83**, 1205-1216

Balbach, J. J., Ishii, Y., Antzutkin, O. N., Leapman, R. D., Rizzo, N. W., Dyda, F., Reed, J., and Tycko, R. (2000) Amyloid fibril formation by Ab 16-22, a seven-residue fragment of the Alzheimer's b-amyloid peptide, and structural characterization by solid state NMR. *Biochemistry* **39**, 13748-13759

Bamberger, M. E., Harris, M. E., McDonald, D. R., Husemann, J., and Landreth, G. E. (2003) A cell surface receptor complex for fibrillar b-amyloid mediates microglial activation. *The Journal of neuroscience : the official journal of the Society for Neuroscience* **23**, 2665-2674

Barton, S. (2006) Microglia give amyloid plaques the brush off. *Nature reviews. Neuroscience* **7**, 254-255

Bateman, R. J., Xiong, C., Benzinger, T. L., Fagan, A. M., Goate, A., Fox, N. C., Marcus, D. S., Cairns, N. J., Xie, X., Blazey, T. M., Holtzman, D. M., Santacruz, A., Buckles, V., Oliver, A., Moulder, K., Aisen, P. S., Ghetti, B., Klunk, W. E., McDade, E., Martins, R. N., Masters, C. L., Mayeux, R., Ringman, J. M., Rossor, M. N., Schofield, P. R., Sperling, R. A., Salloway, S., and Morris, J. C. (2012) Clinical and biomarker changes in dominantly inherited Alzheimer's disease. *The New England journal of medicine* **367**, 795-804

Beffert, U., and Poirier, J. (1996) Apolipoprotein E, plaques, tangles and cholinergic dysfunction in Alzheimer's disease. *Annals of the New York Academy of Sciences* **777**, 166-174

Benzing, W. C., Wujek, J. R., Ward, E. K., Shaffer, D., Ashe, K. H., Younkin, S. G., and Brunden, K. R. (1999) Evidence for glial-mediated inflammation in aged APP(SW) transgenic mice. *Neurobiology of aging* **20**, 581-589

Benzinger, T. L., Gregory, D. M., Burkoth, T. S., Miller-Auer, H., Lynn, D. G., Botto, R. E., and Meredith, S. C. (1998) Propagating structure of Alzheimer's b-amyloid(10-35) is parallel b-sheet with residues in exact register. *Proceedings of the National Academy of Sciences of the United States of America* **95**, 13407-13412

Berridge, M. V., Herst, P. M., and Tan, A. S. (2005) Tetrazolium dyes as tools in cell biology: New insights into their cellular reduction. *Biotechnology Annual Review* **Volume 11**, 127-152

Betts, V., Leissring, M. A., Dolios, G., Wang, R., Selkoe, D. J., and Walsh, D. M. (2008) Aggregation and catabolism of disease-associated intra-Ab mutations: reduced proteolysis of AbA21G by neprilysin. *Neurobiology of disease* **31**, 442-450

Bianca, V. D., Dusi, S., Bianchini, E., Dal Pra, I., and Rossi, F. (1999) b-amyloid activates the O-2 forming NADPH oxidase in microglia, monocytes, and neutrophils. A possible inflammatory mechanism of neuronal damage in Alzheimer's disease. *The Journal of biological chemistry* **274**, 15493-15499

Bitan, G., Kirkitadze, M. D., Lomakin, A., Vollers, S. S., Benedek, G. B., and Teplow, D. B. (2003) Amyloid b -protein (Ab) assembly: Ab 40 and Ab 42 oligomerize through distinct pathways. *Proceedings of the National Academy of Sciences of the United States of America* **100**, 330-335

Bloom, G. S. (2014) Amyloid-b and Tau: The Trigger and Bullet in Alzheimer Disease Pathogenesis. *JAMA neurology*

Bolmont, T., Haiss, F., Eicke, D., Radde, R., Mathis, C. A., Klunk, W. E., Kohsaka, S., Jucker, M., and Calhoun, M. E. (2008) Dynamics of the microglial/amyloid interaction indicate a role in plaque maintenance. *The Journal of neuroscience : the official journal of the Society for Neuroscience* **28**, 4283-4292

Bradford, M. M. (1976) A rapid and sensitive method for the quantitation of microgram quantities of protein utilizing the principle of protein-dye binding. *Analytical biochemistry* **72**, 248-254

Bramblett, G. T., Goedert, M., Jakes, R., Merrick, S. E., Trojanowski, J. Q., and Lee, V. M. (1993) Abnormal tau phosphorylation at Ser396 in Alzheimer's disease recapitulates development and contributes to reduced microtubule binding. *Neuron* **10**, 1089-1099

Bruce, A. J., Boling, W., Kindy, M. S., Peschon, J., Kraemer, P. J., Carpenter, M. K., Holtsberg, F. W., and Mattson, M. P. (1996) Altered neuronal and microglial responses to excitotoxic and ischemic brain injury in mice lacking TNF receptors. *Nature medicine* **2**, 788-794

Buck, M. (1998) Trifluoroethanol and colleagues: cosolvents come of age. Recent studies with peptides and proteins. *Q Rev Biophys* **31**, 297-355

Burdick, D., Soreghan, B., Kwon, M., Kosmoski, J., Knauer, M., Henschen, A., Yates, J., Cotman, C., and Glabe, C. (1992) Assembly and aggregation properties of synthetic Alzheimer's A4/b-amyloid peptide analogs. *The Journal of biological chemistry* **267**, 546-554

Burnette, W. N. (1981) "Western blotting": electrophoretic transfer of proteins from sodium dodecyl sulfate--polyacrylamide gels to unmodified nitrocellulose and radiographic detection with antibody and radioiodinated protein A. *Analytical biochemistry* **112**, 195-203

Bush, A. I., Pettingell, W. H., Multhaup, G., d Paradis, M., Vonsattel, J. P., Gusella, J. F., Beyreuther, K., Masters, C. L., and Tanzi, R. E. (1994) Rapid induction of Alzheimer Ab amyloid formation by zinc. *Science (New York, N.Y.)* **265**, 1464-1467

Bustin, S. A., Benes, V., Nolan, T., and Pfaffl, M. W. (2005) Quantitative real-time RT-PCR--a perspective. *J Mol Endocrinol* **34**, 597-601

Buttini, M., Yu, G. Q., Shockley, K., Huang, Y., Jones, B., Masliah, E., Mallory, M., Yeo, T., Longo, F. M., and Mucke, L. (2002) Modulation of Alzheimer-like synaptic and cholinergic deficits in transgenic mice by human apolipoprotein E depends on isoform, aging, and overexpression of amyloid beta peptides but not on plaque formation. *The Journal of neuroscience : the official journal of the Society for Neuroscience* **22**, 10539-10548

Cagnin, A., Brooks, D. J., Kennedy, A. M., Gunn, R. N., Myers, R., Turkheimer, F. E., Jones, T., and Banati, R. B. (2001) *In-vivo* measurement of activated microglia in dementia. *Lancet* **358**, 461-467

Cameron, B., and Landreth, G. E. (2010) Inflammation, microglia, and Alzheimer's disease. *Neurobiology of disease* **37**, 503-509

Carrell, R. W., and Lomas, D. A. (1997) Conformational disease. *Lancet* **350**, 134-138

Chakrabarty, P., Ceballos-Diaz, C., Beccard, A., Janus, C., Dickson, D., Golde, T. E., and Das, P. (2010) IFN-gamma promotes complement expression and attenuates amyloid plaque deposition in amyloid beta precursor protein transgenic mice. *Journal of immunology (Baltimore, Md. : 1950)* **184**, 5333-5343

Chang, Y. J., and Chen, Y. R. (2014) The coexistence of an equal amount of Alzheimer's amyloid-b 40 and 42 forms structurally stable and toxic oligomers through a distinct pathway. *The FEBS journal*

Chapman, M. R., Robinson, L. S., Pinkner, J. S., Roth, R., Heuser, J., Hammar, M., Normark, S., and Hultgren, S. J. (2002) Role of Escherichia coli curli operons in directing amyloid fiber formation. *Science (New York, N.Y.)* **295**, 851-855

Chiti, F., Webster, P., Taddei, N., Clark, A., Stefani, M., Ramponi, G., and Dobson, C. M. (1999) Designing conditions for *in vitro* formation of amyloid protofilaments and fibrils. *Proceedings of the National Academy of Sciences of the United States of America* **96**, 3590-3594

Chou, K. C., Pottle, M., Nemethy, G., Ueda, Y., and Scheraga, H. A. (1982) Structure of b-sheets. Origin of the right-handed twist and of the increased stability of antiparallel over parallel sheets. *Journal of molecular biology* **162**, 89-112

Citron, M., Teplow, D. B., and Selkoe, D. J. (1995) Generation of amyloid b protein from its precursor is sequence specific. *Neuron* **14**, 661-670

Citron, M., Oltersdorf, T., Haass, C., McConlogue, L., Hung, A. Y., Seubert, P., Vigo-Pelfrey, C., Lieberburg, I., and Selkoe, D. J. (1992) Mutation of the b-amyloid precursor protein in familial Alzheimer's disease increases b-protein production. *Nature* **360**, 672-674

Citron, M., Westaway, D., Xia, W., Carlson, G., Diehl, T., Levesque, G., Johnson-Wood, K., Lee, M., Seubert, P., Davis, A., Kholodenko, D., Motter, R., Sherrington, R., Perry, B., Yao, H., Strome, R., Lieberburg, I., Rommens, J., Kim, S., Schenk, D., Fraser, P., St George Hyslop, P., and Selkoe, D. J. (1997) Mutant presenilins of Alzheimer's disease increase production of 42-residue amyloid b-protein in both transfected cells and transgenic mice. *Nature medicine* **3**, 67-72

Cleary, J. P., Walsh, D. M., Hofmeister, J. J., Shankar, G. M., Kuskowski, M. A., Selkoe, D. J., and Ashe, K. H. (2005) Natural oligomers of the amyloid-b protein specifically disrupt cognitive function. *Nature neuroscience* **8**, 79-84

Coalier, K. A., Paranjape, G. S., Karki, S., and Nichols, M. R. (2013) Stability of early-stage amyloid-b(1-42) aggregation species. *Biochimica et biophysica acta* **1834**, 65-70

Colton, C., and Wilcock, D. M. (2010) Assessing activation states in microglia. *CNS & neurological disorders drug targets* **9**, 174-191

Colton, C. A., Mott, R. T., Sharpe, H., Xu, Q., Van Nostrand, W. E., and Vitek, M. P. (2006) Expression profiles for macrophage alternative activation genes in AD and in mouse models of AD. *Journal of neuroinflammation* **3**, 27

Corder, E. H., Saunders, A. M., Strittmatter, W. J., Schmechel, D. E., Gaskell, P. C., Small, G. W., Roses, A. D., Haines, J. L., and Pericak-Vance, M. A. (1993) Gene dose of apolipoprotein E type 4 allele and the risk of Alzheimer's disease in late onset families. *Science (New York, N.Y.)* **261**, 921-923

Coulson, E. J., Paliga, K., Beyreuther, K., and Masters, C. L. (2000) What the evolution of the amyloid protein precursor supergene family tells us about its function. *Neurochemistry international* **36**, 175-184

Cui, Y., Le, Y., Yazawa, H., Gong, W., and Wang, J. M. (2002) Potential role of the formyl peptide receptor-like 1 (FPRL1) in inflammatory aspects of Alzheimer's disease. *Journal of leukocyte biology* **72**, 628-635

Dahlgren, K. N., Manelli, A. M., Stine, W. B., Jr., Baker, L. K., Krafft, G. A., and LaDu, M. J. (2002) Oligomeric and fibrillar species of amyloid-b peptides differentially affect neuronal viability. *The Journal of biological chemistry* **277**, 32046-32053

Davalos, D., Grutzendler, J., Yang, G., Kim, J. V., Zuo, Y., Jung, S., Littman, D. R., Dustin, M. L., and Gan, W. B. (2005) ATP mediates rapid microglial response to local brain injury *in vivo*. *Nature neuroscience* **8**, 752-758

Daw, E. W., Payami, H., Nemens, E. J., Nochlin, D., Bird, T. D., Schellenberg, G. D., and Wijsman, E. M. (2000) The number of trait loci in late-onset Alzheimer disease. *American journal of human genetics* **66**, 196-204

Dawkins, E., and Small, D. H. (2014) Insights into the physiological function of the beta-amyloid precursor protein: beyond Alzheimer's disease. *Journal of neurochemistry* **129**, 756-769

Dawson, G. R., Seabrook, G. R., Zheng, H., Smith, D. W., Graham, S., O'Dowd, G., Bowery, B. J., Boyce, S., Trumbauer, M. E., Chen, H. Y., Van der Ploeg, L. H., and Sirinathsinghji, D. J. (1999) Age-related cognitive deficits, impaired long-term potentiation and reduction in synaptic marker density in mice lacking the b-amyloid precursor protein. *Neuroscience* **90**, 1-13

De Strooper, B., Saftig, P., Craessaerts, K., Vanderstichele, H., Guhde, G., Annaert, W., Von Figura, K., and Van Leuven, F. (1998) Deficiency of presenilin-1 inhibits the normal cleavage of amyloid precursor protein. *Nature* **391**, 387-390

Dickson, D. W. (2004) Apoptotic mechanisms in Alzheimer neurofibrillary degeneration: cause or effect? *The Journal of clinical investigation* **114**, 23-27

Dickson, D. W., Lee, S. C., Mattiace, L. A., Yen, S. H., and Brosnan, C. (1993) Microglia and cytokines in neurological disease, with special reference to AIDS and Alzheimer's disease. *Glia* **7**, 75-83

Dobson, C. M. (2003) Protein folding and misfolding. *Nature* **426**, 884-890

dos Santos, G., Kutuzov, M. A., and Ridge, K. M. (2012) The inflammasome in lung diseases. *Am J Physiol Lung Cell Mol Physiol* **303**, L627-633

Eanes, E. D., and Glenner, G. G. (1968) X-ray diffraction studies on amyloid filaments. *The journal of histochemistry and cytochemistry : official journal of the Histochemistry Society* **16**, 673-677

Edbauer, D., Winkler, E., Regula, J. T., Pesold, B., Steiner, H., and Haass, C. (2003) Reconstitution of g-secretase activity. *Nature cell biology* **5**, 486-488

Eddleston, M., and Mucke, L. (1993) Molecular profile of reactive astrocytes--implications for their role in neurologic disease. *Neuroscience* **54**, 15-36

Edison, P., Archer, H. A., Gerhard, A., Hinz, R., Pavese, N., Turkheimer, F. E., Hammers, A., Tai, Y. F., Fox, N., Kennedy, A., Rossor, M., and Brooks, D. J. (2008) Microglia, amyloid, and cognition in Alzheimer's disease: An [11C](R)PK11195-PET and [11C]PIB-PET study. *Neurobiology of disease* **32**, 412-419

Engele, J., Schubert, D., and Bohn, M. C. (1991) Conditioned media derived from glial cell lines promote survival and differentiation of dopaminergic neurons *in vitro*: role of mesencephalic glia. *Journal of neuroscience research* **30**, 359-371

Ercal, N., Gurer-Orhan, H., and Aykin-Burns, N. (2001) Toxic metals and oxidative stress part I: mechanisms involved in metal-induced oxidative damage. *Current topics in medicinal chemistry* **1**, 529-539

Esen, N., and Kielian, T. (2007) Effects of low dose GM-CSF on microglial inflammatory profiles to diverse pathogen-associated molecular patterns (PAMPs). *Journal of neuroinflammation* **4**, 10

Fagan, A. M., Younkin, L. H., Morris, J. C., Fryer, J. D., Cole, T. G., Younkin, S. G., and Holtzman, D. M. (2000) Differences in the Ab40/Ab42 ratio associated with cerebrospinal fluid lipoproteins as a function of apolipoprotein E genotype. *Annals of neurology* **48**, 201-210

Fassbender, K., Walter, S., Kuhl, S., Landmann, R., Ishii, K., Bertsch, T., Stalder, A. K., Muehlhauser, F., Liu, Y., Ulmer, A. J., Rivest, S., Lentschat, A., Gulbins, E., Jucker, M., Staufenbiel, M., Brechtel, K., Walter, J., Multhaup, G., Penke, B., Adachi, Y., Hartmann, T., and Beyreuther, K. (2004) The LPS receptor (CD14) links innate immunity with Alzheimer's disease. *Faseb j* **18**, 203-205

Fernandez-Busquets, X., de Groot, N. S., Fernandez, D., and Ventura, S. (2008) Recent structural and computational insights into conformational diseases. *Current medicinal chemistry* **15**, 1336-1349

Ferrero-Miliani, L., Nielsen, O. H., Andersen, P. S., and Girardin, S. E. (2007) Chronic inflammation: importance of NOD2 and NALP3 in interleukin-1b generation. *Clinical and experimental immunology* **147**, 227-235

Fowler, D. M., Koulov, A. V., Balch, W. E., and Kelly, J. W. (2007) Functional amyloid--from bacteria to humans. *Trends Biochem Sci* **32**, 217-224

Fraser, P. E., Nguyen, J. T., Inouye, H., Surewicz, W. K., Selkoe, D. J., Podlisny, M. B., and Kirschner, D. A. (1992) Fibril formation by primate, rodent, and Dutch-hemorrhagic analogues of Alzheimer amyloid b-protein. *Biochemistry* **31**, 10716-10723

Frautschy, S. A., Yang, F., Irrizarry, M., Hyman, B., Saido, T. C., Hsiao, K., and Cole, G. M. (1998) Microglial response to amyloid plaques in APPsw transgenic mice. *The American journal of pathology* **152**, 307-317

Ghosh, A. K., and Osswald, H. L. (2014) BACE1 ([small beta]-secretase) inhibitors for the treatment of Alzheimer's disease. *Chemical Society Reviews*

Giacobini, E., and Gold, G. (2013) Alzheimer disease therapy--moving from amyloid-b to tau. *Nature reviews. Neurology* **9**, 677-686

Gill, S. C., and von Hippel, P. H. (1989) Calculation of protein extinction coefficients from amino acid sequence data. *Analytical biochemistry* **182**, 319-326

Glenner, G. G., and Wong, C. W. (1984) Alzheimer's disease: initial report of the purification and characterization of a novel cerebrovascular amyloid protein. *Biochemical and biophysical research communications* **120**, 885-890

Golde, T. E. (2002) Inflammation takes on Alzheimer disease. *Nature medicine* **8**, 936-938

Gong, Y., Chang, L., Viola, K. L., Lacor, P. N., Lambert, M. P., Finch, C. E., Krafft, G. A., and Klein, W. L. (2003) Alzheimer's disease-affected brain: presence of oligomeric Ab ligands (ADDLs) suggests a molecular basis for reversible memory loss. *Proceedings of the National Academy of Sciences of the United States of America* **100**, 10417-10422

González-Scarano, F., and Baltuch, G. (1999) Microglia as mediators of inflammatory and degenerative diseases.

Gotz, J., Chen, F., van Dorpe, J., and Nitsch, R. M. (2001) Formation of neurofibrillary tangles in P301l tau transgenic mice induced by Ab 42 fibrils. *Science (New York, N.Y.)* **293**, 1491-1495

Graeber, M. B. (2010) Changing face of microglia. *Science (New York, N.Y.)* **330**, 783-788

Graeber, M. B., and Streit, W. J. (2010) Microglia: Biology and pathology. *Acta neuropathologica* **119**, 89-105

Graff-Radford, N. R., Crook, J. E., Lucas, J., Boeve, B. F., Knopman, D. S., Ivnik, R. J., Smith, G. E., Younkin, L. H., Petersen, R. C., and Younkin, S. G. (2007) Association of low plasma Ab42/Ab40 ratios with increased imminent risk for mild cognitive impairment and Alzheimer disease. *Archives of neurology* **64**, 354-362

Grundke-Iqbal, I., Iqbal, K., Quinlan, M., Tung, Y. C., Zaidi, M. S., and Wisniewski, H. M. (1986) Microtubule-associated protein tau. A component of Alzheimer paired helical filaments. *The Journal of biological chemistry* **261**, 6084-6089

Haass, C. (1997) Presenilins: genes for life and death. *Neuron* **18**, 687-690

Haass, C. (2004) Take five--BACE and the g-secretase quartet conduct Alzheimer's amyloid b-peptide generation. *The EMBO journal* **23**, 483-488

Haass, C., and Selkoe, D. J. (2007) Soluble protein oligomers in neurodegeneration: Lessons from the Alzheimer's amyloid β-peptide. *Nature Reviews Molecular Cell Biology* **8**, 101-112

Haass, C., Hung, A. Y., Selkoe, D. J., and Teplow, D. B. (1994) Mutations associated with a locus for familial Alzheimer's disease result in alternative processing of amyloid b-protein precursor. *The Journal of biological chemistry* **269**, 17741-17748

Halle, A., Hornung, V., Petzold, G. C., Stewart, C. R., Monks, B. G., Reinheckel, T., Fitzgerald, K. A., Latz, E., Moore, K. J., and Golenbock, D. T. (2008) The NALP3 inflammasome is involved in the innate immune response to amyloid-b. *Nature immunology* **9**, 857-865

Halverson, K., Fraser, P. E., Kirschner, D. A., and Lansbury, P. T., Jr. (1990) Molecular determinants of amyloid deposition in Alzheimer's disease: conformational studies of synthetic b-protein fragments. *Biochemistry* **29**, 2639-2644

Hanamsagar, R., Torres, V., and Kielian, T. (2011) Inflammasome activation and IL-1b/IL-18 processing are influenced by distinct pathways in microglia. *Journal of neurochemistry* **119**, 736-748

Hanamsagar, R., Hanke, M. L., and Kielian, T. (2012) Toll-like receptor (TLR) and inflammasome actions in the central nervous system. *Trends Immunol* **33**, 333-342

Hanisch, U.-K., and Kettenmann, H. (2007) Microglia: active sensor and versatile effector cells in the normal and pathologic brain. *Nat Neurosci* **10**, 1387-1394

Hanke, M. L., and Kielian, T. (2011) Toll-like receptors in health and disease in the brain: mechanisms and therapeutic potential. *Clinical science (London, England : 1979)* **121**, 367-387

Hardy, J. A., and Higgins, G. A. (1992) Alzheimer's disease: the amyloid cascade hypothesis. *Science (New York, N.Y.)* **256**, 184-185

Harper, J. D., and Lansbury, P. T., Jr. (1997) Models of amyloid seeding in Alzheimer's disease and scrapie: mechanistic truths and physiological consequences of the time-dependent solubility of amyloid proteins. *Annual review of biochemistry* **66**, 385-407

Harper, J. D., Wong, S. S., Lieber, C. M., and Lansbury, P. T. (1997) Observation of metastable Ab amyloid protofibrils by atomic force microscopy. *Chem Biol* **4**, 119-125

Harper, J. D., Wong, S. S., Lieber, C. M., and Lansbury, P. T., Jr. (1999) Assembly of A b-amyloid protofibrils: an *in vitro* model for a possible early event in Alzheimer's disease. *Biochemistry* **38**, 8972-8980

Hartley, D. M., Walsh, D. M., Ye, C. P., Diehl, T., Vasquez, S., Vassilev, P. M., Teplow, D. B., and Selkoe, D. J. (1999) Protofibrillar intermediates of amyloid b-protein induce acute electrophysiological changes and progressive neurotoxicity in cortical neurons. *The Journal of neuroscience : the official journal of the Society for Neuroscience* **19**, 8876-8884

Haydon, P. G. (2001) Glia: Listening and talking to the synapse. *Nature Reviews Neuroscience* **2**, 185-193

Hendriks, L., Van Duijn, C. M., Cras, P., Cruts, M., Van Hul, W., Van Harskamp, F., Warren, A., McInnis, M. G., Antonarakis, S. E., Martin, J. J., Hofman, A., and Van Broeckhoven, C. (1992) Presenile dementia and cerebral haemorrhage linked to a mutation at codon 692 of the β-amyloid precursor protein gene. *Nature Genetics* **1**, 218-221

Heneka, M. T., and O'Banion, M. K. (2007) Inflammatory processes in Alzheimer's disease. *Journal of neuroimmunology* **184**, 69-91

Heneka, M. T., Kummer, M. P., Stutz, A., Delekate, A., Schwartz, S., Vieira-Saecker, A., Griep, A., Axt, D., Remus, A., Tzeng, T. C., Gelpi, E., Halle, A., Korte, M., Latz, E., and Golenbock, D. T. (2013) NLRP3 is activated in Alzheimer's disease and contributes to pathology in APP/PS1 mice. *Nature* **493**, 674-678

Herz, J., and Beffert, U. (2000) Apolipoprotein E receptors: linking brain development and Alzheimer's disease. *Nature reviews. Neuroscience* **1**, 51-58

Hilbich, C., Kisters-Woike, B., Reed, J., Masters, C. L., and Beyreuther, K. (1991) Aggregation and secondary structure of synthetic amyloid b A4 peptides of Alzheimer's disease. *Journal of molecular biology* **218**, 149-163

Hoareau, C., Borrell, V., Soriano, E., Krebs, M. O., Prochiantz, A., and Allinquant, B. (2008) Amyloid precursor protein cytoplasmic domain antagonizes reelin neurite outgrowth inhibition of hippocampal neurons. *Neurobiology of aging* **29**, 542-553

Holtzman, D. M., Fagan, A. M., Mackey, B., Tenkova, T., Sartorius, L., Paul, S. M., Bales, K., Ashe, K. H., Irizarry, M. C., and Hyman, B. T. (2000) Apolipoprotein

E facilitates neuritic and cerebrovascular plaque formation in an Alzheimer's disease model. *Annals of neurology* **47**, 739-747

Hortschansky, P., Schroeckh, V., Christopeit, T., Zandomeneghi, G., and Fandrich, M. (2005) The aggregation kinetics of Alzheimer's b-amyloid peptide is controlled by stochastic nucleation. *Protein science : a publication of the Protein Society* **14**, 1753-1759

Huang, J., and Ding, J. (2010) Nanostructured interfaces with RGD arrays to control cell-matrix interaction. *Soft Matter* **6**, 3395-3401

Hutter, E., Boridy, S., Labrecque, S., Lalancette-Hébert, M., Kriz, J., Winnik, F. M., and Maysinger, D. (2010) Microglial Response to Gold Nanoparticles. *ACS Nano* **4**, 2595-2606

Hutter, E., Boridy, S., Labrecque, S., Lalancette-Hebert, M., Kriz, J., Winnik, F. M., and Maysinger, D. (2010) Microglial response to gold nanoparticles. *ACS nano* **4**, 2595-2606

Hyman, B. T. (2011) Amyloid-dependent and amyloid-independent stages of Alzheimer disease. *Archives of neurology* **68**, 1062-1064

Itagaki, S., McGeer, P. L., Akiyama, H., Zhu, S., and Selkoe, D. (1989) Relationship of microglia and astrocytes to amyloid deposits of Alzheimer disease. *Journal of neuroimmunology* **24**, 173-182

Iwata-Ichikawa, E., Kondo, Y., Miyazaki, I., Asanuma, M., and Ogawa, N. (1999) Glial cells protect neurons against oxidative stress via transcriptional up-regulation of the glutathione synthesis. *Journal of neurochemistry* **72**, 2334-2344

Jameson, L., Frey, T., Zeeberg, B., Dalldorf, F., and Caplow, M. (1980) Inhibition of microtubule assembly by phosphorylation of microtubule-associated proteins. *Biochemistry* **19**, 2472-2479

Jan, A., Hartley, D. M., and Lashuel, H. A. (2010) Preparation and characterization of toxic Ab aggregates for structural and functional studies in Alzheimer's disease research. *Nat Protoc* **5**, 1186-1209

Jan, A., Gokce, O., Luthi-Carter, R., and Lashuel, H. A. (2008) The ratio of monomeric to aggregated forms of Ab40 and Ab42 is an important determinant of amyloid-b aggregation, fibrillogenesis, and toxicity. *The Journal of biological chemistry* **283**, 28176-28189

Jana, M., Palencia, C. A., and Pahan, K. (2008) Fibrillar amyloid-b peptides activate microglia via TLR2: implications for Alzheimer's disease. *Journal of immunology (Baltimore, Md. : 1950)* **181**, 7254-7262

Jarrett, J. T., and Lansbury, P. T., Jr. (1992) Amyloid fibril formation requires a chemically discriminating nucleation event: studies of an amyloidogenic sequence from the bacterial protein OsmB. *Biochemistry* **31**, 12345-12352

Jarrett, J. T., Berger, E. P., and Lansbury, P. T., Jr. (1993) The carboxy terminus of the b-amyloid protein is critical for the seeding of amyloid formation: implications for the pathogenesis of Alzheimer's disease. *Biochemistry* **32**, 4693-4697

Johansson, A., Abrahamsson, P., and Davidsson, Ö. (2003) Solid-phase supported chiral lithium amides used in deprotonation reactions. *Tetrahedron: Asymmetry* **14**, 1261-1266

Johnson, G. V., and Jenkins, S. M. (1999) Tau protein in normal and Alzheimer's disease brain. *Journal of Alzheimer's disease : JAD* **1**, 307-328

Johnstone, M., Gearing, A. J., and Miller, K. M. (1999) A central role for astrocytes in the inflammatory response to b-amyloid; chemokines, cytokines and reactive oxygen species are produced. *Journal of neuroimmunology* **93**, 182-193

Jonsson, T., Atwal, J. K., Steinberg, S., Snaedal, J., Jonsson, P. V., Bjornsson, S., Stefansson, H., Sulem, P., Gudbjartsson, D., Maloney, J., Hoyte, K., Gustafson, A., Liu, Y., Lu, Y., Bhangale, T., Graham, R. R., Huttenlocher, J., Bjornsdottir, G., Andreassen, O. A., Jonsson, E. G., Palotie, A., Behrens, T. W., Magnusson, O. T., Kong, A., Thorsteinsdottir, U., Watts, R. J., and Stefansson, K. (2012) A mutation in APP protects against Alzheimer's disease and age-related cognitive decline. *Nature* **488**, 96-99

Kaeothip, S., Paranjape, G., Terrill, S. E., Bongat, A. F. G., Udan, M. L. D., Kamkhachorn, T., Johnson, H. L., Nichols, M. R., and Demchenko, A. V. (2011) Development of LPS antagonistic therapeutics: synthesis and evaluation of glucopyranoside-spacer-amino acid motifs. *RSC Advances* **1**, 83-92

Kang, J., Lemaire, H. G., Unterbeck, A., Salbaum, J. M., Masters, C. L., Grzeschik, K. H., Multhaup, G., Beyreuther, K., and Muller-Hill, B. (1987) The precursor of Alzheimer's disease amyloid A4 protein resembles a cell-surface receptor. *Nature* **325**, 733-736

Kayed, R., Head, E., Thompson, J. L., McIntire, T. M., Milton, S. C., Cotman, C. W., and Glabe, C. G. (2003) Common structure of soluble amyloid oligomers implies common mechanism of pathogenesis. *Science (New York, N.Y.)* **300**, 486-489

Kersse, K., Bertrand, M. J., Lamkanfi, M., and Vandenabeele, P. (2011) NOD-like receptors and the innate immune system: coping with danger, damage and death. *Cytokine & growth factor reviews* **22**, 257-276

Kheterpal, I., Lashuel, H. A., Hartley, D. M., Walz, T., Lansbury, P. T., Jr., and Wetzel, R. (2003) Ab protofibrils possess a stable core structure resistant to hydrogen exchange. *Biochemistry* **42**, 14092-14098

Khurana, R., Coleman, C., Ionescu-Zanetti, C., Carter, S. A., Krishna, V., Grover, R. K., Roy, R., and Singh, S. (2005) Mechanism of thioflavin T binding to amyloid fibrils. *Journal of structural biology* **151**, 229-238

Kielian, T. (2006) Toll-like receptors in central nervous system glial inflammation and homeostasis. *Journal of neuroscience research* **83**, 711-730

Kim, J.-I., Lee, C. J., Jin, M. S., Lee, C.-H., Paik, S.-G., Lee, H., and Lee, J.-O. (2005) Crystal Structure of CD14 and Its Implications for Lipopolysaccharide Signaling. *Journal of Biological Chemistry* **280**, 11347-11351

Kirschner, D. A., Inouye, H., Duffy, L. K., Sinclair, A., Lind, M., and Selkoe, D. J. (1987) Synthetic peptide homologous to b-protein from Alzheimer disease forms amyloid-like fibrils *in vitro*. *Proceedings of the National Academy of Sciences of the United States of America* **84**, 6953-6957

Kloss, C. U. A., Bohatschek, M., Kreutzberg, G. W., and Raivich, G. (2001) Effect of Lipopolysaccharide on the Morphology and Integrin Immunoreactivity of Ramified Microglia in the Mouse Brain and in Cell Culture. *Experimental Neurology* **168**, 32-46

Koffie, R. M., Meyer-Luehmann, M., Hashimoto, T., Adams, K. W., Mielke, M. L., Garcia-Alloza, M., Micheva, K. D., Smith, S. J., Kim, M. L., Lee, V. M., Hyman, B. T., and Spires-Jones, T. L. (2009) Oligomeric amyloid b associates with postsynaptic densities and correlates with excitatory synapse loss near senile plaques. *Proceedings of the National Academy of Sciences of the United States of America* **106**, 4012-4017

Kopito, R. R., and Ron, D. (2000) Conformational disease. *Nature cell biology* **2**, E207-209

Korzeniewski, C., and Callewaert, D. M. (1983) An enzyme-release assay for natural cytotoxicity. *J Immunol Methods* **64**, 313-320

Kowall, N. W., Beal, M. F., Busciglio, J., Duffy, L. K., and Yankner, B. A. (1991) An *in vivo* model for the neurodegenerative effects of b amyloid and protection by substance P. *Proceedings of the National Academy of Sciences of the United States of America* **88**, 7247-7251

Krebs, M. R., Bromley, E. H., and Donald, A. M. (2005) The binding of thioflavin-T to amyloid fibrils: localisation and implications. *Journal of structural biology* **149**, 30-37

Kuperstein, I., Broersen, K., Benilova, I., Rozenski, J., Jonckheere, W., Debulpaep, M., Vandersteen, A., Segers-Nolten, I., Van Der Werf, K., Subramaniam, V., Braeken, D., Callewaert, G., Bartic, C., D'Hooge, R., Martins, I. C., Rousseau, F., Schymkowitz, J., and De Strooper, B. (2010) Neurotoxicity of Alzheimer's disease Ab peptides is induced by small changes in the Ab42 to Ab40 ratio. *The EMBO journal* **29**, 3408-3420

Kyle, R. A. (2001) Amyloidosis: a convoluted story. *Br J Haematol* **114**, 529-538

LaDu, M. J., Falduto, M. T., Manelli, A. M., Reardon, C. A., Getz, G. S., and Frail, D. E. (1994) Isoform-specific binding of apolipoprotein E to b-amyloid. *The Journal of biological chemistry* **269**, 23403-23406

Lambert, M. P., Barlow, A. K., Chromy, B. A., Edwards, C., Freed, R., Liosatos, M., Morgan, T. E., Rozovsky, I., Trommer, B., Viola, K. L., Wals, P., Zhang, C., Finch, C. E., Krafft, G. A., and Klein, W. L. (1998) Diffusible, nonfibrillar ligands derived from Ab(1-42) are potent central nervous system neurotoxins. *Proceedings of the National Academy of Sciences of the United States of America* **95**, 6448-6453

Langeveld, C. H., Jongenelen, C. A., Schepens, E., Stoof, J. C., Bast, A., and Drukarch, B. (1995) Cultured rat striatal and cortical astrocytes protect mesencephalic dopaminergic neurons against hydrogen peroxide toxicity independent of their effect on neuronal development. *Neuroscience letters* **192**, 13-16

Lansbury, P. T., Jr., Costa, P. R., Griffiths, J. M., Simon, E. J., Auger, M., Halverson, K. J., Kocisko, D. A., Hendsch, Z. S., Ashburn, T. T., Spencer, R. G., and et al. (1995) Structural model for the b-amyloid fibril based on interstrand alignment of an antiparallel-sheet comprising a C-terminal peptide. *Nature structural biology* **2**, 990-998

Latz, E., Xiao, T. S., and Stutz, A. (2013) Activation and regulation of the inflammasomes. *Nature Reviews Immunology* **13**, 397-411

Lee, E. B., Leng, L. Z., Zhang, B., Kwong, L., Trojanowski, J. Q., Abel, T., and Lee, V. M. (2006) Targeting amyloid-b peptide (Ab) oligomers by passive immunization with a conformation-selective monoclonal antibody improves learning and memory in Ab precursor protein (APP) transgenic mice. *The Journal of biological chemistry* **281**, 4292-4299

Lee, J., Culyba, E. K., Powers, E. T., and Kelly, J. W. (2011) Amyloid-b forms fibrils by nucleated conformational conversion of oligomers. *Nature chemical biology* **7**, 602-609

Lee, V. M., Balin, B. J., Otvos, L., Jr., and Trojanowski, J. Q. (1991) A68: a major subunit of paired helical filaments and derivatized forms of normal Tau. *Science (New York, N.Y.)* **251**, 675-678

Leroy, K., Ando, K., Laporte, V., Dedecker, R., Suain, V., Authelet, M., Heraud, C., Pierrot, N., Yilmaz, Z., Octave, J. N., and Brion, J. P. (2012) Lack of tau proteins rescues neuronal cell death and decreases amyloidogenic processing of APP in APP/PS1 mice. *The American journal of pathology* **181**, 1928-1940

Leung, B. K., Biran, R., Underwood, C. J., and Tresco, P. A. (2008) Characterization of microglial attachment and cytokine release on biomaterials of differing surface chemistry. *Biomaterials* **29**, 3289-3297

Levy, E., Carman, M. D., Fernandez-Madrid, I. J., Power, M. D., Lieberburg, I., Van Duinen, S. G., Bots Th, G. A. M., Luyendijk, W., and Frangione, B. (1990) Mutation of the Alzheimer's disease amyloid gene in hereditary cerebral hemorrhage, Dutch type. *Science (New York, N.Y.)* **248**, 1124-1126

Lim, J. E., Song, M., Jin, J., Kou, J., Pattanayak, A., Lalonde, R., and Fukuchi, K. (2012) The effects of MyD88 deficiency on exploratory activity, anxiety, motor coordination, and spatial learning in C57BL/6 and APPswe/PS1dE9 mice. *Behavioural brain research* **227**, 36-42

Liu, S., Liu, Y., Hao, W., Wolf, L., Kiliaan, A. J., Penke, B., Rube, C. E., Walter, J., Heneka, M. T., Hartmann, T., Menger, M. D., and Fassbender, K. (2012) TLR2 is a primary receptor for Alzheimer's amyloid-b peptide to trigger neuroinflammatory activation. *Journal of immunology (Baltimore, Md. : 1950)* **188**, 1098-1107

Liu, X., Wu, Z., Hayashi, Y., and Nakanishi, H. (2012) Age-dependent neuroinflammatory responses and deficits in long-term potentiation in the hippocampus during systemic inflammation. *Neuroscience* **216**, 133-142

Lomakin, A., Teplow, D. B., Kirschner, D. A., and Benedek, G. B. (1997) Kinetic theory of fibrillogenesis of amyloid b-protein. *Proceedings of the National Academy of Sciences of the United States of America* **94**, 7942-7947

Lopez-Castejon, G., and Brough, D. (2011) Understanding the mechanism of IL-1b secretion. *Cytokine Growth Factor Rev* **22**, 189-195

Lue, L. F., Kuo, Y. M., Roher, A. E., Brachova, L., Shen, Y., Sue, L., Beach, T., Kurth, J. H., Rydel, R. E., and Rogers, J. (1999) Soluble amyloid b peptide concentration as a predictor of synaptic change in Alzheimer's disease. *The American journal of pathology* **155**, 853-862

Luna-Muñoz, J., Harrington, C. R., Wischik, C. M., Flores-Rodríguez, P., Avila, J., Zamudio, S. R., Cruz, F. D. l., Mena, R., Meraz-Ríos, M. A., and Floran-Garduño, B. (2013) *Phosphorylation of Tau Protein Associated as a Protective Mechanism in the Presence of Toxic, C-Terminally Truncated Tau in Alzheimer's Disease*,

Lynn, D. G., and Meredith, S. C. (2000) Review: model peptides and the physicochemical approach to b-amyloids. *Journal of structural biology* **130**, 153-173

Madine, J., Jack, E., Stockley, P. G., Radford, S. E., Serpell, L. C., and Middleton, D. A. (2008) Structural insights into the polymorphism of amyloid-like fibrils formed by region 20-29 of amylin revealed by solid-state NMR and X-ray fiber diffraction. *Journal of the American Chemical Society* **130**, 14990-15001

Maeda, S., Sahara, N., Saito, Y., Murayama, S., Ikai, A., and Takashima, A. (2006) Increased levels of granular tau oligomers: an early sign of brain aging and Alzheimer's disease. *Neuroscience research* **54**, 197-201

Malm, T. M., Koistinaho, M., Pärepalo, M., Vatanen, T., Ooka, A., Karlsson, S., and Koistinaho, J. (2005) Bone-marrow-derived cells contribute to the recruitment of microglial cells in response to β-amyloid deposition in APP/PS1 double transgenic Alzheimer mice. *Neurobiology of disease* **18**, 134-142

Mann, D. M., Brown, A., Prinja, D., Davies, C. A., Landon, M., Masters, C. L., and Beyreuthers, K. (1989) An analysis of the morphology of senile plaques in Down's syndrome patients of different ages using immunocytochemical and lectin histochemical techniques. *Neuropathology and applied neurobiology* **15**, 317-329

Masters, C. L., Simms, G., Weinman, N. A., Multhaup, G., McDonald, B. L., and Beyreuther, K. (1985) Amyloid plaque core protein in Alzheimer disease and Down syndrome. *Proceedings of the National Academy of Sciences of the United States of America* **82**, 4245-4249

McDonald, D. R., Bamberger, M. E., Combs, C. K., and Landreth, G. E. (1998) b-Amyloid fibrils activate parallel mitogen-activated protein kinase pathways in microglia and THP1 monocytes. *The Journal of neuroscience : the official journal of the Society for Neuroscience* **18**, 4451-4460

McGeer, E. G., and McGeer, P. L. (1998) The importance of inflammatory mechanisms in Alzheimer disease. *Experimental Gerontology* **33**, 371-378

McGeer, P. L., Itagaki, S., Tago, H., and McGeer, E. G. (1987) Reactive microglia in patients with senile dementia of the Alzheimer type are positive for the histocompatibility glycoprotein HLA-DR. *Neuroscience letters* **79**, 195-200

McLean, C. A., Cherny, R. A., Fraser, F. W., Fuller, S. J., Smith, M. J., Beyreuther, K., Bush, A. I., and Masters, C. L. (1999) Soluble pool of Ab amyloid as a determinant of severity of neurodegeneration in Alzheimer's disease. *Annals of neurology* **46**, 860-866

Meda, L., Cassatella, M. A., Szendrei, G. I., Otvos, L., Jr., Baron, P., Villalba, M., Ferrari, D., and Rossi, F. (1995) Activation of microglial cells by b-amyloid protein and interferon-g. *Nature* **374**, 647-650

Medeiros, R., Prediger, R. D. S., Passos, G. F., Pandolfo, P., Duarte, F. S., Franco, J. L., Dafre, A. L., Di Giunta, G., Figueiredo, C. P., Takahashi, R. N., Campos, M. M., and Calixto, J. B. (2007) Connecting TNF-α signaling pathways to iNOS expression in a mouse model of Alzheimer's disease: Relevance for the behavioral and synaptic deficits induced by amyloid β protein. *Journal of Neuroscience* **27**, 5394-5404

Mena, M. A., Casarejos, M. J., Carazo, A., Paino, C. L., and Garcia de Yebenes, J. (1996) Glia conditioned medium protects fetal rat midbrain neurones in culture from L-DOPA toxicity. *Neuroreport* **7**, 441-445

Middleton, D. A. (2011) Solid-state NMR detection of 14N-13C dipolar couplings between amino acid side groups provides constraints on amyloid fibril architecture. *Magnetic resonance in chemistry : MRC* **49**, 65-69

Moechars, D., Dewachter, I., Lorent, K., Reverse, D., Baekelandt, V., Naidu, A., Tesseur, I., Spittaels, K., Haute, C. V., Checler, F., Godaux, E., Cordell, B., and Van Leuven, F. (1999) Early phenotypic changes in transgenic mice that overexpress different mutants of amyloid precursor protein in brain. *The Journal of biological chemistry* **274**, 6483-6492

Mori, H., Takio, K., Ogawara, M., and Selkoe, D. J. (1992) Mass spectrometry of purified amyloid b protein in Alzheimer's disease. *The Journal of biological chemistry* **267**, 17082-17086

Morris, J. C., Roe, C. M., Grant, E. A., Head, D., Storandt, M., Goate, A. M., Fagan, A. M., Holtzman, D. M., and Mintun, M. A. (2009) Pittsburgh compound B imaging and prediction of progression from cognitive normality to symptomatic Alzheimer disease. *Archives of neurology* **66**, 1469-1475

Mortimer, J. A., van Duijn, C. M., Chandra, V., Fratiglioni, L., Graves, A. B., Heyman, A., Jorm, A. F., Kokmen, E., Kondo, K., Rocca, W. A., and et al. (1991) Head trauma as a risk factor for Alzheimer's disease: a collaborative re-analysis of case-control studies. EURODEM Risk Factors Research Group. *International journal of epidemiology* **20 Suppl 2**, S28-35

Mrksich, M. (2009) Using self-assembled monolayers to model the extracellular matrix. *Acta biomaterialia* **5**, 832-841

Mrksich, M., and Whitesides, G. M. (1996) Using self-assembled monolayers to understand the interactions of man-made surfaces with proteins and cells. *Annual review of biophysics and biomolecular structure* **25**, 55-78

Mrksich, M., and Whitesides, G. M. (1996) Using Self-Assembled Monolayers to Understand the Interactions of Man-made Surfaces with Proteins and Cells. *Annual Review of Biophysics and Biomolecular Structure* **25**, 55-78

Mucke, L., Masliah, E., Yu, G. Q., Mallory, M., Rockenstein, E. M., Tatsuno, G., Hu, K., Kholodenko, D., Johnson-Wood, K., and McConlogue, L. (2000) High-level neuronal expression of Ab 1-42 in wild-type human amyloid protein precursor transgenic mice: synaptotoxicity without plaque formation. *The Journal of neuroscience : the official journal of the Society for Neuroscience* **20**, 4050-4058

Murphy, N., Grehan, B., and Lynch, M. A. (2013) Glial Uptake of Amyloid b Induces NLRP3 Inflammasome Formation via Cathepsin-Dependent Degradation of NLRP10. *Neuromolecular Med*

Nagele, R. G., Wegiel, J., Venkataraman, V., Imaki, H., Wang, K. C., and Wegiel, J. (2004) Contribution of glial cells to the development of amyloid plaques in Alzheimer's disease. *Neurobiology of aging* **25**, 663-674

Naslund, J., Haroutunian, V., Mohs, R., Davis, K. L., Davies, P., Greengard, P., and Buxbaum, J. D. (2000) Correlation between elevated levels of amyloid b-peptide in the brain and cognitive decline. *JAMA : the journal of the American Medical Association* **283**, 1571-1577

Nichols, M. R., Moss, M. A., Reed, D. K., Lin, W. L., Mukhopadhyay, R., Hoh, J. H., and Rosenberry, T. L. (2002) Growth of b-amyloid(1-40) protofibrils by monomer elongation and lateral association. Characterization of distinct products by light scattering and atomic force microscopy. *Biochemistry* **41**, 6115-6127

Nikkhah, M., Edalat, F., Manoucheri, S., and Khademhosseini, A. (2012) Engineering microscale topographies to control the cell-substrate interface. *Biomaterials* **33**, 5230-5246

Nilsson, M. R. (2004) Techniques to study amyloid fibril formation *in vitro*. *Methods (San Diego, Calif.)* **34**, 151-160

Nimmerjahn, A., Kirchhoff, F., and Helmchen, F. (2005) Resting microglial cells are highly dynamic surveillants of brain parenchyma in vivo. *Neuroforum* **11**, 95-96

Nixon, R. A. (2007) Autophagy, amyloidogenesis and Alzheimer disease. *Journal of cell science* **120**, 4081-4091

O'Nuallain, B., Freir, D. B., Nicoll, A. J., Risse, E., Ferguson, N., Herron, C. E., Collinge, J., and Walsh, D. M. Amyloid b-protein dimers rapidly form stable synaptotoxic protofibrils. *The Journal of neuroscience : the official journal of the Society for Neuroscience* **30**, 14411-14419

Ojala, J., Alafuzoff, I., Herukka, S. K., van Groen, T., Tanila, H., and Pirttila, T. (2009) Expression of interleukin-18 is increased in the brains of Alzheimer's disease patients. *Neurobiology of aging* **30**, 198-209

Okello, A., Edison, P., Archer, H. A., Turkheimer, F. E., Kennedy, J., Bullock, R., Walker, Z., Kennedy, A., Fox, N., Rossor, M., and Brooks, D. J. (2009) Microglial activation and amyloid deposition in mild cognitive impairment: a PET study. *Neurology* **72**, 56-62

Pandey, B., Tan, Y. H., Fujikawa, K., Demchenko, A. V., and Stine, K. J. (2012) Comparative Study of the Binding of Concanavalin A to Self-Assembled Monolayers Containing a Thiolated a-Mannoside on Flat Gold and on Nanoporous Gold. *Journal of carbohydrate chemistry* **31**, 466-503

Parajuli, B., Sonobe, Y., Horiuchi, H., Takeuchi, H., Mizuno, T., and Suzumura, A. (2013) Oligomeric amyloid b induces IL-1b processing via production of ROS: implication in Alzheimer's disease. *Cell Death Dis* **4**, e975

Paranjape, G. S., Gouwens, L. K., Osborn, D. C., and Nichols, M. R. (2012) Isolated amyloid-b(1-42) protofibrils, but not isolated fibrils, are robust stimulators of microglia. *ACS Chem Neurosci* **3**, 302-311

Paranjape, G. S., Gouwens, L. K., Osborn, D. C., and Nichols, M. R. (2012) Isolated Amyloid-β(1–42) Protofibrils, But Not Isolated Fibrils, Are Robust Stimulators of Microglia. *ACS Chemical Neuroscience* **3**, 302-311

Paranjape, G. S., Terrill, S. E., Gouwens, L. K., Ruck, B. M., and Nichols, M. R. (2013) Amyloid-b(1-42) protofibrils formed in modified artificial cerebrospinal fluid bind and activate microglia. *J Neuroimmune Pharmacol* **8**, 312-322

Park, T. H., and Shuler, M. L. (2003) Integration of cell culture and microfabrication technology. *Biotechnology progress* **19**, 243-253

Pauwels, K., Williams, T. L., Morris, K. L., Jonckheere, W., Vandersteen, A., Kelly, G., Schymkowitz, J., Rousseau, F., Pastore, A., Serpell, L. C., and Broersen, K. (2012) Structural basis for increased toxicity of pathological Ab42:Ab40 ratios in Alzheimer disease. *The Journal of biological chemistry* **287**, 5650-5660

Peri, F., Granucci, F., Costa, B., Zanoni, I., Marinzi, C., and Nicotra, F. (2007) Inhibition of lipid a stimulated activation of human dendritic cells and macrophages by amino and hydroxylamino monosaccharides. *Angewandte Chemie (International ed. in English)* **46**, 3308-3312

Persheyev, S., Fan, Y., Irving, A., and Rose, M. J. (2011) BV-2 microglial cells sense micro-nanotextured silicon surface topology. *Journal of Biomedical Materials Research Part A* **99A**, 135-140

Petkova, A. T., and Tycko, R. (2004) Rotational resonance in uniformly 13C-labeled solids: effects on high-resolution magic-angle spinning NMR spectra and applications in structural studies of biomolecular systems. *Journal of magnetic resonance (San Diego, Calif. : 1997)* **168**, 137-146

Petkova, A. T., Leapman, R. D., Guo, Z., Yau, W. M., Mattson, M. P., and Tycko, R. (2005) Self-propagating, molecular-level polymorphism in Alzheimer's b-amyloid fibrils. *Science (New York, N.Y.)* **307**, 262-265

Petkova, A. T., Ishii, Y., Balbach, J. J., Antzutkin, O. N., Leapman, R. D., Delaglio, F., and Tycko, R. (2002) A structural model for Alzheimer's b-amyloid fibrils based on experimental constraints from solid state NMR. *Proceedings of the National Academy of Sciences of the United States of America* **99**, 16742-16747

Pham, J. D., Chim, N., Goulding, C. W., and Nowick, J. S. (2013) Structures of oligomers of a peptide from b-amyloid. *Journal of the American Chemical Society* **135**, 12460-12467

Phinney, A. L., Calhoun, M. E., Wolfer, D. P., Lipp, H. P., Zheng, H., and Jucker, M. (1999) No hippocampal neuron or synaptic bouton loss in learning-impaired aged b-amyloid precursor protein-null mice. *Neuroscience* **90**, 1207-1216

Pike, C. J., Walencewicz, A. J., Glabe, C. G., and Cotman, C. W. (1991) *In vitro* aging of b-amyloid protein causes peptide aggregation and neurotoxicity. *Brain research* **563**, 311-314

Qiao, X., Cummins, D. J., and Paul, S. M. (2001) Neuroinflammation-induced acceleration of amyloid deposition in the APPV717F transgenic mouse. *The European journal of neuroscience* **14**, 474-482

Reed-Geaghan, E. G., Savage, J. C., Hise, A. G., and Landreth, G. E. (2009) CD14 and toll-like receptors 2 and 4 are required for fibrillar Ab-stimulated microglial activation. *The Journal of neuroscience : the official journal of the Society for Neuroscience* **29**, 11982-11992

Reinhard, C., Hebert, S. S., and De Strooper, B. (2005) The amyloid-b precursor protein: integrating structure with biological function. *The EMBO journal* **24**, 3996-4006

Rentz, D. M., Locascio, J. J., Becker, J. A., Moran, E. K., Eng, E., Buckner, R. L., Sperling, R. A., and Johnson, K. A. (2010) Cognition, reserve, and amyloid deposition in normal aging. *Annals of neurology* **67**, 353-364

Repine, J. E., Eaton, J. W., Anders, M. W., Hoidal, J. R., and Fox, R. B. (1979) Generation of hydroxyl radical by enzymes, chemicals, and human phagocytes in vitro. Detection with the anti-inflammatory agent, dimethyl sulfoxide. *The Journal of clinical investigation* **64**, 1642-1651

Rivera-Escalera, F., Matousek, S. B., Ghosh, S., Olschowka, J. A., and O'Banion, M. K. (2014) Interleukin-1b mediated amyloid plaque clearance is independent of CCR2 signaling in the APP/PS1 mouse model of Alzheimer's disease. *Neurobiology of disease* **69c**, 124-133

Roberson, E. D., Scearce-Levie, K., Palop, J. J., Yan, F., Cheng, I. H., Wu, T., Gerstein, H., Yu, G. Q., and Mucke, L. (2007) Reducing endogenous tau ameliorates amyloid b-induced deficits in an Alzheimer's disease mouse model. *Science (New York, N.Y.)* **316**, 750-754

Rogers, J. (2008) The inflammatory response in Alzheimer's disease. *Journal of periodontology* **79**, 1535-1543

Rogers, J., Webster, S., Lue, L. F., Brachova, L., Civin, W. H., Emmerling, M., Shivers, B., Walker, D., and McGeer, P. (1996) Inflammation and Alzheimer's disease pathogenesis. *Neurobiology of aging* **17**, 681-686

Roher, A., Gray, E. G., and Paula-Barbosa, M. (1988) Alzheimer's disease: coated vesicles, coated pits and the amyloid-related cell. *Proceedings of the Royal Society of London. Series B, Containing papers of a Biological character. Royal Society (Great Britain)* **232**, 367-373

Roher, A. E., Palmer, K. C., Yurewicz, E. C., Ball, M. J., and Greenberg, B. D. (1993) Morphological and biochemical analyses of amyloid plaque core proteins purified from Alzheimer disease brain tissue. *Journal of neurochemistry* **61**, 1916-1926

Roher, A. E., Baudry, J., Chaney, M. O., Kuo, Y. M., Stine, W. B., and Emmerling, M. R. (2000) Oligomerizaiton and fibril asssembly of the amyloid-b protein. *Biochimica et biophysica acta* **1502**, 31-43

Roher, A. E., Lowenson, J. D., Clarke, S., Woods, A. S., Cotter, R. J., Gowing, E., and Ball, M. J. (1993) b-Amyloid-(1-42) is a major component of cerebrovascular amyloid deposits: implications for the pathology of Alzheimer disease. *Proceedings of the National Academy of Sciences of the United States of America* **90**, 10836-10840

Salminen, A., Ojala, J., Kauppinen, A., Kaarniranta, K., and Suuronen, T. (2009) Inflammation in Alzheimer's disease: Amyloid-β oligomers trigger innate immunity defence via pattern recognition receptors. *Progress in neurobiology* **87**, 181-194

Sardi, F., Fassina, L., Venturini, L., Inguscio, M., Guerriero, F., Rolfo, E., and Ricevuti, G. (2011) Alzheimer's disease, autoimmunity and inflammation. The good, the bad and the ugly. *Autoimmunity Reviews* **11**, 149-153

Sasaki, A., Yamaguchi, H., Ogawa, A., Sugihara, S., and Nakazato, Y. (1997) Microglial activation in early stages of amyloid b protein deposition. *Acta neuropathologica* **94**, 316-322

Savage, C. D., Lopez-Castejon, G., Denes, A., and Brough, D. (2012) NLRP3-Inflammasome Activating DAMPs Stimulate an Inflammatory Response in Glia in the Absence of Priming Which Contributes to Brain Inflammation after Injury. *Front Immunol* **3**, 288

Scheuner, D., Eckman, C., Jensen, M., Song, X., Citron, M., Suzuki, N., Bird, T. D., Hardy, J., Hutton, M., Kukull, W., Larson, E., Levy-Lahad, E., Viitanen, M., Peskind, E., Poorkaj, P., Schellenberg, G., Tanzi, R., Wasco, W., Lannfelt, L., Selkoe, D., and Younkin, S. (1996) Secreted amyloid beta-protein similar to that in the senile plaques of Alzheimer's disease is increased in vivo by the presenilin 1 and 2 and APP mutations linked to familial Alzheimer's disease. *Nature medicine* **2**, 864-870

Schon, E. A., and Area-Gomez, E. (2010) Is Alzheimer's disease a disorder of mitochondria-associated membranes? *Journal of Alzheimer's disease : JAD* **20 Suppl 2**, S281-292

Schroder, K., and Tschopp, J. (2010) The inflammasomes. *Cell* **140**, 821-832

Schummers, J., Yu, H., and Sur, M. (2008) Tuned responses of astrocytes and their influence on hemodynamic signals in the visual cortex. *Science (New York, N.Y.)* **320**, 1638-1643

Scudiero, D. A., Shoemaker, R. H., Paull, K. D., Monks, A., Tierney, S., Nofziger, T. H., Currens, M. J., Seniff, D., and Boyd, M. R. (1988) Evaluation of a soluble tetrazolium/formazan assay for cell growth and drug sensitivity in culture using human and other tumor cell lines. *Cancer Res* **48**, 4827-4833

Seker, E., Berdichevsky, Y., Staley, K. J., and Yarmush, M. L. (2012) Microfabrication-Compatible Nanoporous Gold Foams as Biomaterials for Drug Delivery. *Advanced Healthcare Materials* **1**, 172-176

Seker, E., Berdichevsky, Y., Staley, K. J., and Yarmush, M. L. (2012) Microfabrication-compatible nanoporous gold foams as biomaterials for drug delivery. *Advanced healthcare materials* **1**, 172-176

Selkoe, D. J. (1994) Cell biology of the amyloid b-protein precursor and the mechanism of Alzheimer's disease. *Annual review of cell biology* **10**, 373-403

Selkoe, D. J. (1994) Normal and abnormal biology of the b-amyloid precursor protein. *Annu Rev Neurosci* **17**, 489-517

Selkoe, D. J. (1998) The cell biology of b-amyloid precursor protein and presenilin in Alzheimer's disease. *Trends in cell biology* **8**, 447-453

Selkoe, D. J. (2000) Toward a comprehensive theory for Alzheimer's disease. Hypothesis: Alzheimer's disease is caused by the cerebral accumulation and cytotoxicity of amyloid beta-protein. *Annals of the New York Academy of Sciences* **924**, 17-25

Selkoe, D. J. (2001) Alzheimer's disease: genes, proteins, and therapy. *Physiol Rev* **81**, 741-766

Selkoe, D. J. (2003) Folding proteins in fatal ways. *Nature* **426**, 900-904

Selkoe, D. J. (2004) Cell biology of protein misfolding: the examples of Alzheimer's and Parkinson's diseases. *Nature cell biology* **6**, 1054-1061

Selkoe, D. J. (2011) Alzheimer's disease. *Cold Spring Harbor perspectives in biology* **3**

Selkoe, D. J., and Podlisny, M. B. (2002) Deciphering the genetic basis of Alzheimer's disease. *Annual review of genomics and human genetics* **3**, 67-99

Senechal, Y., Larmet, Y., and Dev, K. K. (2006) Unraveling *in vivo* functions of amyloid precursor protein: insights from knockout and knockdown studies. *Neuro-degenerative diseases* **3**, 134-147

Senechal, Y., Prut, L., Kelly, P. H., Staufenbiel, M., Natt, F., Hoyer, D., Wiessner, C., and Dev, K. K. (2008) Increased exploratory activity of APP23 mice in a novel environment is reversed by siRNA. *Brain research* **1243**, 124-133

Serpell, L. C., Blake, C. C., and Fraser, P. E. (2000) Molecular structure of a fibrillar Alzheimer's Ab fragment. *Biochemistry* **39**, 13269-13275

Seubert, P., Oltersdorf, T., Lee, M. G., Barbour, R., Blomquist, C., Davis, D. L., Bryant, K., Fritz, L. C., Galasko, D., Thal, L. J., and et al. (1993) Secretion of b-amyloid precursor protein cleaved at the amino terminus of the b-amyloid peptide. *Nature* **361**, 260-263

Sheedy, F. J., Grebe, A., Rayner, K. J., Kalantari, P., Ramkhelawon, B., Carpenter, S. B., Becker, C. E., Ediriweera, H. N., Mullick, A. E., Golenbock, D. T., Stuart, L. M., Latz, E., Fitzgerald, K. A., and Moore, K. J. (2013) CD36 coordinates NLRP3 inflammasome activation by facilitating intracellular nucleation of soluble ligands into particulate ligands in sterile inflammation. *Nature immunology* **14**, 812-820

Sherman, M. Y., and Goldberg, A. L. (2001) Cellular defenses against unfolded proteins: a cell biologist thinks about neurodegenerative diseases. *Neuron* **29**, 15-32

Shivaprasad, S., and Wetzel, R. (2006) Scanning cysteine mutagenesis analysis of Ab-(1-40) amyloid fibrils. *The Journal of biological chemistry* **281**, 993-1000

Shoji, M., Golde, T. E., Ghiso, J., Cheung, T. T., Estus, S., Shaffer, L. M., Cai, X. D., McKay, D. M., Tintner, R., Frangione, B., and et al. (1992) Production of the Alzheimer amyloid b protein by normal proteolytic processing. *Science (New York, N.Y.)* **258**, 126-129

Shulga, O. V., Jefferson, K., Khan, A. R., D'Souza, V. T., Liu, J., Demchenko, A. V., and Stine, K. J. (2007) Preparation and Characterization of Porous Gold and its Application as a Platform for Immobilization of Acetylcholine Esterase. *Chemistry of materials : a publication of the American Chemical Society* **19**, 3902-3911

Simard, A. R., and Rivest, S. (2004) Role of inflammation in the neurobiology of stem cells. *Neuroreport* **15**, 2305-2310

Sisodia, S. S., Koo, E. H., Beyreuther, K., Unterbeck, A., and Price, D. L. (1990) Evidence that b-amyloid protein in Alzheimer's disease is not derived by normal processing. *Science (New York, N.Y.)* **248**, 492-495

Smith, P. K., Krohn, R. I., Hermanson, G. T., Mallia, A. K., Gartner, F. H., Provenzano, M. D., Fujimoto, E. K., Goeke, N. M., Olson, B. J., and Klenk, D. C. (1985) Measurement of protein using bicinchoninic acid. *Analytical biochemistry* **150**, 76-85

Stalder, M., Phinney, A., Probst, A., Sommer, B., Staufenbiel, M., and Jucker, M. (1999) Association of microglia with amyloid plaques in brains of APP23 transgenic mice. *The American journal of pathology* **154**, 1673-1684

Stewart, C. R., Stuart, L. M., Wilkinson, K., van Gils, J. M., Deng, J., Halle, A., Rayner, K. J., Boyer, L., Zhong, R., Frazier, W. A., Lacy-Hulbert, A., El Khoury, J., Golenbock, D. T., and Moore, K. J. (2010) CD36 ligands promote sterile inflammation through assembly of a Toll-like receptor 4 and 6 heterodimer. *Nature immunology* **11**, 155-161

Stine, W. B., Jr., Dahlgren, K. N., Krafft, G. A., and LaDu, M. J. (2003) *In vitro* characterization of conditions for amyloid-b peptide oligomerization and fibrillogenesis. *The Journal of biological chemistry* **278**, 11612-11622

Strittmatter, W. J., Weisgraber, K. H., Huang, D. Y., Dong, L. M., Salvesen, G. S., Pericak-Vance, M., Schmechel, D., Saunders, A. M., Goldgaber, D., and Roses, A. D. (1993) Binding of human apolipoprotein E to synthetic amyloid b peptide: isoform-specific effects and implications for late-onset Alzheimer disease. *Proceedings of the National Academy of Sciences of the United States of America* **90**, 8098-8102

Sunde, M., and Blake, C. (1997) The structure of amyloid fibrils by electron microscopy and X-ray diffraction. *Advances in protein chemistry* **50**, 123-159

Sutterwala, F. S., Haasken, S., and Cassel, S. L. (2014) Mechanism of NLRP3 inflammasome activation. *Annals of the New York Academy of Sciences*

Syed, M. M., Phulwani, N. K., and Kielian, T. (2007) Tumor necrosis factor-alpha (TNF-α) regulates Toll-like receptor 2 (TLR2) expression in microglia. *Journal of Neurochemistry* **103**, 1461-1471

Tagliavini, F., Giaccone, G., Frangione, B., and Bugiani, O. (1988) Preamyloid deposits in the cerebral cortex of patients with Alzheimer's disease and nondemented individuals. *Neuroscience letters* **93**, 191-196

Takenouchi, T., Iwamaru, Y., Sugama, S., Tsukimoto, M., Fujita, M., Sekigawa, A., Sekiyama, K., Sato, M., Kojima, S., Conti, B., Hashimoto, M., and Kitani, H. (2011) The activation of P2X7 receptor induces cathepsin D-dependent production of a 20-kDa form of IL-1b under acidic extracellular pH in LPS-primed microglial cells. *Journal of neurochemistry* **117**, 712-723

Tamaoka, A. (2013) [The pathophysiology of Alzheimer's disease with special reference to "amyloid cascade hypothesis"]. *Rinsho byori. The Japanese journal of clinical pathology* **61**, 1060-1069

Tan, M. S., Yu, J. T., Jiang, T., Zhu, X. C., and Tan, L. (2013) The NLRP3 Inflammasome in Alzheimer's Disease. *Mol Neurobiol* **48**, 875-882

Tan, Y. H., Terrill, S. E., Paranjape, G. S., Stine, K. J., and Nichols, M. R. (2014) The influence of gold surface texture on microglia morphology and activation. *Biomaterials Science* **2**, 110-120

Tan, Y. H., Liu, M., Nolting, B., Go, J. G., Gervay-Hague, J., and Liu, G. Y. (2008) A nanoengineering approach for investigation and regulation of protein immobilization. *ACS nano* **2**, 2374-2384

Tan, Y. H., Liu, M., Nolting, B., Go, J. G., Gervay-Hague, J., and Liu, G.-y. (2008) A Nanoengineering Approach for Investigation and Regulation of Protein Immobilization. *ACS Nano* **2**, 2374-2384

Tan, Y. H., Schallom, J. R., Ganesh, N. V., Fujikawa, K., Demchenko, A. V., and Stine, K. J. (2011) Characterization of protein immobilization on nanoporous gold using atomic force microscopy and scanning electron microscopy. *Nanoscale* **3**, 3395-3407

Terada, K., Yamada, J., Hayashi, Y., Wu, Z., Uchiyama, Y., Peters, C., and Nakanishi, H. (2010) Involvement of cathepsin B in the processing and secretion of interleukin-1b in chromogranin A-stimulated microglia. *Glia* **58**, 114-124

Thies, W., and Bleiler, L. (2012) 2012 Alzheimer's disease facts and figures. *Alzheimer's & dementia : the journal of the Alzheimer's Association* **8**, 131-168

Thies, W., and Bleiler, L. (2013) 2013 Alzheimer's disease facts and figures. *Alzheimer's & dementia : the journal of the Alzheimer's Association* **9**, 208-245

Tiiman, A., Palumaa, P., and Tougu, V. (2013) The missing link in the amyloid cascade of Alzheimer's disease - metal ions. *Neurochemistry international* **62**, 367-378

Tsuchiya, S., Kobayashi, Y., Goto, Y., Okumura, H., Nakae, S., Konno, T., and Tada, K. (1982) Induction of maturation in cultured human monocytic leukemia cells by a phorbol diester. *Cancer Res* **42**, 1530-1536

Turner, C. K., Blieden, T. M., Smith, T. J., Feldon, S. E., Foster, D. C., Sime, P. J., and Phipps, R. P. (2004) A novel ELISpot method for adherent cells. *J Immunol Methods* **291**, 63-70

Tycko, R. (2011) Solid-state NMR studies of amyloid fibril structure. *Annual review of physical chemistry* **62**, 279-299

Tzounopoulos, T., Kim, Y., Oertel, D., and Trussell, L. O. (2004) Cell-specific, spike timing-dependent plasticities in the dorsal cochlear nucleus. *Nature neuroscience* **7**, 719-725

Udan, M. L., Ajit, D., Crouse, N. R., and Nichols, M. R. (2008) Toll-like receptors 2 and 4 mediate Ab(1-42) activation of the innate immune response in a human monocytic cell line. *Journal of neurochemistry* **104**, 524-533

Ulrich, J. D., Burchett, J. M., Restivo, J. L., Schuler, D. R., Verghese, P. B., Mahan, T. E., Landreth, G. E., Castellano, J. M., Jiang, H., Cirrito, J. R., and Holtzman, D. M. (2013) In vivo measurement of apolipoprotein E from the brain interstitial fluid using microdialysis. *Molecular neurodegeneration* **8**, 13

Virchow, R. (1851) Ueber den Cretinismus, namentlich in Franken, und ueber pathologische Schaedelformen. *Verh Phys Med Gesellsch Wuerzburg* **2**, 231-271

von Koch, C. S., Zheng, H., Chen, H., Trumbauer, M., Thinakaran, G., van der Ploeg, L. H., Price, D. L., and Sisodia, S. S. (1997) Generation of APLP2 KO mice and early postnatal lethality in APLP2/APP double KO mice. *Neurobiology of aging* **18**, 661-669

Voskerician, G., Shive, M. S., Shawgo, R. S., Recum, H. v., Anderson, J. M., Cima, M. J., and Langer, R. (2003) Biocompatibility and biofouling of MEMS drug delivery devices. *Biomaterials* **24**, 1959-1967

Wajant, H., Pfizenmaier, K., and Scheurich, P. (2003) Tumor necrosis factor signaling. *Cell Death and Differentiation* **10**, 45-65

Walsh, D. M., Lomakin, A., Benedek, G. B., Condron, M. M., and Teplow, D. B. (1997) Amyloid b-protein fibrillogenesis. Detection of a protofibrillar intermediate. *The Journal of biological chemistry* **272**, 22364-22372

Walsh, D. M., Tseng, B. P., Rydel, R. E., Podlisny, M. B., and Selkoe, D. J. (2000) The oligomerization of amyloid b-protein begins intracellularly in cells derived from human brain. *Biochemistry* **39**, 10831-10839

Walsh, D. M., Klyubin, I., Fadeeva, J. V., Cullen, W. K., Anwyl, R., Wolfe, M. S., Rowan, M. J., and Selkoe, D. J. (2002) Naturally secreted oligomers of amyloid b protein potently inhibit hippocampal long-term potentiation *in vivo*. *Nature* **416**, 535-539

Walsh, D. M., Hartley, D. M., Kusumoto, Y., Fezoui, Y., Condron, M. M., Lomakin, A., Benedek, G. B., Selkoe, D. J., and Teplow, D. B. (1999) Amyloid b-protein fibrillogenesis. Structure and biological activity of protofibrillar intermediates. *The Journal of biological chemistry* **274**, 25945-25952

Walter, S., Letiembre, M., Liu, Y., Heine, H., Penke, B., Hao, W., Bode, B., Manietta, N., Walter, J., Schulz-Schuffer, W., and Fassbender, K. (2007) Role of the toll-like receptor 4 in neuroinflammation in Alzheimer's disease. *Cell Physiol Biochem* **20**, 947-956

Wang, J., Dickson, D. W., Trojanowski, J. Q., and Lee, V. M. (1999) The levels of soluble versus insoluble brain Ab distinguish Alzheimer's disease from normal and pathologic aging. *Experimental neurology* **158**, 328-337

Wang, X., and Terpstra, E. J. (2013) Ubiquitin receptors and protein quality control. *Journal of molecular and cellular cardiology* **55**, 73-84

Wataha, J. C., Hanks, C. T., and Sun, Z. (1994) Effect of cell line on *in vitro* metal ion cytotoxicity. *Dental materials : official publication of the Academy of Dental Materials* **10**, 156-161

Wegener, J., Keese, C. R., and Giaever, I. (2000) Electric Cell–Substrate Impedance Sensing (ECIS) as a Noninvasive Means to Monitor the Kinetics of Cell Spreading to Artificial Surfaces. *Experimental Cell Research* **259**, 158-166

Wegiel, J., and Wisniewski, H. M. (1990) The complex of microglial cells and amyloid star in three-dimensional reconstruction. *Acta neuropathologica* **81**, 116-124

Weingarten, M. D., Lockwood, A. H., Hwo, S. Y., and Kirschner, M. W. (1975) A protein factor essential for microtubule assembly. *Proceedings of the National Academy of Sciences of the United States of America* **72**, 1858-1862

Wisdom, G. B. (2005) Conjugation of antibodies to horseradish peroxidase. *Methods in molecular biology (Clifton, N.J.)* **295**, 127-130

Wisniewski, H. M., Wegiel, J., Wang, K. C., Kujawa, M., and Lach, B. (1989) Ultrastructural studies of the cells forming amyloid fibers in classical plaques. *Can J Neurol Sci* **16**, 535-542

Wittstock, A., Zielasek, V., Biener, J., Friend, C. M., and Baumer, M. (2010) Nanoporous gold catalysts for selective gas-phase oxidative coupling of methanol at low temperature. *Science (New York, N.Y.)* **327**, 319-322

Wu, Z., Sun, L., Hashioka, S., Yu, S., Schwab, C., Okada, R., Hayashi, Y., McGeer, P. L., and Nakanishi, H. (2013) Differential pathways for interleukin-1b production activated by chromogranin A and amyloid b in microglia. *Neurobiology of aging* **34**, 2715-2725

Wyss-Coray, T., Borrow, P., Brooker, M. J., and Mucke, L. (1997) Astroglial overproduction of TGF-b 1 enhances inflammatory central nervous system disease in transgenic mice. *Journal of neuroimmunology* **77**, 45-50

Yamaguchi, H., Hirai, S., Morimatsu, M., Shoji, M., and Ihara, Y. (1988) A variety of cerebral amyloid deposits in the brains of the Alzheimer-type dementia demonstrated by b protein immunostaining. *Acta neuropathologica* **76**, 541-549

Yankner, B. A., Dawes, L. R., Fisher, S., Villa-Komaroff, L., Oster-Granite, M. L., and Neve, R. L. (1989) Neurotoxicity of a fragment of the amyloid precursor associated with Alzheimer's disease. *Science (New York, N.Y.)* **245**, 417-420

Yates, S. L., Burgess, L. H., Kocsis-Angle, J., Antal, J. M., Dority, M. D., Embury, P. B., Piotrkowski, A. M., and Brunden, K. R. (2000) Amyloid b and amylin fibrils induce increases in proinflammatory cytokine and chemokine production by THP-1 cells and murine microglia. *Journal of neurochemistry* **74**, 1017-1025

Ye, C. P., Selkoe, D. J., and Hartley, D. M. (2003) Protofibrils of amyloid b-protein inhibit specific K^+ currents in neocortical cultures. *Neurobiology of disease* **13**, 177-190

Yin, Y. I., Bassit, B., Zhu, L., Yang, X., Wang, C., and Li, Y. M. (2007) g-Secretase Substrate Concentration Modulates the Ab42/Ab40 Ratio: IMPLICATIONS FOR ALZHEIMER DISEASE. *The Journal of biological chemistry* **282**, 23639-23644

Zahs, K. R., and Ashe, K. H. (2013) b-Amyloid oligomers in aging and Alzheimer's disease. *Frontiers in aging neuroscience* **5**, 28

Zheng, H., and Koo, E. H. (2006) The amyloid precursor protein: beyond amyloid. *Molecular neurodegeneration* **1**, 5

Zhong, Y., and Bellamkonda, R. V. (2008) Biomaterials for the central nervous system. *Journal of the Royal Society, Interface / the Royal Society* **5**, 957-975

VITA

Shana E Terrill-Usery is the daughter of Tony and Gail Terrill. She was born in Hannibal, Missouri, on January 6, 1987. She graduated from Hannibal High School in May of 2005 and continued on to attend Lindenwood University, in St. Charles, Missouri. She graduated with her Bachelors of Arts in Chemistry with an emphasis in Biochemistry in May of 2009. In the fall of 2009 she entered into the graduate program at the University of Missouri-St. Louis (UMSL) and joined the laboratory of Dr. Michael R. Nichols. She earned her MS in Chemistry and Biochemistry from UMSL in December 2011. She married Brian Usery, son of Kevin and Carol Usery, on May 4, 2013.